OPTOELECTRONIC PROPERTIES OF QUANTUM DOTS FOR BIOMEDICINE AND ENERGY-TO-LIGHT CONVERSION

Sofia Paulo Mirasol

UNIVERSITAT ROVIRA i VIRGILI

Optoelectronics properties of Quantum dots for biomedicine and energy-to-light conversion.

Sofia Paulo Mirasol

Doctoral Thesis

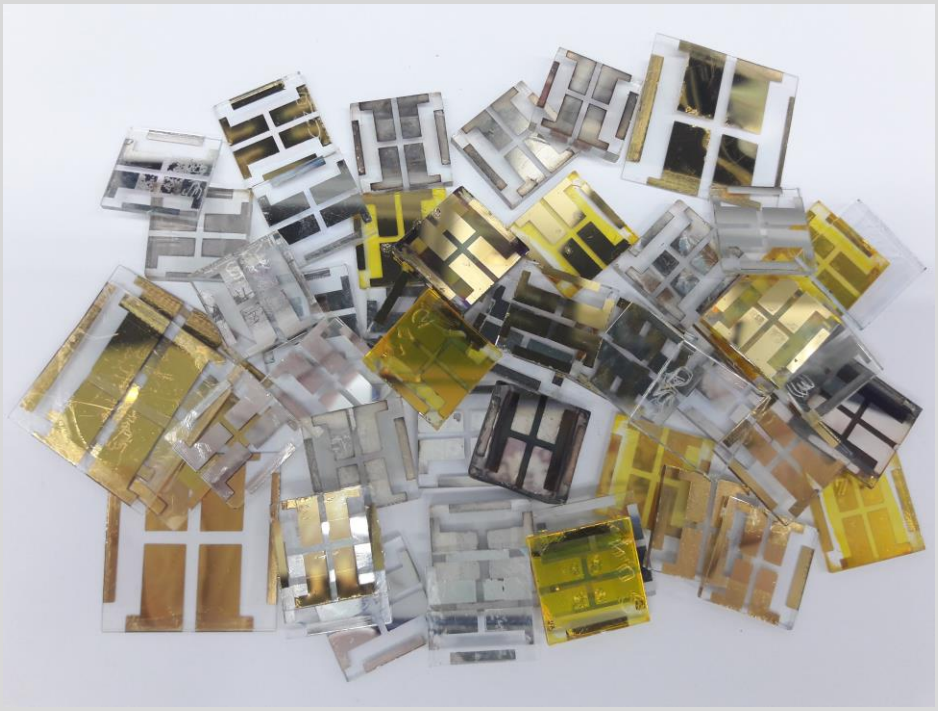

Supervised by,

Dra. Eugenia Martínez Ferrero
Prof. Emilio José Palomares Gil

Tarragona,2019

UNIVERSITAT ROVIRA I VIRGILI
OPTOELECTRONIC PROPERTIES OF QUANTUM DOTS FOR BIOMEDICINE AND ENERGY-TO-LIGHT CONVERSION
Sofia Paulo Mirasol

UNIVERSITAT ROVIRA I VIRGILI
OPTOELECTRONIC PROPERTIES OF QUANTUM DOTS FOR BIOMEDICINE AND ENERGY-TO-LIGHT CONVERSION
Sofia Paulo Mirasol

Sofia Paulo Mirasol

Optoelectronics properties of Quantum dots for biomedicine and energy-to-light conversion

Doctoral Thesis

Supervised by Prof. Emilio Palomares Gil and
Dra. Eugenia Martínez Ferrero

Institut Català d'Investigació Química-
Universitat Rovira i Virgili- Eurecat Centre
Tecnològic de Catalunya

UNIVERSITAT ROVIRA i VIRGILI

Tarragona June 2019

UNIVERSITAT ROVIRA I VIRGILI
OPTOELECTRONIC PROPERTIES OF QUANTUM DOTS FOR BIOMEDICINE AND ENERGY-TO-LIGHT CONVERSION
Sofia Paulo Mirasol

Emilio Palomares Gil, Group Leader at the Institute of Chemical Research of Catalonia (ICIQ) in Tarragona, and Research and Advanced Studies (ICREA) in Barcelona.

Eugenia Martínez Ferrero, Head of the Photonics Line in Centre Tecnològic de Catalunya Eurecat in Barcelona.

CERTIFY:

That the present research study, entitled “Optoelectronics properties of Quantum dots for biomedicine and energy-to-light conversion” presented by Sofia Paulo Mirasol for the award of the degree of doctor has been carried out under our supervision in ICIQ and Eurecat.

Tarragona, June 2019

Eugenia.

ICIQ
Dr. Emilio Palomares

Dra. Eugenia Martínez-Ferrero

Prof. Emilio Palomares Gil

eurecat
Centre Tecnològic de Catalunya

UNIVERSITAT ROVIRA i VIRGILI

ICIQ
Institut Català d’Investigació Química

UNIVERSITAT ROVIRA I VIRGILI
OPTOELECTRONIC PROPERTIES OF QUANTUM DOTS FOR BIOMEDICINE AND ENERGY-TO-LIGHT CONVERSION
Sofia Paulo Mirasol

“Trial and error”

UNIVERSITAT ROVIRA I VIRGILI
OPTOELECTRONIC PROPERTIES OF QUANTUM DOTS FOR BIOMEDICINE AND ENERGY-TO-LIGHT CONVERSION
Sofia Paulo Mirasol

Agraïments

Després de quatre anys em trobo aquí escrivint uns agraïments. Això vol dir que l'aventura s'està acabant i una nova segurament m'està esperant. Per això abans de que l'obra de teatre baixi el teló m'agradaria donar les gràcies a tots aquells que d'alguna manera o altra hagin format part d'aquest espectacle.

Les dues primers persones a les que m'agradaria agrair aquesta tesis són els meus dos directors: Dra Eugenia Martínez Ferrero i Prof. Emilio Palomares, pel suport, la paciència, l'energia i per acompanyar-me durant aquests quatre anys. En especial, a l'Eugenia per la seva immensa paciència i per saber escoltar i reforçar-me en els pitjors moments d'aquesta travessia i a l'Emilio per donar-me l'oportunitat de poder fer la tesis amb ell i per donar-nos la llibertat de poder marxar-nos d'estància i deixar que provéssim coses en el laboratori encara que sabies que no funcionarien.

Als meus companys del laboratori de l'ICIQ pels "tuppers share", calçotades i paelles a la platja Llarga. Especialment a Santiaguín per ser el meu company/marit de laboratori, sense ell la meitat d'aquesta tesis no existiria. I a la Lydia perquè durant el temps que vam coincidir juntes va ser una gran recolzament per a mi. Ens veiem aviat a Grenoble! També m'agradaria agrair aquesta tesis als companys de Eurecat per tractar-me com una més i ajudar-me durant el temps que vaig estar allà. I finalment a tots els companys que al llarg d'aquest quatre anys hem compartit ciència, riures, treball dur i moltes moltes hores al laboratori ja sigui al Japó o Grècia.

A les companyes de la Chirigota: "¡Pon pa' un lao la capa que la liamos y no hay secador!" "¡Heroinas hasta el final!". Ha estat màgic compartir aquests mesos de riures, assajos y molt de "cante". A l'Andrea y al Daniel por ser "mis soles de Tarragona". Nos seguiremos encontrando por el mundo, estoy segurísima.

A les meves noies de Coitus Interruptus! Bárbara, y tanto que nos quedaba pista y la que nos queda aún por recorrer. Irene, has sido para mi un gran descubrimiento y me siento muy agradecida de saber que te tengo como amiga

y compañera de batalla. Cristina compañera de laboratorio y amiga, lo que Palomares ha unido que no lo separe los futuros jefes! De veritat, és un plaer poder parlar amb vosaltres de política, feminisme i coses lleugeres en general, jejeje. El món és un lloc almenys més divertit i comprensiu des de que formeu part de la meva vida.

Als amics de la universitat: Irene, Marcs, Anna, Ivan, Elena i Marta pels riures i els sopars anuals. ¿Qui ho anava a dir, ehh? Em sento molt afortunada de haver-vos trobat a primer de carrera i que després de 13 anys seguim compartint la passió per viure i gaudir dels bon moments.

A les meves nenes de Barcelona i London que han estat allà des del principi dels temps... literalment! 25 anys d'amistat, sou un membre més de la família. Només puc dir-vos que gràcies, pels bons moments, pels sopars, viatges, birres, riures i plors. Encara que visquem en països o ciutats diferents que trobem sempre moments per poder veure'ns i riure'ns de la vida.

A la meva família: papes, abueli i tata, sense ells això no hauria estat possible. "I pensar que volia deixar la carrera al primer any…." Gràcies al meus pares per haver-nos inculcat a ser independents i a pensar per una mateixa sense deixar-nos influenciar per ningú. Us estimo moltíssim. A l'abueli perquè encara que ara necessites un bastó per caminar, ets la dona més forta del món. A la meva germana, només puc dir-li una cosa: gràcies per tot, de veritat. Ets la millor tata que es pot tenir. Et trobo molt a faltar però sé que a San Francisco estàs molt bé.

I finalment, m'agradaria agrair-li a la meva nova família que de moment consta de dos gats: Ratafia, Currupipi i un veronès. Ilario company de vida, amic, i amant. Ets el millor company de vida que he trobat en aquest món i saber que encara ens queda tant de camí per omplir-ho de viatges, discussions i molt de riure i amor... No sé on acabarem en aquest món però el que sí que sé és que ho farem junts.

"I vet aquí un gat, vet aquí un gos, aquest conte ja s'ha fos."

A la meva família, a la iaia i a l'Ilario.

Table of contents

List of abbreviations

A Ampere

a.u. Arbitrary units

Abs Absorbance

CB Conduction Band

Cd Candela

CIE

CQDs Carbon Quantum dots

CV Cycle Voltammetry

DLS Dynamic light scattering

DMF Dimethylformamide

DMSO Dimethylsulfoxide

EDA ethylendiamine

EL Electroluminescence

EL Electroluminescence

EtOH Ethanol

F8BT Poly(9,9'-dioctylfluorene-co-benzothiadiazole)

FT-IR Fourier transform infrared spectroscopy

FTO Fluorine-doped tin oxide

FWHM Full width at half maximum

h Hours

HDA 1-hexadecylamine

HOMO Highest occupied molecular orbital

HTL Hole Transport Layer

HTM hole transport material

hv Photon light

I Current density

IPA 2-propanol

ITO

LED Light-emitting diode

LEDs Light-emitting diode

LUMO Lowest unoccupied molecular orbital

mA/cm^2 milliamp per square centimeter

MA^+ methylamonium cation

MABr methylamonium bromide

NPs Nanoparticle

OA Oleic acid

ODE octadecene

OLA Oleyamine

PBS solution buffer phosphate

PEDOT-PSS Poly(3,4-ethylenedioxythiophene) polystyrene sulfonate

PeLED Perovskite light-emitting diode

PL Photoluminescence

PPD *p*-phenyldiamine

PVK Poly (9-vinylcarbazole)

QDs Quantum Dots

QLED Quantum dot light-emitting diode

QY Quantum yield

RPM Revolutions per time

s second

SEM Scanning electron microscopy

SWV Square wave voltammetry

TCSPC Time correlated single photon-counting

TEM Transmission electron microscopy

TiO_2 titanium dioxide

TMPyPB 5,10,15,20-Tetrakis(1-methyl-4-pyridinio)porphyrin

UV-vis Ultraviolet-visible spectroscopy

ZnO Zinc oxide

SnO_2 Tin dioxide

V Voltage

VB Valence band

XRD X-ray diffraction

λ wavelength

Abstract

In the last decade, nanoscience has emerged as a novel technology due to its versatility to be employed in many research areas. Nanoscience studies the structures and materials on the nanometers scale. One of the most promising nanomaterials, colloidal quantum dots have been deeply studied in the last decades for their extraordinary optoelectronic properties and their versatility in order to use in different fields, such as bioimaging, sensor, optoelectronic devices, etc.

Colloidal quantum dots technologies have burst in both academic and industrial field. Quantum dots are defined as nanometer scale semiconductor crystal with a physical size smaller than exciton Bohr radius, and as consequence quantum confinement. This means that their bandgap changes according to their size. Regarding the optical properties, they show broad absorption, narrow emission and color purity, especially when compared to organic semiconductors.

The present thesis is focused on the synthesis of different quantum dots as well as their use in LEDs, perovskites solar cells and sensors. Three different Quantum Dots have been synthetized: cadmium, perovskites and carbon based quantum dots. The first two material present a high quantum yield and narrow emission band. However their high toxicity is an important weakness. In order to avoid the use of those material we synthetized carbon quantum dots. Their low toxicity and biocompatibility is a good alternative to heavy metal-containing nanomaterials. In addition, carbon based material can be prepared using ordinary products as sugar or orange juice and solved in non-chloro solvents such as ethanol or water.

Quantum dots LEDs (QLEDs) have emerged in the last year as new LEDs generation due to better color definition over the entire visible spectrum. Basically, the structure consists of a sandwiched layer of emissive quantum dots between electron and hole transport layers, so when a bias is applied hole and electrons are radiatively recombined in the quantum dot layer emitting light.

The second application we worked on during this thesis was perovskites solar cells. Converting solar energy efficiently into either electrical or fuel sources remains one of mankind's biggest challenges. Despite the rapid progress that has been made in recent years in research into third generation solar cells, silicon is still the biggest and most important player in the PV industry. Such new technologies, as mixed halide perovskite solar cells are quickly catching-up efficiency (the current record of efficiency is above 22% at 1 sun). The synthetized and tested CQDs as hole transport material in order to replace the actual on, Spiro-OMeTAD because of the high production cost.

Finally,a different application of QDs has been explored, two different biosensors have fabricated in order to detect and quantify elastase in human samples. We fabricated two different sensors: an Optical and an electrochemical sensors. Both sensors present better properties such as low cost, real-time and high sensitivity and specificity comparing with the conventional analytical techniques.

The work discussed in this thesis was carried out at Institute of Chemical Research of Catalonia (ICIQ) and Eurecat, the technological center of Catalonia, between March 2015 and March 2019.

Resum

En la darrera dècada, la nanociència ha sorgit com una nova tecnologia a causa de la seva versatilitat per ser emprada en moltes àrees de recerca. La nanociència estudia les estructures i els materials a escala de nanòmetres. Un dels nanomaterials més prometedors, els punts quàntics han estat profundament estudiats per les seves propietats optoelectròniques i la seva versatilitat per utilitzar-los en diferents camps, com ara bioimaging, sensor, dispositius optoelectrònics, etc.

Els punts quàntics es defineixen com a cristalls semiconductors a escala nanomètrica amb una grandària física menor que el radi exciton de Bohr i, com a conseqüència, presenten confinament quàntic. Això significa que el seu bandgap canvia segons la mida de la partícula. Pel que fa a les propietats òptiques, mostren una àmplia absorció, una emissió estreta i una puresa de color, especialment si es compara amb semiconductors orgànics.

Aquesta tesis doctoral es centra en la síntesis i caracterització de diferents punts quàntics, així com en el seu ús en LEDs, cèl·les solars perovskites i sensors. S'han sintetitzat tres punts quàntics diferents: cadmi, perovskites i punts quàntics basats en carboni. Els dos primers materials presenten una banda de emissions reduïdes de rendiment quàntic elevat. No obstant, la seva alta toxicitat és un inconvenient que s'ha de tenir en comte . Com alternativa al seu ús, hem sintetitzat punts quàntics fets de carboni. Gràcies a la seva baixa toxicitat i biocompatibilitat els punts quàntics fer de carboni es presenten com una bona alternativa als nanomaterials que contenen metalls pesants. A més, els punts quàntics fets de carboni es pot preparar amb productes normals com sucre o suc de taronja i resolt en dissolvents no clorats com ara l'etanol o l'aigua.

Quantum Dots LEDs (QLEDs) es van produir durant el darrer any com a nova generació de LEDs a causa d'una millor definició de color a tot l'espectre visible. Bàsicament, l'estructura consisteix en una capa intercalada de punts quàntics emissius entre les capes de transport d'electrons i forats, de manera que quan s'aplica un biaix el forat i els electrons es recombinen radiativament a la capa quàntica que emet la llum

Quantum Dots (QLEDs) han sorgit en els últims anys com una nova generació de LEDs a causa de les seves propietats. Bàsicament, l'estructura consisteix en una capa intercalada de punts quàntics emissius entre capes de materials transportadors d'electrons i forats, de manera que quan s'aplica un biaix el forat i els electrons es recombinen radiativament a la capa quàntica que emet la llum.

La segona aplicació que hem treballar durant el desenvolupament d'aquesta tesis van ser amb cel·les solars de Perovskites. La conversió de l'energia solar de manera eficient en fonts elèctriques o de combustible continua sent un dels grans reptes de la humanitat. Malgrat els avenços ràpids realitzats en els darrers anys en la investigació de cèl·les solars de tercera generació, el silici continua sent el qui presenta millor eficiències. Les noves tecnologies, com les cèl·les solars de perovskites es presenten com una bona alternativa a la tecnologia actual pel seu baix cost de fabricació i per la seva eficiència (l'actual registre d'eficiència és superior al 22%). Vam sintetitzar punts quàntics de carboni i els vam testar com a transportador de forats per reemplaçar l'actual, Spiro-OMeTAD pel seu elevat cost de producció.

Finalment, s'han fabricat dos biosensors per detectar i quantificar l'elastasa en mostres humanes. Hem fabricat dos sensors diferents: un òptic i un sensor electroquímic. Els dos presenten característiques com baix cost de producció, mesures en temps real i també presenten una alta sensibilitat i especificitat en comparació amb les tècniques analítiques convencionals.

El treball tractat en aquesta tesis es va desenvolupar en l'Institut d'Investigació Química de Catalunya (ICIQ) i en el centre tecnològic de Catalunya (Eurecat), entre març de 2015 i març de 2019.

Contribution to scientific community

S. Paulo-Mirasol, G. Stoica, W. Cambarau, E. Martinez-Ferrero, E. Palomares, Carbon quantum dots as new hole transport material for perovskite solar cells. *Synth. Met.* **222**, 17–22 (2016).

S. Paulo-Mirasol, E. Palomares, E. Martínez-Ferrero, Graphene and Carbon Quantum Dot-Based Materials in Photovoltaic Devices: From Synthesis to Applications. *Nanomaterials*. **6** (2016), p. 157.

S. Paulo-Mirasol, E. Martinez-Ferrero, E.J. Palomares. Direct White Light Emission from Carbon Nanodots (C-dots) in solution processed Light Emitting Diodes. *Nanoscale* **2019**.

Manuscripts in preparation

S.Paulo-Mirasol, S.Gené, E.Martínez-Ferrero, E.Palomares, Carbon Quantum Dots as hole transport layer in Light Emitting diodes.

Introduction

During the last decades, colloidal quantum dots (QDs) have been extensively studied due to their optoelectronic properties and their potential for applications in electronic and biological systems. In this chapter, we will describe the synthesis of colloidal quantum dots and their applications in Light Emitting Diodes (LEDs), perovskites solar cells and biological applications.

Chapter 1

Table of contents

Chapter 1

1.1 Quantum dots: Introduction and general properties.

In 1856, Faraday reported the first study of how material properties can vary with size describing the optical properties of nanoparticles of gold [1]. Since their discovery in the early 1980's, Colloidal Quantum dots (QDs) have been extensively studied due to their optoelectronic properties in various application areas. In 1981, the Russian solid state physicist Alexey I. Ekimov Link, working at the Vavilov State Optical Institute in St. Petersburg discovered quantum dots in a glass matrix. Later, an American chemist Louis E. Brus working at AT&T Bell Laboratories synthesized quantum dots in a colloidal solution [2]. However, it was not until the early 1990's when appeared the first paper written by Murray, Norris and Bawendi, which described the hot injection synthesis for colloidal quantum dots [3,4].

Nanoparticles can be divided depending on the size, shape and composition [4]. In this thesis, we worked with metal oxide nanoparticles (ZnO NPs) and three quantum dots made of different materials: cadmium, carbon and perovskites based Quantum Dots.

Colloidal Quantum Dots are zero dimensional semiconductor nanoparticles, which are composed of an inorganic core with an organic capping. The electronic structure of colloidal QDs, typically from 2 nm to 12 nm in diameter, which is generally smaller than the exciton Bohr radius (the diameter of the particle is in the same order of magnitude than the wavelength of the electron), present quantum confinement [5]. This Quantum confinement effect is responsible of the increase of energy difference between energy states and band gap. The band gap generally refers to the energy difference (in electron volts) between the top of the valence band and the bottom of the conduction band in insulators and semiconductors. This effect is more remarkable in semiconductors material because they have a conduction and valence band[3]. Such effect is important because as consequence, Colloidal Quantum Dots possess optical and electronic properties that differ from large particles, such

as wide absorption, narrow band emission, color tunability and long fluorescence lifetime.

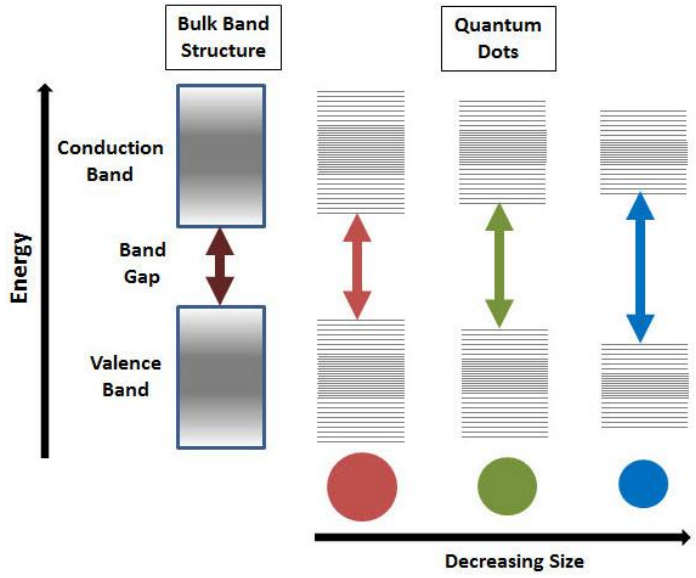

Figure 1. 1 Quantum confinement schema.

Colloidal Quantum Dots (QDs) have an intrinsic energy band gap that depends on the size of the nanoparticle and influences the absorption and emission spectra. The color emission band of a Colloidal Quantum Dots is directly related to its size, the smallest QDs produce shorter wavelength and bluer color light, while the biggest particles produce red color light.

Typically, QDs present a narrow emission Full Width at Half Maximum (FWHM) around 20 nm due to their quantum confinement, thus they give more advantages than conventional organic dyes. The emission spectra of QD can be tuned varying the size distribution, in comparison with dyes whose broader emission band cannot. This is a very important advantage because in order to identify different emission peaks, we can modulate them avoiding the overlapping bands.

In addition, QDs present better advantages compared with the conventional dyes as broader absorption, narrower emission spectra, major resistance

photobleaching, long luminescence decay time and a large stoke shift, which is the energy difference between the maximum of the first absorption band and the maximum of the fluorescence spectrum [6,7].

1.1.1 Types of Quantum Dots.

A wide range of quantum dot materials have been fabricated for investigation and use in various applications, including CdS, CdSe, ZnS, PbS, SnS, SnSe, PbTe, PbSe, InAs, GaAs, InP, Carbon Quantum dots and halide perovskites.

Under simplistic point of view, QDs are formed by an inorganic core and organic ligand. Due to the inorganic semiconductor cores, QDs have a higher stability than organic dyes to degradation caused by effects such as photobleaching. The organic ligands give to the quantum dot stability against the aggregation.

In this thesis, we focused in the synthesis and test of optoelectronic properties of QDs made of the following materials: cadmium, carbon and perovskites quantum dots, all of them deposited onto ZnO nanoparticles (ZnO NPs).

1.1.1.1 Cadmium based quantum dots.

Cadmium based Quantum Dots is the most deeply studied nanomaterial due to their high quantum yield, and have been tested in many applications [8, 9, 10, 11].

The most common way to synthesize cadmium based quantum dots achieving high quantum yield was via hot injection method. This synthesis was described by Murray et al [3] in 1993. Briefly, the synthesis of Cd-based QDs is carried out using metal chalcogenide precursors, organic ligands in order to avoid the aggregation and a high boiling point inert solvent to homogenize the solution. The temperature during the synthesis must be high enough to promote the crystals formation. The ligand used must be ambipolar because the polar heads must bind in the surface of QDs while the non-polar part control the diffusion of the precursor and solubilizes it.

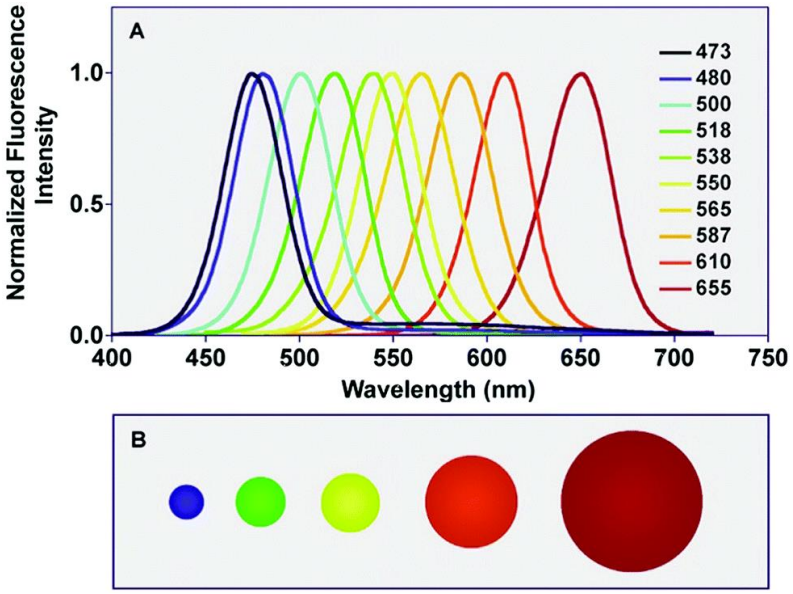

Figure 1. 2. Size dependent fluorescence spectra of cadmium based quantum dots. From the left to right, the particles diameters are 2.1 nm, 2.5 nm, 4.7 nm and 7.5 nm. Ref A. M. Smith and S. Nie, *Analyst*, 2004, **129**, 672–677.[12]

In the case of Cadmium based quantum dots the bandgap tunability can be modified during the reaction time[12]. Figure 1.3 shows a picture of different aliquots that we took during the synthesis of CdSe QDs. We can observe the emission color shift from green to red.

Figure 1. 3. Pictures of different aliquots of the same synthesis of CdSe QDs.

Since the surface-to-volume ratio of QDs is high, their surface has to be protected in order to obtain high photoluminescence intensity. [13]. The growth of a second material on top of a inorganic core has a powerful advantage in order to improve their photoluminescence quantum efficiency and protecting against the oxidation and trap formations [14].

Two heterostructures can be divided depending on the core/shell. Figure 1.4 show the diagram of both heterostructures. In type-I, the conduction band of the shell is lower in energy than the core's one and both carriers are confined in the core as CdSe@ZnS, InP@ZnS. In type-II, one carrier is confined in the shell and the other in the core it means that the electron and hole wave functions are centered in different materials, and thus in different segments of the hetero-NC (e.g., CdSe/ZnTe, CdSe/CdTe).It means that the emission can be tuned modifying the size of the core and the shell. However, they present longer radiative lifetimes due to the slow electron-hole recombination, an as consequence these structures present a poor PLQY.

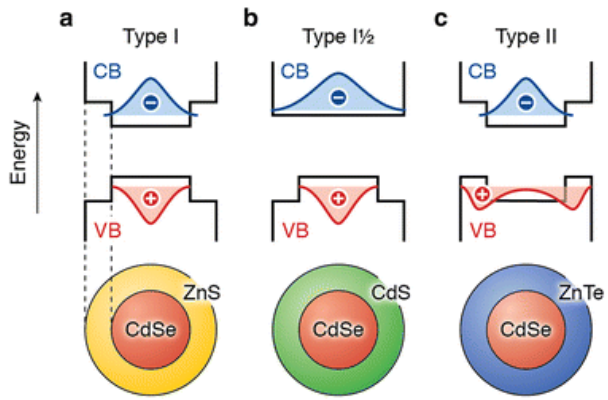

Figure 1. 4. Diagram of core/Shell heterostructures [13].

In this thesis, we synthetized two types of cadmium based quantum dots: CdSe passivated with ZnS [15]. In Figure 1.5 shows an example of PL spectra of CdSe capping with ZnS. This improvement of the PL intensity is caused because the

ZnS coating suppresses deep trap emissions by passivating the vacancies and trap sites on the crystallite surface.

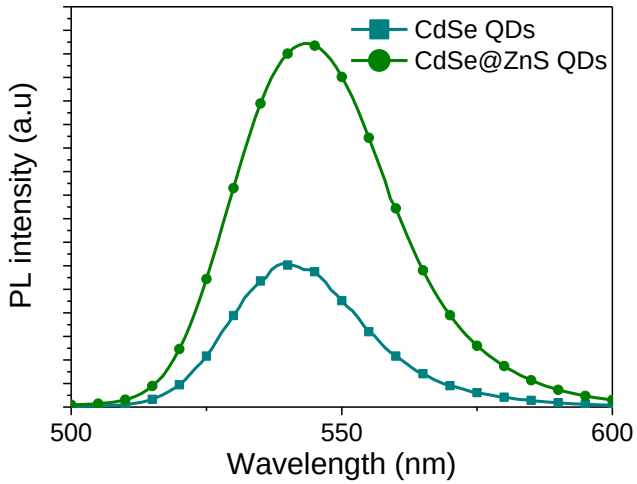

Figure 1. 5. PL spectra of CdSe QDs and CdSe@ZnS QDs solved in chloroform at room temperature, after excitation at 480 nm.

1.1.1.2 Perovskites based quantum dots.

Perovskites (named after the Russian mineralogist Lev Perovski who discover them in 1839) are any class of materials with a similar structure as calcium titanium oxide mineral ($CaTiO_3$), so the general chemical formula of perovskites is ABX_3. Where A= CH_3NH_3, CH_5N_2, Cs; B= Pb, Sn; X= Cl, Br, I. Perovskites are considered the most promising nanomaterial to be used in solar cells and other optoelectronic devices such as electric vehicle batteries, displays, sensors, lasers.

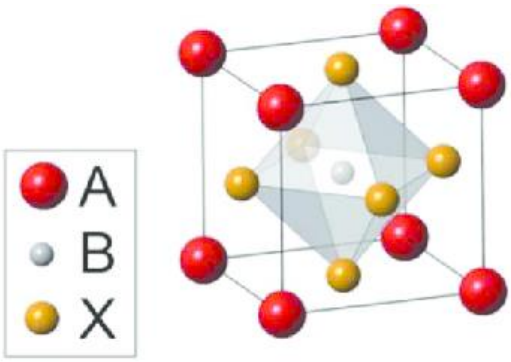

Figure 1. 6. The structure of organic-lead trihalide perovskites ABX_3.

Their optoelectronic properties such as high absorption coefficient, tunable optical band gaps, low exciton binding energy, have been explored for new applications for instance, solar cells and light emitting diodes. The most studied application is the use of this material as active layer in solar cells, although others applications have been reported. For instance, Nikolaou and coworkers immobilized perovskite on top of Graphite/SiO_2 hybrid electrodes as electrochemical sensor to detect an antihypertensive drug [16]. Regarding solar cells, the current record efficiency is above 20 % at 1 sun [17].

In addition, this material can be solved in many organic solvents, which means that can be deposited using different techniques such as roll-to-roll or inkjet printing [18], this is very important under the scale up point of view [19].

As we mentioned previously, Nanomaterials size and shape can be controlled by changing the reaction time, surfactant and temperature reaction. In this thesis, we worked with perovskites thin film and perovskites nanoparticles.

Perovskites Quantum Dots have gained significant attention for research and commercial applications for their potential in many applications [20, 21, 22].

This material presents remarkable tunable emission wavelength over the entire spectra of 410-700 nm, changing the anion ratio [23] (See Figure 1.7). This property differ from other quantum dots whose band gap tuneability can be modified with the reaction time or doping with heteroatom such as nitrogen or phosphor [24].

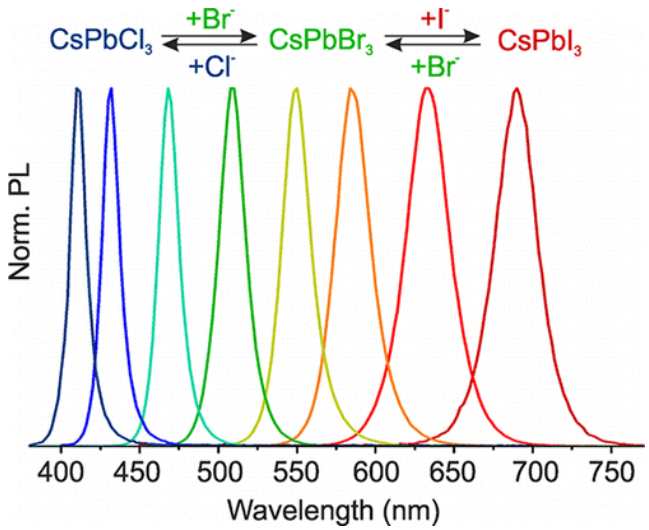

Figure 1. 7. Schematic emission band of cesium lead halide perovskite [25].

Some papers have published an anion exchange via post-synthetic reactions. For instance, Akkerman *et al.*[26] reported an easy post-synthesis using different routes depending on the desired emission wavelength. They demonstrated that the anion exchange did not affect to the final crystal structure. In the last years, many synthesis approach changing the anion and the cation of perovskites materials have been published [27]. The reasons were because of the poor ambient stability and the thermal stability of the material as well as to increase their efficiency in both solar cells and LEDs.

There are some approaches to obtain perovskites nanoparticles depending on the desired size and shape [28].

1. LARP synthesis.

The synthesis of perovskites was carried out in air conditions at room temperature. The colloidal NPs were synthetized preparing a solution of methylamonium lead halide precursors solved in DMF. Then, part of this solution was dropped in toluene in the presence of a long alkyl chain such as oleic acid, oleyamine, etc. In the LARP method, the particles presented different size and shape distributions. Schmidt and coworkers synthetized colloidal

solutions of $CH_3NH_3PbX_3$ nanoparticles with sizes below 10 nm [29]. CH_3NH_3Br with a long chain alkyl was reacted with $PbBr_2$ in the presence of oleic acid and octadecene. The ammonium ions act as capping ligand while alkyl chains control the stability of perovskites against the aggregation.

1. Hot injection method.

This method is carried out in inert conditions. In a three neck round bottom flask, a mixture of the lead halide with a high boiling point solvents is mixed. Then, a solution of cesium-oleate is injected. For this growth, a high initial temperature is needed and the addition of the precursor in order to control the nanoparticle nucleation. This method allows to obtain high quantum yield material (up 80 %) and narrow band-width emission (10-40 nm) although it is needed to work in inert conditions. Furthermore, the size of quantum dot can be modified but changing the anion ration and the temperature.

2. Other approaches.

There are other examples of perovskites nanoparticles synthesis in air conditions. For instance, Akkerman *et al.*[30] reported the synthesis of perovskites nanoparticles tuning their emission wavelength changing the ratio of isopropanol (IPA) and hexane. Two solutions are prepared at room temperature: 1) A solution of cesium carbonate is solved in propionic acid at room temperature, 2) lead bromide is solved in a mixture of butylamine, isopropanol and acid propionic (PrAc). Then, both solutions are dropped to a solution of hexane/IPA. The quantum yield of some of the solutions is up to 70%.

Figure 1. 8. Perovskite solution with different ratio of hexane/IPrOH under UV-vis lamp excitation.

Other example was reported by Schmidt and coworkers [29]. They synthetized 6 nm of methylamnonium or octylammonium lead bromide nanoparticles at room temperature. The nanoparticles were synthesized using a simple preparation method in which a mixture of CH_3NH_3Br with long chain alkyl ammonium bromide was reacted with $PbBr_2$ in the presence of oleic acid and -1-octadecene. These nanoparticles were solved in aprotic, moderate polarity, organic solvent with a stability of three months. The narrow band-width was 20 nm and the quantum yield 17%.

1.1.1.3 Carbon quantum dots.

Since their discovery in early 2000s, carbon-based quantum dots have been the focus of intensive research because of their excellent luminescent properties, good solubility and biocompatibility [31].This research effort increased exponentially after the Nobel Prize awarded to Novoselov and Geim for discovering graphene and describing its properties [32]. By definition, carbon quantum dots (CQDs) are quasi-spherical nanoparticles less than 10 nm in diameter, formed by crystalline sp2 graphite cores, or amorphous aggregations, which have a quantum confinement effect.

Many papers describing synthetic procedures to prepare carbon quantum dots can be classified in two main approaches: bottom-up and top-down. Specifically, the bottom up route builds nanostructures from small organic molecular precursors by pyrolysis, combustion or hydrothermal methods while the top-down approach is based in cutting small sheets via physical, chemical or electrochemical techniques until reaching the required size. In both cases, post treatment is done to purify or modify the surface functionalization to improve the performance of the CQDs.

For example, the quantum yield increases after surface passivation of CQDs or functionalization due to the disappearance of the emissive traps on the surface. On the other hand, doping with heteroatoms such as nitrogen, phosphor or metals such as Au or Mg improve the electrical conductivity and solubility of CQDs and GDs, as well [33].

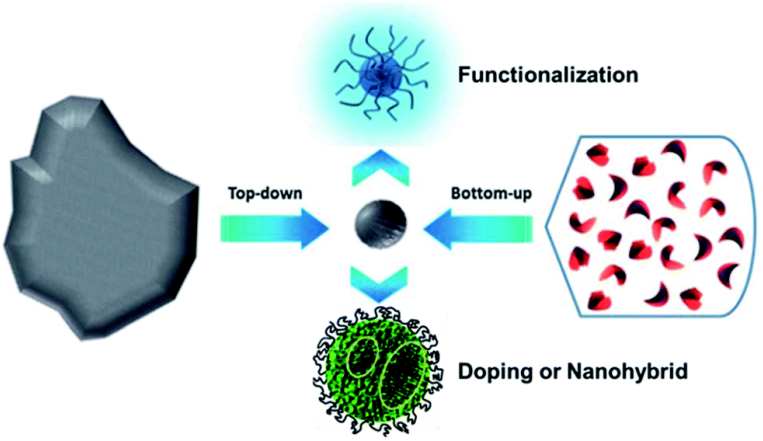

Figure 1. 9 Schematic figure of top-down, bottom-up approach to synthetize CQDs[34].

Bottom-up approach.

1. Hydrothermal/solvothermal synthesis

The hydrothermal synthesis is a wide-spread procedure that consists in one-step synthetic procedure where an organic precursor is heated in a Teflon line

to achieve high temperature and pressure. Using different organic precursors and modifying the temperature, the optoelectronic properties of the dots are tuned. It is, thus, a low cost, non-toxic method. In addition, hydrothermal methods lead to dots of 10 nm of diameter that are bigger than dots produced by other techniques such as electrochemical preparations (3-5 nm). For instance, Zhang *et al*.[35] prepared the CQDs from citric acid and ethylendiamine in aqueous solution heated for 10 h at 250 °C obtaining uniform 1–2 nm size particles , whereas Liu et al.[36] synthesized the CQDs combining polystyrene-co-maleic and ethylendiamine dissolved in DMF at 200°C for 5 h. Both papers described the use of CQDs as electron transport layer improving the charge carriers in organic solar cells.

Some papers have described different application to use these materials. Pioneering work by Mirtchev and coworkers introduced the use of carbon quantum dots as sensitizers in dye-sensitized solar cells (DSSC) prepared by dehydrating G-butyrolactone [37].

2. Microwave irradiation synthesis

As well as the speed of the synthesis, another important advantage that microwave synthetic methods have over hydrothermal synthesis is that they can be used at lower temperatures. Dao *et al.* [38] obtained high quality CDs by this synthetic approach. They mixed citric acid and urea in distilled water and the solution was then heated in a microwave oven at 700 W for 4 min. The supernatant was neutralized with sodium bicarbonate and cleaned with distilled water. The resulting dots were doped with Au by chemical reduction of $HAuCl_4$ with formic acid to prepare three dimensional raspberry-like particles with a diameter of 200 nm formed by gold branches that originated high surface areas. In addition, Tsai and coworkers synthesized water soluble CQDs by microwave irradiation using glucose as carbon source and water as solvent heating at 700 W for 11 min. The CQDs measured 3.4 nm measured by TEM [39].

Top-down approach

1. Electrochemical methods

Electrochemical methods allows the fine tunning of carbon nanostructures by controlling the voltage/current applied. For instance, appliying a controlled bias to a bulk of carbon precursors leads to electrochemical corrosion reactions over the carbon reactants and subsequently to carbon nanostructure [40]. It is important to notice that this particular technique does not require of high temperatures, is easy to scale-up and can proceed under aqueous or non-aqueous solution, being one of the fastest routes to prepare Graphene sheets [41].

2. Acidic oxidation or chemical ablation

In essence, this two-step procedure consists in the exfoliation of graphite powder using concentrated mineral acids and oxidizing agents under refluxing conditions. This approach, also known as Hummers method, is one of the most popular procedures described to obtain graphite oxide. The first step is often followed by further chemical reduction to prepare the quantum dots.

1.2 Applications.

As we explained previously, Quantum Dots have a great potential due to their optoelectronic properties to use in many research field [42]. The thesis aimed to synthetize different Quantum Dots for using them in applications in lighting, photovoltaics and biological sensor. These applications are discussed in more detail below.

1.2.1 Biosensor applications.

In 1962, Clark and Lyons published the first biosensors [43]. They presented an electrode that monitored the glucose in blood. From that moment, the variety of applications using this kind of sensors has increased. Under simplistic point of view, a biosensor can be defined as a device used for the detection of an

analyte, that combines a biological structure such as peptide , enzyme, RNA, with a physicochemical detector [44, 45, 46,47]. The first enzyme sensor was reported by Updike and Hicks in 1967 [48]. Inside the clinical research, the use of biomarkers to detect and diagnose disease is one of the most studied fields, because of their high specificity and selectivity. The working principle of a biosensor depends on the type of transducer used, which is selected according to the analysis required. In addition, biosensors have received attention for the rapid detection, low cost and portability.

In this thesis two different sensors have been tested using the optoelectronic properties of Quantum Dots. Figure 1.10 shows a schema of both sensors that we used during this thesis.

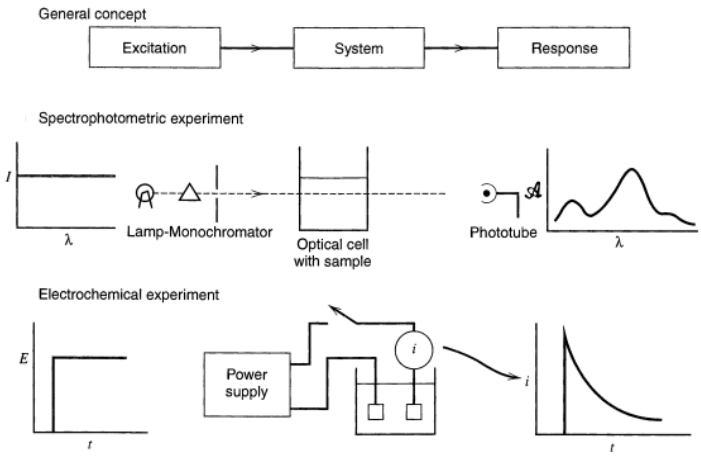

Figure 1. 10. Schema of two sensors fabricated during the thesis.

In 1998, Bruchez *et al*. [49] published the synthesis of CdSe covered with ZnS or CdS encapsulated in silica shell to use label fibroblast cells. From that publication, plenty of papers have been published using quantum dots as bioimaging, labeling in a cells. The possibility of an easy post-synthesis modification of the surface has allowed to immobilize organic molecules on the surface of Quantum dots. Different techniques have been studied to immobilize for example, enzymes, peptides or aptamers onto the support [50].

There are many ways to immobilize our biological receptor on top of the electrode such as entrapment within self-assembled monolayers, using a permeable membrane, polymeric matric or covalent bonding. We used the covalent bonding of receptors onto Nanospheres surface or in the surface of carbon quantum dots, using glutaraldehyde.

1.2.1.1. Optical sensor.

Optical biosensors use the interaction between light and matter to report the presence of the analyte. Amongst optical biosensors, the most common one use fluorescence as the detection technique, which involves the absorption of one photon and the emission of a second photon of lower energy. The fluorescence signal is isolated and collected using a detector. In this thesis, we took advantage of the outstanding emission properties of quantum dots.

Regarding the electro-optical properties of QDs used as sensing system, there are different energy transfers processes: fluorescence resonance energy transfer (FRET) bioluminescence and chemiluminescence resonance energy transfer (BRET and CRET) [51], charge transfer (CT) and electrochemiluminescence (ECL).

In this work, we have designed optical sensors that use FRET for detection of biological analyte. FRET is a physical phenomenon that shifts energy from an electronically excited molecule (donor) to a neighboring molecule (acceptor). To allow this process to happen, two requisites are necessary: 1) the donor emission band has to partially overlap to the acceptor absorption band, and 2) the acceptor and the donor must be close to each other [52].

Many literature examples reported the use of both fluorescence optical sensors, taking profit of the emission properties of QDs. The most studied sensor application was glucose detection [53] , but other examples can be found; Lowe and coworkers reported a sensor to detect at the same time two enzymes, proteases and kinases. They attached a specific enzyme onto gold nanoparticles. [54]. Algar *et. al*. presented another sensor based on FRET

process between quantum dot an enzyme.[55] They anchored directly two enzymes onto the surface of QDs.

1.2.1.2. Electrochemical sensor.

Electrochemical sensors are the most common commercially available sensor devices, due to their low cost, high sensitivity and specificity. An electrochemical sensor can be defined as a device which can measure the concentration of an analyte that is present in the environment because of the current change of the cell.

The electrochemical sensor is formed by three electrodes: the working electrode, the auxiliary and reference electrode. When the analyte gets in contact with the sensor, an oxidation or reduction reaction occurs. In this reaction, a charge transfer between the analyte and the electrode happens and, as a consequence, an electric current is generated in the system. An electrochemical sensor provides a rapid and specific response for a specific analyte. Electrochemical sensors are the most versatile and highly developed chemical sensors, and can be divided in several types depending on the electrical response they measure: potentiometric (voltage), amperometric (current) or conductometric (conductivity).

In our case, we fabricated an electrochemical sensor based on amperometric measurements, where adsorbed molecules on the surface cause a change in current intensity. Different materials can be used in this type of sensors such as conducting polymers, organic semiconductors and metal oxide semiconductors.

We used the surface of CQDs to anchor a specific peptide to recognize a specific enzyme. The modification of the quantum dots surface opened a new technology based nanomaterials. The easily surface tunable of quantum dots allow to achieve high selectivity and sensitivity.

1.2.2. Light emitting diodes (LEDs).

Incandescent light bulb was invented in XIX century and became the most popular light source. The emission of light is caused by heating a filament, but this emission is not efficient since 95% of energy supplied to the lamp is lost as heating. Thomas Edison is considered the inventor of the light bulb, which on October of 1878 registered his first patent for “Improvement in Electric Lights”. Although, there were a number of people who invented some prototypes before him. One of those was a physicist Joseph Wilson Swan who received the first patent for a complete incandescent light bulb with a carbon filament in 1879. Furthermore, Swan’s house was the first to light up with an incandescent bulb. The average rated life for this kind of bulb are between 750-2000 hours [56].

In 1896 a new technology of fluorescent light sources appeared. An electric current in the gas excited the mercury vape, which produces short-wave ultraviolet light that then excites a phosphor coating on the inside of the lamp. There are three types of fluorescent lamps: cold cathode, hot cathode and electroluminescent. They all use phosphors excited by electrons to create light. The efficiency was improved considerately due to its narrowband emission concentrated in the visible part of the spectra. Another advantage is their longer startup time, around 10.000-20.000 hours. Some weaknesses of these light sources are the use of mercury and other environmentally unfriendly materials. In addition, the color is limited by the narrowband emission.

LEDs work on the electroluminescent principle. They present advantages such as low energy consumption, small size, longer lifetime and faster switching than incandescence lamps.

In 1961, Gary Pittman and Bob Biard found that gallium-arsenide diode emits infrared light accidentally while they were working on laser diodes. It was not until 1962, when Nick Holonyak invented the first LED that could produce visible red light using the semiconductor gallium arsenide. In LEDs, the current is used to inject electrons and holes from the cathode and anode to the active semiconductor material. Due to radiative recombination, light is emitted in a narrow band, allowing higher efficiencies compared with the conventional

bulbs. In 2014 Akasaki, Amano & Nakamura received the Nobel Prize in Physics for the invention of efficient blue light emitting diodes[1].

Organic light emitting diodes (OLEDs) are promising candidates for general illumination since they offer the possibility to realize large area light sources, which can even be transparent and flexible. The advantages of using LEDs instead of incandescent light source are the lower energy consumption, longer lifetime, improved physical robustness, smaller size, and faster switching. An OLED is a solid-state device based on an organic compounds that emits light from an active layer which is sandwiched between the cathode and the anode, all deposited on top of a substrate. In order to improve the efficiency, OLEDs can be fabricated with two or more materials as active layer. OLED technology has been incorporated in many applications such as, display for mobile phones, TV, etc.

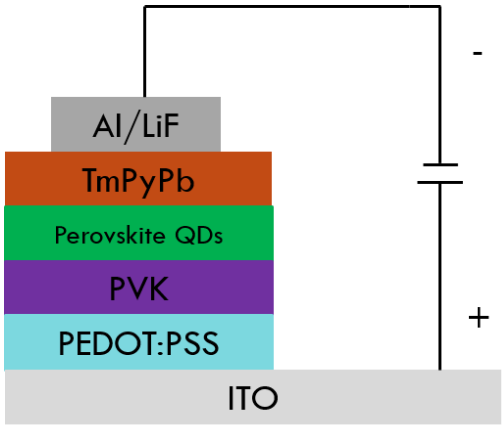

Figure 1. 11. Example of OLEDs fabricated in ICIQ.

In order to integrate metal oxides into devices that give robustness against the degradation of the devices, a new type of hybrid organic light emitting diodes have developed in the last decades. Hybrid organic/inorganic light-emitting diodes combine thin, metal oxide layers together with light-emitting organic semiconductors to create devices that are more resistant to ambient conditions than standard devices [57]. The electron injection takes place from ITO through the metal oxide conduction band to the LUMO of the organic material.

Different materials can be used as emissive layer in both arquitectures. The most used were small molecules and polymers [58,59]. However, since the discovery of quantum dots, the use of this materials as active layers in LEDs have increased. As we mentioned previously their optoelectronic properties as narrow emission, high color purity, high brightness with low turn/on voltage. QLEDs have become one of the most hotspots in display field for their large-are production, solution progress fabrication and high color saturation.

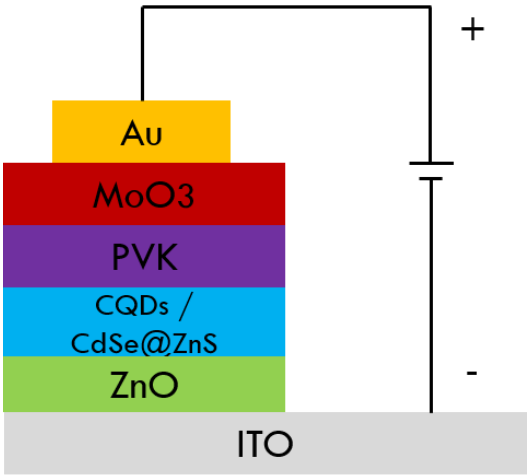

Figure 1. 12. Example of hybrid organic LEDs fabricated in ICIQ.

1.2.2.1. Device measurements.

Current density-voltage (J-V) measurements are used to evaluate the performance of the fabricated diodes. From this measurements some important parameters can be extracted, such as turn-on voltage, maximum luminance and luminous current efficiency. Figure 1.13 shows an example of the IV curve of LEDs fabricated in our group using F8BT as emissive layer and ZnO NPs as electron transport layer.

From these curves, some parameters related to LEDs performance can be obtained, as described below.

Turn-on voltage (V_{on}) is defined as the voltage at which the Luminance achieved at 0.1 Cd/m^2.

Maximum Luminance (L_{max}). It is defined as the amount of light that passes through, is emitted or reflected from a particular area, and falls within a given solid angle. The SI unit for luminance is candela per square meter (Cd/m^2).

Luminous current efficiency (η_L) is used to quantify the emission properties of LEDs. The luminous efficiency is defined as the ratio between the luminous intensity and the current intensity. The SI unit is candela per Ampere (Cd/A).

$$\eta_L = \frac{\mathrm{A}\ x\ L}{I} \quad \left(\frac{Cd}{A}\right)$$

Where A is the area (m^2), L the luminance of the diode (Cd/m^2) and I is the current (I).

The electroluminescence is a good technique in order to understand the characteristics of the emitted photons on the radiative centers inside the devices. The electrical injection (holes/electrons) move from the anode or cathode until the active layers where these carriers recombine emitting a photon.

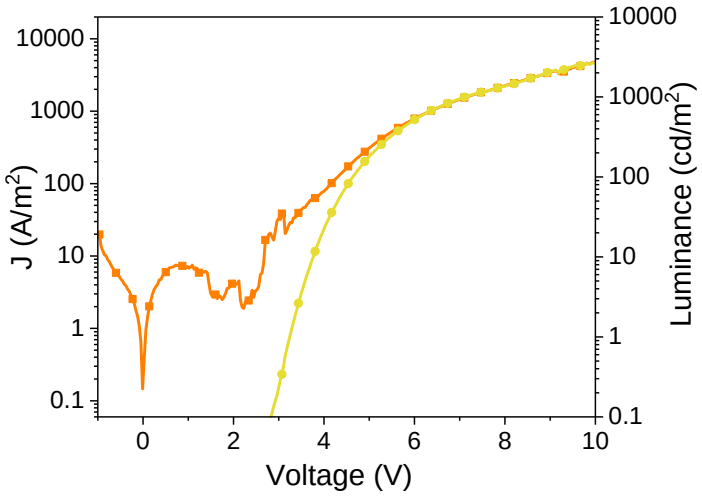

Figure 1. 13. Current density (orange line) and luminance (yellow line) versus applied voltage of the HyLED using F8BT as emissive layer and ZnO NPs as electron transport layer.

1.2.2.2 Emissive color measurement (CIE).

There are different ways to characterize LEDs, and from an industrial point of view, there are some standards that we have obey, such as color consistency, and color and lumen maintenance. Traditional lights are classified by brightness and warm or cold white color. LEDs are measured by their luminous flux and their chromaticity. For that, there are two different ways to measure the optical properties: correlated color temperature (CCT), color rendering index (CRI) or (CIE).

CCT is to classify the color between warm and cold color meanwhile the CRI represents the quality of the light that a source emits. The CRI compares light sources measured at the same temperature, against a reference source. The last one, CIE, is the standard color rendering which give us information about the optical properties of LEDs. This method to characterize the LEDs color was described by David MacAdam in the mid-20th century. The emissive color was measured using Ocean Optics spectrometers, where an integrating sphere captured all the flux that the LED emitted. Then, the saturated colors can be localized in the perimeter of the paraboloid and the white color in the center (Figure 1. 14).

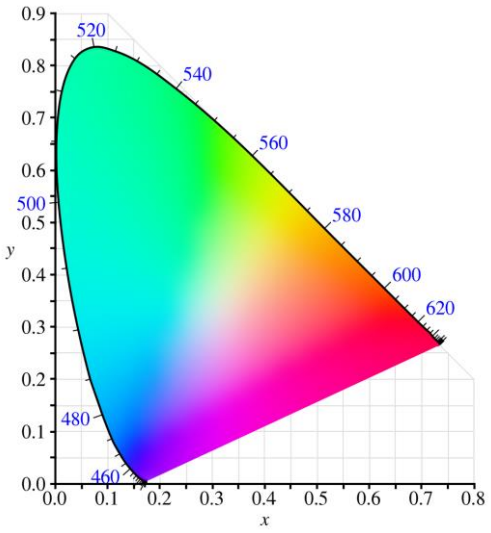

Figure 1. 14.Chromaticity diagram.

1.2.3 Perovskites solar cells.

In 1839, Alexader Edmond Becquerel observed the photovoltaic effect via the absorption of the light by a conductive material creating electrical voltage. From that date, the study and the development of solar cell technology have been studied by several scientists such as Charles Fritts which created the first solar cell by coating selenium with a layer of gold at 1883 or Heinrich Hertz who observed the photoelectric effect for the first time at 1887 [60].

In 1954, Bell Laboratories discovered and started to sell silicon PV technologies with a 6% of efficient based on p-n junction. To date, the efficiency of silicon PV is 42.3 % for certain multijunction solar cells. Certain disadvantages, including toxicity and high costs because of the high needed purity of silicon wafers, have led researchers to seek for a low-cost and environmentally friendly solar cell technology. Several semiconductors materials have been tested in order to achieve better efficiency and low-cost procedures compared with silicon PV. The most remarkable ones are dye sensitized solar cells (DSSC), inorganic solar cells, organic solar cells (OPV), and perovskite solar cells [11].

DSSCs are a regenerative photoelectrochemical cells based on the sensitization of a semiconductor such as titanium dioxide with a dye which absorbs a wide range of the spectrum, invented in 1991 by Professor Michael Graetzel and Dr. Brian O'Regan. The light-sensitive dye is responsible for converting photons into electrons[61].

Inorganic solar cells are formed by a p-n junction of inorganic materials [62]. Different materials such as, doped monocrystalline, polycrystalline or amorphous silicon have been tested in solar cells achieving a efficiency of 25 %, 20 % and 13 %, respectively. Although, this technology has not been able to produce flexible substrates, which limited their used to rigid flat surfaces and large-scale production.

The organic photovoltaics (OPV) combined the use of two organic materials as either hole transport layer or electron transport layer sandwiched between two metals. The first OPV presented was at 1986 by Tang [63] with a power conversion of 1 %. This technology present advantages compared with inorganic solar cells or silicon PV such as ease of fabrication, flexibility and low cost fabrication.

Perovskites solar cells have attracted interest since 2009, Miyasaka et al. applied methylamonium lead iodide ($MAPbI_3$) and methylamonium lead bromide ($MAPbBr_3$) as sensitizers in dye-sensitized solar cells [64]. Since this new photovoltaic technology has emerged in the field, halide perovskites have demonstrated exceptional progress in PV cell performance, from 3.8% in 2009 to a certified 22% in 2016, a value that is highly competitive in comparison with silicon solar cells. Due to their broad spectral absorption and conducting properties, perovskite- based solar cells have recently attracted the research community. However, $MAPbI_3$ presented a poor stability and they suffer from degradation caused by moisture or oxygen. In order to give more robustness to the materials against the moisture and give stability to the final, some researchers have used perovskites with mixed cations or halides [65]. For instance, Saliba *et. al.* has demonstrated that the mixture of cesium, methylammonium and formanidium provides stability and high power conversion efficiency (PCE) [66].

Depending on the final structure, perovskite solar cells can be divided in conventional (n-i-p) or inverted (p-i-n) [67]. In this thesis, we worked with conventional perovskite solar cells where, TiO_2 worked as electron transport layer, and Spiro-OMeTAD as hole transport layer.

1.2.3.1 Device measurements.

J-V curveis the most used measurement performed to a solar cell. The cell is illuminated with a calibrated lamp, with the appropriate set of filters for the correct simulation of the 1.5 AM G solar spectrum. While the cell is illuminated the current versus voltage is recorded. Figure 1.15 shows an example of one of the perovskites solar cells fabricated in the Palomares Group.

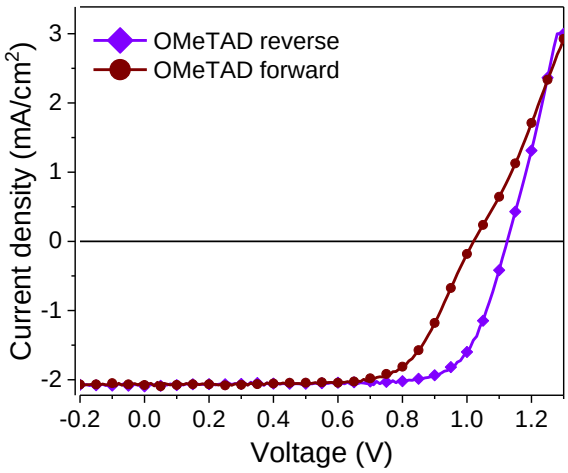

Figure 1. 15. Example of JV curve of Perovskites/OMeTAD solar cell.

From these curves, some parameters related to solar cells parameters can be taken. The description of each one is described below.

Power conversion Efficiency (PCE) is calculated by the following equation:

$$PCE = FF\,\frac{J_{SC}V_{OC}}{P_{in}}$$

Where FF is the fill factor, Jsc is the short circuit current, Voc is the open circuit voltage.

Open Circuit Voltage (Voc). The open circuit voltage occurs when there is no current passing through the cell. In an ideal solar cell, Voc is independent of the illumination intensity.

Fill Factor (FF). Fill factor is the measure of the quality of the solar cells. It gives information about the shape of the J-V curve.

$$FF = \frac{J_m \cdot V_m}{J_{CS} \cdot V_{OC}}$$

Short Circuit Current Density (Jsc). The short Circuit Density corresponds to the short circuit condition when the voltage is 0. Dividing this current by the area of the solar cell under test, we can obtain the current density, Jsc (mA/cm^2).

1.3 References.

1. J. Heber. Nobel Prize 2014: Akasaki, Amano & Nakamura. *Nat. Phys.* **2014**, 10, 791.
2. Nanotechnology timeline. National Nanotechnology Initiative. http://www.nano.gov/timeline. (accessed Mar 6, 2019).
3. C.B. Murray, D.J. Norris, M.G. Bawendi. Synthesis and characterization of nearly monodisperse CdE (E = sulfur, selenium, tellurium) semiconductor nanocrystallites. *J. Am. Chem. Soc.* **1993**, 115 (19), 8706–8715.
4. J. Jeevanandam, A. Barhoum, Y.S. Chan, A. Dufresne, M.K. Danquah. Review on nanoparticles and nanostructured materials: history, sources, toxicity and regulations. *Beilstein J. Nanotechnol.* **2018**, 9, 1050–1074.
5. V. Wood, V. Bulović. Colloidal quantum dot light-emitting devices. *Nano Rev.* **2010**, 1 (1), 5202.
6. U. Resch-Genger, M. Grabolle, S. Cavaliere-Jaricot, R. Nitschke, T. Nann. Quantum dots versus organic dyes as fluorescent labels. *Nat. Methods* **2008**, 5, 763.
7. T. Nann, W.M. Skinner. Quantum Dots for Electro-Optic Devices. *ACS Nano* **2011**, 5 (7), 5291–5295.
8. D. Hu, P. Zhang, P. Gong, et al. A fast synthesis of near-infrared emitting CdTe/CdSe quantum dots with small hydrodynamic diameter for in vivo imaging probes. *Nanoscale* **2011**, 3 (11), 4724–4732.
9. K.-H. Lee, C.-Y. Han, H.-D. Kang, et al. Highly Efficient, Color-Reproducible Full-Color Electroluminescent Devices Based on Red/Green/Blue Quantum Dot-Mixed Multilayer. *ACS Nano* **2015**, 9 (11), 10941–10949.
10. J. Albero, J.N. Clifford, E. Palomares. Quantum dot based molecular solar cells. *Coord. Chem. Rev.* **2014**, 263-264, 53–64.

11. J. Albero, P. Riente, J.N. Clifford, M.A. Pericàs, E. Palomares. Improving CdSe Quantum Dot/Polymer Solar Cell Efficiency Through the Covalent Functionalization of Quantum Dots: Implications in the Device Recombination Kinetics. *J. Phys. Chem. C* **2013**, 117 (26), 13374–13381.

12. A.M. Smith, S. Nie. Chemical analysis and cellular imaging with quantum dots. *Analyst* **2004**, 129 (8), 672–677.

13. F.T. Rabouw, C. de Mello Donega. Excited-State Dynamics in Colloidal Semiconductor Nanocrystals. *Top. Curr. Chem.* **2016**, 374 (5), 58.

14. M.A. Malik, P. O'Brien, N. Revaprasadu. A Simple Route to the Synthesis of Core/Shell Nanoparticles of Chalcogenides. *Chem. Mater.* **2002**, 14 (5), 2004–2010.

15. B.O. Dabbousi, J. Rodriguez-Viejo, F. V Mikulec, et al. (CdSe)ZnS Core−Shell Quantum Dots: Synthesis and Characterization of a Size Series of Highly Luminescent Nanocrystallites. *J. Phys. Chem. B* **1997**, 101 (46), 9463–9475.

16. P. Nikolaou, I. Vareli, E. Deskoulidis, et al. Graphite/SiO2 film electrode modified with hybrid organic-inorganic perovskites: Synthesis, optical, electrochemical properties and application in electrochemical sensing of losartan. *J. Solid State Chem.* **2019**, 273, 17–24.

17. C. Huang, W. Fu, C.-Z. Li, et al. Dopant-Free Hole-Transporting Material with a C3h Symmetrical Truxene Core for Highly Efficient Perovskite Solar Cells. *J. Am. Chem. Soc.* **2016**, 138 (8), 2528–2531.

18. Q. Wang, N. Phung, D. Di Girolamo, P. Vivo, A. Abate. Enhancement in lifespan of halide perovskite solar cells. *Energy Environ. Sci.* **2019**, 12 (3), 865–886.

19. J.-A. Alberola-Borràs, J.A. Baker, F. De Rossi, et al. Perovskite Photovoltaic Modules: Life Cycle Assessment of Pre-industrial Production Process. *iScience* **2018**, 9, 542–551.

20. D. Chen, X. Chen. Luminescent perovskite quantum dots: synthesis, microstructures, optical properties and applications. *J. Mater. Chem. C*

2019, 7 (6), 1413–1446.

21. F. Liu, Y. Zhang, C. Ding, et al. Highly Luminescent Phase-Stable CsPbI3 Perovskite Quantum Dots Achieving Near 100% Absolute Photoluminescence Quantum Yield. *ACS Nano* **2017**, 11 (10), 10373–10383.

22. W. Xu, Q. Hu, S. Bai, et al. Rational molecular passivation for high-performance perovskite light-emitting diodes. *Nat. Photonics* **2019**.

23. Q. Van Le, K. Hong, H.W. Jang, S.Y. Kim. Halide Perovskite Quantum Dots for Light-Emitting Diodes: Properties, Synthesis, Applications, and Outlooks. *Adv. Electron. Mater.* **2018**, 4 (12), 1800335.

24. X.T. Zheng, A. Ananthanarayanan, K.Q. Luo, P. Chen. Glowing graphene quantum dots and carbon dots: Properties, syntheses, and biological applications. *Small* **2015**, 11 (14), 1620–1636.

25. G. Nedelcu, L. Protesescu, S. Yakunin, et al. Fast Anion-Exchange in Highly Luminescent Nanocrystals of Cesium Lead Halide Perovskites (CsPbX3, X = Cl, Br, I). *Nano Lett.* **2015**, 15 (8), 5635–5640.

26. Q.A. Akkerman, V. D.Innocenzo, S. Accornero, et al. Tuning the Optical Properties of Cesium Lead Halide Perovskite Nanocrystals by Anion Exchange Reactions. *J. Am. Chem. Soc.* **2015**, 137 (32), 10276–10281.

27. Q. Shan, J. Song, Y. Zou, et al. High Performance Metal Halide Perovskite Light-Emitting Diode: From Material Design to Device Optimization. *Small* **2017**, 13 (45), 1701770.

28. H. Huang, L. Polavarapu, J.A. Sichert, et al. Colloidal lead halide perovskite nanocrystals: synthesis, optical properties and applications. *Npg Asia Mater.* **2016**, 8, e328.

29. L.C. Schmidt, A. Pertegás, S. González-Carrero, et al. Nontemplate Synthesis of CH3NH3PbBr3 Perovskite Nanoparticles. *J. Am. Chem. Soc.* **2014**, 136 (3), 850–853.

30. Q.A. Akkerman, M. Gandini, F. Di Stasio, et al. Strongly emissive perovskite nanocrystal inks for high-voltage solar cells. *Nat. Energy*

2016, 2, 16194.

31. X. Xu, R. Ray, Y. Gu, et al. Electrophoretic Analysis and Purification of Fluorescent Single-Walled Carbon Nanotube Fragments. *J. Am. Chem. Soc.* **2004**, 126 (40), 12736–12737.

32. K.S. Novoselov, A.K. Geim, S. V Morozov, et al. Electric Field Effect in Atomically Thin Carbon Films. *Science (80-.).* **2004**, 306 (5696), 666 LP – 669.

33. Y.-Q. Zhang, D.-K. Ma, Y. Zhuang, et al. One-pot synthesis of N-doped carbon dots with tunable luminescence properties. *J. Mater. Chem.* **2012**, 22 (33), 16714–16718.

34. Y. Wang, A. Hu. Carbon quantum dots: synthesis, properties and applications. *J. Mater. Chem. C* **2014**, 2 (34), 6921–6939.

35. H. Zhang, Q. Zhang, M. Li, et al. Investigation of the enhanced performance and lifetime of organic solar cells using solution-processed carbon dots as the electron transport layers. *J. Mater. Chem. C* **2015**, 3 (48), 12403–12409.

36. C. Liu, K. Chang, W. Guo, et al. Improving charge transport property and energy transfer with carbon quantum dots in inverted polymer solar cells. *Appl. Phys. Lett.* **2014**, 105 (7), 073306.

37. P. Mirtchev, E.J. Henderson, N. Soheilnia, C.M. Yip, G. a. Ozin. Sup Info Solution phase synthesis of carbon quantum dots as sensitizers for nanocrystalline TiO2 solar cells. *J. Mater. Chem.* **2012**, 22 (4), 1265.

38. V.-D.A.-D. Dao Van-Duong A4 - Kim, Poeun A4 - Baek, Seunghyeon A4 - Larina, Liudmila L. A4 - Yong, Kijung A4 - Ryoo, Ryong A4 - Ko, Seung Hyeon A4 - Choi, Ho-Suk. Facile synthesis of carbon dot-Au nanoraspberries and their application as high-performance counter electrodes in quantum dot-sensitized solar cells. *Carbon N. Y.* **2016**, v. 96, pp. 139–144 – 2016 v.96.

39. M.-L. Tsai, W.-C. Tu, L. Tang, et al. Efficiency Enhancement of Silicon Heterojunction Solar Cells via Photon Management Using Graphene Quantum Dot as Downconverters. *Nano Lett.* **2016**, 16 (1), 309–313.

40. M. Sun, X. Ma, X. Chen, et al. A nanocomposite of carbon quantum dots and TiO2 nanotube arrays: enhancing photoelectrochemical and photocatalytic properties. *RSC Adv.* **2014**, 4 (3), 1120–1127.

41. M. Zhang, L. Bai, W. Shang, et al. Facile synthesis of water-soluble{,} highly fluorescent graphene quantum dots as a robust biological label for stem cells. *J. Mater. Chem.* **2012**, 22 (15), 7461–7467.

42. S.Y. Lim, W. Shen, Z. Gao. Carbon quantum dots and their applications. *Chem. Soc. Rev.* **2015**, 44 (1), 362–381.

43. L.C. Clark Jr., C. Lyons. ELECTRODE SYSTEMS FOR CONTINUOUS MONITORING IN CARDIOVASCULAR SURGERY. *Ann. N. Y. Acad. Sci.* **1962**, 102 (1), 29–45.

44. C.S. Huertas, D. Fariña, L.M. Lechuga. Direct and Label-Free Quantification of Micro-RNA-181a at Attomolar Level in Complex Media Using a Nanophotonic Biosensor. *ACS Sensors* **2016**, 1 (6), 748–756.

45. U. Yogeswaran, S. Chen. A Review on the Electrochemical Sensors and Biosensors Composed of Nanowires as Sensing Material. **2008**, 290–313.

46. D.R. Thévenot, K. Toth, R.A. Durst, G.S. Wilson. Electrochemical biosensors: recommended definitions and classification1International Union of Pure and Applied Chemistry: Physical Chemistry Division, Commission I.7 (Biophysical Chemistry); Analytical Chemistry Division, Commission V.5 (Electroanalytical Chemistry).1. *Biosens. Bioelectron.* **2001**, 16 (1), 121–131.

47. M. Soler, C.S. Huertas, L.M. Lechuga. Label-free plasmonic biosensors for point-of-care diagnostics: a review. *Expert Rev. Mol. Diagn.* **2019**, 19 (1), 71–81.

48. S.J. UPDIKE, G.P. HICKS. The Enzyme Electrode. *Nature* **1967**, 214 (5092), 986–988.

49. M. Bruchez, M. Moronne, P. Gin, S. Weiss, A.P. Alivisatos. Semiconductor Nanocrystals as Fluorescent Biological Labels. *Science (80-.).* **1998**, 281 (5385), 2013 LP – 2016.

50. S. Datta, L.R. Christena, Y.R.S. Rajaram. Enzyme immobilization: an overview on techniques and support materials. *3 Biotech* **2013**, 3 (1), 1–9.

51. F.M. Raymo, I. Yildiz. Luminescent chemosensors based on semiconductor quantum dots. *Phys. Chem. Chem. Phys.* **2007**, 9 (17), 2036–2043.

52. A.R. Clapp, I.L. Medintz, B.R. Fisher, G.P. Anderson, H. Mattoussi. Can Luminescent Quantum Dots Be Efficient Energy Acceptors with Organic Dye Donors? *J. Am. Chem. Soc.* **2005**, 127 (4), 1242–1250.

53. J. Wang. Electrochemical Glucose Biosensors. *Chem. Rev.* **2008**, 108 (2), 814–825.

54. S.B. Lowe, J.A.G. Dick, B.E. Cohen, M.M. Stevens. Multiplex Sensing of Protease and Kinase Enzyme Activity via Orthogonal Coupling of Quantum Dot–Peptide Conjugates. *ACS Nano* **2012**, 6 (1), 851–857.

55. W.R. Algar, A.P. Malanoski, K. Susumu, et al. Multiplexed Tracking of Protease Activity Using a Single Color of Quantum Dot Vector and a Time-Gated Förster Resonance Energy Transfer Relay. *Anal. Chem.* **2012**, 84 (22), 10136–10146.

56. History of the light bulb www.bulbs.com/ learning/history.aspx (accessed Mar 6, 2019).

57. M. Sessolo, H.J. Bolink. Hybrid Organic–Inorganic Light-Emitting Diodes. *Adv. Mater.* **2011**, 23 (16), 1829–1845.

58. M. Reig, G. Bubniene, W. Cambarau, et al. New solution-processable carbazole derivatives as deep blue emitters for organic light-emitting diodes. *RSC Adv.* **2016**, 6 (11), 9247–9253.

59. E. Smarsly, D. Daume, F. Braig, et al. Poly(para-phenyleneethynylene)s as emitters in polymer LEDs. *J. Mater. Chem. C* **2018**, 6 (41), 11002–11006.

60. No Title.

61. B. O'Regan, M. Gratzel. A low-cost, high-efficiency solar cell based on

dye-sensitized colloidal TiO2 films. *Nature* **1991**, 353 (6346), 737–740.

62. R.W. Miles, G. Zoppi, I. Forbes. Inorganic photovoltaic cells. *Mater. Today* **2007**, 10 (11), 20–27.

63. C.W. Tang. Two-layer organic photovoltaic cell. *Appl. Phys. Lett.* **1986**, 48 (2), 183–185.

64. A. Kojima, K. Teshima, Y. Shirai, T. Miyasaka. Organometal Halide Perovskites as Visible-Light Sensitizers for Photovoltaic Cells. *J. Am. Chem. Soc.* **2009**, 131 (17), 6050–6051.

65. D. Bi, W. Tress, M.I. Dar, et al. Efficient luminescent solar cells based on tailored mixed-cation perovskites. *Sci. Adv.* **2016**, 2 (1), e1501170.

66. M. Saliba, T. Matsui, J.-Y. Seo, et al. Cesium-containing triple cation perovskite solar cells: improved stability, reproducibility and high efficiency. *Energy Environ. Sci.* **2016**, 9 (6), 1989–1997.

67. M. Saliba, J.-P. Correa-Baena, C.M. Wolff, et al. How to Make over 20% Efficient Perovskite Solar Cells in Regular (n–i–p) and Inverted (p–i–n) Architectures. *Chem. Mater.* **2018**, 30 (13), 4193–4201.

2

Motivation and aims of the thesis.

Chapter 2

Since the first scientific publication of gold nanoparticles (Au NP) solution by Michael Faraday in 1857, the usage of this new materials has exponentially increased and studied as Nanomaterials represent an active area of research due to their physical, chemical and biological applications. In the last few decades, the investigation of semiconductor fluorescent materials has been a hot topic because of their advantages and their multidisciplinary use.

The principal objective of this thesis is to study the optoelectronic properties of colloidal quantum dots in order to apply them in different fields such as solar cells, bioimaging and light emitting diodes. During the development of this thesis, three types of colloidal quantum: Cadmium, perovskites and carbon-based quantum dots, have been synthesized using different methods reported in the bibliography with some modifications. After that, all the materials have been tested in light emitting devices, solar cells or as biosensors. Consequently, this thesis is organized in nine chapters divided into three main blocks based on the different application given to the Quantum dots. The research has been developed at two institutions: Institute of Chemical Research of Catalonia (ICIQ) and Eurecat, the technological center of Catalonia, between March 2015 and March 2019.

In the next section, a summary and main objective of each chapter is provided

In **Chapter 1** describe an overview of the fundamentals properties of Quantum dots and of each of the applications given in this thesis. The main goal is to describe and discuss the fundamentals and relevance of each application that we worked with. The description of the synthesis of Carbon Quantum dots and their applications in solar cells was published in 2016: **S. Paulo-Mirasol**, E. Palomares, E. Martinez-Ferrero, Graphene and Carbon Quantum Dot-Based Materials in Photovoltaic Devices: From Synthesis to Applications. *Nanomaterials*. **6** (2016), p. 157.

In **Chapter 3** all the techniques used during the thesis to characterize the materials and LEDs are described. In addition, the synthesis and

characterization of ZnO NPs is also included, since we used it during the fabrication of the LEDs described in several chapters.

In **Chapter 4**, two different sensors are described. First, we started developing a biosensor based on the encapsulation of two cadmium-based quantum dots in a silica nanosphere to detect and quantify the enzyme elastase in human stool. Due to the low reproducibility of the method, we decided to search for an alternative. Therefore, we fabricated an electrochemical sensor based on carbon quantum dots (CQDs) to detect the same enzyme. The fabrication of these electrochemical sensors started during my short stay at the University of Patras under the supervision of Dr. Emmanuel Topoglidis. We were not able to finish the project although the preliminary results are very interesting. We plan to finish this project in the near future. This chapter was also done with the collaboration of Santi Genè.

In Chapter 5 I show the synthesis and characterization of three different cadmium based Quantum dots that are appliedin the emissive layer in LEDs. The synthesis of Cadmium based quantum dots was done in inert conditions and the fabrication was performed under air conditions. This chapter was mainly focused on optimizing the inverted structure of LEDs and it was the starting point of the use of differents Quantum dots as an active layer in LEDs.

In **Chapter 6**, a similar study was performed but in this case using Perovskites materials as the emissive layer in LEDs. This project was started during my international internship in National Institure of Materials in Science (NIMS) in Japan under the supervision of Dr. Masatoshi Yanagida during three months.

From **Chapter 7** to **Chapter 9**, we describe the synthesis and use of Carbon based quantum dots as either active material in the hole transport layer or emissive layer in LEDs and perovskite solar cells.

In Chapter 7 the synthesis of CQDs was carried out in order to use them as an unique emissive layer in LEDs to obtain white light emission. The different fabrication steps were carried out in air conditions although the synthesis was done in inert conditions. The project was recently submitted to Nanoscale Journal: **S.Paulo-Mirasol**, E. Martinez-Ferrero, E. Palomares, Direct White Light Emission from Carbon Nanodots in solution processed Light Emitting diodes, Nanoscale.

In the case of **Chapter 8**, carbon quantum dots capped with different ligands were synthesized to use them as the hole transport layer (HTL) in LEDs using F8BT as emissive layer and ZnO NPs as the electron transport layer. The aim of this project was to study how the capping ligand, as well as the hole mobility and energy alignment, influence the optoelectronic properties of the devices. CQDs were compared with the most widely used HTM in LEDs, MoO_3 and PEDOT: PSS.

To end up this section, **Chapter 9** described the use of CQDs as HTL in perovskites solar cells. This project was published in 2016: **S. Paulo-Mirasol**, G. Stoica, W. Cambarau, E. Martinez-Ferrero, E. Palomares, Carbon quantum dots as new hole transport material for perovskite solar cells. *Synth. Met.* **222**, 17–22 (2016).

Finally, **Chapter 10** presents a brief summary of all the results obtained during the development of this thesis, as well as the main conclusions and perspectives.

3

Methods and experimental systems.

In this chapter, all the techniques used in this thesis to characterize the materials as well as the device fabrication are explained. The facilities are accessible in the Institute of Chemical Research of Catalonia (ICIQ), Eurecat-Technological Center of Catalonia and Servei de Recursos Científics i Tècnics at University Rovira and Virgili.

Chapter 3

Table of contents

Chapter 3

3.1 Introduction.

In this chapter, general information about experimental procedures that were used during the synthesis and device preparation are explained. The specific syntheses of the different materials that we used during the thesis are described more deeply in each chapter as well as the fabrication conditions of the devices. The synthesis and characterization of zinc oxide nanoparticles (NPs) are described here because is a commom material in all the LEDs devices. However, all the information related to solar cell preparation is adequately explained in Chapter 9.

3.2 Materials characterization.

3.2.1 Absorbance and emission measurements.

Both absorbance and emission measurements are widely used to characterize optoelectronic materials because they are non-destructive techniques that provide information about the optical and electronic structure.

UV-vis absorption spectra were measured on a Shimadzu UV-1700PC spectrophotometer equipped with a photomultiplier detector, double beam optics, and D2 and W light source for both films and solutions using 1 cm cuvette at room temperature. The spectra profile were obtained in transmission mode using a cuvette with the same solvent than the sample as reference to give the absorbance (Abs).

$$\mathrm{Abs} = -log\left(\frac{\%T}{100}\right) \qquad \text{Equation 3.1}$$

Where %T is Transmitance recorded as a percentatge.

Photoluminescence measurements of both films and solutions were carried out in a Fluorolog Horiba Jobin Ivon spectrophotometer at room temperature in air conditions.

From these measurements, we have estimated the photoluminescence quantum efficiency that is defined as the total photons emitted per total photons absorbed (equation 3.2).

$$\eta = \frac{\Sigma(emitted)}{\Sigma(absorbed)} \qquad \text{Equation 3.2}$$

Figure 3.1 shows an example of the absorbance and emission spectra of CdSe QDs synthetized in ICIQ. CdSe QDs presents a maximum emission peak at 570nm with a FWHM of 20nm. The absorbance shows a band at 550nm and smaller shoulders at 450nm.

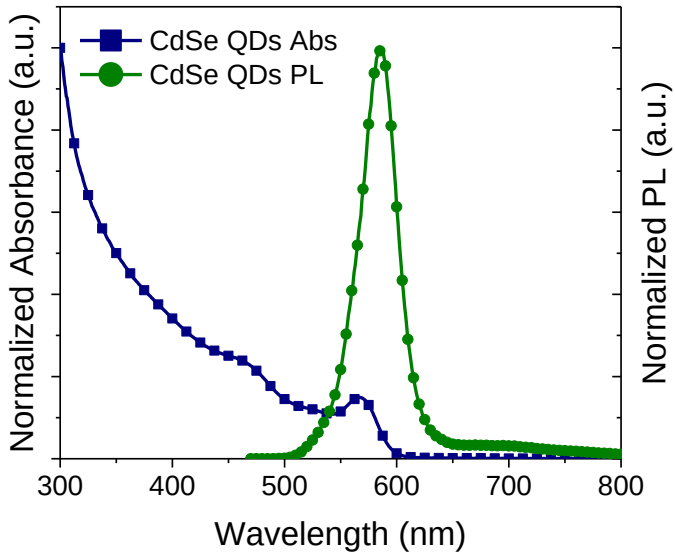

Figure 3.1. Experimental UV-vis absorption and photoluminescence emission spectra of CdSe QDs in chloroform after excitation at 440 nm at room temperature.

3.2.2 Quantum yield calculation.

The definition of quantum yield by the IUPAC is “the number of defined events occurring per photon absorbed by the system”. In this thesis we have used the relative quantum yield that is calculated using a standard fluorophore as a reference. Table 3.1 shows the fluorophores used as references to calculate the quantum yield of our materials in this thesis [1].

Table 3.1. Characteristics of the Fluorophores solved in ethanol at room temperature.

dye	Qy_{ref}(urel)	excitation range (nm)	emission range (nm)
C-102	0.764 (±0.039)	340-420	430-530
C-153	0.544 (±0.028)	360-470	485-635
Rh-101	0.913 (±0.046)	515-565	585-665

The quantum yield was obtained by using the following equation:

$$QY = QY_{ref}\left(\frac{I_{em\,sample}}{I_{em\,ref}}\right)\cdot\left(\frac{Abs_{ref}}{Abs_{sample}}\right)\cdot\left(\frac{n_{sample}}{n_{ref}}\right)^2 \quad \text{Equation 3.3}$$

Where QY_{ref} is the quantum yield of the fluorophore used as reference, QY_{ref} is the quantum yield of the dye, I_{em} is the area of the emission band, Abs is the absorbance excitation wavelength and n is the refractive index.

3.2.3 Time Correlated Single Photon-Counting.

Time correlated single photon-counting (TCSPC) is a technique to measure the fluorescence lifetime. The measurement is based on the detection of single photons and their arrival times in respect to a reference signal, which is a short-laser pulse. The signal is fitted by exponential equations that permit to estimate the decay lifetime of the different processes.

$$PL(t) = A_1 e^{-(\frac{t}{\tau 1})} + A_2 e^{-(\frac{t}{\tau 2})}$$ Equation 4

The fluorescence lifetime was recorded by using an Edinburgh Instruments LifeSpec II spectrometer based on the time-correlated single photon counting technique, equipped with PMT detectors, double subtractive monochromator, and picosecond pulsed diode lasers sources.

Figure 3.2 shows a TCSPC example of $CsPbBr_3$ QDs synthesized at ICIQ. The lifetime decay fits to a biexponential equation due to the presence of two different radiative processes.

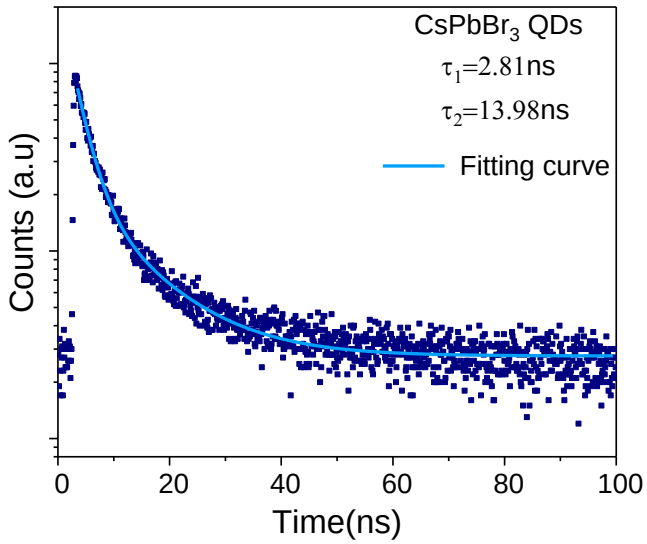

Figure 3. 2 . Experimental fluorescence-decay curve of $CsPbBr_3$ QDs solved in hexane measured after excitation at 405 nm at room temperature.

3.2.4 Infrared spectroscopy.

Infrared spectroscopy (FT-IR) is a technique to characterize the structure of the material and their functional groups through the analysis of the peaks originated by the absorption of certain frequencies that match the vibrational frequency of

the bonds. The working ranges are in the middle region range between 400 cm^{-1} and 4000 cm^{-1}. The sample were measured using single reflection Attenuated total reflection (ATR) accessory. This allows us to record the solid or liquid sample directly without any pre-treatment or without dispersing in any matrix. ATR uses the attenuated total reflection by measuring the changes that occur in a totally internally reflected infrared beam, when it comes into contact the sample. Figure 3.3 shows an example of ATR-FTIR measurements of carbon quantum dots doped with Yb and Er.

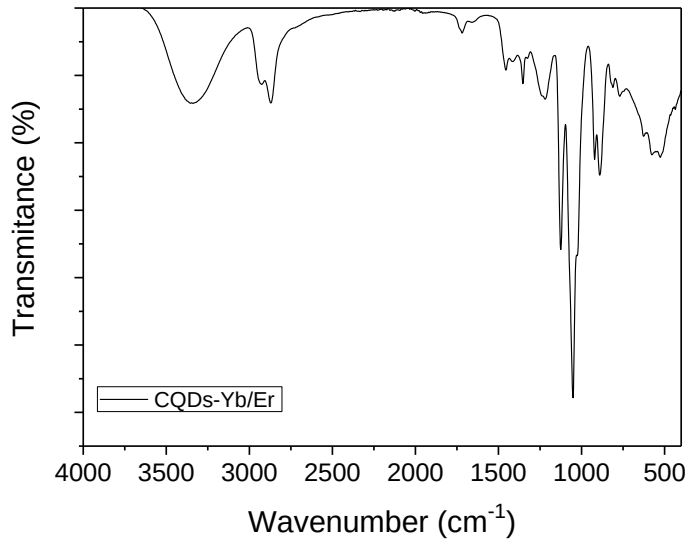

Figure 3.3. Experimental FT-IR of CQDs doped with Yb and Er.

3.2.5 Transmission Electronic Microscopy.

Transmission Electronic Microscopy (TEM) was used to estimate the size and the shape of our materials. TEM is a technique in which the beam of electrons are transmitted through a sample to form an image. The image is created from the interaccions between the electrons and the sample. TEM images were captured using a JEOL 1011 microscope. Figure 3.4 shows some of materials prepared during the thesis.

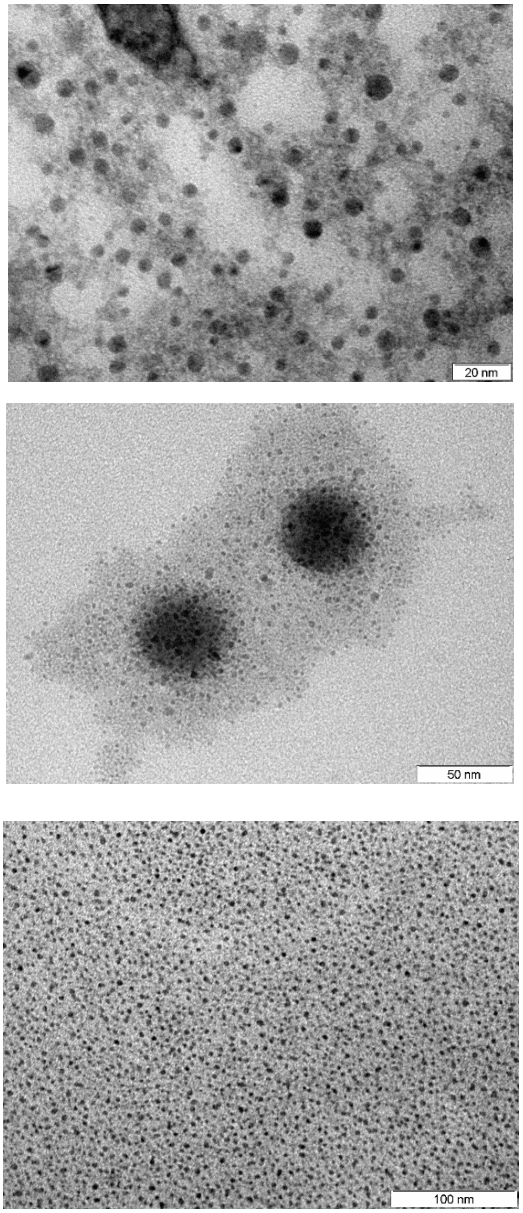

Figure 3.4. TEM image of a) Carbon Quantum dots doped with Yb and Er. b) Silica Nanospheres filled with two types of cadmium based quantum dots, c) $MAPbBr_3$ QDs.

3.2.6 Electrochemical characterization.

There are different electrochemical approaches in order to characterize and understand the basic the electrochemical of a substance. During the thesis, we used cyclic voltammetry (CV) and the square-wave voltammetry (SWV) to calculate the energy of the valence band (VB) and conduction band (CB) of carbon quantum dots in solution and in film. If the material presents reversible oxidation or reduction bands the CB and VB can be calculated using CV. In the case that the oxidation/reduction process are irreversible SWV was used instead.

3.2.6.1 Cyclic Voltammetry.

The Cyclic Voltammetry (CV) was measured by a PARSTAT 2273 (Princeton Applied Research) in 0.1 M of tetrabutylammonium hexafluorophosphate as a supporting electrolite solved in the same organic solvent than our sample. We used a commercial Ag/AgCl non-aqueous Ag/Ag^+ reference electrode, a platinum wire as a counter electrode and a platinum disc as working electrode. All the solutions were desgassed bubling nitrogen and the CV spectra were recorded in the presence and absence of Ferrocene/$Ferrocene^+$ as internal standard.

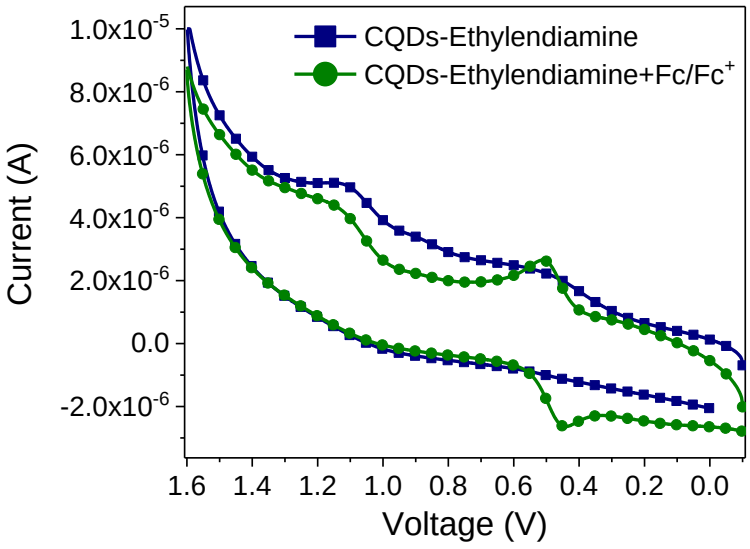

Figure 3.5. Cyclic voltammetry of CQDs solved in dichloromethane recorded in 0.1M tetrabutylammonium hexafluorophosphate at a scan rate of 10 mV s^{-1} at room temperature.

CV is recorded in order to estimate the energy level of the highest occupied molecular orbital (HOMO) and the lowest unoccupied molecular orbital (LUMO) levels in organic compounds and the valence and conduction band (VB/CB) in inorganic semiconductors. One of the important process inside optoelectronic devices is the charge injection. The level alignment between the electrodes and the HOMO and LUMO or VB and CB levels of active layers determine how the electron and hole can easily move through the devices. The following Equations describe how we calculate the energetic levels in solutions.

$$\mathrm{E}_{HOMO} = -(E_{OX} + 4.8) \qquad \text{Equation 3.5}$$

$$\mathrm{E}_{LUMO} = \mathrm{E}_{HOMO} + \mathrm{E}_{o-o} \qquad \text{Equation 3.6}$$

$$\mathrm{E}_{o-o} = h \cdot \frac{c}{\lambda} \qquad \text{Equation 3.7}$$

Eox is the oxidation potential from the CV, $E_{o\text{-}o}$ is the band gap and λ is the wavelength resulting of the intersection between the absorbance and the

emission band, h is the Planck constant $6.62607004 \cdot 10^{-34}$ m^2 kg / s and c is the speed of the light $3 \cdot 10^8$ m/s.

3.2.6.2 Square wave voltammetry.

Square wave voltammetry (SWV) is one of the most used pulsed voltammetry techniques. During the recording of a SWV both forward and reverse pulses are measured giving a similar information than that obtained in cyclic voltammeter. This technique was used in the cases where the oxidation or reduction processes are irreversible.

The equations to calculate the energetic levels and the electrodes used to measure the SWV are the same that the ones described in the cyclic voltammetry section. Figure 3.6 shows an example of a SWV measure using the same material as CV example (Figure 3.5).

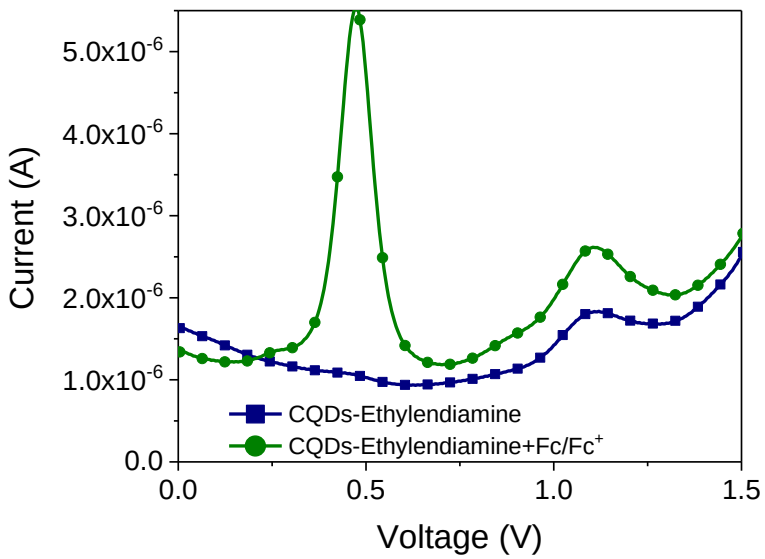

Figure 3.6. SWV of CQDs solved in dichloromethane. The working parameters for CV experiments were chosen as: initial potential 0V, final potential 1.6V and scan rate 10 mV s^{-1}.

3.2.7 Dynamic light scattering.

Dynamic light scattering technique is one of the most useful techniques to determine the average size of particles. The measurements were carried out in a Malvern Zetasizer (Nano-ZS) instrument at room temperature. It is a non-invasive technique and requires only small quantities of sample. In addition, this technique allows us to detect amount of traces. DLS measures the diffusion behavior of particles or molecules in solution. The sample is exposed to a monochromatic wave of light, the scattering and the diffusion of the particles, which interact with the wave of light, is detected measuring the size. The relationship between those parameters determine the size of the particles.[2] In Figure 3.7 shows an example of DLS measurement of CQDs. The average size of CQDs using oleyamine as capping ligand is 1 nm. Each curve belongs to the measure of the sample. The Figure 3.7 shows an example of a DLS, where the sample was measured three time. The DLS displayed a unique size of particles of 1 nm.

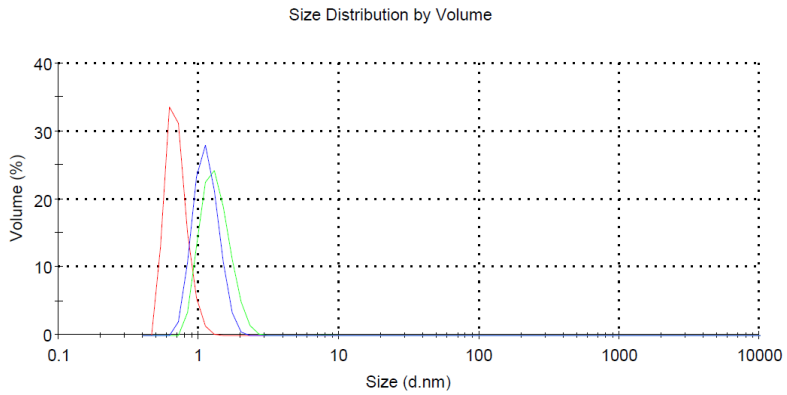

Figure 3.7. Experimental DLS signal of CQDs-OLA solved in hexane measured in air conditions.

3.3 Fabrication of films and devices.

In this section, the preparation of films as well as light emitting diodes and solar cells devices are described. The devices fabrication have done in a Class C clean room (ISOE) environment and in a nitrogen atmosphere glovebox (<0.1 ppm of O_2 and H_2O).

3.3.1 Synthesis of ZnO NPs.

ZnO NPs were synthesized modifying the method reported by Krebs et. al.[3] Firstly, 11.89 g of zinc acetate were dissolved in 500 mL of methanol while 6 g potassium hydroxide were dissolved in 250 mL of methanol too. Both solutions were heated at 67 ºC. Then the potassium hydroxide solution was added to the zinc acetate solution and was heated up between 65 ºC and 67 ºC during 3 hours to obtain a white solid. The solution was cooled down to room temperature, transferred to a bottle filled with nitrogen and left during 3 hours until all the white solid was decanted at the bottom of the bottle. Then, the supernatant was discarded and the white solid was transferred to smaller bottle and more methanol was added to the flask and kept overnight. The solid must not be dried during the cleaning/washing process. Finally, the supernatant was removed and we added methanol, according to the desired concentration.

To improve the stability of ZnO NPs in methanol, small amounts of 2-[2-(2-Methoxyethoxy)ethoxy]acetic acid (MEA) were added in the zinc oxide solution and sonicated in a ultrasound bath until the solution became colorless. The amount of MEA must not be higher than 16%w/w with respect to the final concentration.

The main chemical reactions occurring during the ZnO growth process are described below:

$$Zn(CH_3COO)_2 \leftrightarrow Zn^{2+} + 2\ CH_3COO^-$$

$$Zn^{+2} + 2OH^- \leftrightarrow ZnO + H_2O$$

3.3.2 Physicochemical characterization of ZnO NPs.

Different physicochemical techniques were used to characterize zinc oxide nanoparticles. Spectroscopy techniques are good to give us information related to the structure and atomic composition of the material. In addition, TEM analysis was performed in order to measure the size of the nanoparticles, the XRD to identify the crystal structure and the dynamic light scattering to measure the average particle size.

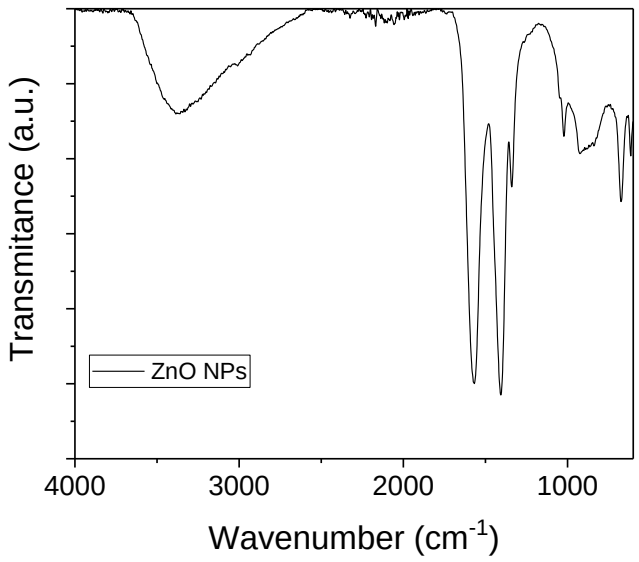

Figure 3.8. Experimental FTIR of ZnO NPs powder.

FT-IR technique provides good information related to the structure and the composition of nanoparticles, due to its good approach to identify the functional groups. Figure 8 shows the infrared spectra of ZnO NPs, where three predominant peaks appear in the spectrum. There are two vibration bands at – OH stretching and 1490cm^{-1} Zn-O vibrations.

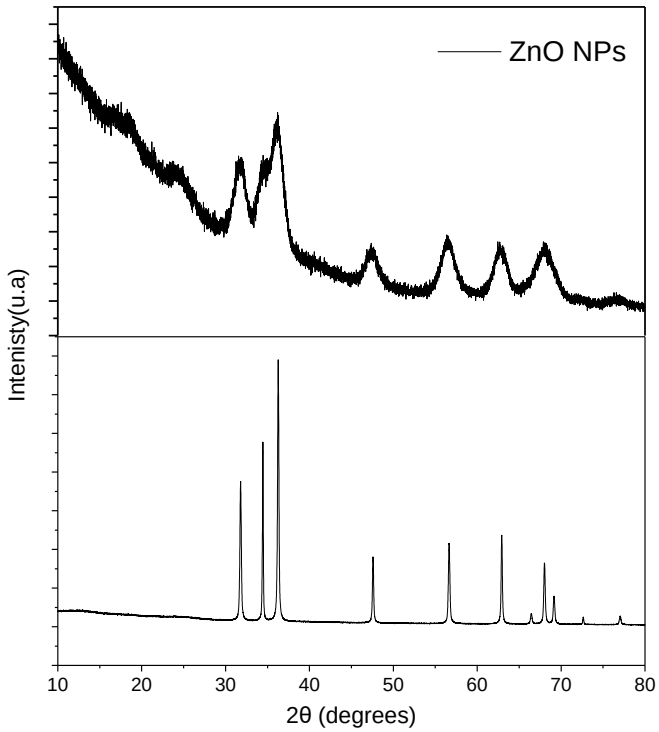

Figure 3.9. Experimental X-ray diffraction pattern of ZnO nanoparticles.

XRD analysis is also a good technique to identify the crystal structure of the materials. The XRD analysis of ZnO NPs (Figure 9) powder showed three peaks between 30 and 40 degrees belonging to wurtzite ZnO structure. The XRD sample was compared with wurzite ZnO standard diffraction data based [4].

$$\lambda = 2d \sin\theta \quad \text{Equation 3.8}$$

Dynamic light scattering was performed to measure the average particle size. Figure 3.10 shows the experimental DLS of ZnO NPs with approximate size of 10 nm. The sample was measuring three times.

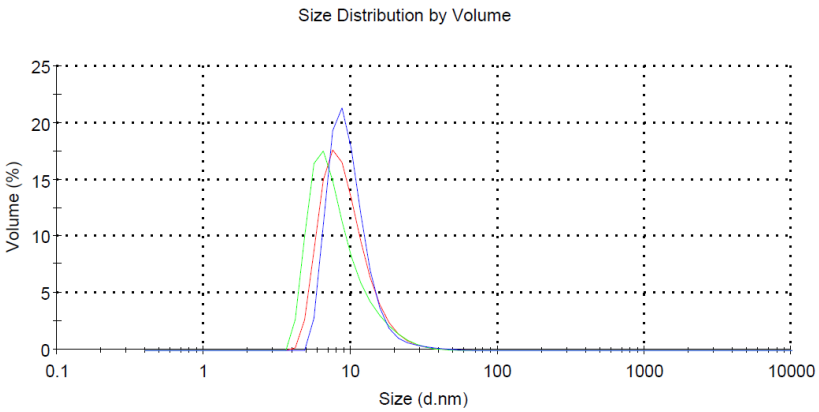

Figure 3.10. Experimental DLS signal of ZnO NPs solved in methanol. Size distribution by volume.

Figure 3.11 shows that the average size of ZnO determined by Transition electronic microscope was 7 ± 1 nm.

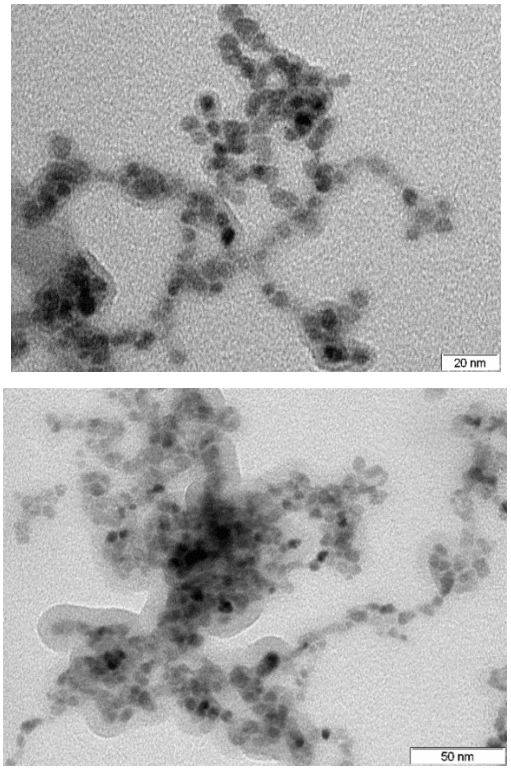

Figure 3.11. TEM images of ZnO NPs with an average particle size of 7 ± 0.9 nm.

3.3.3 Substrate cleaning.

The devices were fabricated onto 15x15 mm^2 or 30x30 mm^2 (10 Ω/square) glass substrates coated with ~150 nm thick ITO in the center. Substrates were cleaned in acetone and isopropanol and sonicated during 20 min. When using PEDOT:PSS as hole transport layer, the substrates were exposed to an ozone containing atmosphere during 30 min to improve the wettability between ITO and PEDOT:PSS.

3.3.4 Device assembly.

Spin coating is the most common laboratory deposition technique for thin films on flat substrates. Few drops of our active materials were deposited on the center of substrates, then the substrates were rotated under a speed and acceleration conditions during a specific time. The angular speed of rotation and acceleration parameters determine the final thickness. After that, the substrate was heated up at a temperature, depending on the solvent boiling point to dry the film.

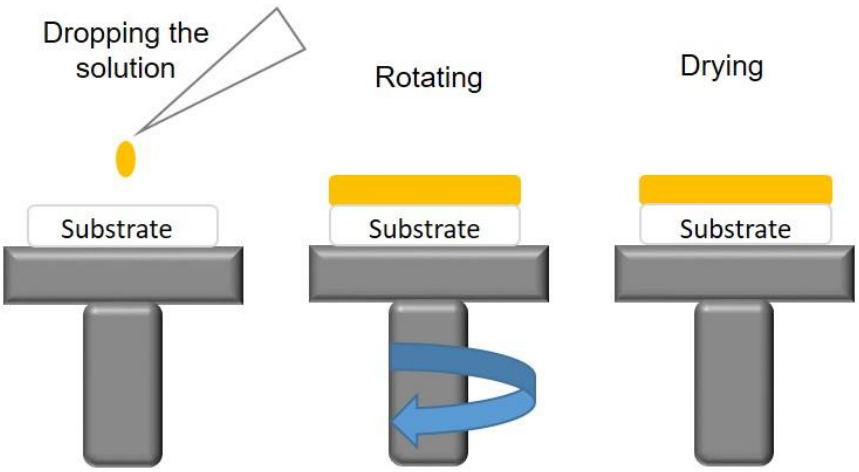

Figure 3.12. Graphical description of the thin film deposition by using spin coating technique.

The metal electrode such as gold, silver and aluminum as well as charge transport layers such as molybdenum oxide and lithium fluoride were deposited via thermal evaporation under high vacuum ($1 \cdot 10^{-6}$ mbar) through a metal mask.

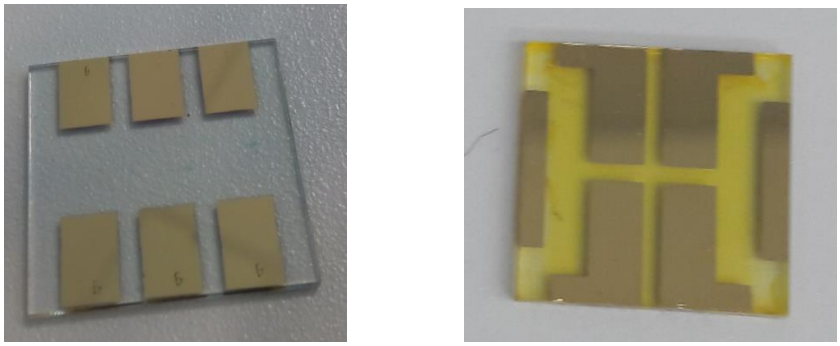

Figure 3.13. Picture of real devices used for the preparation of LEDs with two different active areas (the active area is 25 mm^2 on the left and 9 mm^2 on the right).

3.4 Device characterization.

3.4.1 Current voltage and luminance characterization.

During my thesis, I worked with two different set-ups in order to characterize LEDs.

In ICIQ, the current intensity versus voltage was recorded using Keithley 2400 while the luminance versus applied voltage was measured using a Konica Minolta LS100 luminance meter. The camera has a photo-detector fixed at a known distance above the diode to measure the emission intensities.

Figure 11 shown an example of a diode characterization using ZnO NPs as electron transport layer and F8BT as active layer.

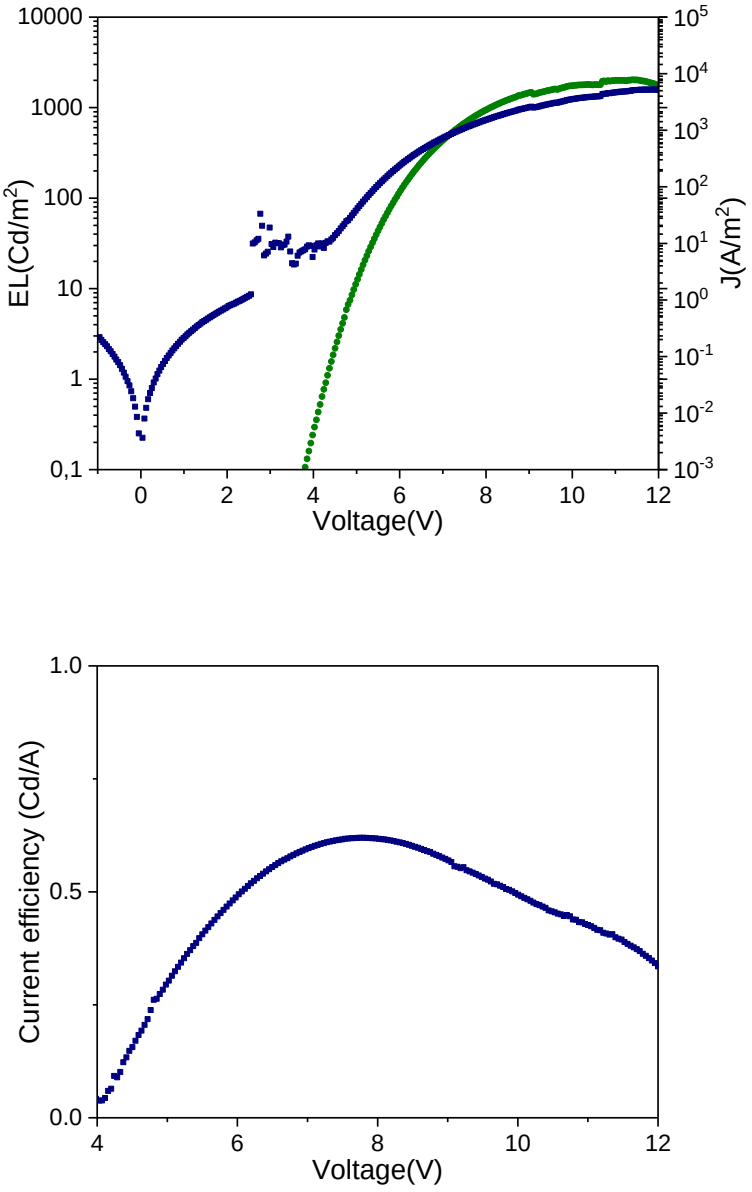

Figure 3.14. Luminance current versus voltage (green line), current density versus voltage (blue) characteristic (top) and current efficiency versus voltage characteristic (bottom).The device structure was: ITO/ZnO/F8BT/MoO_3/Au

In Eurecat, both the current intensity and photogenerated current versus voltage is recorded using a Keithley 2400 in combination with a photodiode.

Due to the way that the human eye can perceive the radiometric units, we have to convert radiometric (watts) units in a photometric units (candela/m^2). Candelas are correlated to watts through the comparison of the electroluminescence spectrum of the sample with the standard luminosity function, which represents the human eye's sensitivity to the light at a given wavelength.

3.4.3 Calculations of the Hole mobility.

This device consist of two contacts that are only hole-injecting, meaning that the current–voltage curve of these devices is not determined by the recombination of electrons and holes. [5] If to a device with hole injecting contacts was applied a certain range of voltage, the current-voltage in that range would depend on mobility and concentration of holes. In the space charge limited domain, the current is dominated by charge carriers injected from the contacts and the current-voltage characteristics becomes quadratic ($I \sim V^2$). The current density dependence with applied voltage can be fitted by the Space charge limited current (SCLC) model.

3.4.3.1 Fabrication of hole-only devices.

Clean ITO coated glass was treated with UV ozone during 20 min to improve its hydrophilicity. PEDOT:PSS (Clevios P VP AI 4083) previously filtered with a 0.45 µm cellulose acetate filter, was spin coated on top of cleaned ITO using two different spin-coating steps: 1) 4500 RPM during 30 s and 2) 3500 RPM during 30 s, followed by an annealing at 120 ºC during 20 min. Different CQDs were spin coated on top of PEDOT:PSS using the same conditions described in **7.3 Device fabrication**. Finally, 120nm of gold was thermally evaporated on top of CQDs under a pressure of 10^{-6} mbar.

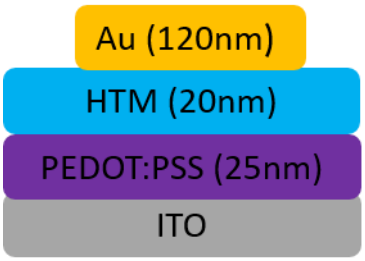

Figure 3.15. Schema of a hole-only device.

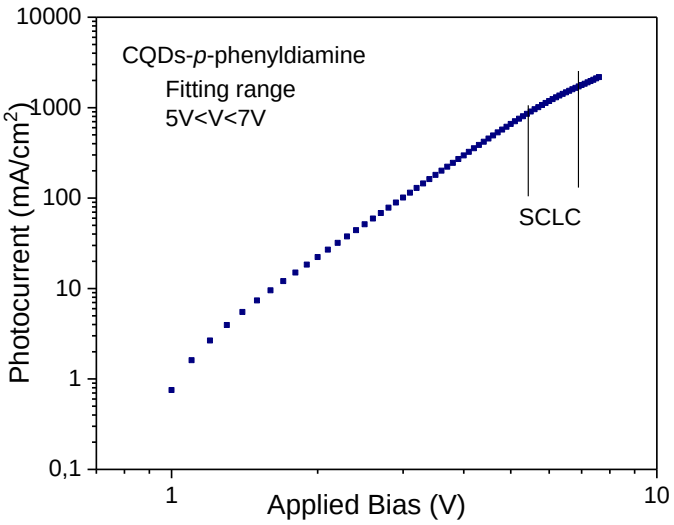

Figure 3.16. Photocurrent - voltage measurements for hole mobility using SCLC method.

Hole mobilities were measured to study the charge transport and the hole mobility using the Space charge-limited current (SCLC) model. The curves were fitted using the Mott-Gurney law, (equation 9) [6].

$$J_{SCL} = \frac{9}{8} \in_0 \in_R \mu_h \frac{V_1^2}{L_1^3} \qquad \text{Equation 3.9}$$

Where, $\in_0$ is the permittivity of free space, $\in_R$ is the dielectric constant and L is the thickness of the active material. In figure 16 appears one example of the hole mobility of CQDs using *p*-phenyldiamine as capping ligand.

3.5 References.

1. K. Rurack, M. Spieles. Fluorescence Quantum Yields of a Series of Red and Near-Infrared Dyes Emitting at 600−1000 nm. *Anal. Chem.* **2011**, 83 (4), 1232–1242.

2. J. Stetefeld, S.A. McKenna, T.R. Patel. Dynamic light scattering: a practical guide and applications in biomedical sciences. *Biophys. Rev.* **2016**, 8 (4), 409–427.

3. F.C.K. and Y.T. and R.T. and J.W. Andreasen. A simple nanostructured polymer/ZnO hybrid solar cell—preparation and operation in air. *Nanotechnology* **2008**, 19 (42), 424013.

4. E.H. Kisi, M.M. Elcombe. Parameters for the wurtzite structure of ZnS and ZnO using powder neutron diffraction. *Acta Crystallogr. Sect. C* **1989**, 45 (12), 1867–1870.

5. T. Kirchartz. Influence of diffusion on space-charge-limited current measurements in organic semiconductors. *Beilstein J. Nanotechnol.* **2013**, 4, 180–188.

6. P.N. Murgatroyd. Theory of space-charge-limited current enhanced by Frenkel effect. *J. Phys. D. Appl. Phys.* **1970**, 3 (2), 151.

Chapter 3

4

Nanophotonic biosensor for detection and quantification of elastase.

In this chapter, we present an optical and an electrochemical biosensor based on quantum dots to detect and quantify elastase in human stool samples.This project was developped in two different centers: ICIQ and Univeristy of Patras. The optical biosensor was fabricated and characterized in ICIQ with the collaboration of Santi Genè. The electrochemical one was developped during my stay in the University of Patras under the supervision of Dr. Emmanuel Topoglidis The human samples were collected in Hospital Parc Taulí in Terrasa.

Table of Contents

4.1 Introduction.

The research of new sensors has been developed in response to the need for real-time analytical measurements in healthcare, environmental and biotechnology industry. Biosensors are directly related to new diagnosis methods of diseases via detection and quantification of biomolecules such as enzyme, aptamer, etc. A biosensor is a physical or chemical signal which can be related to a biological recognition process. There are different kinds of biosensor: optical, electrochemical, thermometric, magnetic and piezoelectric.

In this chapter, we show the results of detection and quantification of the elastase enzyme in human stool samples. Elastase enzyme has been used as a biomarker to evaluate pancreas function related to pancreatic insufficiency (PEI). PEI is a reduction of the activity of pancreatic enzymes that is inadequate to maintain normal digestive processes, resulting in malabsorption of nutrients, diarrhea, weight loss, and other symptoms. The early diagnosis is one of the main goals in order to improve the quality of life of patients.

To detect it, we fabricated two different biosensors: an optical and an electrochemical biosensors. This chapter starts with the optical biosensor section, for which CdTe quantum dots were employed, and continues with the electrochemical-based sensor, which uses carbon quantum dots. The second sensor was fabricated in order to solve the scale-up problems of the optical sensor that we found during the project development. The electrochemical biosensor was done with the collaboration of Dr. Emmanuel Topoglidis in the University of Patras (Greece). This project is still in its preliminary steps, nonetheless, the results obtained are very promising.

Electrochemical sensors have attracted considerable attention due to their intrinsic advantages, such as easy use, rapid response, low-cost and inexpensive instrumentation. Signal amplification strategies have also been applied to improve the sensitivity and selectivity of electrochemical methods by

the use of nano-/micro- materials [1]. Moreover, Carbon quantum dots have gained considerable interest due to their properties, such as water solubility, biocompatibility, tunable surface functionalities, good conductivity and good photostability [2]. In addition, their photoluminescence properties allow their use as optical sensors and makes them easy to monitor by absorbance or photoluminescence techniques.
On the other hand, optical biosensors are one of the most studied sensors since they present some advantages compared with conventional analytical techniques such as real-time, label-free detection, high sensitivity, specificity and cost-effectiveness[3, 4, 5].

We fabricated an optical sensor starting with the synthesis and functionalization of mesoporous silica nanoparticles with colloidal cadmium-based quantum dots. Silica nanoparticle is one the most promising material due to their biocompatibility, low-cost procedure, and easy surface functionalization. [6 7 8]. Silica nanospheres present less aggregation than polymer nanoparticles. Additionally, the quantum dots trapped inside the nanoparticles are protected from the degradation and the aggregation [9]. There are two approaches to prepare silica Nanospheres based on the reaction media,i..e the Stöber process [10] and the microemulsion method [11].

Colloidal quantum dots (QDs) have been extensively studied due to their optoelectronic properties such as narrow emission, color tuneability and their potential for applications in electronic and biological systems [12]. We worked with two types of cadmium-based quantum dots. This platform is based in a ratiometric relation between a quantum dot and a dye anchored to the nanoparticles surface. The ratiometric method has been proven to be a good choice to improve the practical applications of sensors because it reduces the environmental influence and provides a more accurate signal through their self-referencing capability.

In our case, we used quantum dots as a detector to determine the elastase concentration of human stool samples. In this purpose, two different emitting cadmium-based quantum dots were encapsulated in silica nanospheres. Then,

a short peptide marked with a 5'-TAMRA dye (5'-Carboxytetramethylrhodamine, with a fluorescence band at 550 nm) is attached to the surface of the nanosphere. The mechanism of our system is quite easy, each quantum has a function: red quantum dots works as a control, meaning that their emission band must remain constant during all the procedure, meanwhile, the blue quantum dot emission decreases depending on the amount of elastase present in the sample. When blue quantum dots are relaxed, after being excited with a lamp, radiative and nonradiative recombination processes happen. Some of this energy is transferred to the photosensitizer dye by FRET (Förster Resonance Energy Transfer). This phenomenon is noticed because the emission band of quantum dots decreases. To allow this process to happen, two requisites are necessary: 1) the donor emission band has to partially overlap to the acceptor absorption band, and 2) the acceptor and the donor must be closer to each other. In our case, the FRET approach is used to detect and quantify elastase. This approach was previously used for the ratiometric detection of trypsine enzyme involved in pancreatic diseases.

The pancreatic function can be classified in three different groups: normal, >200 µg E1/g stool; moderate exocrine pancreatic insufficiency, 100-200 µg E1/g stool; and severe exocrine pancreatic insufficiency, <100 µg E1/g stool [13].

Finally, we present a test to evaluate the pancreatic function from the human stool samples with the aim of developing a point-of-care device. The platform tested 14 samples from patients from Hospital Parc Taulí.

4.2 Material and synthesis.

Reagents.

The following materials were used as received: phosphate buffer solution(PBS, Sigma-Aldrich), Pancreatic elastase (Sigma-Aldrich,) peptide 5`-TAMRA-Ala-Ala-Ala-Cys (Biotrend, >95%), Acetone (Sigma-Aldrich), Trilite ™ Blue-Carboxyl CdSeS@ZnS Core Nanocrystals.

4.2.1 Synthesis and fabrication of silica nanosphere.

4.2.1.1 Synthesis of CdTe QDs.

CdTe QDs were prepared via hot injection using TOPO and ODPA as capping ligands reported in the bibliography[14]. In a three-neck flask, 0.234 g of $CdCl_2$, 132 µL of MPA were solved in 100mL of H_2O. The pH mixture was adjusted to 11 by adding dropwise sodium hydroxide solution and heated up until 100 ºC in inert conditions. When the solution became colorless, a solution of 0.0252 g of Te with 0.140 g of $NaBH_4$ dissolved in 1.5 mL of H_2O was injected into the reaction mixture under a nitrogen atmosphere. The reaction was running for 10 min to achieve the desired quantum dots size without any purification steps and cool at room temperature.

4.2.1.2 Fabrication of Dual QDs coated silica nanosphere and their surface functionalization.

The silica nanospheres were synthesized using a multistep procedure, which involved the formation of the silica sphere followed by functionalization of their surface adding APTMS [15]. The function of silica nanospheres is to protect the quantum dots from the degradation and from their high toxicity as well as to help to put in contact both the quantum dot with the fluorophore.

The nanospheres were synthesized using two different procedures: reverse microemulsion and layer by layer method. To assemble them, we stirred 15 mL cyclohexane, 3.6 mL of n-hexanol, 3,6 mL of Triton X-100 and 2 ml of CdTe QDs during 15 min. Then, we added 120 µL of TEOS and mixed during 30 min, then we added 100µL of NH_3 and 40µL of APTMS to the microemulsion system and stirred during 24 h in dark conditions at room temperature. To stop the reaction, 15 mL of acetone was added to the microemulsion. The sample was centrifuged and cleaned two times with ethanol and water to remove the excess of reactants.

The second step of the reaction was to add blue quantum dots to the system using the layer-by-layer method. To do that, we added first 150 µL APTMS and 500 µL CdSeS QDs and we mixed it during 60 min to allow building the first layer. Then, we centrifuged and cleaned two times with H_2O to remove the excess of reactants. Finally, we added 150 µL APTMS to the mixture and we stirred 30 min to create the second positive layer, where the 5-TAMRA dye will be anchored.

To functionalize, the sample was blended in 20 mL of water and 250 µL of glutaraldehyde was added. The sample was stirred during 4 hours at 37 ºC in dark conditions. Then we centrifuged and cleaned it with H_2O two times. Then, the sample was redispersed in 20 mL PBS and 800 µL of TAMRA-labelled peptide was added and stirred at 4 ºC 20 hours. The sample was centrifuged and cleaned two times with PBS. The solid was dissolved in 45 mL of PBS.

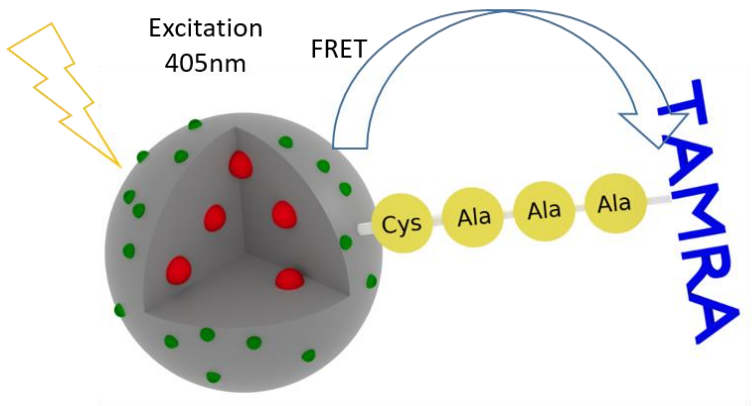

Figure 4. 1. Description of the nanoparticles with cadmium-based quantum dots with the peptide anchored on the surface.

4.2.1.3 Sample preparation.

The pancreatic elastase does not get degraded during intestinal transit; this makes fecal sample a perfect non-invasive probe of pancreatic function. However, the complexity of fecal sample such as morphology must be taken into account in order to optimize the elastase assay[16,17]. To further assess the specificity of the proposed method, we performed different experiments to choose the best relative concentration of the faecal sample.

500 mg of human stool was dissolved in 14 ml of PBS. Then, samples were centrifuged to remove the excess of solid. After that, 50 µL of supernatant was added in 1 ml of 2-nanoSi and brought to 2 ml with PBS.

4.2.2 Fabrication of film-based sensor.

The synthesis and characterization of CQDs-ethylenediamine (CQDs-EDA) are described in **Chapter 7**. The fabrication of films was done following the paper reported in the bibliography with some modifications[18].Fluorine-doped tin oxide (FTO) conducting glass substrate was cleaned with a detergent solution and 2-propanol (IPA). SnO_2 was screen printed onto FTO. The resulting film was heated at 450 ºC under airflow for 20 min. CQDs were deposit onto SnO_2 by spin coating at 1000 RPM for 30 min and heated at 110 ºC during 10 min. Then the film was cleaned with PBS to remove the CQDs that was not absorbed by

the SnO_2. Glutaraldehyde (GA) dropped cast to CQDs. The peptide was dropped cast onto GA overnight.

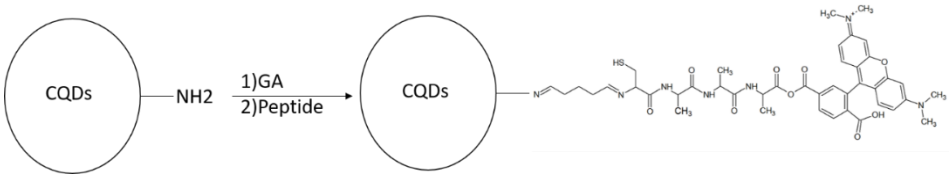

Figure 4. 2. Schematic functionalization of CQDs.

4.3 Results and discussion.

4.3.1 Physicochemical characterization of quantum dots and Nanospheres.

Two different methods were carried out to synthesize the nanosphere: Stöber and layer-by-layer approaches. The first step is to prepare the nanosphere filled with CdTe QDs, which presents an emission band at 660 nm, in the core of it. This method was developed by Stöber in 1968 [10]. Since its publication, the method was modified using different silica sources [19], although the most common one is TEOS [20].

The second step was a layer by layer self-assembly based in the electrostatic interaction. This method allows coating different biomolecules, cells and other materials [21] onto a surface in a simple and versatile way [22]. In our sensor, the amine functionalization provides negative charges from SiO^{2-} groups which can interact with the positive charge of APTMS and CdSeS@ZnS QDs.

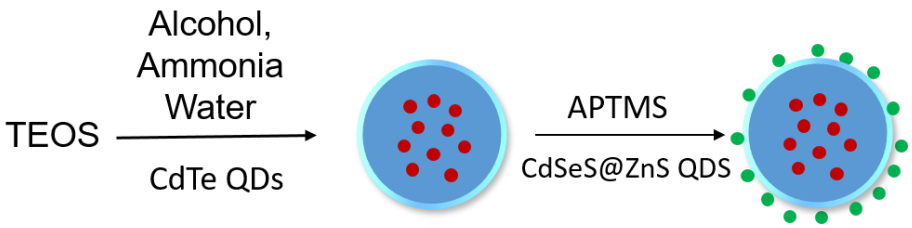

Figure 4. 3. Techniques in silica nanosphere synthesis.

Figure 4. 4 shows the photoluminescence spectra of nanosilica filled with CdTe QD and CdSeS@ZnS QD. The sample was excited at 405 nm, which both quantum dots and the 5'-TAMRA dye absorbed. There are three emission band at 500 nm, 560 nm and 660 nm, which belong to CdSeS@Zns QDs, TAMRA labeled with the peptide and CdTe QDs, respectively. The UV-vis and PL spectra of each quantum dots and the 5'TAMRA labeled peptide dye are shown in the **Annex A4**. All the optical measurements were carried out at room temperature in air conditions.

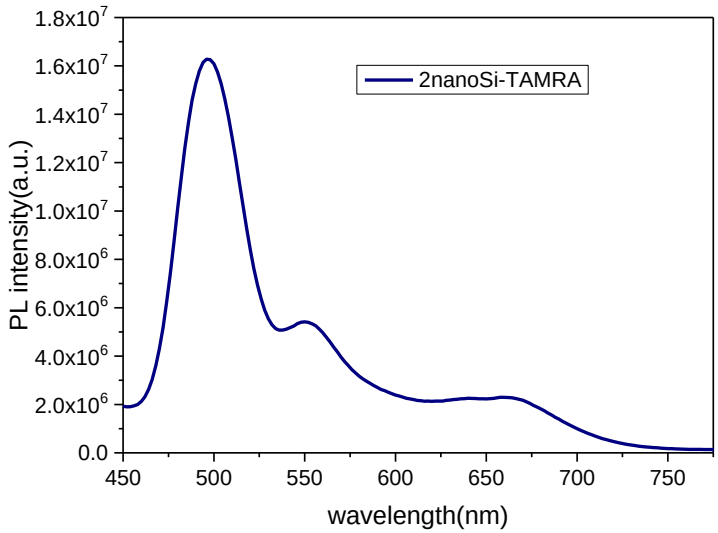

Figure 4. 4 Emission spectra of nanosphere filled with two cadmium-based quantum dot and the peptide anchored to the nanosphere surface. λexc=405nm.

Figure 4. 5 shows the TEM image of the nanoparticles filled with both quantum dots. The average size of the nanosphere was 90 nm, CdTe QDs was 4 nm and ZnCdSeS@ZnS was 2 nm.

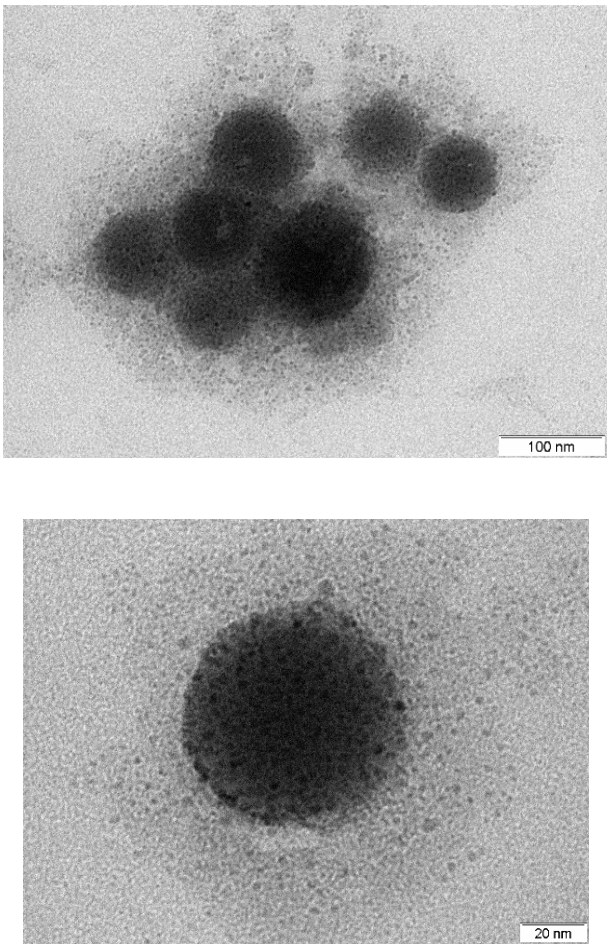

Figure 4. 5. TEM image of nanosphere. The average size of the nanosphere was 90nm, CdTe QDs was 4 nm and ZnCdSeS@ZnS was 2 nm.

4.3.2 Functionalization of silicon dioxide.

The shell modified surface plays a role in different applications such as drug delivery, bioimaging, sensors [23]. There are different approaches to conjugate the nanoparticles to biomolecules such as physical adsorption, cross-link, covalent bonding, etc [24]. For a specific application, different molecules should

be bonded to the nanoparticle surfaces, including drugs, targeting agents, fluorescent molecules, permeation enhancers, biocompatible molecules, etc.

Surface modification of silica particles is most easily achieved by reaction with an alkoxysilanes/halosilanes. In our case, the surface was modified using glutaraldehyde and APTMS. The amine group of the APTMS reacted with the silanol groups via a condensation reaction. Then the aldehyde group from the glutaraldehyde reacted with the amine groups of 3-(Aminopropyl) trimethoxysilane (APTMS). Using glutaraldehyde (GA), any biomolecule with an amine group can be easily immobilized due to the covalent bond between the aldehyde group and the amine group. In Figure 4. 6 appear the molecular structure of APTMS and GA.

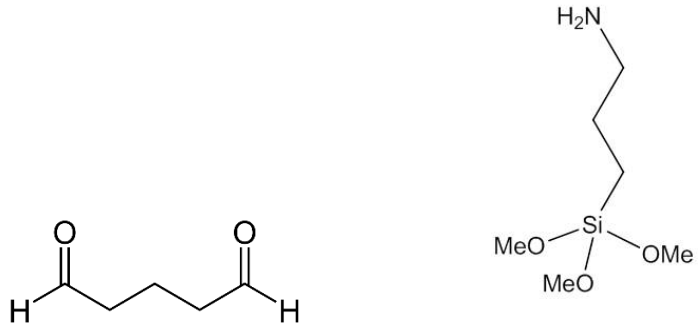

Figure 4. 6.Glutaraldehyde and 3-(aminopropyl) trimethoxysilane molecule.

Nanoparticles were functionalized using two steps: the first one was adding glutaraldehyde and APTMS, followed by binding the dye-labeled peptidic chain. Figure 4. 7 shows the final structure of the silica coating with the attached TAMRA-peptide. The peptide chain is 5'-TAMRA-Ala-Ala-Ala-Cys, the substrate for elastase.

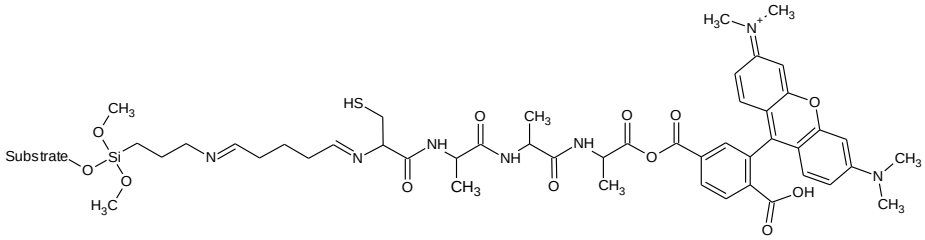

Figure 4. 7.Molecular covalent immobilization of peptide.

4.3.3 Kinetic procedures.

Prior to start the valorization of the platform, the enzyme activity was determined by testing the amount of elastase that interacts with the specific peptide in order to study their kinetics mechanism and their optimal time. The time, concentration and certain compounds that may interact with the sample were studied to determine the optimal incubation time. The kinetic measurements were performed using a wide range of elastase concentrations (0-625 µg/L). Each sample was monitored during 3 hours and the PL spectra were recorded each 5minutes. Figure 4. 8 shows the ratio between I496/I660 using different amounts of elastase at different times. we observed that our platform did not work as a common enzyme activity. We thought that at a certain point, the system reached equilibrium and the elastase stopped to interact with the sample.

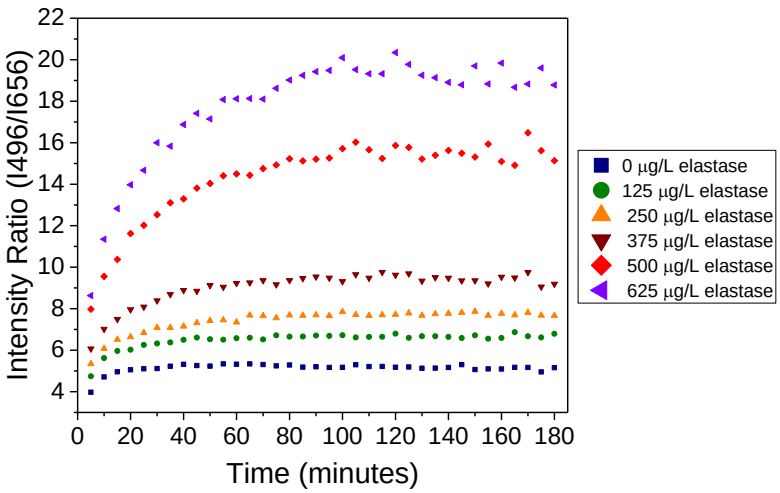

Figure 4. 8.Kinetics of enzymatic digestion using different concentrations of elastase as a function of time.

4.3.4 Optimization protocol of the human stool samples.

One of the main issues was that the concentration and morphology of the human stool affect significantly the photoluminescence spectra. We realized that working with a high concentration of human samples increases the red emission peak strength and widens the green emission peak. In Figure 4. 9 is shown the PL of different concentrations of human fecal, the lowest concentration gave the best photoluminescence profile, while blue and green lines showed distorted PL spectra.

Using the higher relative concentration gave incorrect values. One possible explanation might be because the fecal solid had some insoluble particles that might destroy or interfere in our system. In addition, the consistency of the human samples affected significantly the measurements. Two different human samples, with a similar estimated elastase value, exhibited different PL spectra. Depending on the fecal consistency, the PL spectra showed the green and the red peak emission with different width.

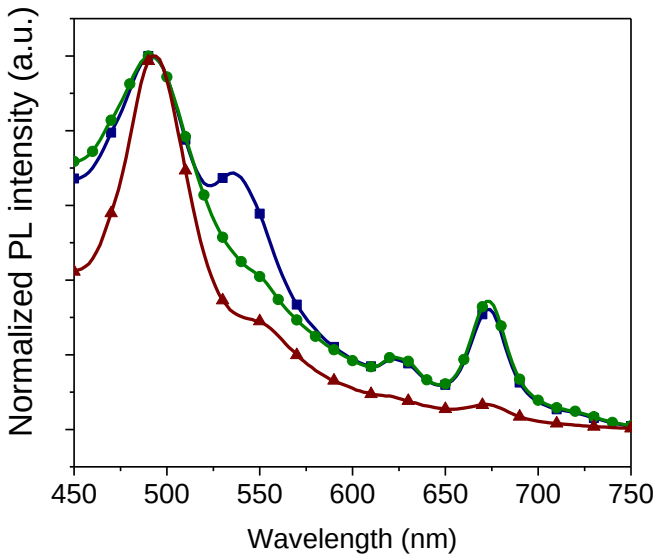

Figure 4. 9.Photoluminescence spectra of our platform got in contact with different human fecal concentrations.180 mg/ml (blue line), 2 mg/mL (green line) and 0.89 mg/mL (red line).

4.3.5 Validation.

Before validating the method, the presence of FRET approach was need to verify between ZnCdS@ZnS and TAMRA dye had to be confirmed. As we mentioned in the introduction, there is a FRET transfer between the blue QDs and the TAMRA dye is alredy stablished. Two conditons must be matched i) the donor emission band has to overlap to the acceptor absorption band; ii) and the acceptor and donor must be close each other. To verify it, PL spectra of the donor and UV-vis spectra of the acceptar were measured at room temperature. Figure A4.4 shows the overlap area between both material confirming the energy transfer between them.

As there is an emission dependence between the green emission band and the amount of elastase, the ratio between green and red QDs, on one side, and elastase concentrations, on the other side, can be modeled according to the following linear curves. The photoluminescence spectra of each curve are shown in the **Annex A4**.

$$I500/I600 = 3.81 \cdot 10^{-3}[\text{elastase}] + 15.83$$
$$I500/I600 = 2.96 \cdot 10^{-3}[\text{elastase}] + 9.66$$

Even both sets of nanospheres were synthesized using the same procedure, their emission intensity differs. The reason is that we could not control the amount of QDs that came into the nanospheres. For that, we needed to control via curve calibration the emission intensity of our system. Figure 4.10 shows both calibration curve that we used to determine and quantify 14 samples of human stool.

a)

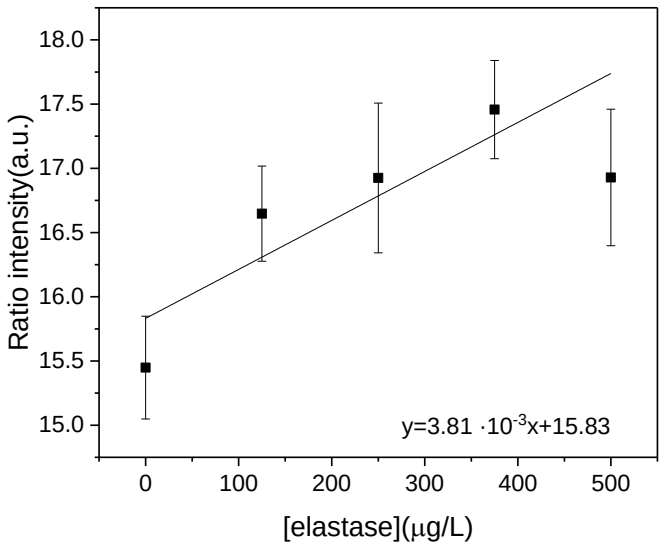

b)

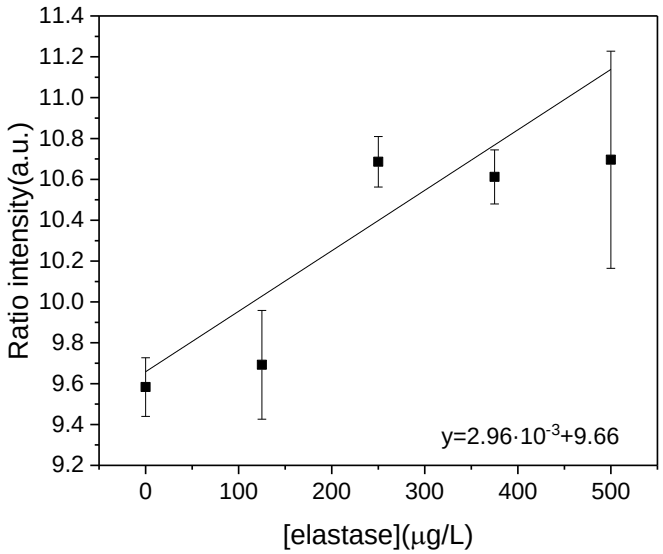

Figure 4. 10. Calibration curve fitting the ratio intensity between I500/I660 and the elastase concentration.

Using the procedure described above, we tested 14 fecal samples from different patients to quantify the amount of elastase. The results were compared with the reference values from the Parc Taulí hospital. (Table 4.1)

$$X\ \frac{\mu g}{L} x \frac{2ml}{0{,}05ml} x \frac{14 \cdot 10^{-3} L}{Pmg} x \frac{1000mg}{1g} = \ [\text{elastase}]\ (\mu g/g)$$

Table 4.1. Analytical results of elastase determination in fecal samples. Where, LD is the limit detection.

Sample	*[elastase] (µg/g) Exp*	*[elastase] (µg/g) Hospital*
M1	*415*	*396*
M2	*314*	*846*
M3	*424*	*920*
M4	*<L.D*	*<L.D*
M5	*115*	*<L.D*
M6	*<L.D*	*<L.D*
M7	*<L.D*	*<L.D*
M8	*<L.D*	*<L.D*
M9	*<L.D*	*<L.D*
M10	*174*	*<L.D*
M11	*178*	*<L.D*
M12	*216*	*<L.D*
M13	*<L.D*	*320*
M14	*<L.D*	*345*

Each sample's PL spectrum is measured three times, then using the formula reported above the elastase concentration was calculated. The average of this

concentration is the result that appears in Table 4.1. The PL spectrum of each sample is shown in the **Annex A4**.

From these 14 samples, we have calculated the specificity (false positive) and selectivity (true positive) of the method. The sensitivity and specificity were calculated to validate the clinical tests. Those parameters are independent of the population of interest[25]. .By definition, sensitivity is the ability of the test to correctly identify the patients with the disease. The specificity is the ability of the test to detect the patients without the disease. The reliability of the method was tested on 14 patients, obtaining 90% sensitivity and 70% specificity.

Regarding the promising results, we decided to try to scale-up the process. The problem that we found was that the system was not as reproducible as we expected. There are a lot of parameters such as peptide anchoring, stabilization of nanospheres etc, that it is important to take into account. While we were trying to solve this inconvenience, we proceeded to fabricate a new sensor which could improve some of the weakness of our system. For that, we fabricate an electrochemical sensor based on carbon quantum dots [21, 2]. This part was done in collaboration with Patras University under the supervision of Dr. Topoglidis.

4.3.6 Electrochemical sensor results.

This section is divided into two parts: The first one is dedicated to measuring the Cyclic Voltammetry (CV) of CQDs and how the conductivity improved when a layer of metal oxides is deposit between FTO and CQDs. In the second one, we studied how the CV changed when small amounts of elastase were added to the system.

The idea to try CQDs without adding any interlayer was to verify if the CQDs could enlarge the surface area to increase the conductivity of the electrode. For that purpose, we deposited on top of Indium tin oxide (ITO) 50 μL of CQDs by spin cast. Unfortunately, we did not observe any anodic or cathodic bands, because the layer of CQDs was too thick and they worked as an insulator. To

solve this problem, we attempted different strategies: first, we deposit 10 µL on the bottom of glassy carbon, since the conductivity of glassy carbon is higher than the one of indium tin oxide. Still, we did not observe any band. Then, We tried depositing the QDs by spin coating on top of Fluorine doped tin oxide (FTO), but the layers that we obtained were not homogeneous due to the low wettability between the FTO and CQDs. Finally, we obtained suitable samples by depositing a layer of a metal oxide on top of FTO; namely SnO_2 and ZnO Nanoparticles NPs, and on top of them a layer of CQDs.

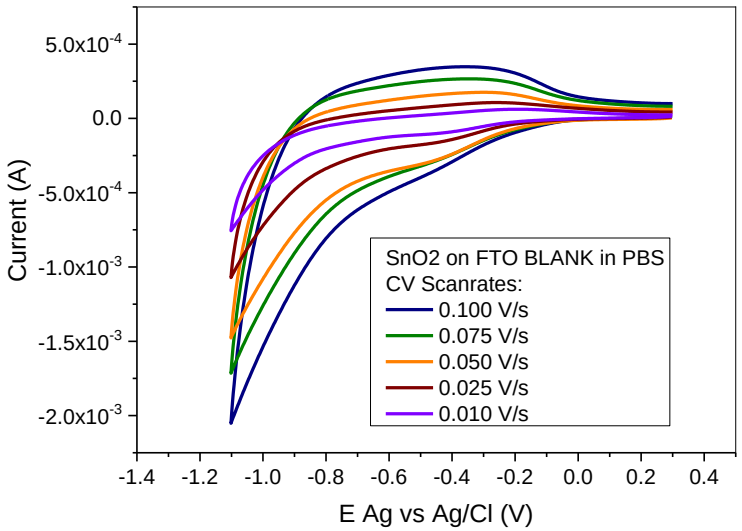

Figure 4. 11. Cyclic voltamogram of SnO_2 deposit on top of FTO at different scan rates at pH=7.

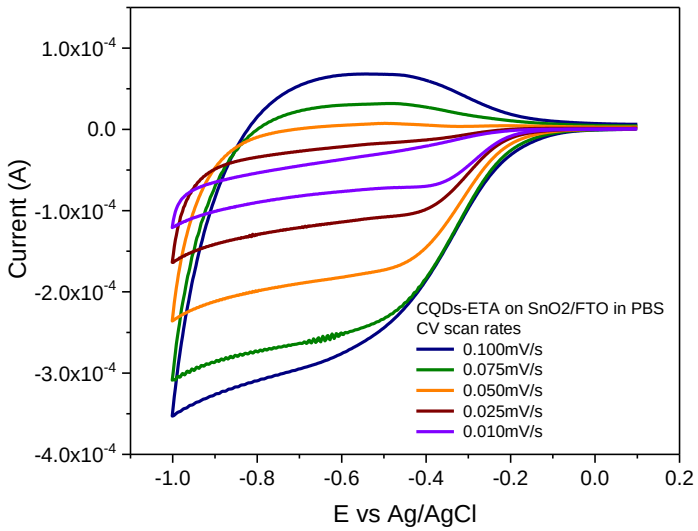

Figure 4. 12. Cyclic voltamogram of CQDs-EDA deposit on top of SnO_2/FTO at different scan rates at pH=7.

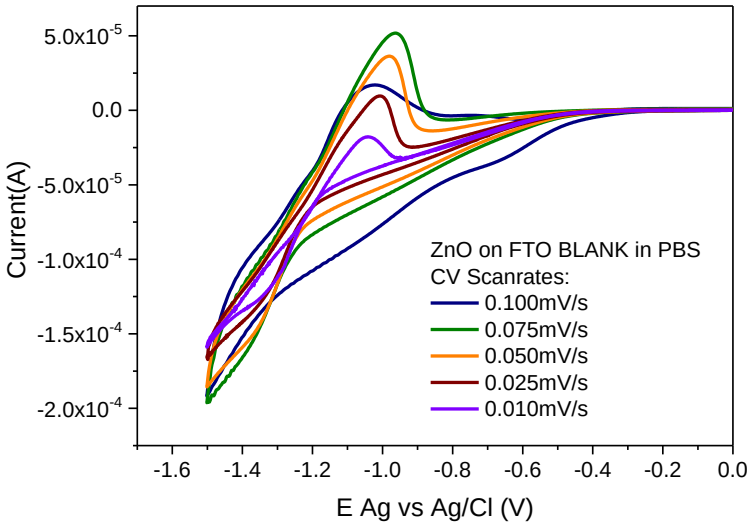

Figure 4. 13.Cyclic voltamogram of ZnO NPs deposit on top of FTO at different scan rates at pH=7.

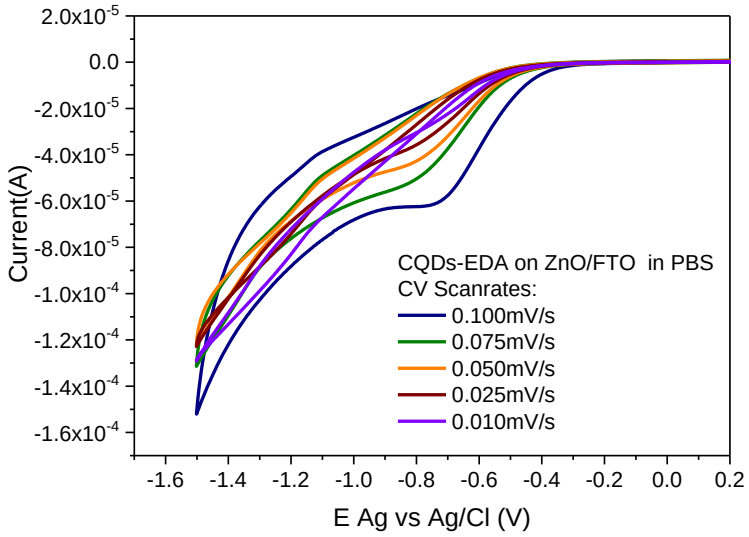

Figure 4. 14. Cyclic voltamogram of CQDs-EDA deposit on top of ZnO/FTO at different scan rates at pH=7.

Once the CQDs were deposited on top of SnO_2, the film was soaked into the peptide solution overnight. Then, the film was cleaned with water and PBS. Figure 4.15 shows the CV scan of the final sensor. We observed three different reduction bands at -0.5V, -0.7V and -1.0V. The reduction band at -1.0V is attributed to the peptide, confirming that it was covalently bound to the amine on the CQDs. The reduction band at -0.5V is attributed to the CQDs.

a)

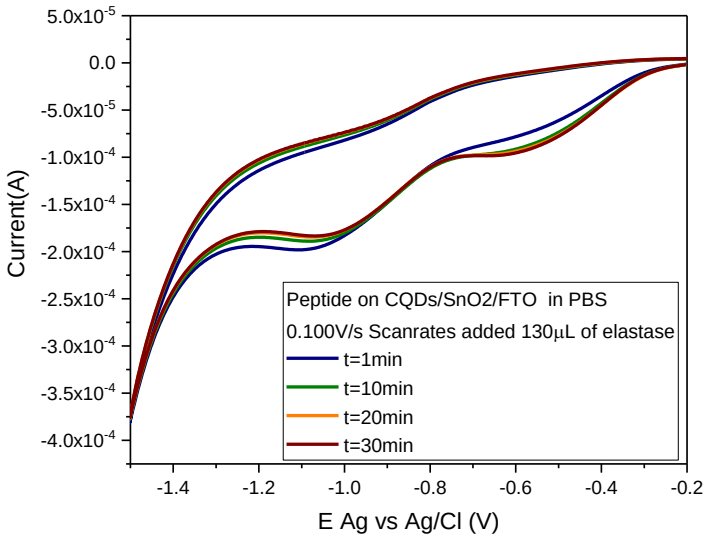
5.0x10-5
0.0
-5.0x10-5
-1.0x10-4
-1.5x10-4
-2.0x10-4
-2.5x10-4
-3.0x10-4
-3.5x10-4
-4.0x10-4
Current(A)
-1.4
-1.2
-1.0
-0.8
-0.6
-0.4
-0.2
E Ag vs Ag/Cl (V)
Peptide on CQDs/SnO2/FTO in PBS
0.100V/s Scanrates added 130µL of elastase
t=1min
t=10min
t=20min
t=30min

b)

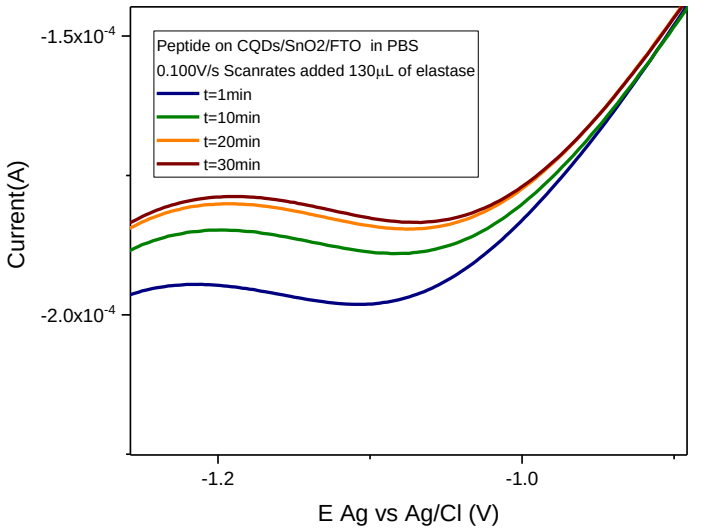
-1.5x10-4
-2.0x10-4
Current(A)
-1.2
-1.0
E Ag vs Ag/Cl (V)
Peptide on CQDs/SnO2/FTO in PBS
0.100V/s Scanrates added 130µL of elastase
t=1min
t=10min
t=20min
t=30min

c)

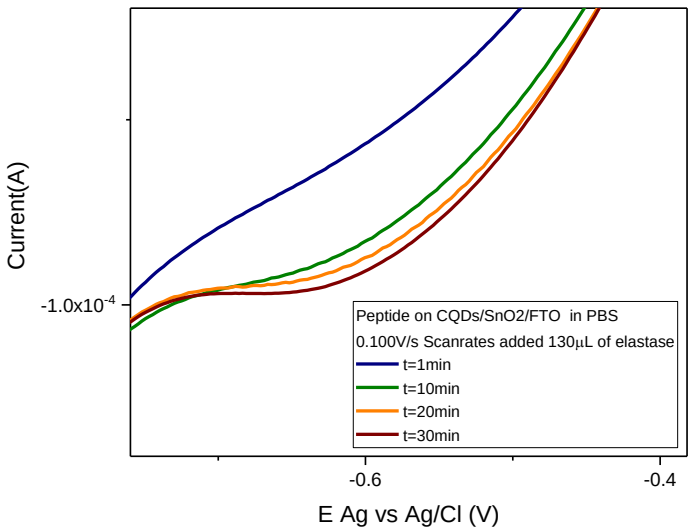

Figure 4.15. Schematic functionalization of CQDs. a)CV measurements at different time 0.100V/s scan rates. b) A magnification of the first anodic peak from Figure (a). c) A magnification of the second anodic peak from Figure (a).

We added to the electrochemical cell 130µL of elastase, our enzym of interest, to cut the peptide, and we recorded the CV at different times. We observed that at longer times the reduction bands of peptide decreased, while one of the CQDs increased. (See Figure 4.15 middle and Figure 4.15 bottom).

These phenomena could be explained because once the elastase enzyme cuts the peptide, the amount of peptide anchored to CQDs surface decreased and as a consequence their reduction band as well. The reduction bands attributed to CQDs increased because the amount of free CQDs increased

4.4 Conclusions.

We present an optical biosensor based on encapsulated cadmium-based quantum dots to detect and quantify elastase enzyme in human fecal samples. The method presents high sensitivity and specificity in identifying patients with

cystic fibrosis. The reliability of the method was tested on 14 patients, obtaining 90% sensitivity and 70% specificity.

The optical properties of QDs such as photostability and long fluorescence time compared with organic fluorophores widen the potential applications of this material for future applications. Although our system does not present toxicity thanks to QDs encapsulation in silica Nanospheres. However, we are working trying to replace cadmium-based quantum dots for carbon-based.
This platform allows us to detect and quantify elastase enzyme in human stool to detect pancreatic insufficiency. This pathology is caused by a reduction of pancreatic enzyme and as consequence abnormal digestion and malabsorption of nutrients. In addition, this new method allows us to bind different peptides depending on which enzyme we want to quantify. This proof-of-concept pilot study opens new opportunities to detect and quantify biomolecules in a rapid and non-invasive way.

As we mentioned previously, the problem that we found was the low reproducibility that our platform presented. We tried to increase the robustness of the method but the desorption process ocurring in the nanosilica surface, blocked the possibility to scale up the process. We studied different approaches in order to detect the elastase in human stools using other techniques. We started to construct a sensor based on electrochemical measurements. Moreover, we replaced the cadmium-based quantum dots for carbon quantum dots. We tried to functionalize its surface adding the peptide directly. Even the promising results, this project is still in an early stage and a further and deeply studied is needed.

4.5 References

1. F.R. Baptista, S.A. Belhout, S. Giordani, S.J. Quinn. Recent developments in carbon nanomaterial sensors. *Chem. Soc. Rev.* **2015**, 44 (13), 4433–4453.
2. Z. Wang, Z. Dai. Carbon nanomaterial-based electrochemical biosensors: an overview. *Nanoscale* **2015**, 7 (15), 6420–6431.
3. B. Turk. Targeting proteases: successes, failures and future prospects. *Nat. Rev. Drug Discov.* **2006**, 5, 785.
4. A.R.Y.S. Ghadeer, J. Deema, B.S. Mayadah, Z. Mohammed. Proteinases as Biomarkers in Breast Cancer Prognosis and Diagnosis. *Mini-Reviews Med. Chem.* **2017**, 17 (7), 583–592.
5. P. Damborský, J. Švitel, J. Katrlík. Optical biosensors. *Essays Biochem.* **2016**, 60 (1), 91–100.
6. T. Zhao, N.-T. Nguyen, Y. Xie, et al. Inorganic Nanocrystals Functionalized Mesoporous Silica Nanoparticles: Fabrication and Enhanced Bio-applications. *Front. Chem.* **2017**, 5, 118.
7. Q. Ma, X. Su. Recent advances and applications in QDs-based sensors. *Analyst* **2011**, 136 (23), 4883–4893.
8. Y. Wang, Q. Zhao, N. Han, et al. Mesoporous silica nanoparticles in drug delivery and biomedical applications. *Nanomedicine Nanotechnology, Biol. Med.* **2015**, 11 (2), 313–327.
9. N. Thanh, L. Green. Functionalisation of nanoparticles for biomedical applications; **2010**; Vol. 5.
10. W. Stöber, A. Fink, E. Bohn. Controlled growth of monodisperse silica spheres in the micron size range. *J. Colloid Interface Sci.* **1968**, 26 (1), 62–69.
11. L. Ernawati, R. Balgis, T. Ogi, K. Okuyama. Tunable Synthesis of Mesoporous Silica Particles with Unique Radially Oriented Pore Structures from Tetramethyl Orthosilicate via Oil–Water Emulsion Process. *Langmuir* **2017**, 33 (3), 783–790.
12. K.E. Sapsford, T. Pons, I.L. Medintz, H. Mattoussi. Biosensing with

Luminescent Semiconductor Quantum Dots. *Sensors (Basel).* **2006**, 6 (8), 925–953.

13. W. Soldan, J. Henker, C. Sprössig. Sensitivity and Specificity of Quantitative Determination of Pancreatic Elastase 1 in Feces of Children. *J. Pediatr. Gastroenterol. Nutr.* **1997**, 24 (1), 53–55.
14. H. Zhang, L. Wang, H. Xiong, et al. Hydrothermal Synthesis for High-Quality CdTe Nanocrystals. *Adv. Mater.* **2003**, 15 (20), 1712–1715.
15. H.A. Ketelson, R. Pelton, M.A. Brook. Colloidal Stability of Stöber Silica in Acetone. *Langmuir* **1996**, 12 (5), 1134–1140.
16. B. Lindkvist. Diagnosis and treatment of pancreatic exocrine insufficiency. *World J. Gastroenterol.* **2013**, 19 (42), 7258–7266.
17. S. Naruse, H. Ishiguro, S.B.H. Ko, et al. Fecal pancreatic elastase: a reproducible marker for severe exocrine pancreatic insufficiency. *J. Gastroenterol.* **2006**, 41 (9), 901–908.
18. A. Panagiotopoulos, A. Gkouma, A. Vassi, et al. Hemin Modified SnO2 Films on ITO-PET with Enhanced Activity for Electrochemical Sensing. *Electroanalysis* **2018**, 30 (9), 1956–1964.
19. E.D.E.R. Hyde, A. Seyfaee, F. Neville, R. Moreno-Atanasio. Colloidal Silica Particle Synthesis and Future Industrial Manufacturing Pathways: A Review. *Ind. Eng. Chem. Res.* **2016**, 55 (33), 8891–8913.
20. X. Lv, L. Zhang, F. Xing, H. Lin. Controlled synthesis of monodispersed mesoporous silica nanoparticles: Particle size tuning and formation mechanism investigation. *Microporous Mesoporous Mater.* **2016**, 225, 238–244.
21. E. Ahn, T. Lee, M. Gu, et al. Layer-by-Layer Assembly for Graphene-Based Multilayer Nanocomposites: The Field Manual. *Chem. Mater.* **2017**, 29 (1), 69–79.
22. J.J. Richardson, J. Cui, M. Björnmalm, et al. Innovation in Layer-by-Layer Assembly. *Chem. Rev.* **2016**, 116 (23), 14828–14867.
23. A. Alvarez-Toral, B. Fernández, J. Malherbe, et al. Synthesis of amino-functionalized silica nanoparticles for preparation of new laboratory standards. *Spectrochim. Acta Part B At. Spectrosc.* **2017**, 138, 1–7.
24. A. Liberman, N. Mendez, W.C. Trogler, A.C. Kummel. Synthesis and surface functionalization of silica nanoparticles for nanomedicine. *Surf.*

Sci. Rep. **2014**, 69 (2), 132–158.

25. A.G. Lalkhen, A. McCluskey. Clinical tests: sensitivity and specificity. *Contin. Educ. Anaesth. Crit. Care Pain* **2008**, 8 (6), 221–223.
26. M.A. Hink, N. V Visser, J.W. Borst, A. Van Hoek, A.J.W.G. Visser. Practical Use of Corrected Fluorescence Excitation and Emission Spectra of Fluorescent Proteins in Förster Resonance Energy Transfer (FRET) Studies. **2003**, 13 (2), 1–4.
27. I.L. Medintz, S.A. Trammell, H. Mattoussi, J.M. Mauro. Reversible Modulation of Quantum Dot Photoluminescence Using a Protein- Bound Photochromic Fluorescence Resonance Energy Transfer Acceptor. *J. Am. Chem. Soc.* **2004**, 126 (1), 30–31.

A4 ANNEX

A4.1 Supplementary Figure 4.s and tables.

Figure A4. 1 shows the absorbance and photoluminescence spectra of both quantum dots that we were working with the fabrication an optimization of the biosensor.

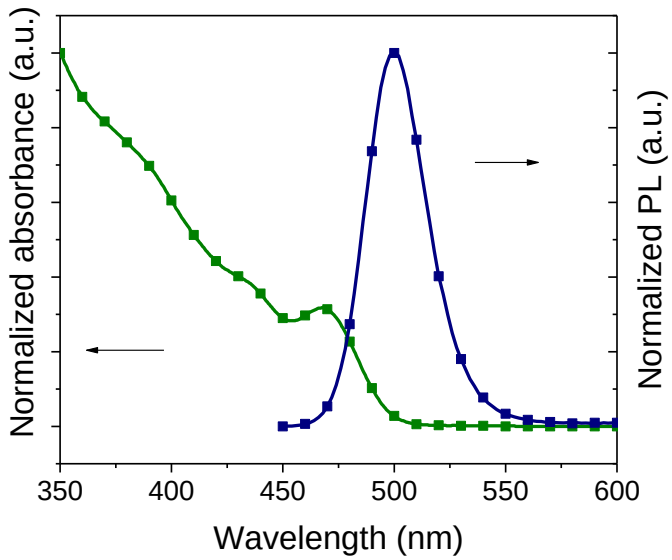

Figure A4. 1. Absorbance and emission spectra of CdSeS@ZnS QDs which present an emission band at 500 nm.

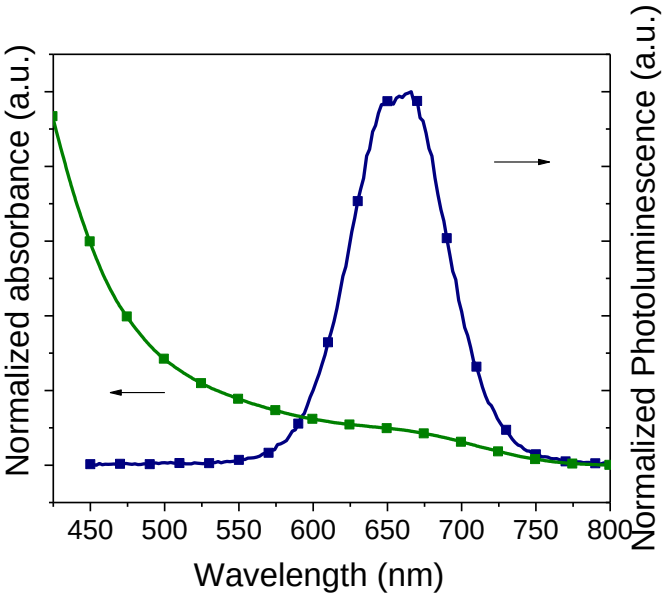

Figure A4. 2. Absorbance and emission spectra of CdTe QDs with an emission band at 660 nm.(Bottom)

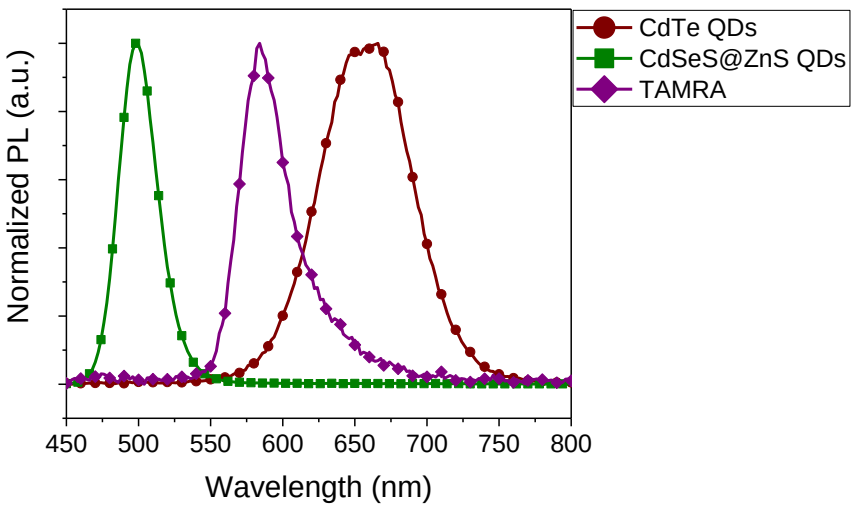

Figure A4. 3.Emission spectra of QD500nm (green). 5'TAMRA dye(violet) and QD660nm (red).

A4.2 Fret calculations.

The FRET efficiency derived from QD quenching using following equations. Figure A4. 4 (bottom) shows the overlap spectra between the Green quantum dots and the dye absorption[26,27].

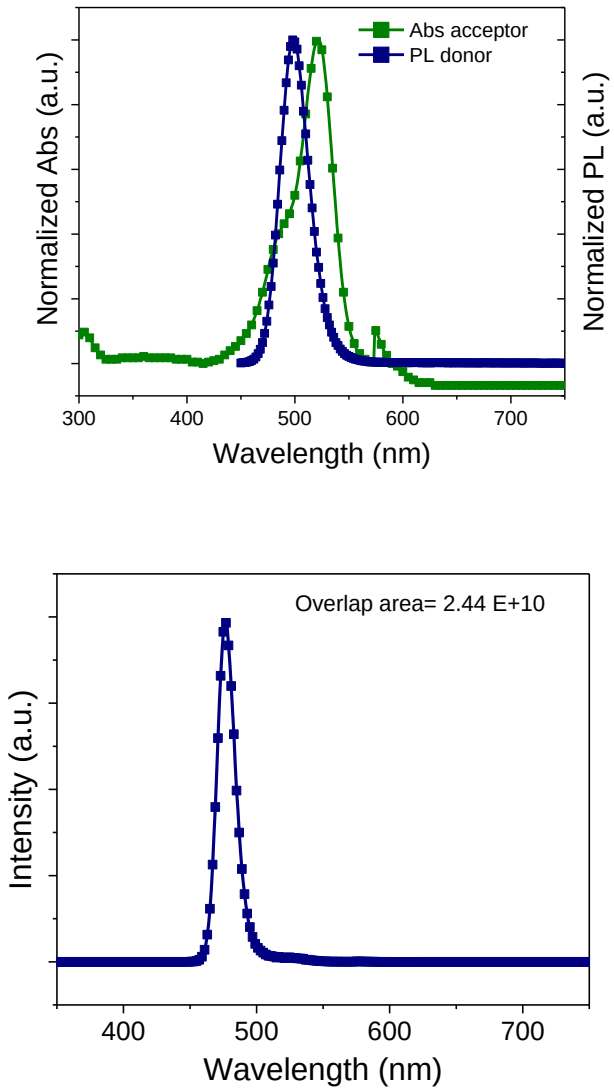

Figure A4. 4. Absorbance spectra of Dye and photoluminesce spectra of CdSeS@ZnS measured in solution at room temperatura (top) and the overlap spectra area between both materials (bottom).

The experimental efficiciency, E is definided by:

$$E = \left(\frac{F_{DA}}{F_D}\right) x100$$

Where, F_D is the fluorescence intensity of donor and F_{DA} is the fluorescence intensities in presence of the acceptor.
The FRET efficiency was calculated using the following equation:

$$E = 1/[1 + (r/R_0)^6]$$

Where R_0 is the Förster distance between the donor-acceptor separation at 50% energy transfer Efficiency and r is the distance between the donor and acceptor pair.

R_0 can be expressed as:

$$R_0 = 0.211\ (k^2 n_D^{-4} Q_D J(\lambda))^{1/6}$$

Where n_D is the refractive index of the medium Qd is the donor quantum yield in the absence of acceptor (50%), J(is the spectral overlap area and $k^2$is the dipole orientation factor (0.66).

For our platform, we obtained Ro=7.55 nm, r= 10 nm and E=15 %

A4.3 Calibration curve.

a)

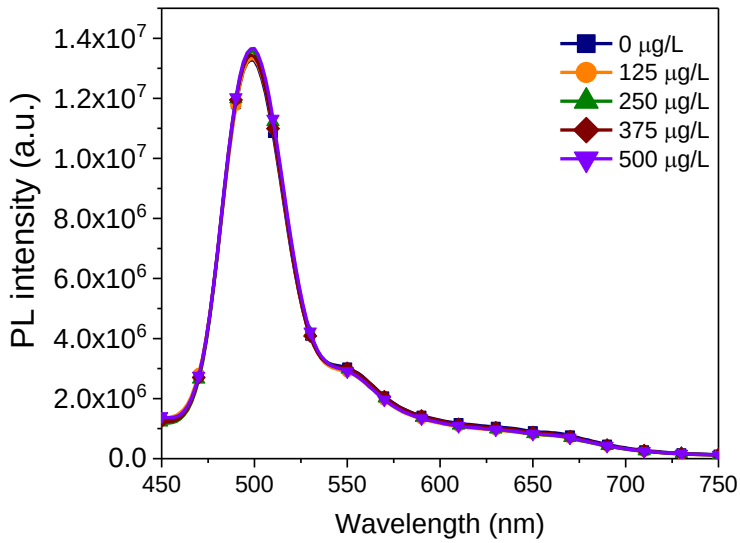

b)

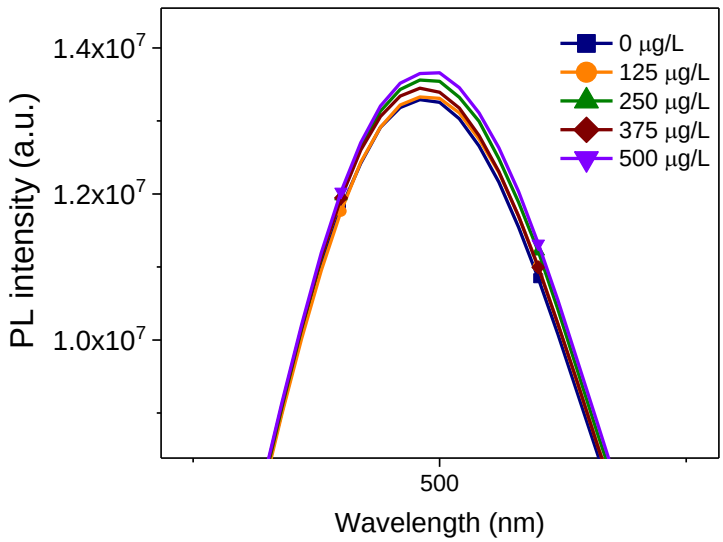

c)

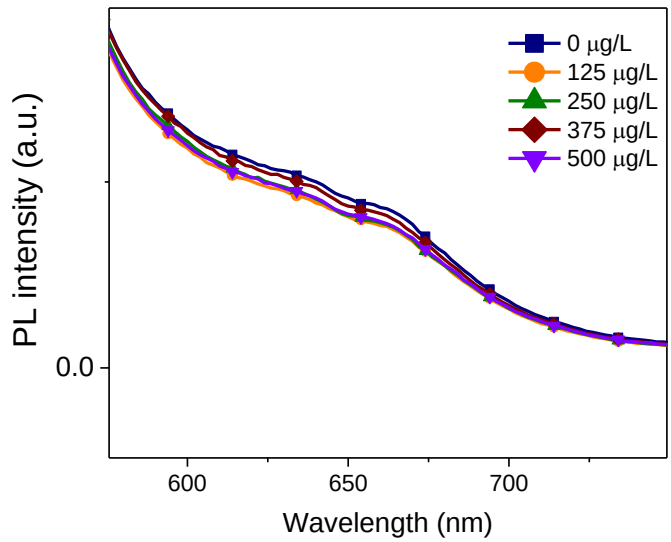

Figure A4.5.a) Emission spectra of nanosphere increasing the amount of elastase. b) magnification of the first emission band of nanosphere and c) the second emission band of nanosphere.

a)

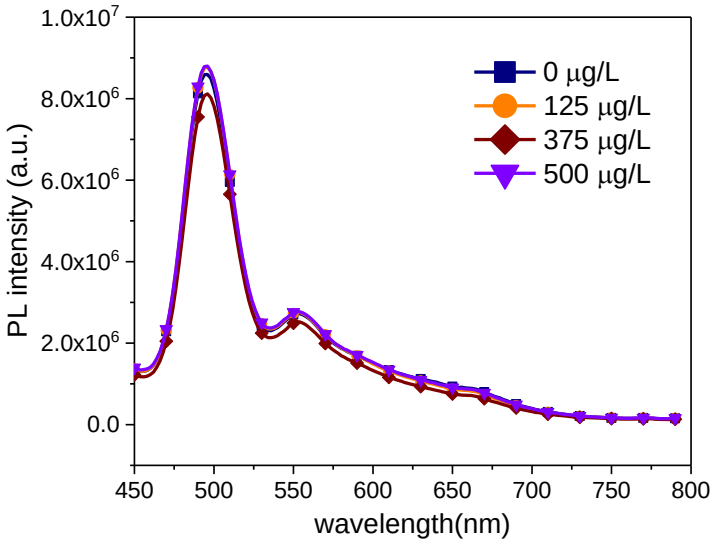

b)

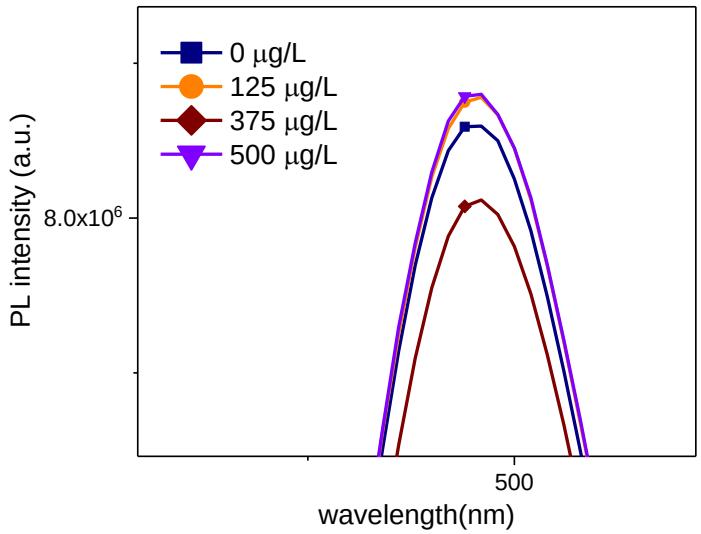

c)

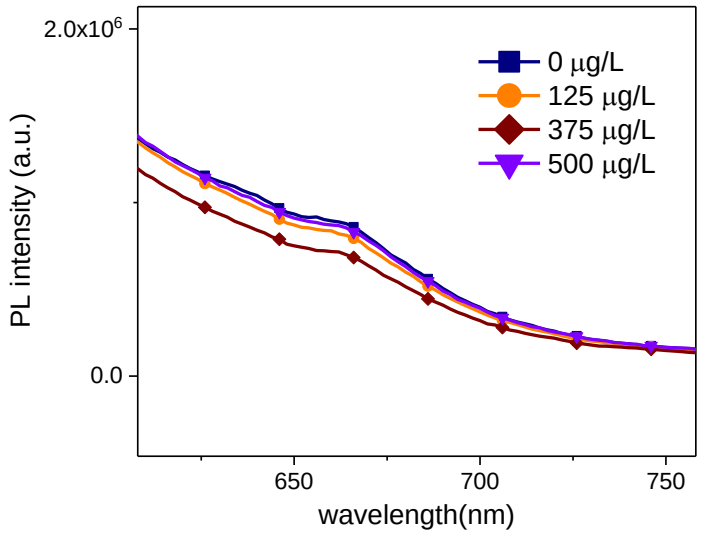

Figure A4. 6.a) Emission spectra of nanosphere increasing the amount of elastase.b) magnification of the first emission band of nanosphere and c) the second emission band of nanosphere.

5

Cadmium based quantum dots as emissive layer in LEDs.

Cadmium based quantum dots are the most studied nanomaterial in the emitting layer of LEDs. In this chapter, we show the results of using green, red and blue light emitting quantum dots in the photoactive layer.

Chapter 5

Table of contents

Chapter 5

5.1 Introduction.

During the last decades, colloidal quantum dots have been extensively studied due to their optoelectronic properties and their multiple applications in electronic and biological systems[1] . Cadmium/ Zinc calchogenides quantum dots core-shell have extraordinary optoelectronic properties, such as narrow emission and broad absorption that convert them in a very interesting nanomaterial to work with. Futhermore, capping a quantum dot with a layer of ZnS is a good alternative to suppress deep trap emission by passivating most of the vacancies resulting in improved quantum efficiency [2]. In addition, the easiness to tune the bandgap with the size of the quantum dot, determined by the synthetic procedure, allows the preparation of light emitting diodes from UV-vis to infrared. This color tunability increases the number of application of the QDsLED, for example as photodetector, laser applications or white light emitting diodes, combining red, green and blue QDs [3].

In our case, we use colloidal quantum dots as emitter layer or hole conductor material in light emitted diodes (LEDs).
The use of metal oxides in light emitting diodes are nowadays attracting great attention due to their intrinsic air stability and solution processability, which could result in low-cost, large area, light emitting devices. In addition, the inverted charge injection structure reduce the charge carrier injection barrier from anode/cathode [4,5].

We fabricated QDLED using ZnO NPs as electron transport layer (ETL), Cadmium based Quantum dots as unique emissive layer, poly(9-vynilcarvazole) (PVK) as hole transport layer (HTL), and polyethylenimine ethoxylated (PEIE) as interlayer between ETL and Quandtum dots. This polymer works as a surface modifiers, reducing the work function of electrodes including transparents metal oxide, electrode or organic material [6]. In our case, we deposit a layer of PEIE to reduce the work function of ZnO, helping the injection current [7].

We fabricated solution-processed QDsLED in air conditions. This conditions are relevant in order to try to scale up the process using other printing techniques such as ink jetprinting or slot die roll-to-roll printing [8,9] [10]. All the layers were deposited by spin coating in air conditions with the execption of MoO_3 and gold that were thermal evaporated.
Three different cadmium based quantum dots were synthetized by hot injection method. They were synthetized in inert conditions using oleic acid (OA) as capping ligand to mediate their size and shape and stabilize their dispersion.

This chapter is focused on optimizing the inverted structure using cadmium based quantum dots. The aim is to understand how the interface charge traps and energy transfer between the active layer and the contact could affect to the final device efficiency. In addition it was the starting point to use the inverted LEDs to use with other emissive layer like Perovkites nanoparticles or Quantum dots or Carbon Quantun dots (CQDs).

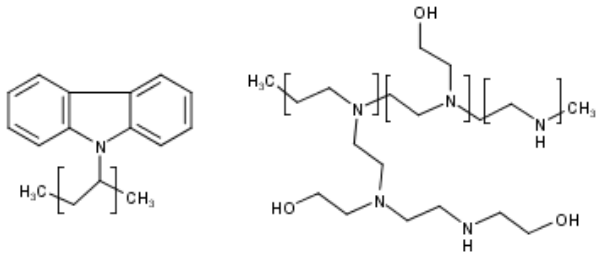

Figure 5. 1. Molecular structure of PVK (right) and PEIE (left).

5.2 Experimental part.

Cadmium based quantum were synthetized by a hot inject process in inert conditions. The synthesis of ZnO NPs is described in **Chapter 3.**

5.2.1Synthesis of green, red and blue CdSe@ZnS.

5.2.1.1 Green ZnCdSe@ZnS QDs.

CdSe@ZnS QDs were syntethized following a procedure reported previously in the bibliography [11]. Briefly, in 100 ml three-neck flask equipped with a reflux condenser and heating mantel, 0.14 mmol Cd(OAc)2, 3.41 mmol ZnO, 7 mL of oleic acid and 15 ml of 1-octadecene (ODE) were mixed together and put under an argon atmosphere. The mixture was heated up to 150 ºC. In another bottom flask, 5 mmol of Se, 5 mmol of S was solved in 5 ml of TOP under an argon flow. Then the solution was heated up to 190 ºC and 0.3 ml of Se/S-TOP solution was added as fast was possible. The reaction was heated during 1 minute. After cooling, we added acetone to precipitate CdSe@ZnS QDs. The mixture was centrifuged and the precipitate was washed with ethanol/hexane(4:1) three times to achieve pure CdSe@ZnS nanocrystals. Finally, CdSe@ZnS were resdispersed in $CHCl_3$ and stored at room temperature.

5.2.1.2 Red CdSeS@ZnS QDs.

CdSeS@Zns were prepared via hot injection reported in the bibliography[12]. In 10 mL three-neck flask equipped with a reflux condenser and heating mantel, 0.060 gr CdO, 0.224 gr of octadecylphosphonic (ODPA) and 3 gr trioctylphospine oxide (TOPO) was mixed 150 ºC during 30 min under inert conditions. After that, the sample was heated up to 305 ºC. A solution of 0.27 mmol Se, 0.03 mmol S with 0.5 ml of trioctylphosphine was added quickly. The reaction was heated during 10 min. The quantum dots were precipitated with acetone and purified with a mixture of toluene/acetone(1:4).

For producing the ZnS shell , 172 mg of QDs were solved in 25 ml ODE and heated at 270 ºC at inert conditions. Then, a solution of 2.86 mmol $Zn(ac)_2 \cdot H_2O$, 4 ml OA and 1 ml ODE was added to a solution of 6.75 mmol of Sulphur with 3.5 mL of TOP. The reaction was maintained during 10 min at 270 ºC. The quantum dots were precipitated with acetone and purified with a mixture of toluene/acetone(1:4).

5.2.1.3 Blue ZnCdS@ZnS QDs.

ZnCdS@Zns were prepared via hot injection method reported in the bibliography[12]. ZnCdS@ZnS QDs were prepared as follows: 1 mmol of CdO, 10 mmol ZnO, 7 ml oleic acid (OA) and 15 mL of ODE were mixed at 150 ºC during 30 min under inert conditions. The mixture was heated up to 310 ºC until the solution lost its color. Then a solution of 1.6 mmol of sulfur diluted with 2.4 ml of ODE was injected. The reaction was kept during 12 min. Once the reaction was at room temperature, an excess of acetone was added to precipitate CdZnS QDs. To purify the solid, a mixture of toluene and acetone was added and finally stored in toluene.

For producing the ZnS shell, CdZnS QDS were solved in 25ml ODE and heated at 270 ºC at inert conditions. Then, a solution of 2.86 mmol $Zn(ac)_2 \cdot H_2O$, 4 ml OA and 1 ml ODE was added to a solution of 6.75 mmol of Sulphur with 3.5 mL of TOP. The reaction was maintained during 10 min at 270 ºC. The quantum dots were precipitated with acetone and purified with a mixture of toluene/acetone(1:4).

5.3 Device fabrication.

Patterned ITO (Indium doped Tin Oxide) coated glasses (Xinyan Technology, resistance 10 Ω/square, 15x15 mm) were cleaned with acetone for 15 minutes and 2-propanol for 15 minutes in an ultrasound bath. Cleaned ITO (Indium doped tin oxide) substrates were used as anode, on top of ITO a layer of ZnO (80mg/ml in methanol) was deposited by spin coating at 5000 RPM 60 seconds and heated up 30 minutes at 150 ºC. Polyethylenimine ethoxylated (PEIE 0.2 %wt 2-methoxyethanol) was spin coated on top at 6000 RPM 60 s and annealed at 110 ºC for 30 minutes. After that, the solution of cadmium based solved in hexane (the concentration was different depending on the material) were deposited on top of PEIE at 1000 RPM 60 s and baked at 110 ºC 10 minutes. Poly(N-vinyl carbazole) (PVK) dissolved in chlorobenzene (10 mg/ml) was deposited on top of Cadmium based quantum dots at 1000 RPM and 2000

RPM 60 s and annealed at 110 ºC 10 minutes. Both solutions were filtered with a PTFE 0.2 µm filter. Finally, thermal evaporation of 80 nm Au was done at 10^{-6} mbar. The final area of the devices is 9 or 25 mm^2.

5.4 Results and discussion.

5.4.1 Physicochemical Characterization.

This section is divided in 3 parts, depending on the cadmium based quantum dot characterization. The optical and physicochemical characterization were done to determine the size and shape of quantum dots as well as their maximum emission wavelength and their Quantum Yield (QY), see annex for this case. At the end of this section a summary table is shown with all the optical parameters of three cadmium based quantum dots. The synthesis and physico-chemical of ZnO are shown in **Chapter 3.**

1.Green ZnCdSe@ZnS

The absorbance and emission spectra were recorded at room temperature in air conditions. Figure 5. 2 shows both spectra. The PL displayed a maximum wavelength at 540 nm and FWHM 17 nm , after excitation of the sample at 540 nm. As we expected ZnCdSe@ZnS presented a narrow emission and broad absorption spectra.

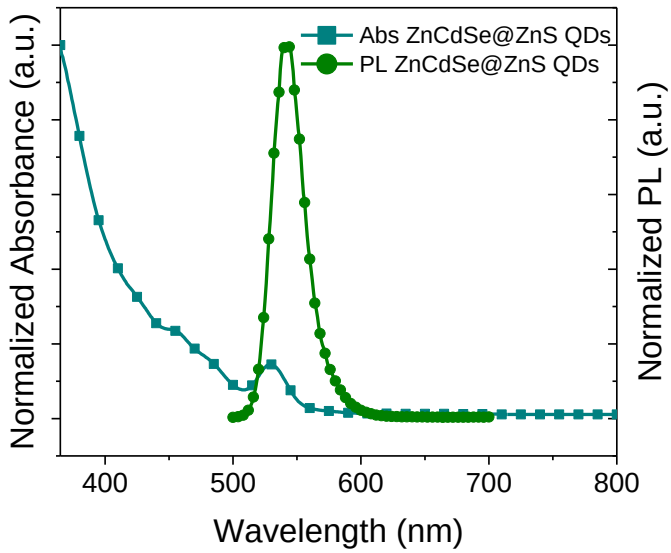

Figure 5. 2. Absorption and emission spectra of ZnCdSe@ZnS solved in chloroform at room temperature. The emission spectra present an unique peak at 540nm, the sample was excited at 480nm.

TEM images at different scales rate were taken in order to determine the size and the shape. The images shows a few groups of quantum dots well dispersed (see Figure 5.3). The average particle size was 7.286 ± 0.857 nm.

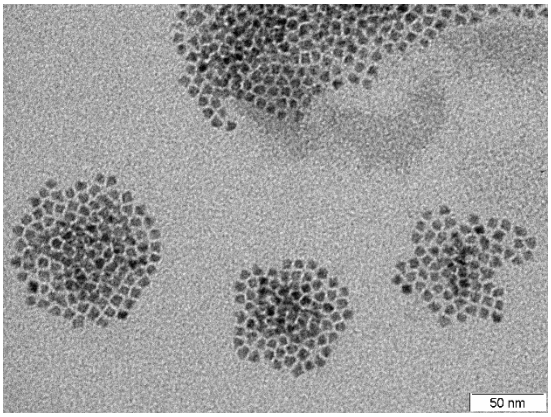

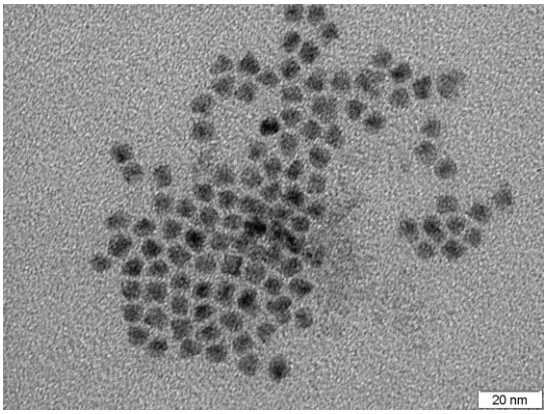

Figure 5. 3. TEM images of ZnCdSe@ZnS at different scales.

2. Red CdSeS@ZnS

The absorbance and emission spectra were recorded at room temperature in air conditions. Figure 5.4 shows both spectra. The PL displayed a maximum wavelength at 670 nm and FWHM 37 nm , excited the sample 450 nm. As we expected ZnCdSe@ZnS presented a narrow emission and broad absorption spectra.

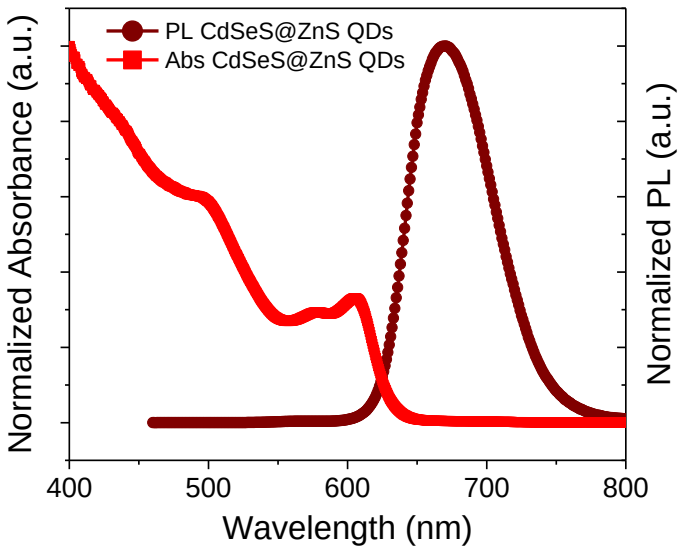

Figure 5. 4. Absorption and emission spectra of CdSeS@ZnS solved in chloroform at room temperature. The emission spectra present an unique peak at 670 nm, the sample was excited at 450 nm.

Figure 5.5 shows TEM images of CdSeS@ZnS QDs which average particle size was 11.86 ± 1.62 nm.

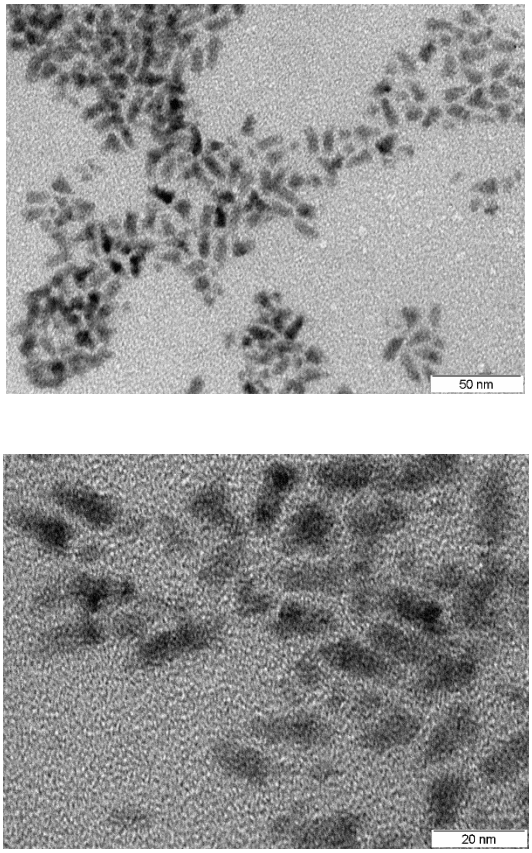

Figure 5. 5. TEM images of CdSSe@ZnS at different scales.

3. Blue ZnCdS@ZnS

The absorbance and emission spectra were recorded at room temperature in air conditions. Figure 5. 6 shows both spectra. The PL displayed a maximum wavelength at 460 nm and FWHM 22 nm , excited the sample 340 nm. As we expected ZnCdSe@ZnS presented a narrow emission and broad absorption spectra.

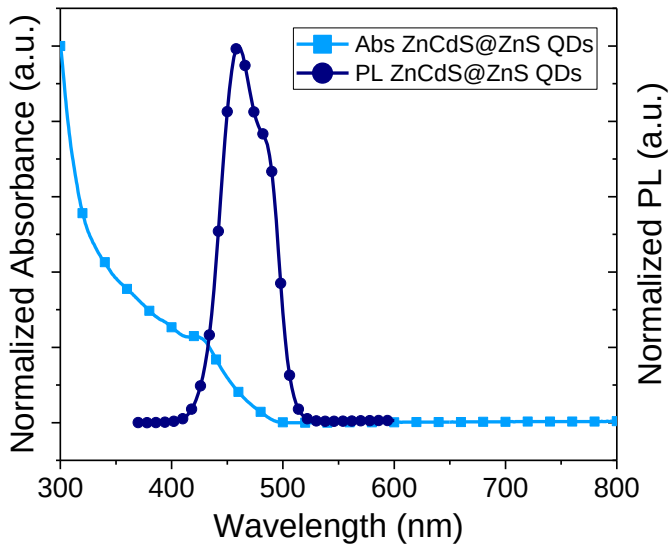

Figure 5. 6. Absorption and emission spectra of ZnCdS@ZnS solved in chloroform at room temperature. The emission spectra present an unique peak at 460 nm, the sample was excited at 340 nm.

TEM images sshowed a well dispersion particles with an average size of 6.86 ± 0.84 nm (see Figure 5.7).

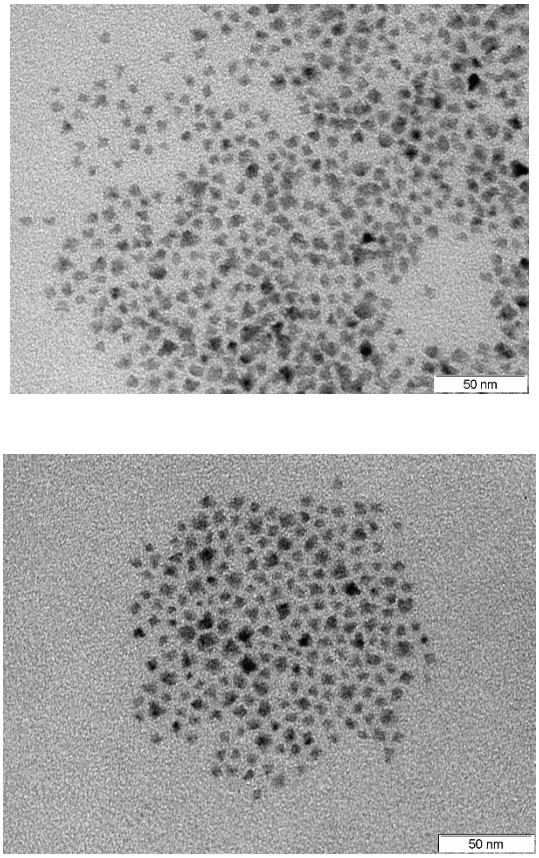

Figure 5. 7. TEM images of ZnCdS@ZnS at different scales.

Table 5.1 displayed the summary of the optical properties of Quantum Dots that we used to fabricated QLEDs. The samples were solved in hexane or chloroform and measure at room temperature.

Table 5. 1. Optical properties of QDs in solution.

Color	PL λmax	FMWH	QY(%)
Green	540	17	0.78
Red	670	37	0.25
Blue	460	22	0.32

5.4.2 Device Characterization.

Inverted structure QLEDs were fabricated using ITO-covered glass and ZnO as electron transport layer, Cadmiun based quantum dots as emissive layer and PVK and MoO_3 as hole transport layer (see Figure 5.9). ZnO was fabricated using a method described by Frederik *et al*. [13]. Zinc oxide nanoparticles present electrical properties such as high electron mobility and lower valence band that makes them suitable for electron transport layer while forming compact layers that allow flexibility. In this section, we want to explain in detail the optimization process that we carried out to fabricate the final device. Briefly, we divided this section in three parts in order to examine the role that PEIE and PVK play in the sandwiched QDLEDs: 1) The thickness of PEIE, 2) Solvent orthogonality and 3) Energy transfer between Quantum dots and PVK.

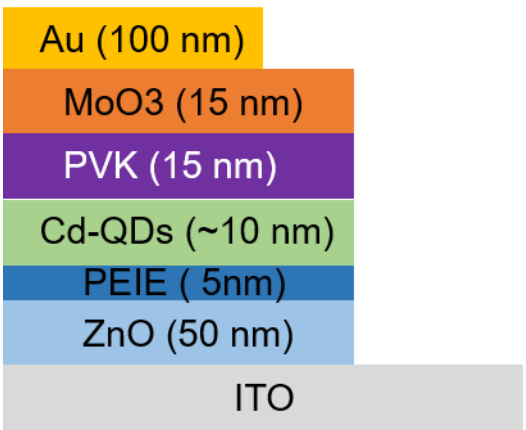

Figure 5. 8. Description of the structure.

A layer of Polyethylenimine ethoxylated (PEIE) was deposited between zinc oxide and carbon quantum dots. PEIE is a well-known surface modifier which can be easily deposited on top of ZnO. Some groups have reported that PEIE or PEI thin layer enhances electron injection/transport from the metal oxide and also induces uniform surface of the quantum dot layer due to the aliphatic amine groups that reduce the work function of ZnO [14,15].

We worked with three different relative concentration of PEIE in order to check which thickness was the best one because,as reported in the literature, a thicker layer of PEIE may work as insulator material [6]. We used a mixture of PEIE and methanol of1wt%, 0.5 wt% and 0.2 wt%. Figure 5.10 shows the current and luminance versus voltage spectra of QDLEDs. Table 5.2 displays the results of using differents concentrations of PEIE and the luminance is clearly higher when the weigh concentration is lower. We do not show any IV curve using PEIE 1%wt because the current was too low and we could not record any current and luminance versus voltage spectra.

Table 5.2 Summary of the device performances. Von is the turn-on voltage at 0.1 Cd/m^2.

device	PEIE	Turn-on voltage V^{on} (V)	Max. Luminance (Cd/m^2)[a]	Current Efficiency (Cd/A)
1	0.5 wt%	7.6	12	$8.0 \cdot 10^{-2}$
2	0.2 wt%	5.6	400	$1.2 \cdot 10^{-2}$
3	1 wt%	--	--	--

As shown in Figure 5.9, an increase of PEIE thickness in devices fabrication decreases the current density of the device getting lower luminance as well. As we mentioned previously, thicker layer of PEIE can work as an insulator.

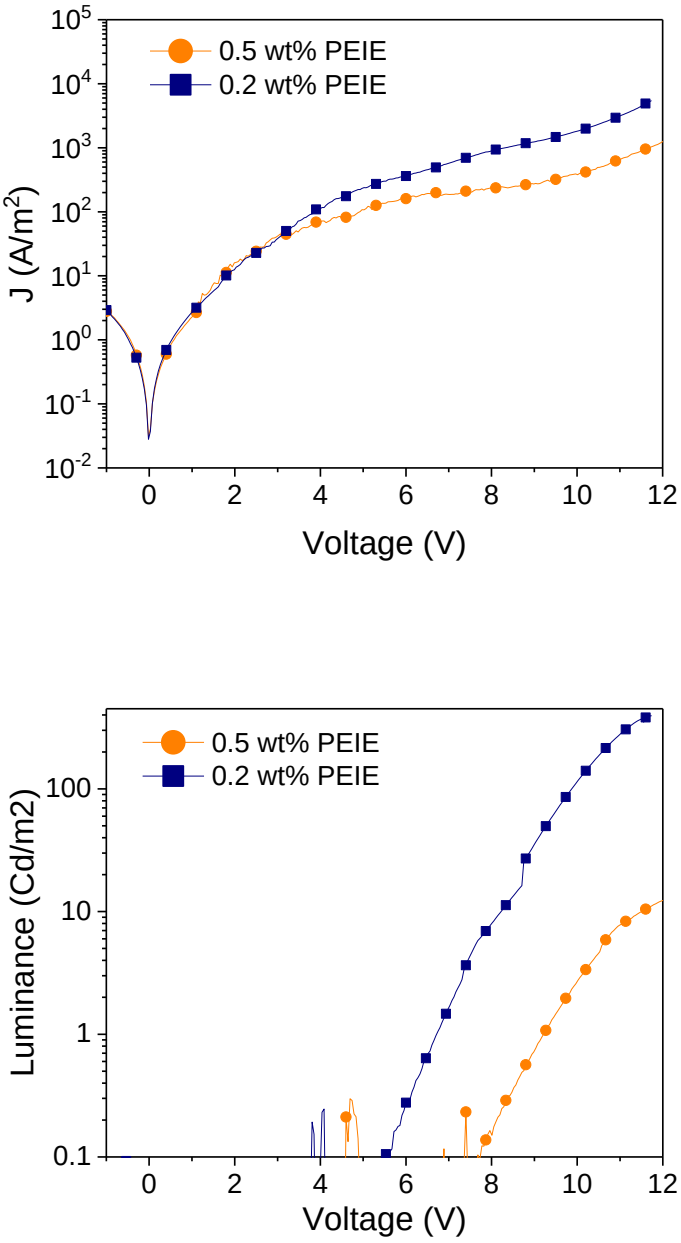

Figure 5. 9. Current density (top) and luminance (bottom) versus applied voltage of the QDLED using CdSe@ZnS QDs as unique emissive layer.

One of the aim of this project was to fabricate a solution-processing QDLEDs. It means that all the layers are deposited via spin coating conditions from solutions with the exception of MoO_3 and Au that are deposited by thermal evaporation. For that reason, it is necessary to work with orthogonal solvents to avoid the damage between the layers. The problem that we observed was that the majority of solvent used to dissolve the PVK degrade the layer of quantum dots, and when we deposited PVK over quantum dot layer, part of it is removed. It can be seen in Figure 5.10 where we prepared three different films deposited layer after layer. The quantum dot emission band decreases significantly after deposition of the PVK layer that may decrease the electroluminescence efficiency.

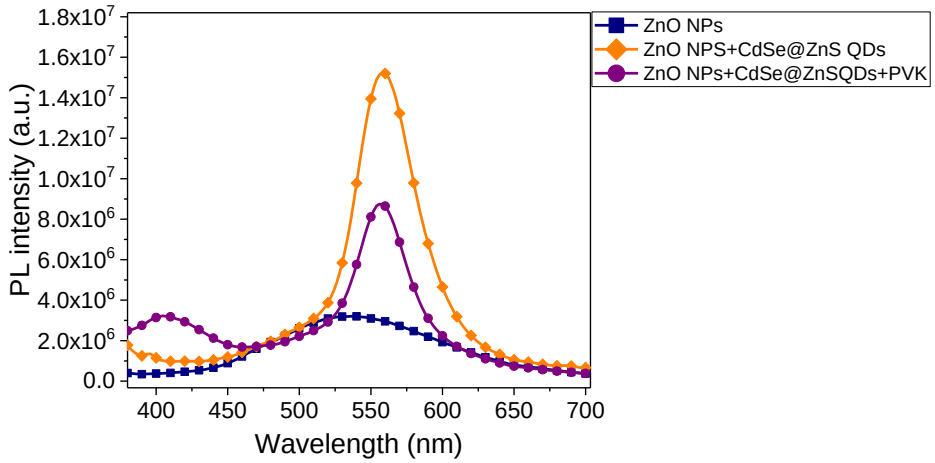

Figure 5. 10. PL spectra of three different films. λexc=360nm at room temperature.

PVK is one of the most useful hole transport layer due to their strong hole properties and weak electron properties in addition, it is important to stress because PVK can also be used as emitting layer. We observed that depending on the PVK thickness the recombination may occur in the polymer instead of quantum dots. It could be caused by two possible explanation: i) the poor hole mobility of PVK compared with the high electron mobility of ZnO [16], ii) the

valence band of QDs and LUMO level of PVK are closer,and some charges can move from the emissive layer to PVK.

Figure 5.11 shows two pictures of a diode applying a bias. As can be seen , in the first picture both material emits at the same time. The violet color belongs to PVK and the yellow one belongs to CdSe@ZnS. As the voltage was increased, the violet intensity increased while the yellow one decreased. Some possible solutions may be to change the organic polymer for other which has a higher LUMO or decrease the thickness film of the hole transport material. The problem of decreasing the thickness of PVK would be the poor layer coverage of the polymer on top of QDs layers, allowing short circuits inside the diode.

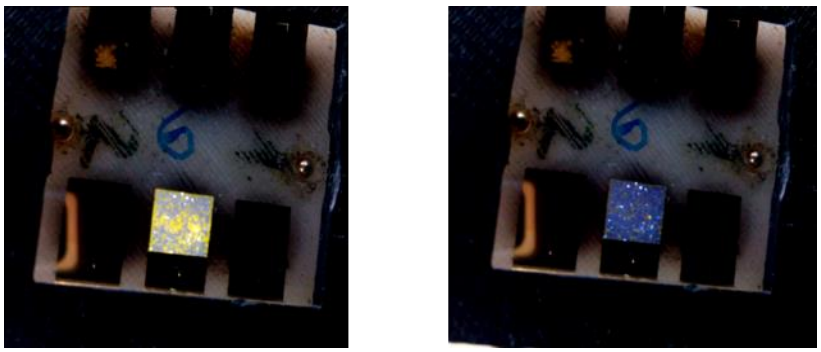

Figure 5. 2. Two different images of a QDLED using cadmium based quantum dots as emissive layer. The applied voltage increases from 5 (left) to 9 (right).

Once we established the optimal thickness of PVK and PEIE, we fabricated QDLEDs, which the final active area was 25 mm^2, using green, red and blue cadmium based quantum as unique emissive layer in air conditions. The IV curves were measured in air conditions using a Keithley described in Chapter 3. Figure 5.12 shows the current and luminance versus voltage of Green-QLEDs measured in air conditions.

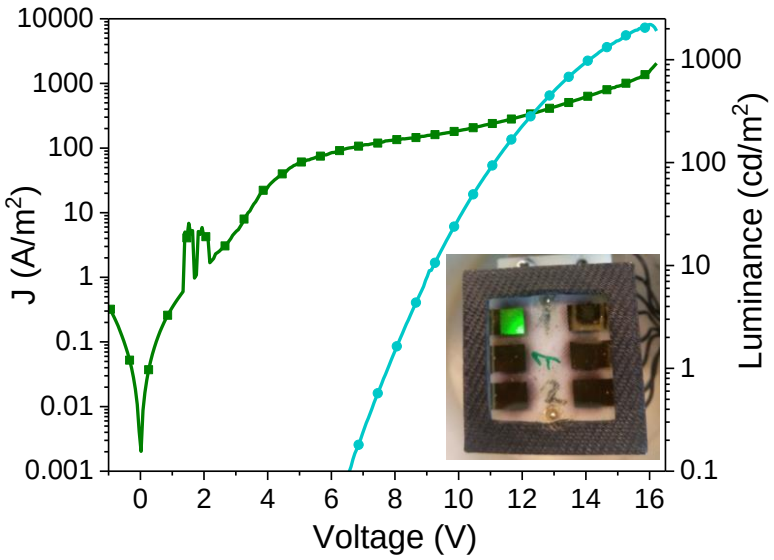

Figure 5. 3. Current density (dark green line) and luminance (light green line) versus applied voltage of the QDLED using ZnCdSe@ZnS QDs as unique emissive layer. The inset displays the light emission of green QLEDs.

Figure 5.13 shows the electroluminescence spectra of QLEDs using CdSe@ZnS as emissive layer. The λmax of emission is at 540 nm whereas CIE color coordinates are (0.287,0.691).

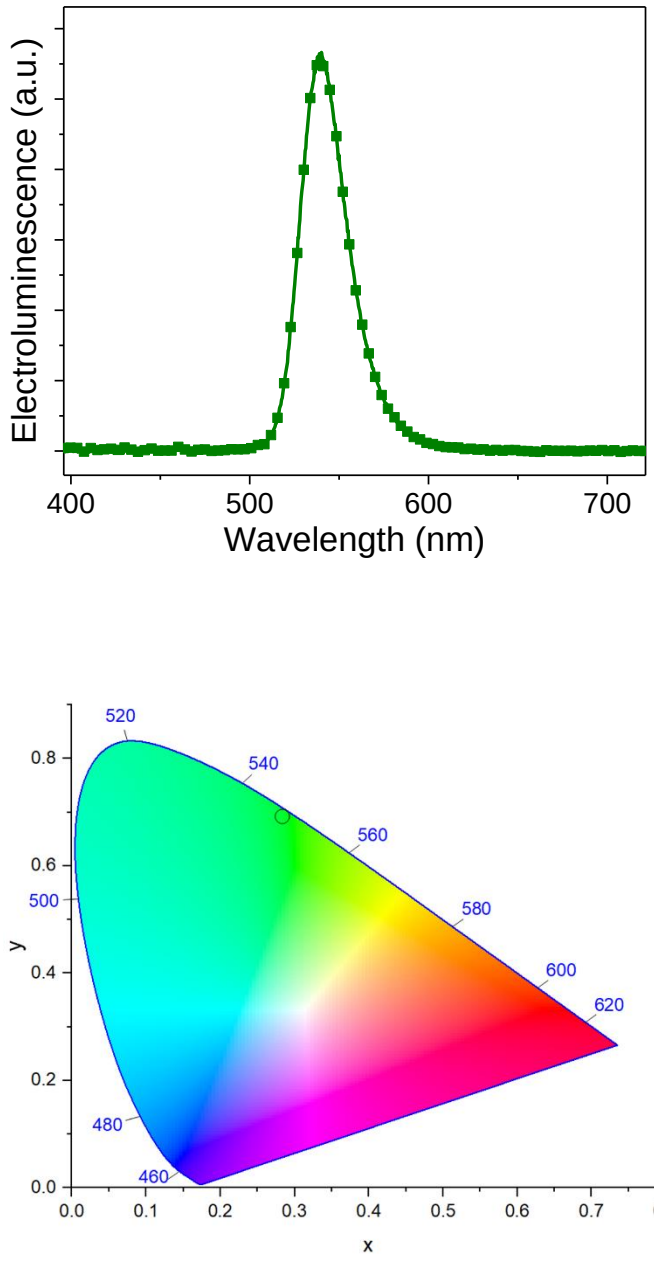

Figure 5. 13. Electroluminescence of ITO/ZnO/PEIE/ZnCdSe@ZnS/PVK/MoO3/Au at room temperature (top) CIE color coordinates of QLEDs with QDs as emissive layer (bottom).

The current and luminance versus voltage of red-QLEDs are shown in Figure 5.14. All the devices were measured in air conditions without any encapsulation.

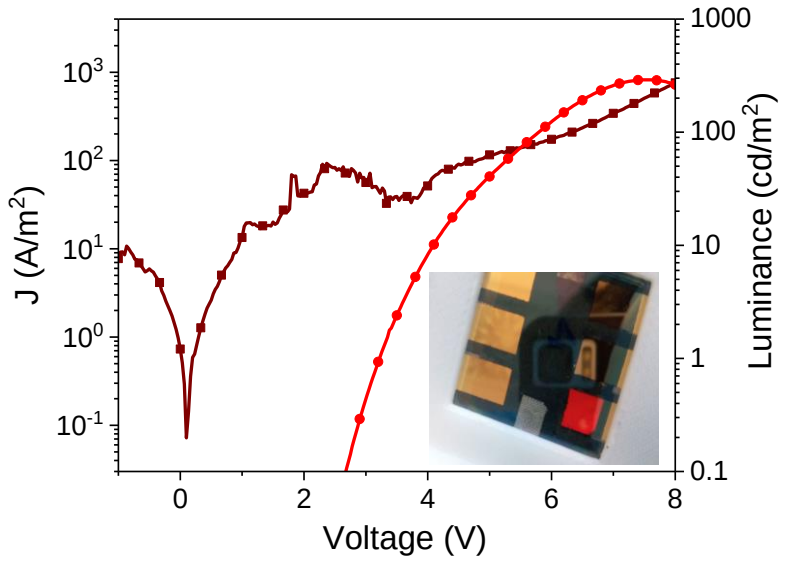

Figure 5. 44. Current density (dark red) and luminance (ligth red) versus applied voltage of the QDLED. Inset: light emission of red QLEDs.

Figure 5.15 shows the electroluminescence spectra of QLEDs using CdSe@ZnS as emissive layer. The λmax of emission is at 650nm whereas CIE color coordinates area at (0.320 , 0.362).

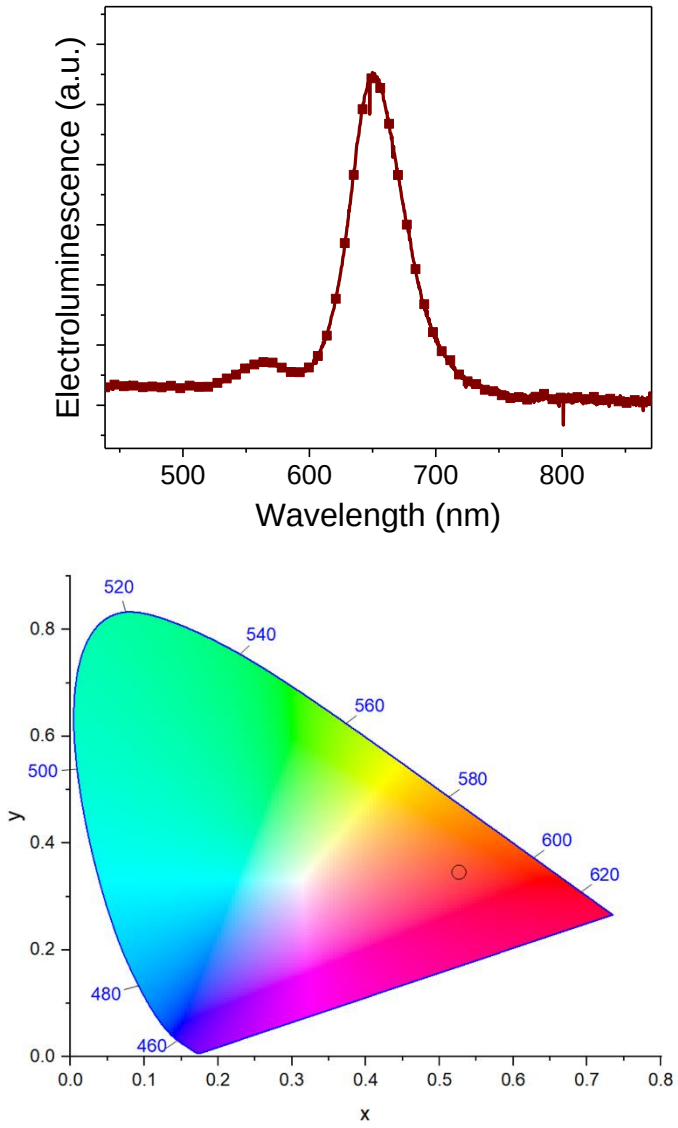

Figure 5. 5. Electroluminescence of ITO/ZnO/PEIE/CdSeS@ZnS/PVK/MoO3/Au at room temperature (top) CIE color coordinates of QLEDs with QDs as emissive layer (bottom).

The current and luminance versus voltage of blue-QLEDs is shown in Figure 5.16.The devices were measured in air conditions.

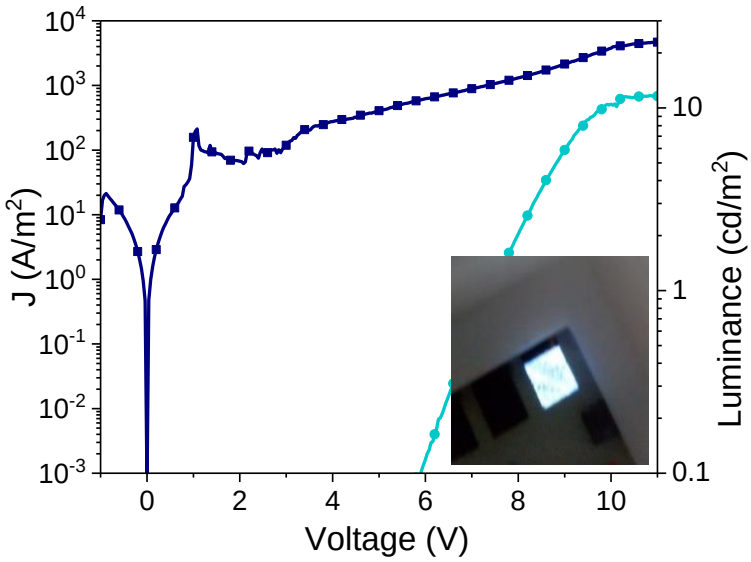

Figure 5. 16. Current density (dark blue) and luminance (ligth blue) versus applied voltage of the QDLED. Inset displays the light emission of blue QLEDs.

Figure 5.17 shows the electroluminescence spectra of QLEDs using CdSe@ZnS as emissive layer. The λmax of emission is at 540nm whereas CIE color coordinates are at (0.287,0.691). As the electroluminescence spectra was not as good as photoluminescence spectra we calculated the CIE using the PL spectra.

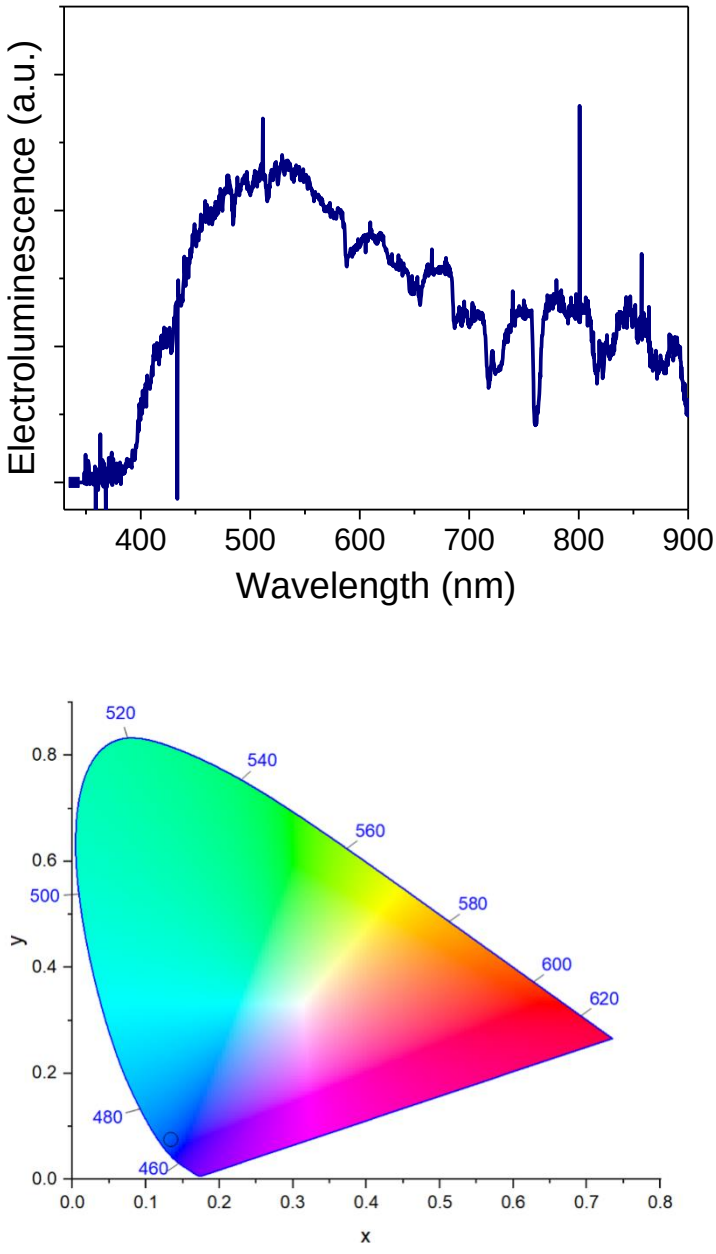

Figure 5. 6. Electroluminescence of ITO/ZnO/PEIE/ZnCdS@ZnS/PVK/MoO3/Au at room temperature (top) CIE color coordinates of QLEDs with QDs as emissive layer (bottom).

To sum up the optoelectronics results, Table 5.3 displays the final results using green, red and bluen cadmium based quantum dots as emissive layer. The most remarkable results are the lower turn on voltage using red and blue QDsLEDs. However, the luminace was not as we expected since the reported values in the literature are higher and further optimization is needed.Using green quantum dots as emissive layer shows an average luminance of 1736 cd/m^2 and a current efficiency of 2.36 cd/A. Using CdSeS@ZnS QDs as unique emissive layer present an average luminance of 275 cd/m^{2,}, turn-on voltage of 3 V and a Current Efficiency 0.19 cd/A.

Table 5. 2. Summary of the electrical Properties QLEDs.

Color	Von (V)[a]	Luminance (cd/m^2)[a]	Current Efficiency (cd/A)	CIE index (x,y)
Green	6.62 (6.74)	2199 (1736)	2.36	(0.287,0.691)
Red	2.69 (3.00)	291 (275)	0.19	(0.320,0.362)
Blue	2.46 (2.79)	12 (11)	$5\cdot10^{-3}$	(0.131,0.075)

[a] The average turn on voltage and Luminance repored in round brackets. V[a] is the turn-on voltage at 0.1 Cd/m^2.

5.5 Conclusions.

We synthetized three Core-shell cadmium/ zinc calchogenides quantum dots, synthetized by one-step method in inert conditions to use as unique emissive layer in QLEDs. Then we fabricated and characterized red, green and blue solution processed QLEDs in air conditions.

We used PEIE as surface modifiers that allow easy low cost fabrication.Regarding the results, we observed the important role that PEIE as interlayer plays inside the sandwiched structure in order to control the charges inside the diode. Futhermore, we observed how the thickness of PEIE can drop

the injection current. It is remarkable that the poor hole mobility of PVK compared with the high electron mobility of ZnO as well as the closer energy alignment between the valence band of QDs and the LUMO level of PVK can assist that the charges recombine in the PVK instead of QDs layer.

To summarize, this chapter reflects the first approach to fabricate devices with quantum dot in the emissive layer by solution processing in order to replace the cadmium based emissive layers for others emissive as CQDs and Perovkistes based nanoparticles. As we highlighted previously the aim was to learn to deposit all the materials by solution processing, observe the interactions at the interface and stablish the optimum conditions to set the first step for scaling-up in future projects.

5.6 References.

1. D. Bera, L. Qian, T.-K. Tseng, P.H. Holloway. Quantum Dots and Their Multimodal Applications: A Review. *Materials (Basel).* **2010**, 3 (4), 2260–2345.

2. A.E. Raevskaya, A.L. Stroyuk, S.Y. Kuchmiy, et al. Optical study of CdS- and ZnS-passivated CdSe nanocrystals in gelatin films. *J. Phys. Condens. Matter* **2007**, 19 (38), 386237.

3. D. Mo, L. Hu, G. Zeng, et al. Cadmium-containing quantum dots: properties, applications, and toxicity. *Appl. Microbiol. Biotechnol.* **2017**, 101 (7), 2713–2733.

4. X. Liang, S. Bai, X. Wang, et al. Colloidal metal oxide nanocrystals as charge transporting layers for solution-processed light-emitting diodes and solar cells. *Chem. Soc. Rev.* **2017**, 46 (6), 1730–1759.

5. J. Kwak, W.K. Bae, D. Lee, et al. Bright and Efficient Full-Color Colloidal Quantum Dot Light-Emitting Diodes Using an Inverted Device Structure. *Nano Lett.* **2012**, 12 (5), 2362–2366.

6. D. Kim, Y. Fu, S. Kim, et al. Polyethylenimine Ethoxylated-Mediated All-Solution-Processed High-Performance Flexible Inverted Quantum Dot-Light-Emitting Device. *ACS Nano* **2017**, 11 (2), 1982–1990.

7. H.H. Kim, S. Park, Y. Yi, et al. Inverted Quantum Dot Light Emitting Diodes using Polyethylenimine ethoxylated modified ZnO. *Sci. Rep.* **2015**, 5, 8968.

8. M.K. Choi, J. Yang, K. Kang, et al. Wearable red–green–blue quantum dot light-emitting diode array using high-resolution intaglio transfer printing. *Nat. Commun.* **2015**, 6, 7149.

9. V. Wood, M.J. Panzer, J. Chen, et al. Inkjet-Printed Quantum Dot–Polymer Composites for Full-Color AC-Driven Displays. *Adv. Mater.* **2009**, 21 (21), 2151–2155.

10. T. Kim, K.-S. Cho, E.K. Lee, et al. Full-color quantum dot displays fabricated by transfer printing; **2011**; Vol. 5.

11. K.-H. Lee, J.-H. Lee, H.-D. Kang, et al. Over 40 cd/A Efficient Green Quantum Dot Electroluminescent Device Comprising Uniquely Large-Sized Quantum Dots. *ACS Nano* **2014**, 8 (5), 4893–4901.

12. K.-H. Lee, C.-Y. Han, H.-D. Kang, et al. Highly Efficient, Color-Reproducible Full-Color Electroluminescent Devices Based on Red/Green/Blue Quantum Dot-Mixed Multilayer. *ACS Nano* **2015**, 9 (11), 10941–10949.

13. C.K. Frederik, T. Yi, T. Ralf, W.A. Jens. A simple nanostructured polymer/ZnO hybrid solar cell—preparation and operation in air. *Nanotechnology* **2008**, 19 (42), 424013.

14. D.I. Son, H.H. Kim, D.K. Hwang, S. Kwon, W.K. Choi. Inverted CdSe-ZnS quantum dots light-emitting diode using low-work function organic material polyethylenimine ethoxylated. *J. Mater. Chem. C* **2014**, 2 (3), 510–514.

15. Y. Zhou, C. Fuentes-Hernandez, J. Shim, et al. A Universal Method to Produce Low{\textendash}Work Function Electrodes for Organic Electronics. *Science (80-.).* **2012**, 336 (6079), 327–332.

16. J. Pan, J. Chen, Q. Huang, L. Wang, W. Lei. A highly efficient quantum dot light emitting diode via improving the carrier balance by modulating the hole transport. *RSC Adv.* **2017**, 7 (69), 43366–43372.

A5 Annex

Quantum yield calculation.

The quantum yield of CQDs was calculated using Couramine 102 and Couramine 153 as reference dye applying the following equation.

$$QY = QY_{ref}\left(\frac{I_{em\,sample}}{I_{em\,ref}}\right)\cdot\left(\frac{Abs_{ref}}{Abs_{sample}}\right)\cdot\left(\frac{n_{sample}}{n_{ref}}\right)^2 \quad \text{Equation A5.1}$$

Where QY_{ref} is the reference quantum yield, I_{em} is the area of the emission band, Abs is the absorbance excitation wavelength and η is the refractive index.

ZnCdSe@ZnS.

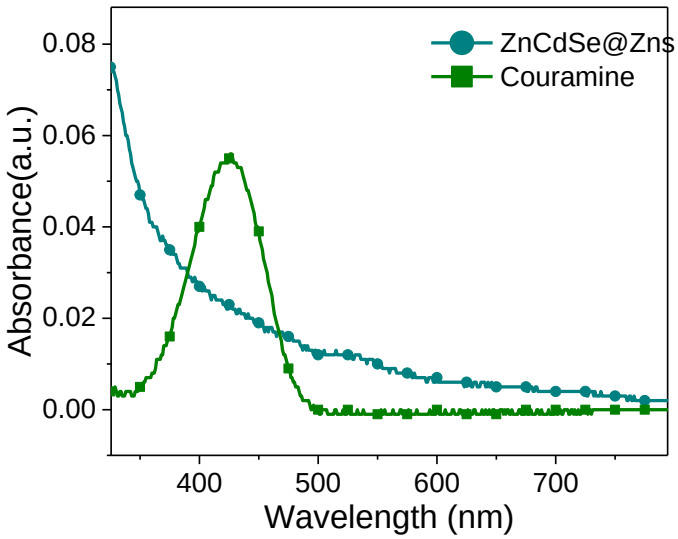

Figure A5. 1. Absorbance spectra of Rodhamine (violet line) and CdSeS@ZnS (dark red line) at room temperature.

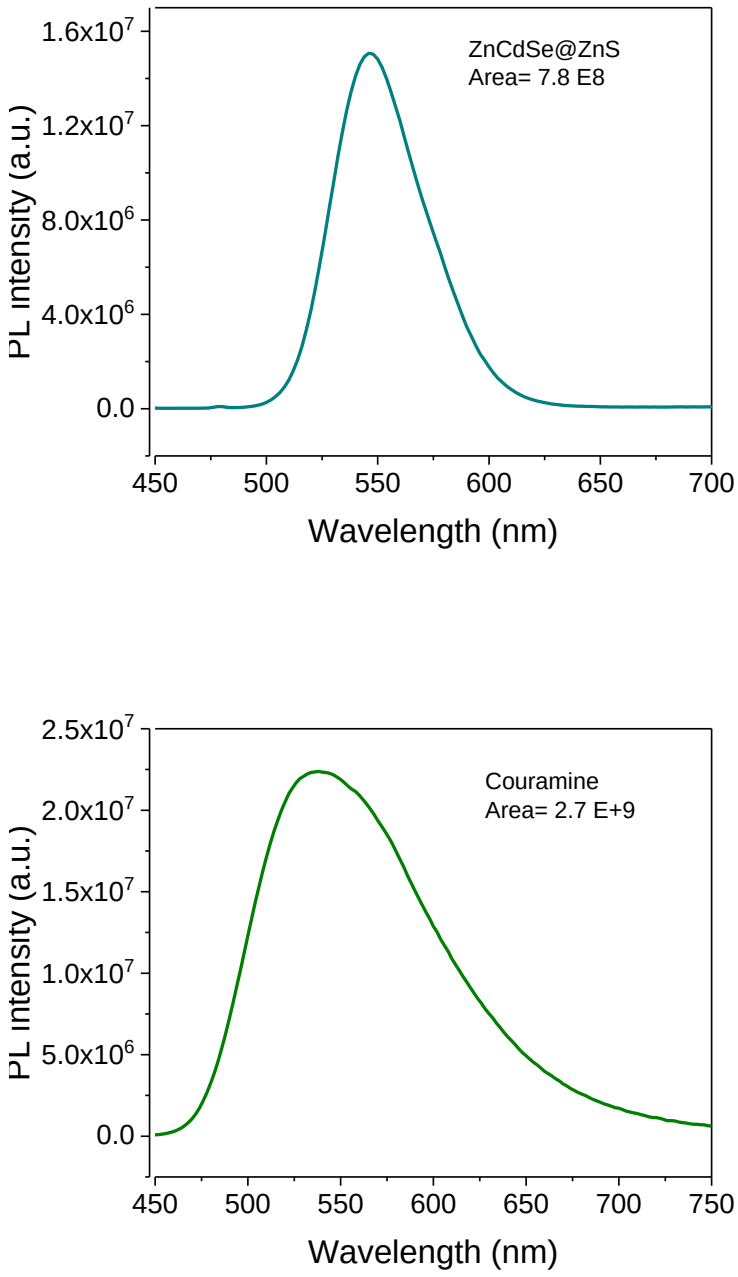

Figure A5. 2. Emission spectra of ZnCdSe@ZnS (top) and Rodhamine (bottom) measured at λexc=420 nm at room temperature.

CdSeS@ZnS.

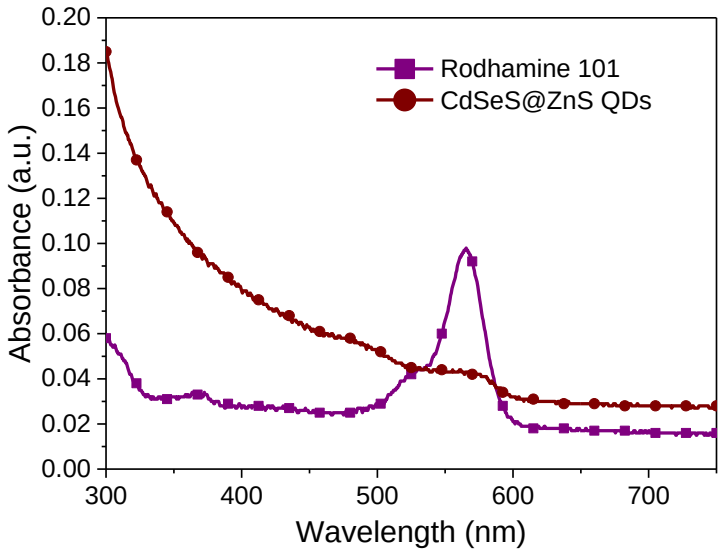

Figure A5. 3. Absorbance spectra of Rodhamine (violet line) and CdSeS@ZnS (dark red line) at room temperature.

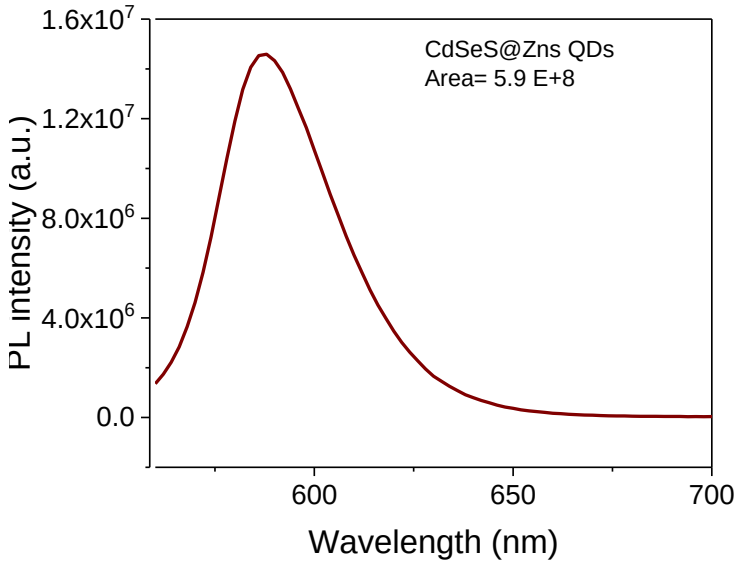

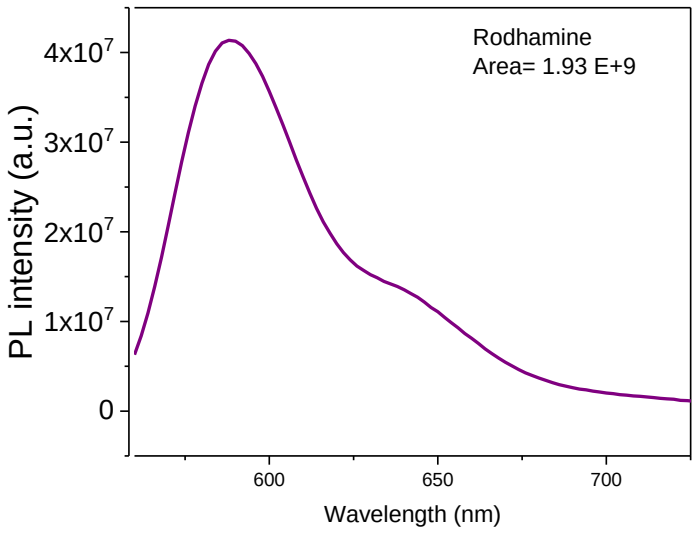

Figure A5. 4. Emission spectra of CdSeS@ZnS (top) and Rodhamine (bottom) measured at λexc=540 nm at room temperature.

ZnCdS@ZnS

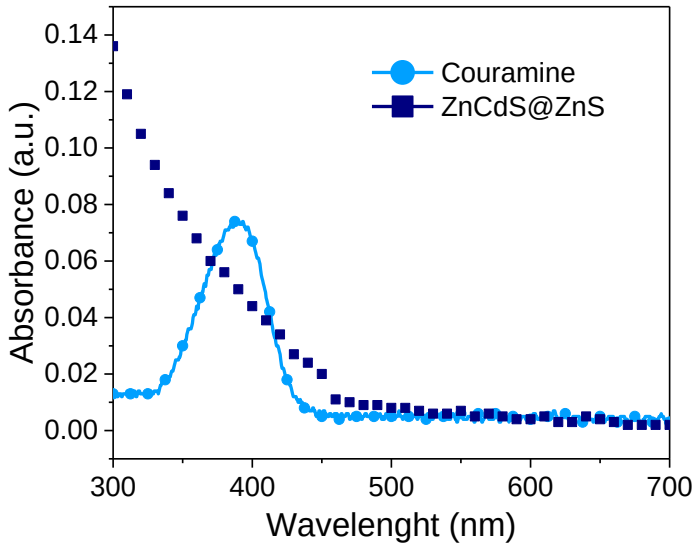

Figure A5. 5. Absorbance spectra of Couramine (light blue line) and ZnCdS@ZnS (dark blue line) at room temperature.

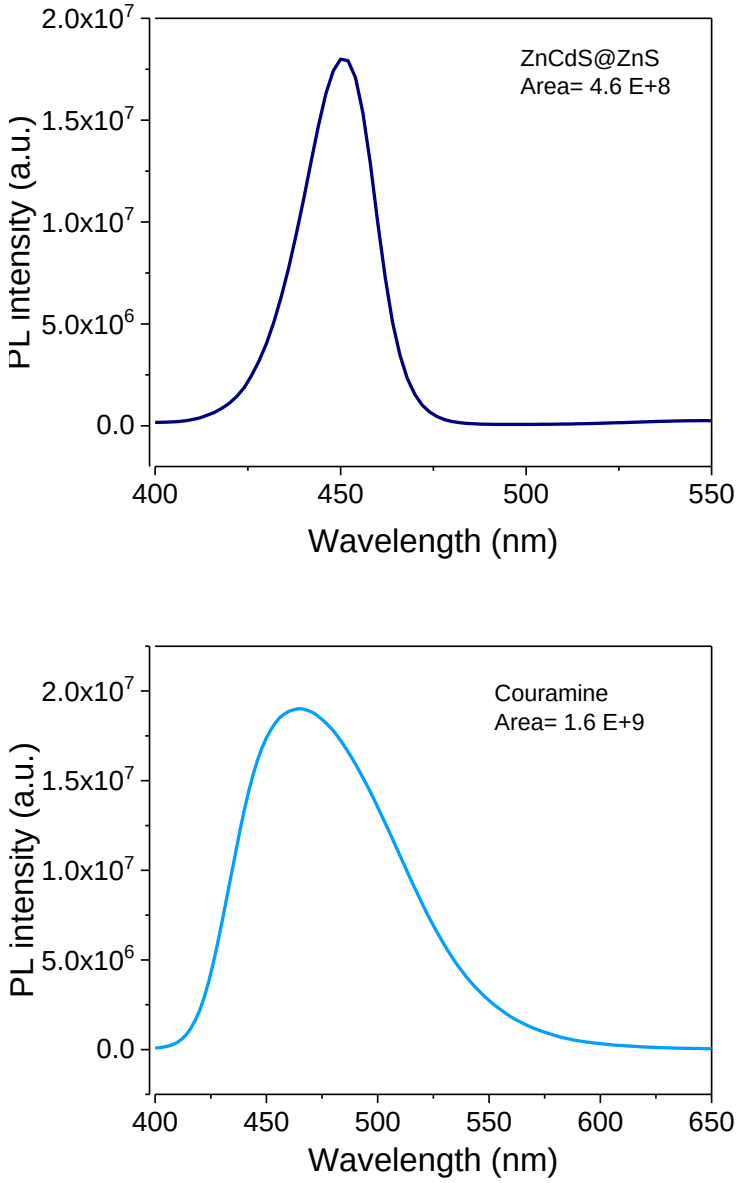

Figure A5. 6. Emission spectra of ZnCdS@ZnS (top) and Couramine (bottom) measured at λexc=380 nm at room temperature **.**

Chapter 5

6

Synthesis and fabrication of Perovskite Light Emitting Diodes (PeLEDs).

This project was about the synthesis and characterization of perovskites halides nanoparticles for light devices, studying their intrinsic properties as high photoluminescence, color tuneability, high absorption coefficient to apply in the field of optoelectronic. This project was done during my stay in the National Institute for Materials Science (NIMS) in Japan under the supervision of Doctor Masatoshi Yanagida.

Chapter 6

Table of Contents

Chapter 6

6.1 Introduction.

Interest in hybrid perovskites have increased due to their optoelectronic properties suitable for a variety of applications like solar cells[1, 2], light emitting diodes[3] and detectors[4]. In 1989 Goto *et al.*[5] published a paper describing this material as active layer in LEDs but it was not since 2014 when researchers started to study further perovskite emitters for LEDs again. In 2015 Friend *et al.*[6] published that the electroluminescence emission peak brightness from trihalide organic-inorganic ($CH_3NH_3PbI_{3-x}Cl_x$) perovskite-based LED was 300 cd/m^2. Zeng and coworkers reported the synthesis of $CsPbX_3$ quantum dots and its application for PeLEDs [3]. To date, the number of papers describing solution synthesis of perovskite and their applications as active layer in light emitting diodes has increased significantly [7].

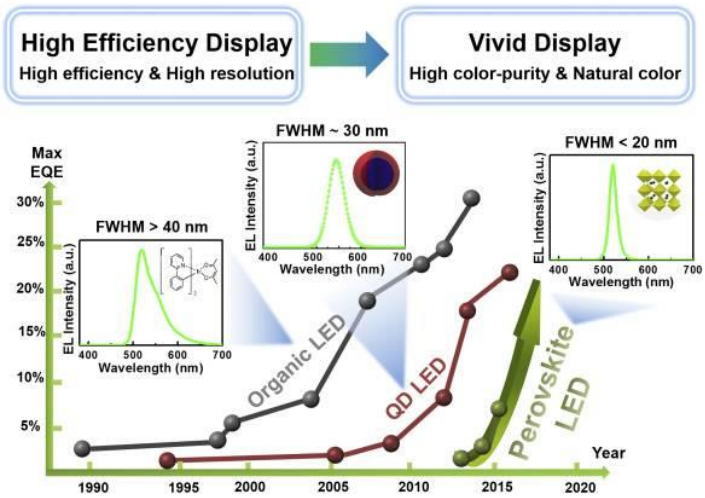

Figure 6.1. Trend of LED papers[7].

Trihalide perovskites have the general formula AMX_3 where A is the cation, which can be organic such as methylamonium, formamidinium, or inorganic as cesium. M^{2+} is the metal that can be Pb^{2+}, Sn^{2+}, Ge^{2+} and X^- is the halide compound as Cl^-, Br^-, I^-. This material gained interest due to its narrow emission and color purity compared with other materials such as inorganic quantum dots

emitters and organics emitters. Depending on the anion of $CsPbX_3$, the emission of perovskite could be tuned over the entire visible spectrum.

Reviewing the literature, there are two ways to obtain the $CsPbX_3$ perovskites: thin film and nanoparticles (NPs). Both materials have been used as solar cells and LEDs [8]. In the case of thin film, one-step spin coating is still the simplest and most widely used fabrication method to date. As published in the bibliography, a smoother films achieved is via a two-step method in which precursor were deposit, dropping a non-solvent on top of perovskite films during the spin-coating deposition[9].

On the other hand, perovskite NPs can be divided into two groups depending on their size: perovskite quantum dots and perovskite nanocrystals [2]. The synthesis of perovskite quantum dots must be carried on in inert conditions, although the synthesis of nanocrystals can be performed in air conditions [10].

The emission wavelength of perovskite can be tuned across the whole visible spectrum, depending on the halide anion (X= Cl, Br, I). Changing the ratio anion halide, the emission band can be tuned to blue (Cl^-), green (Br^-) or red (I^-) wavelength regions. However, one of the main problems of working with $CsPbI_3$ or $MAPbI_3$ is their instability in air conditions and in polar solvents [11,12].

The aim of this project was to synthetize different perovskite nanoparticles to use as emissive layer in LEDs. Furthermore, a secondary goal was to use these nanoparticles for both solar cells and LEDs. Regarding in the literature, there are some examples of the use of these materials in both applications. For instance, Swarnkar *et al.*[13] published a synthesis of $CsPbI_3$ QDs. Their energy alignment was suitable for both applications. The most important issue was the low stability in air conditions, and the high difficulty to obtain them. Different approaches were used to synthetize this material, for instance the anion exchange from cesium lead bromide nanoparticles or the direct synthesis by hot injection method.

This chapter is divided in two sections. The first one describes the synthesis of different perovskite materials that we carried out during the thesis as well as the study of their optoelectronic properties. The second one is the device fabrication of two types of perovskites LEDs (PeLEDs). As we mentioned in the abstract, this project was done during my three months stay in the National Institute for Materials Science (NIMS) in Japan under the supervision of Doctor Masatoshi Yanagida.

6.2 Synthesis of Perovskite materials.

In this section, some of the synthesis that we performed to construct LEDs are described. The aim of this project was to use these nanoparticles in optoelectronic devices: solar cells and LEDs. The best perovskite composition for both devices was $CsPbI_3$ due to its molecular levels, but this material has a lot of problems of stability in air. For that reason, we started synthesizing $CsPbBr_3$ nanoparticles which have better stability and then the anion was exchanged.

6.2.1 Synthesis of $CsPbBr_3$ NPs.

The synthesis was described previously in the bibliography by Du *et al.*[14]. The precursor solution was prepared mixing 3.45 mmol of cesium bromide (CsBr), 4.6 mmol lead bromide ($PbBr_2$) and 115 μL n-octylamine in 5 mL dimethylformamide (DMF). Then, 1 mL of precursor solution was dropped into 5 mL of a toluene solution containing 100 μL of oleic acid (OA), with vigorous stirring. Adjusting the amount of oleic acid, the size of nanoparticles can be tuned. The solution changed from colourless to a yellow-green color immediately upon mixing. The dispersion was centrifuged at 3000 RPM for 10 minutes to remove the largest particles.

6.2.2 Synthesis of $CsMAPbBr_3$ thin film.

To fabricate perovskite thin film we need to prepare two solutions, firstly 234 mg of CsBr and 183.5 mg of $PbBr_2$ were dissolved in 2 mL of dimethyl sulfoxide (DMSO), then 1.96 mg of methylamonium bromide (MABr) in 2 mL DMSO. Both solutions were stirred all the night at 30 °C in a nitrogen filled glovebox. Finally, 500 µL of first solution and 50 µL of second one were mixed and stirred together. Perovskite solution was spin coated with a two-step sequence: a first step at 3000 RPM during 100 s and a second step at 4000 RPM during 10 s. Prior to the end of the second step 70 µl of toluene were poured onto the spinning samples to obtain uniform pin-hole-free perovskite films and with smaller grain size. Finally, devices were annealed at 100 °C for 20 min.

6.2.3 Synthesis of $CsPbI_3$ QDs.

The synthesis of $CsPbI_3$ was done using a method described in the bibliography[15]. Briefly, 435 mg lead iodide (PbI_2), 2.5 mL oleylamine (OLA) and 2.5 mL oleic acid (OA) were solved in 25 mL of 1-octadecene (ODE). The solution was stirred in a three-neck flask under vacuum during 1hour at 120 ºC. Then, the solution was heated up to 150 ºC. After that, 2 mL of Cs-oleate solution (0.125 M in ODE) was injected. After 5 seconds, the solution was immediately cooled at room temperature. The solution was centrifuged at 4500 RPM during 20 min to discard the supernatant. Then the solid was solved in 1.5 mL in hexane and centrifuged again. After a second centrifugation, the solid was discarded to avoid the biggest particles and 3 ml of hexane was added to the supernatant and centrifuged again to discard the precipitate.

6.3 Devices fabrication.

6.3.1 Fabrication of PeLEDs with a $CsMAPbBr_3$ thin film as emissive layer.

Indium tin oxide patterned glasses were treated with UV ozone 20 min. PEDOT:PSS was spin coated on top of ITO at 3000 RPM 45 s and heated at 120 °C 30 min. Poly (9-vinylcarbazole) (PVK) (10 mg/mL) was spin-coated on top of PEDOT:PSS at 3000 RPM 45 s and baked 120 °C 20 min. To fabricate the perovskite thin film, two solutions were previously prepared: first, 234 mg of CsBr and 183.5 mg $PbBr_2$ were dissolved in 2 mL of dimethyl sulfoxide (DMSO), then 1.96 mg of methylamonium bromide in 2 mL DMSO. Both solutions were stirred overnight at 30 °C in a nitrogen filled glovebox. Finally, 500 µL of first solution and 50 µL of second one were mixed and stirred together. Perovskite solution was spin coated with a two-step sequence: a first step at 3000 RPM during 100 s and a second step at 4000 RPM during 10 s. Prior to the end of the second step 40 µl of toluene were poured onto the spinning samples to obtain uniform pin-hole-free perovskite film with small grain size[13,14]. Then, devices were annealed at 100 °C for 20 min under inert conditions. Finally, 1,3,5-Tri(m-pyridin-3-ylphenyl)benzene,1,3,5-Tris(3-pyridyl-3-phenyl)benzene,3,3′-[5′-[3-(3-pyridinyl)phenyl][1,1′:3′,1″-terphenyl]-3,3″-diyl] bispyridine (TmPYP) (10 mg/mL and 20 mg/mL solved in chloroform) was spin coated at 3000 RPM 45 s and baked at 90 °C for 10 min. To deposit perovskite thin film and TmPYP all the samples were transferred into a nitrogen filled glovebox. Lithium fluoride and aluminum were thermally evaporated in a high vacuum ($1 \cdot 10^{-6}$ mbar).

6.3.2 Fabrication of $CsPbI_3$ QDs LEDs.

Fluorine doped Tin Oxide (FTO) coated glasses (resistance of 8 Ω/cm^2) were cleaned for 15 min in an ultrasound bath with deionized water with Hellmax soap, with deionized water and finally with ethanol. The substrates were dried and an UV/Ozone treatment was performed for 20 min. TiO_2 was prepared by mixing 0.65 mL of Ti (IV) isopropoxide, 0.38 mL of acetylacetone and 5 mL EtOH. The sol-gel TiO_2 was spin-cast at 3000 RPM 60 s and then calcined at 500 ºC for 30 min. $CsPbI_3$ QDs (63 mg/mL) was deposited at 2000, 3000 and 5000 RPM, then annealed at 80ºC during 45 min. 72.3 mg of Spiro-OMeTAD

(1-Material) were dissolved in 1 mL chlorobenzene with the addition of 28.8 mL tert-butylpyridine and 17.5 mL of lithium bis-trifluoromethanesulfonimide solution in acetonitrile (520 mg/mL). The resulting solution was spun (80 µL) onto the perovskite at 2000 RPM for 60 s. Finally, 15 nm of MoO_3 and 100 nm of Ag were deposited via thermal evaporation under $1 \cdot 10^{-6}$ mbar.

6.4 Results and discussion.

This section is divided in three parts. The first is the physic-chemical characterization of perovskite films and nanoparticles, the second part the description and characterization of exchange anion of perovskites and finally, the third part the results of final devices is shown.

6.4.1 Perovskite characterization.

6.4.1.1 $CsMAPbBr_3$ thin film.

We fabricated $CsMAPbBr_3$ films deposited by spin coating on glass and under inert conditions. The purpose was to verify how the stability of perovskite thin film can be influenced by the air or the moisture. We prepared a binary cation mixed perovskites, because as some groups reported, the addition of MA^+ ions are helpful to control the crystal growth to allow better grain formation[16]. Figure 6.2 shows the emission spectra of $CsMAPbBr_3$ films excited at two different excitation wavelength and deposited at two different speeds. The most interesting observation was how the thickness of CsMAPbBr3 could influence directly to the emission intensity. The thinner the perovskite layer, the higher the expected emission intensity.

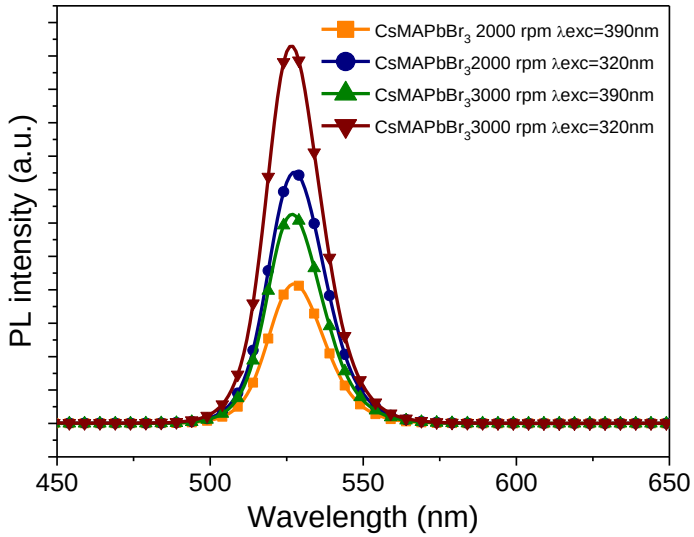

Figure 6.2. PL spectra of $CsMAPbBr_3$ thin film prepared at different spins measured at room temperature after excitation at different wavelength.

In addition, as it can be seen it in Figure 6.3, those devices which were fabricated inside the glovebox, they presented a better homogeneous layer.

Figure 6.3. Thin films of $CsMAPbBr_3$ deposited on glass and these same films under UV-vis light.

One-step solvent exchange was performed during spin coating by dropping toluene onto the sample in order to reduce the grain size and improve the roughness of the film [9]. The morphology of perovskite thin films was studied by the scanning electron microscope (SEM) images. As presented in Figure 6.4, we observed that the film presented pin-holes and big grains.

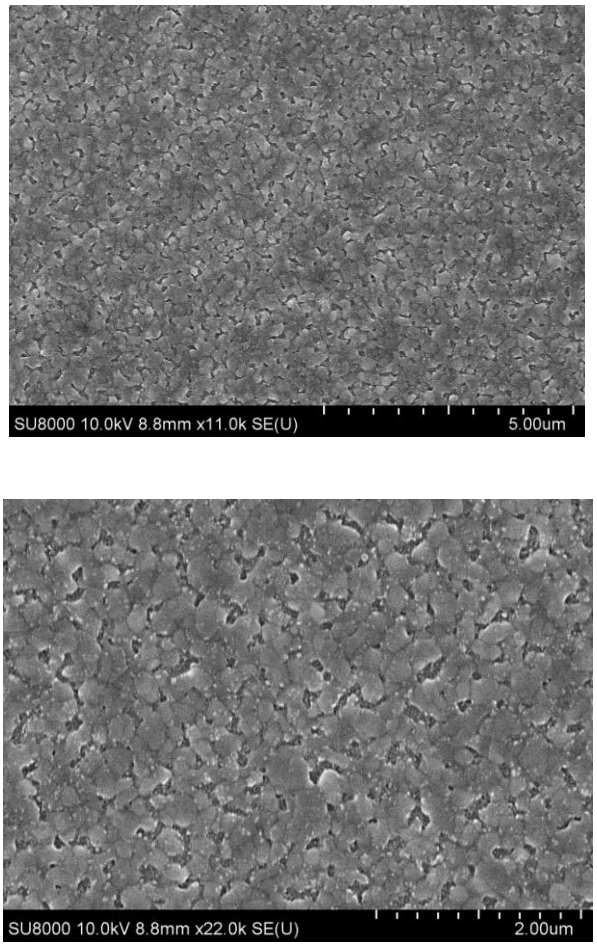

Figure 6.4. View SEM images of a $CsMAPbBr_3$ thin film on glass substrate at different magnification scales.

6.4.1.2 $CsPbBr_3$ NPs.

The photoluminescence spectra of $CsPbBr_3$ solved in chloroform were recorded at room temperature. Figure 6.5 displays the PL spectra of $CsPbBr_3$ NPs deposited either in one or five layers in a glass film.

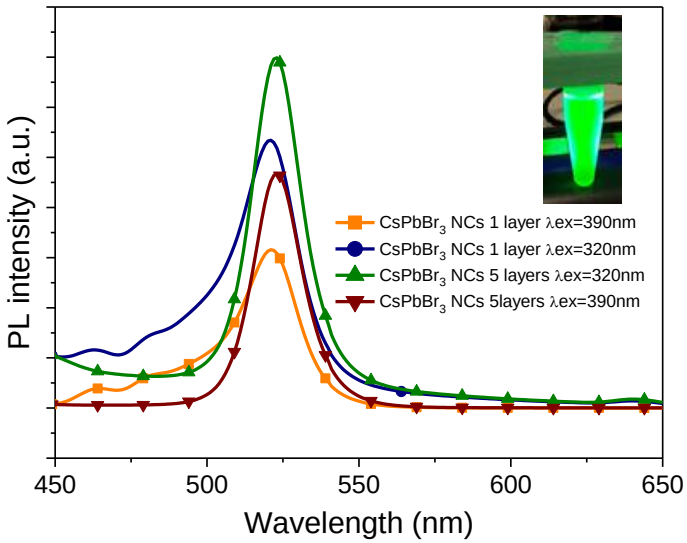

Figure 6.5. PL spectra of $CsPbBr_3$ NPs. Inset image: Perovskite NPs solved in chloroform under UV light.

We can observe that when we increased the thickness of the active layer, the PL intensity increased as well. The PL spectra presented a shift between the $CsPbBr_3$ thin film deposited on glass by spin coating in inert conditions and the $CsPbBr_3$ NPs solved in chloroform. (Figure 6.6). The perovskite thin film presented an emission at 521 nm while the perovskite solution at 512 nm. This shift was attributed to a change in the local strain of the NCs [2].

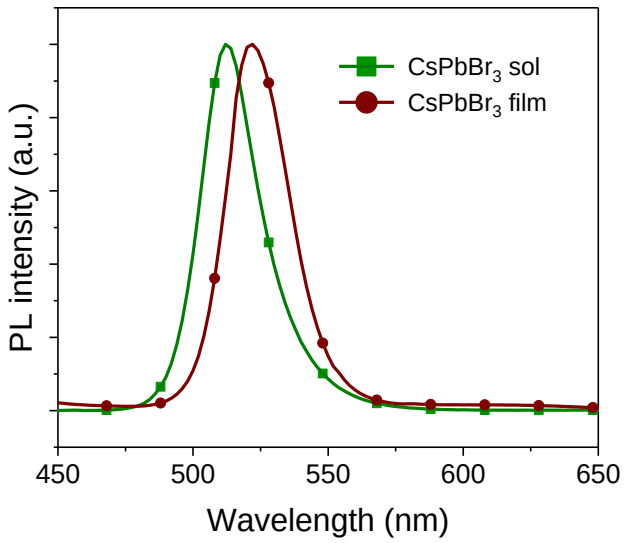

Figure 6.6. Normalized PL of $CsPbBr_3$ in toluene and in thin film.

A top view image of $CsPbBr_3$ NCs is shown in Figure 6.7. We observed big clusters around throughout the film and pinholes. The low quality of the film could be one of the reasons for explaining that when we prepared devices we did not obtain any good result.

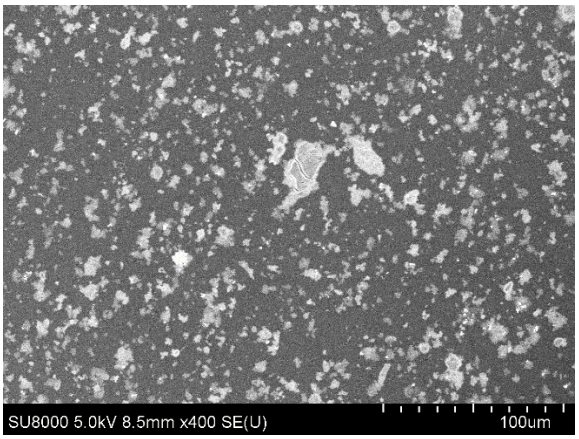

Figure 6.7. Top view SEM image of $CsPbBr_3$ NCs deposited on glass.

Comparing $CsPbBr_3$ NCs with $CsMAPbBr_3$ thin film (see Figure 6.4), this latter presented a better grain formation and smother film. Therefore, we could confirming that adding little amount of methylamonium (MA^+) helps with the smoothness of the film.

Transmission Electron Microscopy (TEM) was used to determine the size and composition of halide perovskite nanoparticles. TEM images (Figure 6.8) shows some spherical nanoparticles with a diameter lower than 10 nm in both cases. Comparing our TEM images with the paper already reported, we did not observe significant differences in their size and shape [17].

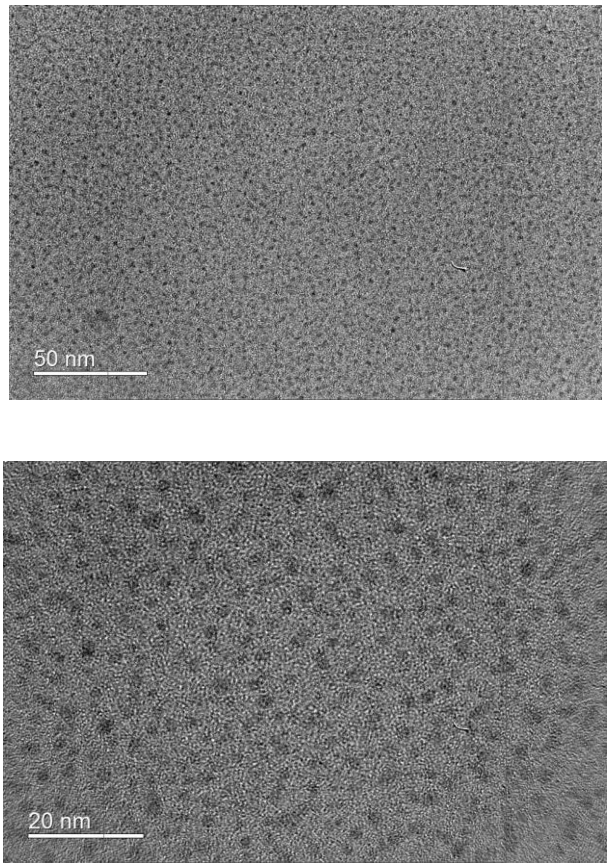

Figure 6.8.TEM images of $CsPbBr_3$ NPs with a size average of 2.1 ± 0.5 nm.

6.4.2.3 $CsPbI_3$ QDs

The absorption and the photoluminescence (PL) spectra of $CsPbI_3$ QDs solved in hexane were recorded at room temperature and under air conditions (Figure 6.9). As we expected, the emission spectrum presented a unique narrow peak at 670 nm with a 25 nm of FWMH. The absorption shows a shoulder at 340nm, 400 nm and 485 nm. The quantum yield of $CsPbI_3$ was 50%.

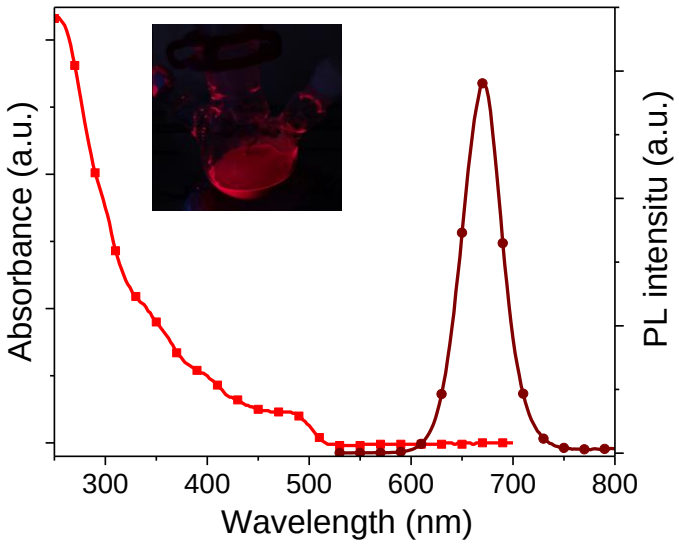

Figure 6.9. UV-vis absorption and photoluminescence spectra of $CsPbI_3$ QDs solved in hexane and recorded at room temperature.

TEM images were recorded to verify the size and shape of $CsPbI_3$ QDs (see Figure 6.10). $CsPbI_3$ QDs presented a cubic shape with an average size of 12 nm, in agreement with the papers which described this synthesis.

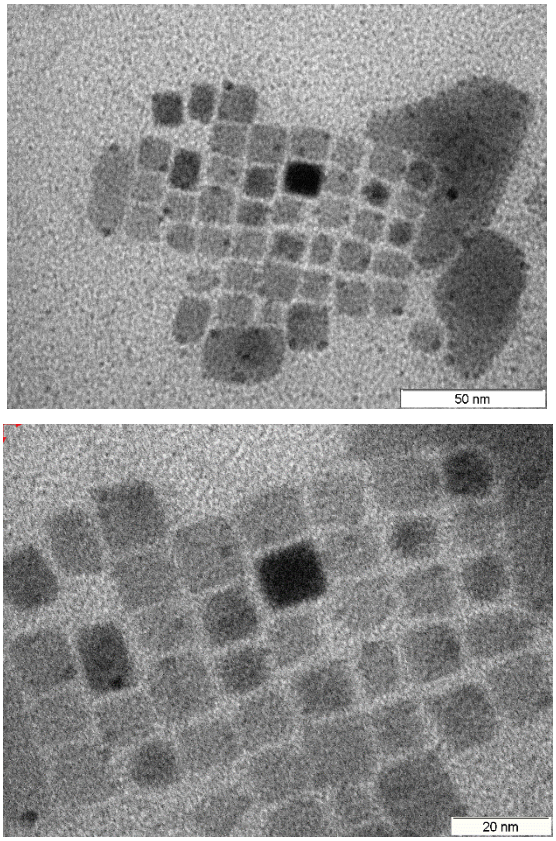

Figure 6.10. TEM images of $CsPbI_3$ QDs taken at different magnification scales with a size average of 12.42 ± 1.8 nm.

6.4.2 Exchange anion

The instability of cubic phase at room temperature is the main problem when working with $CsPbI_3$ NCs. There are many publications trying to protect perovskite nanomaterial against degradation. For instance, Kamat *et al.*[18] published an halide exchange reaction procedure from $CsPbBr_3$ to $CsPbI_3$ under air conditions. The exchange solution was made heating 68 mg of PbI_2 , 0.6 mL oleyamine, 0.4 mL oleic acid and 20 mL of ODE at 100 °C until PbI_2 dissolved. First, we deposited 3 cycles of $CsPbBr_3$ waiting 5 minutes before each deposition. Then, the film was soaked in the PbI_2 solution to anion

exchange during 5 s and heated at 120 °C. Finally, PL spectra were obtained for all the films in order to corroborate if the anion exchange was successfully done.

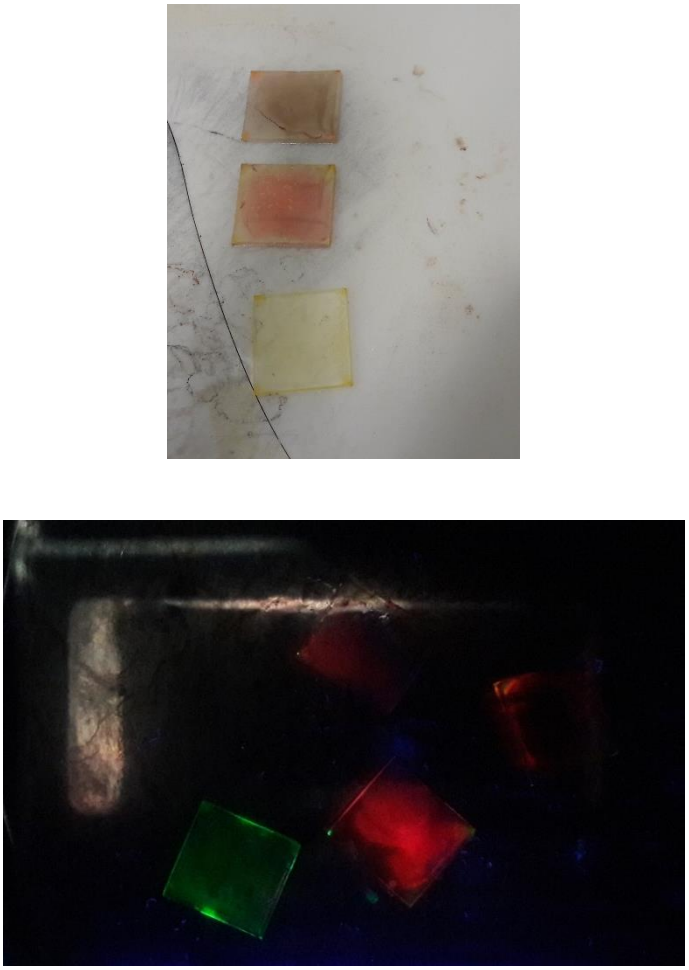

Figure 6.11. Films of $CsPbBr_3$ and $CsPbI_3$ during the anion exchange in air (top) and under UV lamp (bottom).

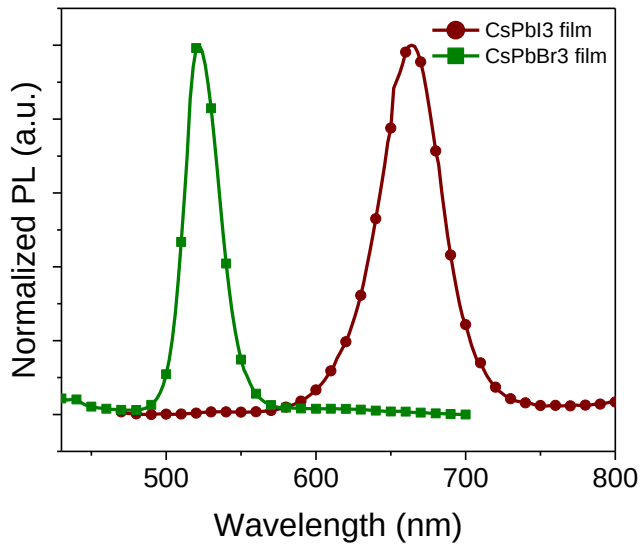

Figure 6.92. Normalized PL spectra of $CsPbBr_3$ and $CsPbI_3$ in thin films. The samples were excited at 410 nm and 450 nm respectively.
The $\lambda_{em}(CsPbBr_3\ film)$ = 522 nm ; $\lambda_{em}(CsPbI_3\ film)$ = 664 nm.

As shown in Figure 6.12, the emission band of perovskite NCs changed from green to red region so indicating that the anion exchange was successfully performed. Nevertheless, as it can be seen in Figure 6.11, the films obtained were not homogeneous. Therefore, to solve this problem the anion exchange was done in solution instead of in film. We followed different strategies to exchange anion in solution and in air conditions. The optimal exchange solution was made heating 17 mg of PbI_2 in 0.15 mL oleyamine, 0.1 mL oleic acid and 5 mL of ODE at 100 °C until PbI_2 dissolved. This solution was added to $CsPbBr_3$ NPs solution.

From the emission band observed in the PL spectrum, the exchange anion was also successfully performed (Figure 6.13). However, the emission intensity decreased significantly and the emission band was broader in comparison to $CsPbBr_3$. This could be due to instability of $CsPbI_3$ NCs in air conditions.

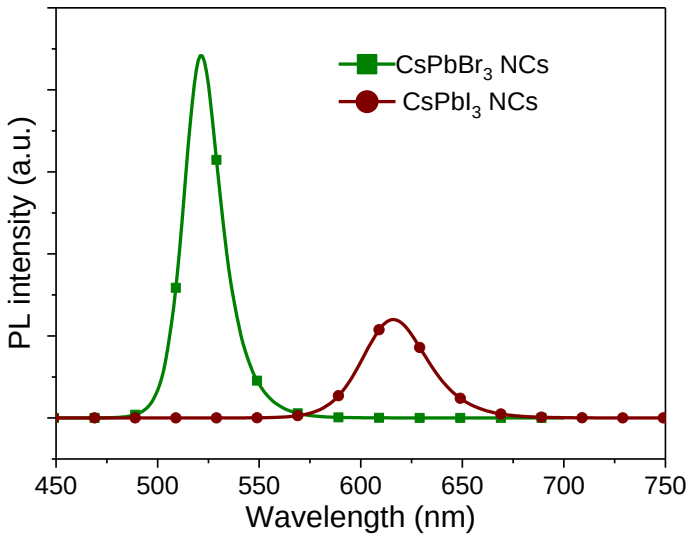

Figure 6. 103. PL spectra of $CsPbBr_3$ NCs and $CsPbI_3$ NCs after excitation at 330 nm and 380 nm respectively.

Figure 6.14 shows top view SEM images of $CsPbBr_3$ (Figure 6.14 top) and $CsPbI_3$ (Figure 6.14 bottom) thin film deposited on glass substrates. Comparing both images, $CsPbI_3$ presented a better film deposition and lower number of pin holes than $CsPbBr_3$ films, after a few days the $CsPbI_3$ films stopped to emit due to their instability in air.

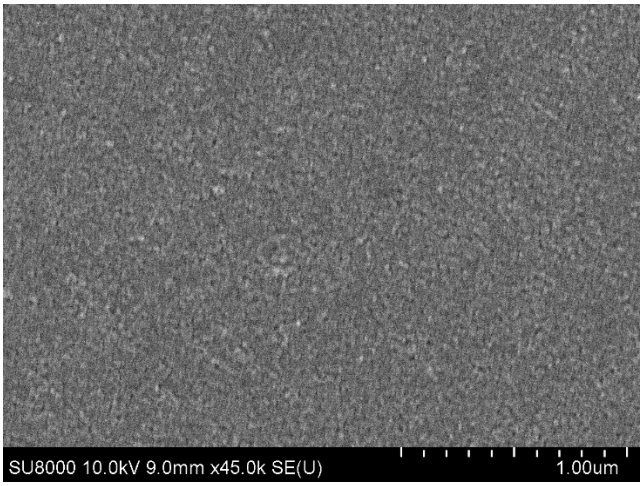

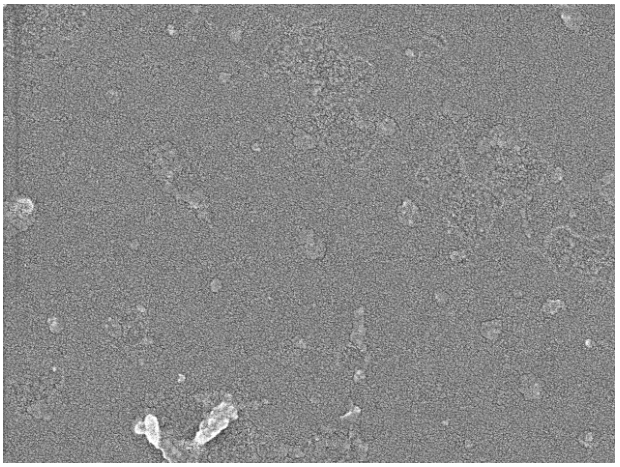

Figure 6.114. SEM images of $CsPbBr_3$ (top) and $CsPbI_3$ (bottom).

The following reaction may explain the perovskite NCs decomposition process:

$$CsPbI_3 \rightarrow CsI + PbI_2$$

$$2.5\ CsPbBr_xI_{1-x} \rightarrow CsPbBr_3 + 1.5\ CsI + 1.5\ PbI_2$$

TEM images of $CsPbI_3$ (Figure 6.15) showed different particle shapes.

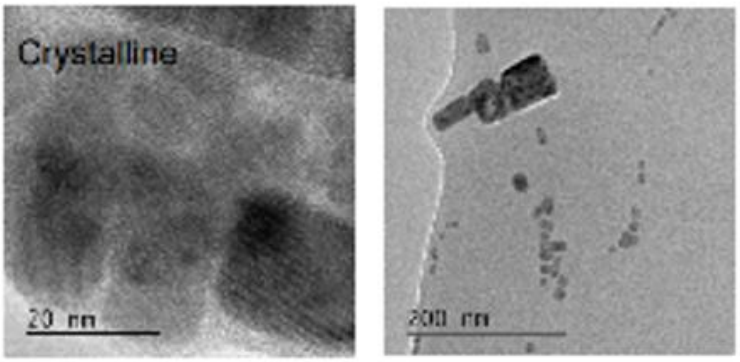

Figure 6.15. TEM images of $CsPbI_3$.

In order to increase the stability of the $CsPbI_3$ NPs, it has been described the possibility to replace oleic acid and oleyamine for phosphoric alkyl acid as passivating ligand because in previous works reported improved stability of colloidal $CsPbX_3$ perovskite nanocrystals[19]. Also with this ligand, the anion exchange worked correctly because PL spectrum showed just one emission peak. However, when working with phosphoric alkyl acid as ligand, the PL intensity obtained was lower than with oleic acid (see Figure 6.16). Both capping layers were tried only once for anion exchange, so more tests should be carried out to confirm these preliminary results.

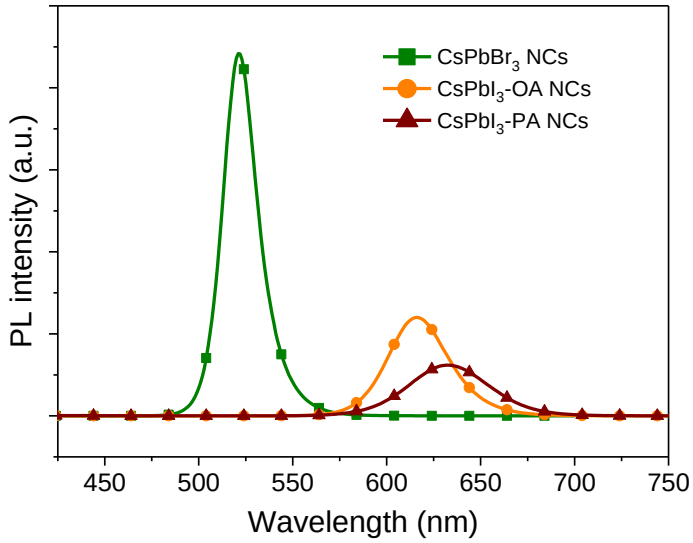

Figure 6.16. PL spectra of $CsPbBr_3$ and $CsPbI_3$ NCs passivated with two different capping ligands after excitation at 330 nm ($CsPbBr_3$ NCs) and 380nm ($CsPbI_3$-OA and $CsPbI_3$-PA).

To summarize this section, anion exchange through different methods was performed as an alternative of the direct $CsPbI_3$ QDs synthesis. Due to the poor stability once the anion was exchanged, we decided to synthetize directly $CsPbI_3$ NCs.

6.4.3 Device results.

Two different devices fabrication were performed to test perovskite based on the materials described: $CsMAPbBr_3$ and $CsPbI_3$.

One of the devices fabricated in this work was a PeLED. It consisted in the fabrication of $CsMAPbBr_3$ thin film sandwiched between a combination of a double hole transport layer and one electron transport layer. In Figure 6.17 a schematic illustration of the energy levels of the layers is reported [20].

PEDOT:PSS and PVK were used as hole-transporting layer and electron blocking layer and TmPYP as electron transport layer improving the electron injection from the cathode [21].

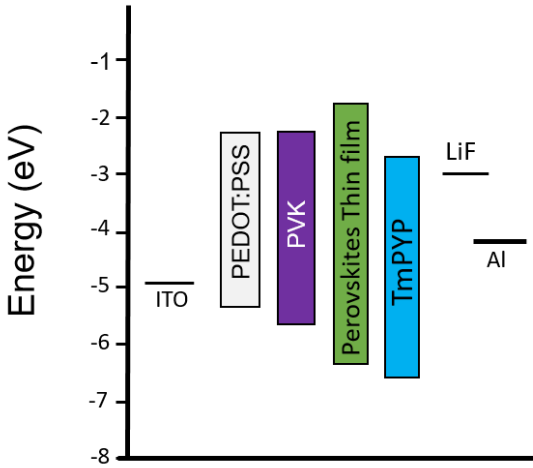

Figure 6.17. Energy level diagram of the PeLED structure [20].

The perovskite composition used for the thin film fabrication consisted of mixing two cations: cesium and methylammonium bromide. The addition of small amounts of $CH_3NH_3^+$ (MA) into the precursor solution decreased the number of the pinholes in the final film [16].

Once the thin film was deposited, 40 µL of toluene was dropped by spin-coating on top of the film to improve the roughness [22].

Current density-luminance-voltage are shown in Figure 6.17. The maximum peak luminance was 35 Cd/m^2 and the turn-on voltage 6.6 V.

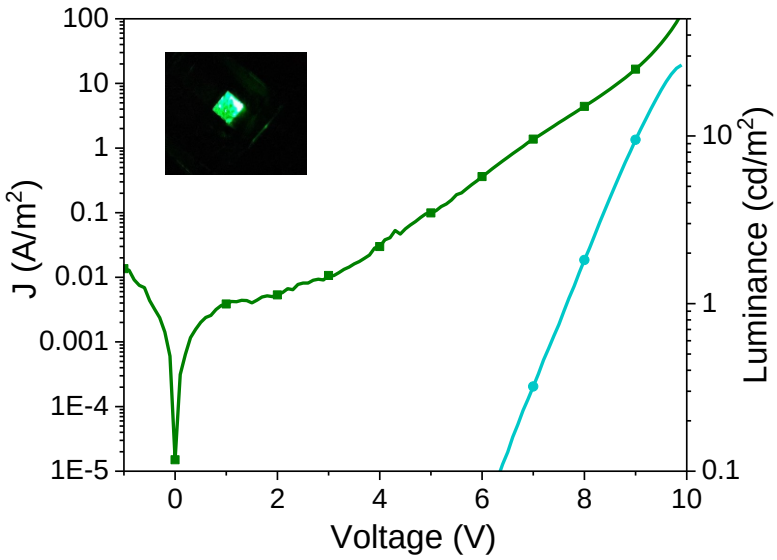

Figure 6.18. Current density (dark green line) and luminance (light green line) versus applied voltage of the PeLED using $CsMAPbBr_3$ thin film as unique emissive layer.

Figure 6.18 shows the electroluminescence spectra of PeLEDs using $CsMAPbBr_3$ as emissive layer. The λ_{max} was at 516 nm which agreed well with the photoluminescence wavelength. Moreover, as it can be seen in the electroluminescence spectra, there was not any emission wavelength shift when we applied higher voltage bias. CIE color coordinates were (0.146, 0.492), see Figure 6.19).

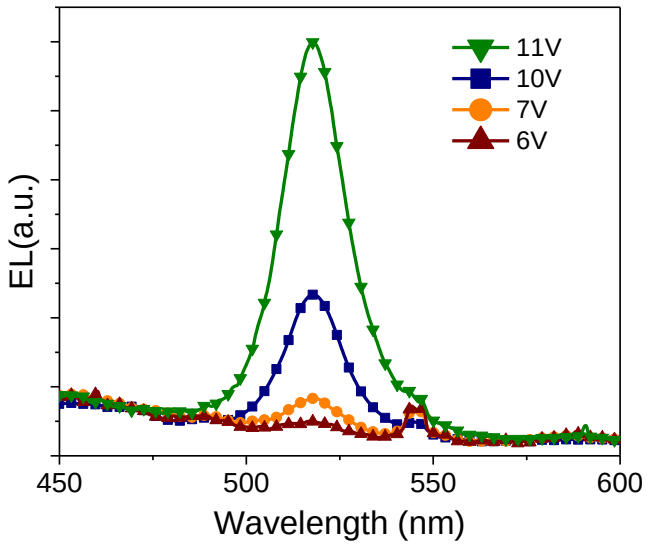

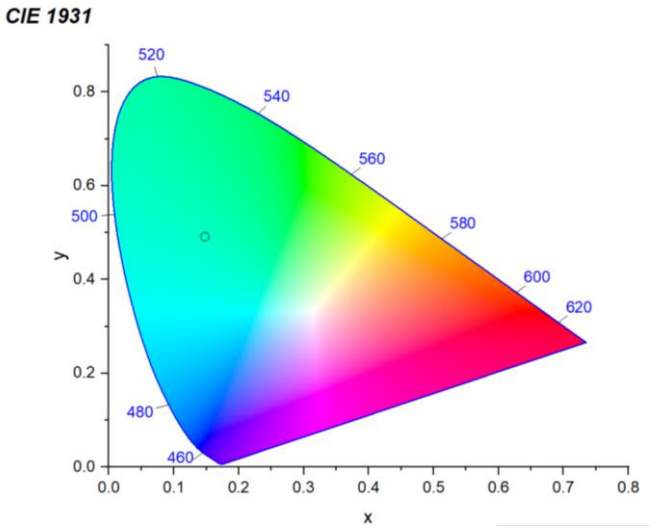

Figure 6.19. Electroluminescence of ITO/PEDOT:PSS/PVK/CsMAPbBr3/ TmPyP/LiF/Al at room temperature (top) and its corresponding CIE color coordinates (bottom**).**

The second structure that we fabricated using $CsPbI_3$ as unique emissive layer, TiO_2 as electron layer and Spiro-OMetad and MoO_3 and hole transport layer [13]. The energy levels, taken from the bibliography[13], are shown in Figure 6.19.

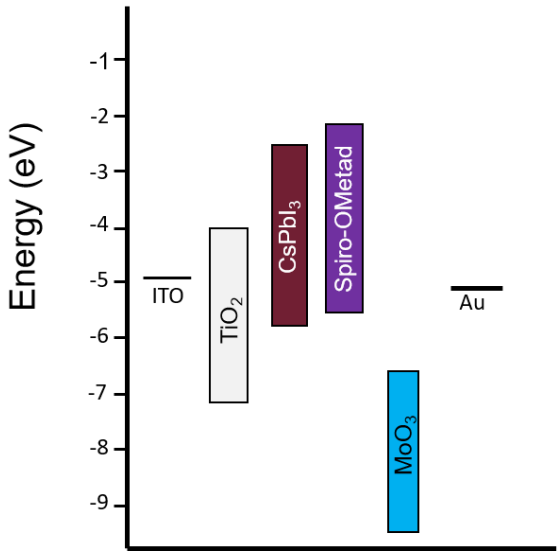

Figure 6.20. Estimated energy level alignment of the materials used to fabricate PeLEDs.

The current and luminance versus voltage of PeLEDs is shown in Figure 6.20. Both synthesis and steps fabrications were performed in inert conditions due to the low stability of this materials in air conditions. The maximum peak luminance was 2 Cd/m^2 and the turn-on voltage 3.2 V.

CIE was calculated from the PL spectra instead of electroluminescence because we could not record the electroluminescence as the low stability of the diodes. CIE color coordinates were (0.716, 0.288) (see Figure 6.22).

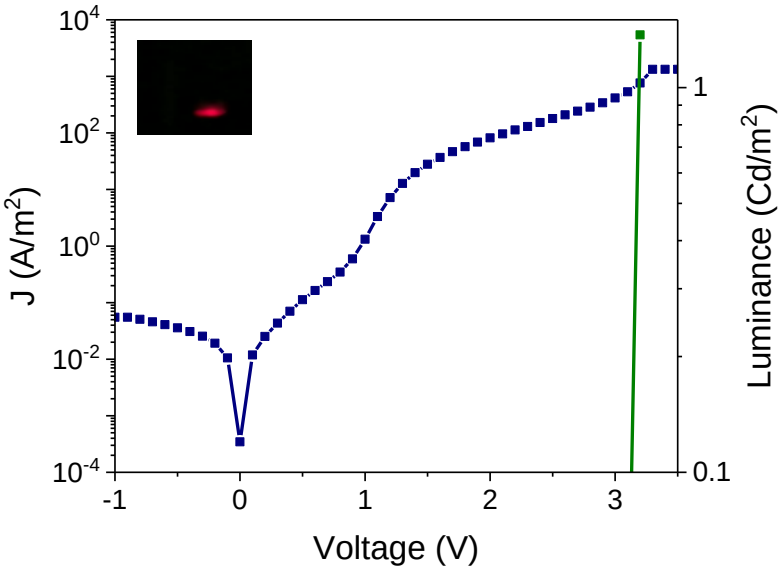

Figure 6.21. IV (blue line) and luminance (green line) versus voltage curves. Inset image: perovskites LED while applying voltage.

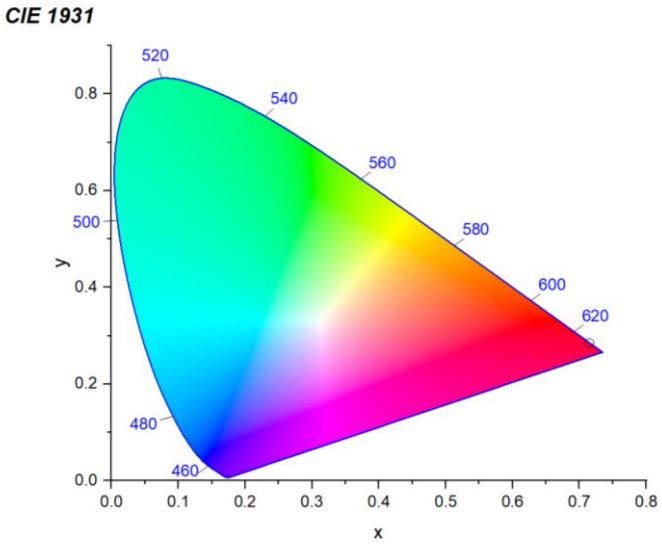

Figure 6.22. CIE of PeLEDs using $CsPbI_3$ as emissive layer.

To sum up the optoelectronics results, Table 6.1 displays the final results using $CsMAPbBr_3$ and $CsPbI_3$ QDs as unique emissive layer in LEDs. In general the results were not as good as the ones reported in the literature [23]. However the low turn-on voltage that $CsPbI_3$-LEDs exhibited was very promising. All the devices were measured in inert conditions, trying to avoid the device degradation.

Table 6.1. Summary of the electrical properties of PeLEDs.

Device	Turn-on voltage V^{on} (V^a)	Max. Luminance (Cd/m^2)	Current Efficiency (Cd/A)
$CsMAPbBr_3$	6.6 (6.7)[a]	35 (23)[a]	$2 \cdot 10^{-1}$
$CsPbI_3$	3.2	2.0	$2 \cdot 10^{-3}$

V^a turn on voltage average and luminance reported in the literature. V^a is the turn-on voltage at 0.1 Cd/m^2.

6.5 Conclusions.

Metal halide has emerged as a new luminescent materials, because their optoelectronic properties are interesting for many applications. In this chapter, we have summarized the synthesis of materials and fabrication of devices performed during this thesis for the fabrication of efficient PeLEDs.

The morphology of perovskite materials is a key parameter to explain their optical properties. The grain size and roughness can directly affect the final device efficiencies, properties assisted to short circuit insides the LEDs. Two strategies to obtain the desired morphology were successfully applied: 1) small amounts of CH_3NH_3Br into the precursor solution decreased the number of the pinholes in the case of $CsMAPbBr_3$ films, and 2) small amounts of toluene during the spin coating improved the roughness too.

$CsPbI_3$ NPs were obtained by using two different ways: 1) direct synthesis by hot injection and 2) indirect anion exchange from $CsPbBr_3$ NPs. The aim was to fabricate a device which can be used as LEDs. Regarding the results, anion exchange was not stable and after few days the perovskites decomposed.

Two PeLEDs using different device arquitecthure were fabricated. The first case, we used a double hole transport layer in order to improve the hole injection from the cathode to the active layer. We synthetized $CsMAPbBr_3$ thin film as emissive layer and TmPyP was used as electron transport layer. The maximum luminance was 35 Cd/m^2. In the second case, we finally achieved to prepare stable $CsPbI_3$ NPs using a hot injection method working in inert conditions and we used a different device architecture because of the energy alignment of the materials. The luminance was 2 Cd/m^2, concluding that a deeply devices optimization is needed.

Regarding the final results, we can conclude that a further optimization on both synthesis and device fabrication is needed. The stability of the perovskites quantum dots is still the main limitation when applied as emissive layers. In addition, the spin coating deposition of the materials is still under study due to the roughness and the homogeneity of the layer.

However, it is important to remark that this chapter 6 was developed during my 3 months stay in NIMS (Japan) and consequently the optimization of the final device was affected by the lack of time.

6.6 References.

1. I. Gelmetti, N. Montcada, A. Perez-Rodriguez, et al. Energy Alignment and Recombination in Perovskite Solar Cells: Weighted Influence on the Open Circuit Voltage. *Energy Environ. Sci.* **2019**.
2. Q.A. Akkerman, M. Gandini, F. Di Stasio, et al. Strongly emissive perovskite nanocrystal inks for high-voltage solar cells. *Nat. Energy* **2016**, 2, 16194.
3. J. Song, J. Li, X. Li, et al. Quantum Dot Light-Emitting Diodes Based on Inorganic Perovskite Cesium Lead Halides (CsPbX3). *Adv. Mater.* **2015**, 27 (44), 7162–7167.
4. P. Nikolaou, I. Vareli, E. Deskoulidis, et al. Graphite/SiO2 film electrode modified with hybrid organic-inorganic perovskites: Synthesis, optical, electrochemical properties and application in electrochemical sensing of losartan. *J. Solid State Chem.* **2019**, 273, 17–24.
5. T. Ishihara, J. Takahashi, T. Goto. Exciton state in two-dimensional perovskite semiconductor (C10H21NH3)2PbI4. *Solid State Commun.* **1989**, 69 (9), 933–936.
6. H. Cho, S.-H. Jeong, M.-H. Park, et al. Overcoming the electroluminescence efficiency limitations of perovskite light-emitting diodes. *Science (80-.).* **2015**, 350 (6265), 1222 LP – 1225.
7. Y.-H. Kim, H. Cho, T.-W. Lee. Metal halide perovskite light emitters. *Proc. Natl. Acad. Sci. U. S. A.* **2016**, 113 (42), 11694–11702.
8. S.D. Stranks, H.J. Snaith. Metal-halide perovskites for photovoltaic and light-emitting devices. *Nat. Nanotechnol.* **2015**, 10, 391.
9. L. Zhao, Y.-W. Yeh, N.L. Tran, et al. In Situ Preparation of Metal Halide Perovskite Nanocrystal Thin Films for Improved Light-Emitting Devices. *ACS Nano* **2017**, 11 (4), 3957–3964.
10. W. Zhang, G.E. Eperon, H.J. Snaith. Metal halide perovskites for energy applications. *Nat. Energy* **2016**, 1, 16048.
11. G. Nedelcu, L. Protesescu, S. Yakunin, et al. Fast Anion-Exchange in Highly Luminescent Nanocrystals of Cesium Lead Halide Perovskites (CsPbX3, X = Cl, Br, I). *Nano Lett.* **2015**, 15 (8), 5635–5640.

12. J.B. Hoffman, A.L. Schleper, P. V Kamat. Transformation of Sintered CsPbBr3 Nanocrystals to Cubic CsPbI3 and Gradient CsPbBrxI3-x through Halide Exchange. *J. Am. Chem. Soc.* **2016**, 138 (27), 8603–8611.
13. A. Swarnkar, A.R. Marshall, E.M. Sanehira, et al. Quantum dot–induced phase stabilization of α-CsPbI3 perovskite for high-efficiency photovoltaics. *Science* **2016**, 354 (6308), 92 LP – 95.
14. X. Du, G. Wu, J. Cheng, et al. High-quality CsPbBr3 perovskite nanocrystals for quantum dot light-emitting diodes. *RSC Adv.* **2017**, 7 (17), 10391–10396.
15. C. Guhrenz, A. Benad, C. Ziegler, et al. Solid-State Anion Exchange Reactions for Color Tuning of CsPbX3 Perovskite Nanocrystals. *Chem. Mater.* **2016**, 28 (24), 9033–9040.
16. W. Zhang, M. Saliba, D.T. Moore, et al. Ultrasmooth organic–inorganic perovskite thin-film formation and crystallization for efficient planar heterojunction solar cells. *Nat. Commun.* **2015**, 6, 6142.
17. Y.-H. Kim, C. Wolf, Y.-T. Kim, et al. Highly Efficient Light-Emitting Diodes of Colloidal Metal–Halide Perovskite Nanocrystals beyond Quantum Size. *ACS Nano* **2017**, 11 (7), 6586–6593.
18. Q.A. Akkerman, V. D.Innocenzo, S. Accornero, et al. Tuning the Optical Properties of Cesium Lead Halide Perovskite Nanocrystals by Anion Exchange Reactions. *J. Am. Chem. Soc.* **2015**, 137 (32), 10276–10281.
19. W. Koh, S. Park, Y. Ham. Phosphonic Acid Stabilized Colloidal CsPbX3 (X=Br, I) Perovskite Nanocrystals and Their Surface Chemistry. *ChemistrySelect* **2016**, 1 (13), 3479–3482.
20. M. Li, W. Zhang, H. Wang, et al. Effect of organic cathode interfacial layers on efficiency and stability improvement of polymer solar cells; **2017**; Vol. 7.
21. F. Meng, C. Zhang, D. Chen, et al. Combined optimization of emission layer morphology and hole-transport layer for enhanced performance of perovskite light-emitting diodes. *J. Mater. Chem. C* **2017**, 5 (25), 6169–6175.

22. L. Zhang, X. Yang, Q. Jiang, et al. Ultra-bright and highly efficient inorganic based perovskite light-emitting diodes. *Nat. Commun.* **2017**, 8, 15640.
23. Q. Van Le, K. Hong, H.W. Jang, S.Y. Kim. Halide Perovskite Quantum Dots for Light-Emitting Diodes: Properties, Synthesis, Applications, and Outlooks. *Adv. Electron. Mater.* **2018**, 4 (12), 1800335.

A6 Annex.

A6.1 Quantum yield.

The quantum yield of CQDs was calculated using Rodhamine 101 as reference dye.

The calculation was done using the following equation:

$$QY = QY_{ref}\left(\frac{I_{em\,sample}}{I_{em\,ref}}\right)\cdot\left(\frac{Abs_{ref}}{Abs_{sample}}\right)\cdot\left(\frac{n_{sample}}{n_{ref}}\right)^2 \quad \text{Equation A6.1}$$

Where QY_{ref} is the reference quantum yield, I_{em} is the area of the emission band, Abs is the absorbance excitation wavelength and η is the refractive index.

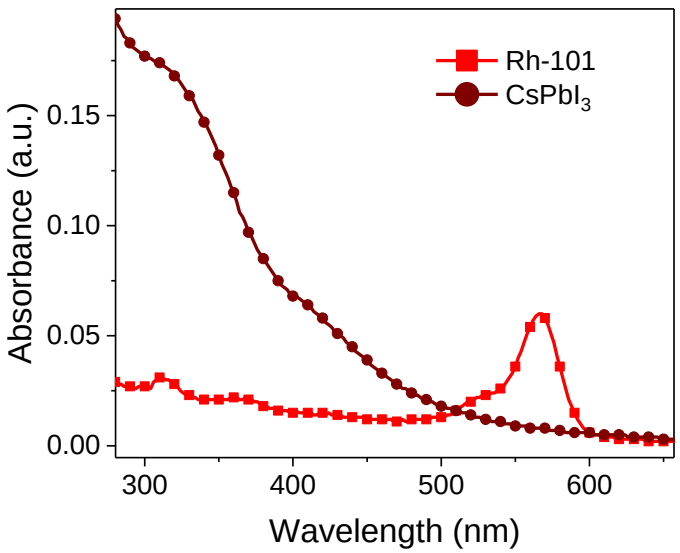

Figure A6.1. Absorbance spectra of $CsPbI_3$ (dark red line) and Rodhamine 101 (light red line) at room temperature.

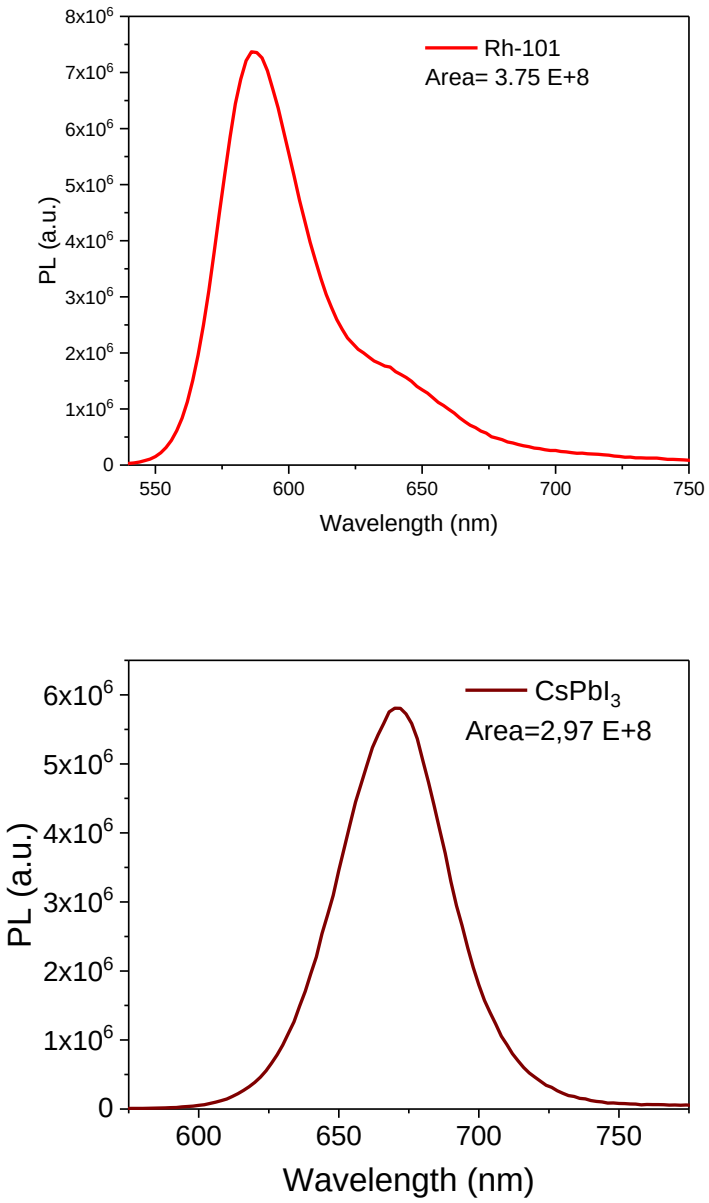

Figure A6.2. Emission spectra of Rodhamine 101 (top) and $CsPbI_3$ (bottom) measured at λexc=510nm at room temperature.

Chapter 6

7

Carbon Quantum dots in the emissive layer in LEDs.

In this chapter, we report a facile synthesis of Carbon Quantum Dots (CQDs) using a hot injection method in order to obtain heavy metal free quantum dots. CQDs have been used as emissive layer in light emitting diodes obtaining white light emission.

Chapter 7

Table of Contents

Chapter 7

7.1 Introduction.

Over the past 15 years, technologies based on colloidal quantum dots have burst in both the academic and the industrial field [1,2]. Quantum dots are defined as nanometer scale semiconducting crystals with a physical size smaller than the radius of the Bohr exciton, that, consequently, show quantum confinement. This means that, in general, the bandgap changes according to their size, and thus their optical properties.[3] In addition, the shape can be tuned to rods, nanowires or dots using different capping ligands. Regarding the optical properties, they show broad absorption, narrow emission peaks and color purity, especially when compared to organic semiconductors.

Due to these interesting optical properties, the nanocrystals have been used in optoelectronic devices like quantum dots light emitting diodes (QLEDs) that have emerged during the last years as the new LEDs generation due to better color definition over the entire visible spectrum [3,4,5]. The structure of these devices consists of a sandwiched layer of emissive quantum dots between electrodes and charge transport layers. When a bias is applied, hole and electrons are injected and recombine radiatively in the quantum dot layer, which results in the emission of light.

The most studied quantum dots were those composed of III-V elements such as GaP, InP or GaN and II-VI elements such as ZnS, CdTe, CdSe whose size ranges between 1-10 nm. More recently, perovskites based quantum dots are also being intensively studied due their optoelectronic properties similar to cadmium based quantum dots such as high quantum yield or narrow emission[6,7].To date, the best results are obtained using cadmium based or perovskite based quantum dots as emissive layer with a quantum yield higher than 80 %[8,9,10,11] .

However, these materials contain toxic elements such as cadmium, lead, or selenium. As an alternative, a new generation of fluorescent quantum dots based in carbon has recently emerged. Their low toxicity and biocompatibility is a good

alternative to heavy metal-containing nanomaterials. In addition, carbon quantum dots (CQDs) can be prepared using ordinary products like sugar or orange juice and can be solved in non-halogenated solvents such as ethanol or water[12]. The efforts of the research community have resulted in examples of carbon dots applied in bioimaging [13,14], sensors [15], hole transport material in solar cells [16] or light emitting diodes[17].

However, there are some limitations such as their low quantum yield and the color emission tuneability. Despite the efforts to improve the quantum yield, it remains lower compared to the cadmium-based quantum dots[18,19]. In addition, the origin of the photoluminescence emission of CQDs is still under study, because the reaction time does not modify the band gap and as consequence the emission wavelength of the quantum dots[19, 20].

In this chapter, we describe the use of carbon quantum dots as emissive layer for light emitting diodes. These type of devices combine the robustness given by the transition metal oxides in the charge transport layers with the emissive properties of the carbon quantum dots. In the literature, there are previous examples using carbon dots in organic electroluminescent devices, such as those provided by Zhang in 2013 and Wang in 2011, used 1-hexadecylamine (HDA) as passivating ligand of CQDs that are applied as active layer for OLEDs [21,22]. Other examples of devices using this material can be found in light converting phosphors for white LED[23,24].

Here we present a structure based on sandwiched device using ZnO as electron transport layer and Poly(9-vinylcarbazole) (PVK) in combination with molybdenum oxide as hole transport layer. PVK is a widely used polymer in LEDs due to its good conductivity and optical properties. We will show our studies with 1-hexadecylamine as capping ligand with devices prepared by solution processing under ambient conditions. To the best of our knowledge, this is the first example of inverted device structure using CQDs as emissive layer.

7.2 Experimental part.

CQDs were synthesized by a bottom-up approach in inert conditions. The synthesis of ZnO NPs is described in **Chapter 3.**

7.2.1 Synthesis of CQDs.

The synthesis of carbon quantum dots is done in a one-step hot-injection process according to the method reported by Fu Wang *et al*.[25] and as it is described in Figure 7. 1. Typically, 15 mL of 1-octadecene (ODE) and 1.5 g of 1-hexadecyl amine (HDA) were stirred in a three-neck flask under inert conditions during 30 minutes at room temperature. Then, the solution was heated up to 300 ºC. At this point, 1 g of citric acid was added as quickly as possible and the solution was stirred during 3 hours. Once the solution was cooled down at room temperature, acetone was added to precipitate the carbon quantum dots that were recovered after centrifugation at 4500 RPM during 20 minutes. Then, the supernatant was discarded and the solid was washed three times with hexane. The final solution was solved in hexane for further use.

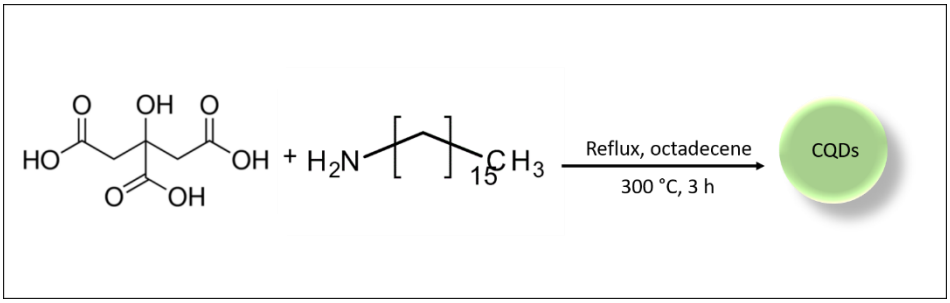

Figure 7. 1. Schematic illustration of the synthesis of CQDs.

7.3 Device fabrication.

Patterned ITO (Indium doped Tin Oxide) coated glasses (Xinyan Technology, resistance 10 Ω/square, 15x15 mm) were cleaned with acetone for 15 minutes and 2-propanol for 15 minutes in an ultrasound bath. Cleaned ITO (Indium doped tin oxide) substrates were used as anode, on top of ITO a layer of ZnO (80 mg/ml in methanol) was deposited by spin coating at 5000 RPM 60 s and heated up 30 minutes at 150 ºC. Polyethylenimine ethoxylated (PEIE 0.2 %wt 2-methoxyethanol) was spin coated on top at 6000 RPM 60 s and annealed at 110 ºC for 30 minutes. After that, the solution of carbon quantum dots in hexane with different two concentrations was spin coated at 1000 RPM 60 s and baked at 110 ºC 10 minutes. Poly(N-vinyl carbazole) (PVK) dissolved in chlorobenzene (20 mg/ml) was deposited on top of CQDs at 1000 RPM or 2000 RPM 60 s and annealed at 110 ºC 10 minutes. Both solutions were filtered with a PTFE 0.2 µm filter. Finally, thermal evaporation of 80 nm Au was done at 10^{-6} mbar. The final area of the devices is 9 mm^2.

7.4 Results and discussion.

After the synthesis, the CQDs were characterized in solution and film. The physicochemical characterization of ZnO NPs is described in **Chapter 3**.

7.4.1 Physicochemical Characterization.

To analyze the chemical structure of the surface, Fourier Transform infrared (FTIR) was used (Figure 7. 2) confirming the presence of stretching vibrations of C=C and C=N at 1500-1600 cm^{-1} that are assigned to passivating HDA molecules [26,25].

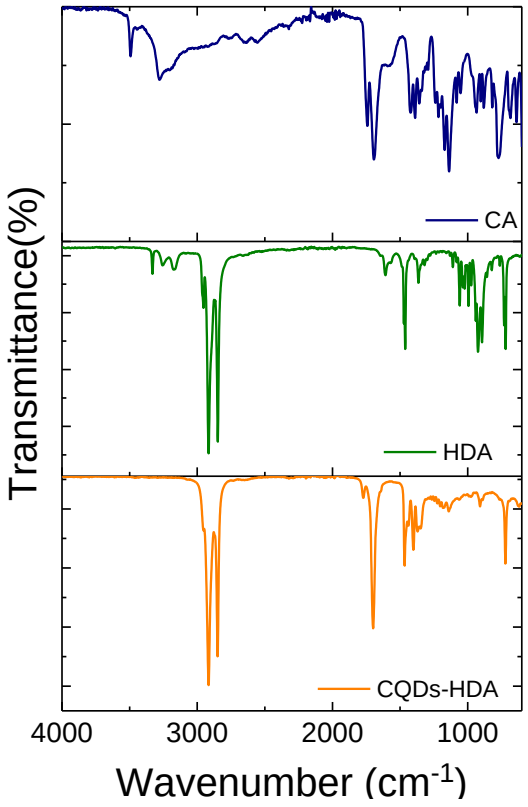

Figure 7. 2. FT-IR spectrum of citric acid (CA), 1-hexadecylamine (HDA) and CQDs prepared with HDA.

The size and the morphology of the CQDs were investigated by TEM (Figure 7. 3) and Dynamic Light Scattering (DLS) (Figure 7. 4). The average size between TEM images and DLS can differ because the DLS cannot distinguish between a large particle or an aggregation. The DLS measurement was recorded by intensity and by volume. In the first one, the intensity of the population depends on the number of particles with similar size in the sample, and the second one depends on the space occupied by a nanoparticle. Figure 7. 3 shows three different images of CQDs at different scales of magnification. The CQDs present a spherical shape and are well dispersed without any aggregation. The average size was estimated at 6 ± 1.9 nm.

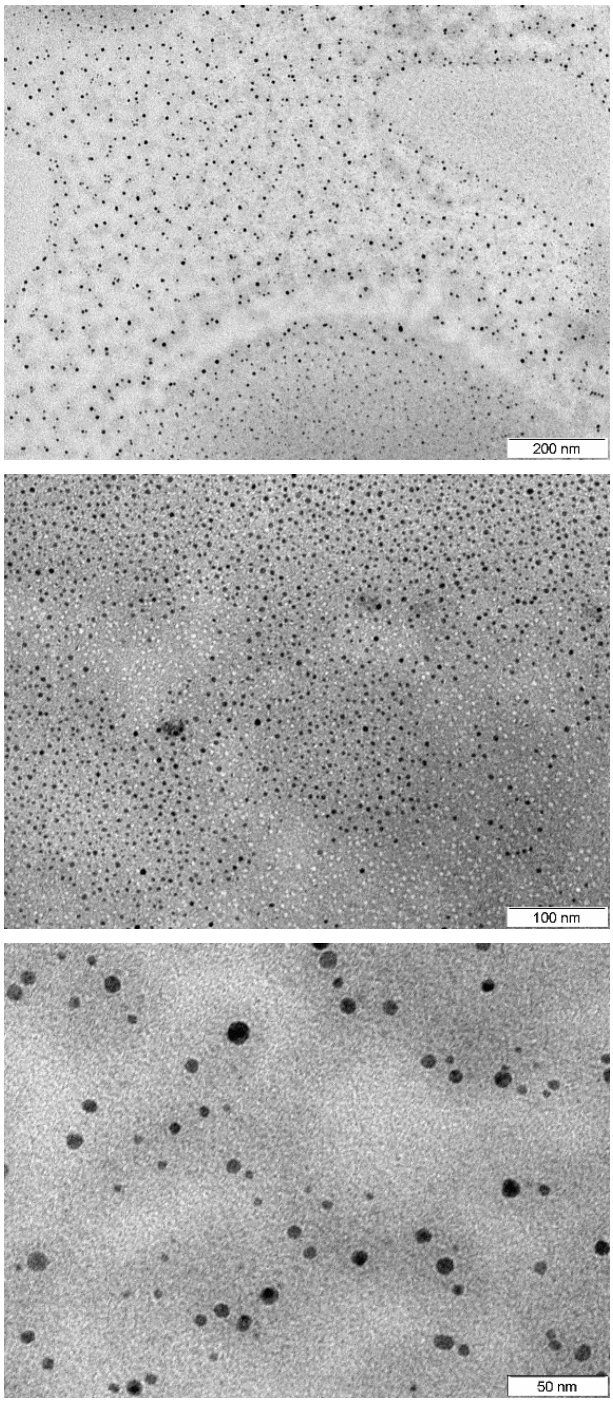

Figure 7. 3. TEM images of CQDs at different magnifications.

Regarding dynamic light scattering, the sample was measured two times (red and green line), and both graphs displayed the average size distribution by intensity and by volume. In the first case, we observed some aggregates with a size of 100 nm and 900 nm. We do not observe the same in DLS by volume because those larger particles are minority in the sample. From the data showed in Figure 7.4, we estimate that the smaller particles have an average size of 5 nm.

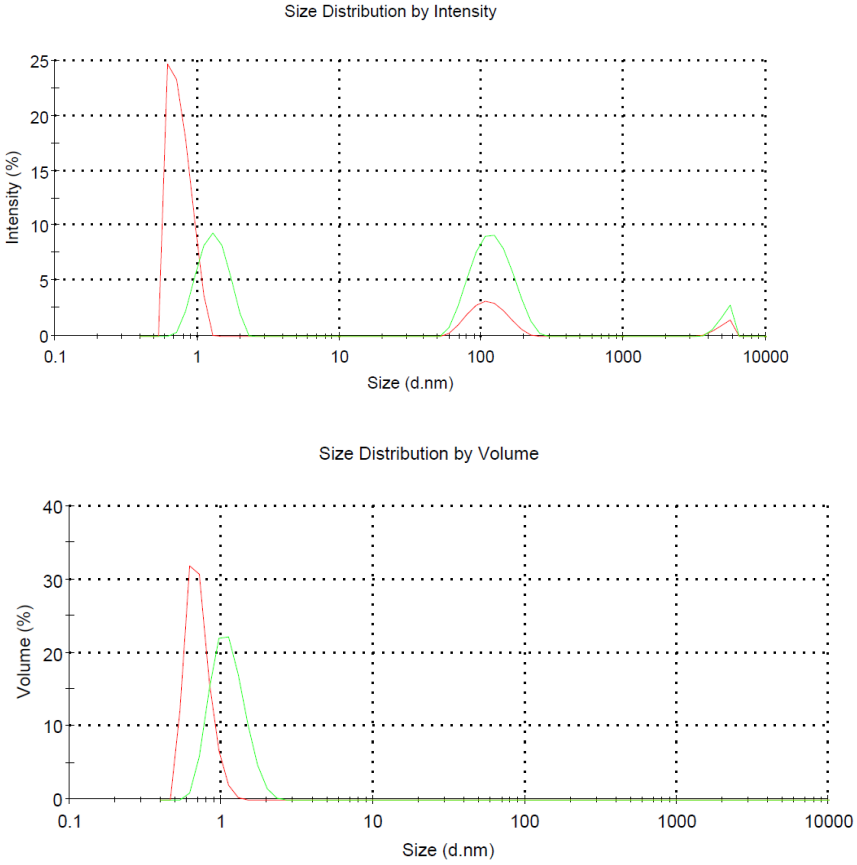

Figure 7. 4. DLS signal of CQDs-HDA. Size distribution by intensity and by volume.

The absorption and the photoluminescence (PL) spectra of CQDs in hexane are shown on Figure 7. 5. The sample was measured at room temperature.

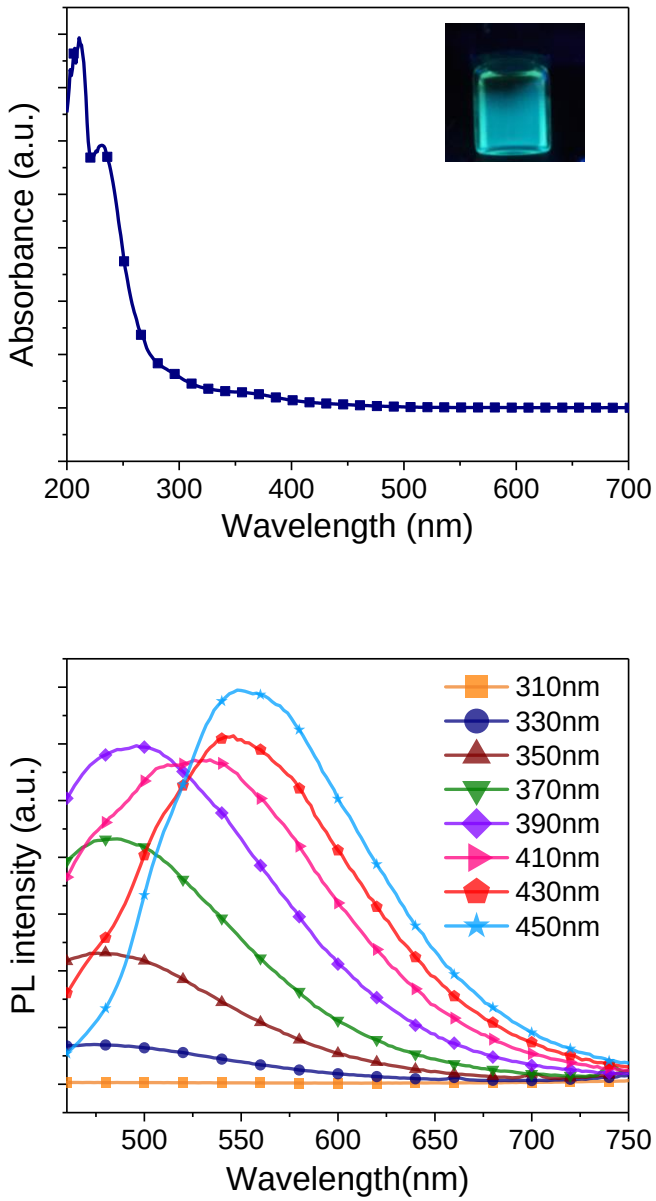

Figure 7. 5. The absorption spectra (top) and emission spectra (bottom) obtained after excitation at different wavelength from 310 nm to 450 nm on the left in 20 nm increments, respectively at room temperature.

The CQDs-HDA show strong exciton absorption bands at 230nm and a shoulder at 365 nm in the UV-vis. These two bands are attributed to two different processes. The first band belongs to π→π* transition carbonyl group C=C bonds and the shoulder is attributed to n→π* transition related to amino-functionalized connected to the surface groups [27 ,20]. PL emission is excitation dependent and thus the emission peak shifts from 496 nm to 548 nm depending on the excitation wavelength. This shift is attributed to a different radiative recombination process that happens inside the CQDs. Data obtained after excitation at 340 nm shows maximum emission at 460 nm with a full width at half maximum (FWHM) of 125 nm, and PLQY of 44%.

Even the origin of the photoluminescence mechanism in carbon dots is still under discussion, different explanations have been developed to explain this excitation wavelength dependence. For instance, Jiang et al. published that this dependence is correlated to two processes: an emission independent of the excitation wavelength from 275 nm to 400 nm and a second dependent emission to the excitation from 425 nm to 550 nm. They attributed the dual emission mechanism to the presence of organic fluorophore for the excitation- independent wavelength and carbogenic cores for the excitation dependent [27]. Hu et al demonstrated that O-containing groups on sp^2-hybridized carbon can induce a local distortion and then create different energy levels below the lowest occupied molecular orbital (LUMO). When the excitation wavelength is increased, different radiative recombination paths occurs. Thus giving rise to excitation dependent PL emission from the O-state (see Figure 7. 5)[28]. In other example, Zhu *et al*. [20] explain that there are two photoluminescence mechanism, one from the core and other from the surface ligand that can be identified separately [29, 30]. From our data, we assign the emission at different wavelength to the electronic transitions at the C=O groups, that will occur mainly at the core of the CQDs and the electronic transition at the C=N groups, which will take place at the surface of the CQDs where the surface passivation ligands are covalently attached.

To obtain more information about this point, the fluorescence decay lifetime of CQDs in solution (Figure 7. 6) was measured after excitation at 270 nm, 405 nm and 470nm using a multidimensional time correlated single photon counting method (TCSPC). The decay curves of Carbon quantum dots were fitted using a biexponential function shown in equation 7.1. The results shows two lifetimes that can be related with the two different radiative process: the fastest one was the recombination of the carriers at CQDs surface and the slowest was the carrier recombination at the CQDs core in good agreement with previous publications [31].

$$PL(t) = A_1 e^{-(\frac{t}{\tau 1})} + A_2 e^{-(\frac{t}{\tau 2})} \quad \text{Equation 7.1}$$

Where A_1 and A_2 are the amplitude of the radiative lifetime and τ is the lifetime values.

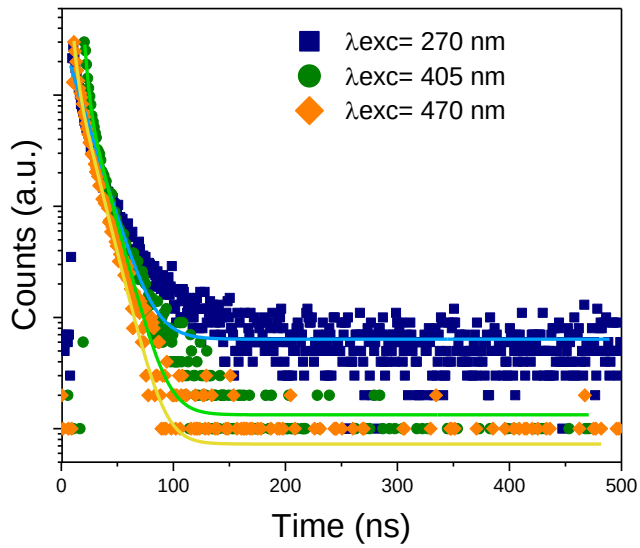

Figure 7. 6. Experimental Fluorescence-decay curves of CQDs measured in solution after excitation at 270 nm, 405 nm and 470 nm at room temperature. The color solid line represent the biexponential fitted decay.

Table 7.1. CQDs measured lifetimes using TCSPC from the biexponential fittings of the decays at different excitation wavelength.

λexc	270 nm			
	A1 %)	τ_1 (ns)	A2 (%)	τ_2 (ns)
CQDs	93.8	4.79	6.2	19.50
λexc	405nm			
	A1(%)	τ_1 (ns)	A2 (%)	τ_2 (ns)
CQDs	99.5	3.80	3.27	14.82
λexc	470 nm			
	A1(%)	τ_1 (ns)	A2 (%)	τ_2 (ns)
CQDs	96.7	2.53	3.27	10.33

It is worth noticing that the energy of the excitation wavelength is related to the lifetime of the decays, since longer lifetimes are observed when the excitation energy is higher.

Finally, with the aim to determine the valence band and the conduction band of the CQDs, electrochemical cyclic voltammetry has been performed. Figure 7.7 (top) shows the cyclic voltammetry of CQDs performed in dichloromethane whereas Figure 7. 7 (bottom) contains the square wave voltammetry. Both have been done using Ferrocene/Ferrocene$^+$ (Fc/Fc$^+$) as internal standard for electrochemical measurements with a reversible redox bands. As the solvent used during the electrochemical measurements was dichloromethane, the ferrocene oxidation/reduction bands are at 0.4-0.6 V. As CQDs-HDA present a unique oxidation band, we have used SQW in order to calculate the Conduction Band (CB) and Valence Band (VB) .The Conduction band was calculated by applying equation 7.2 and the valence band using the equation 7.4.

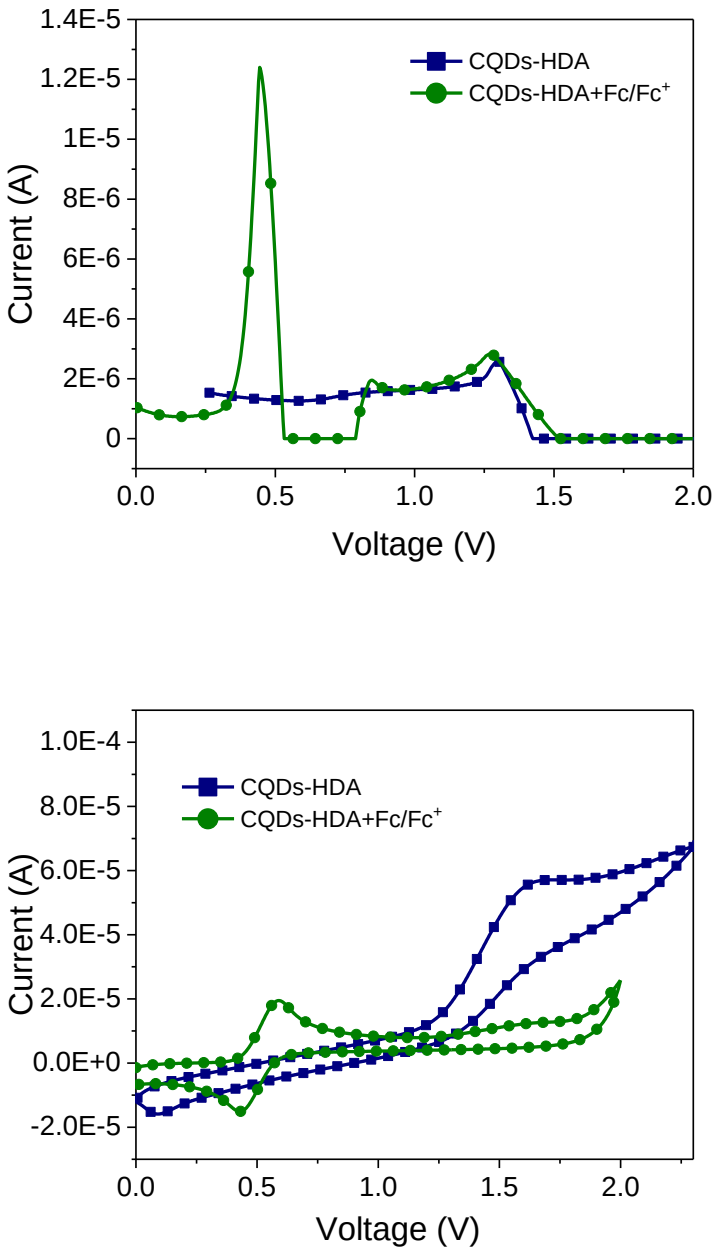

Figure 7. 7. Cyclic voltammetry (top) and Square wave voltammetry of CQDs using ferrocene (Fc/Fc+) as internal reference (bottom) recorded in 0.1M tetrabutylammonium hexafluorophosphate in dichloromethane at room temperature.

Where, E_{ox} is the oxidation potential from the CV, $E_{o\text{-}o}$ is the band gap and λ is the wavelength resulting of the intersection between the absorbance and the emission band, h is the Planck constant $6.62607004 \cdot 10^{-34}$ m^2 kg / s and c is the speed of the light $3 \cdot 10^8$ m/s.

The redox potentials were estimated from the data shown in Figure 7.7 and equation 7.3. Finally, the Valence band and Conduction band levels were calculated using equations 7.3 and 7.4.

$$E_{0-0} = \mathrm{h} \cdot \frac{\mathrm{c}}{\lambda} \qquad \text{Equation 7.2}$$

$$E_{CB} = -(E_{ox} + 4.88) \qquad \text{Equation 7. 3}$$

$$E_{VB} = E_{CB} + E_{o-o} \qquad \text{Equation 7.4}$$

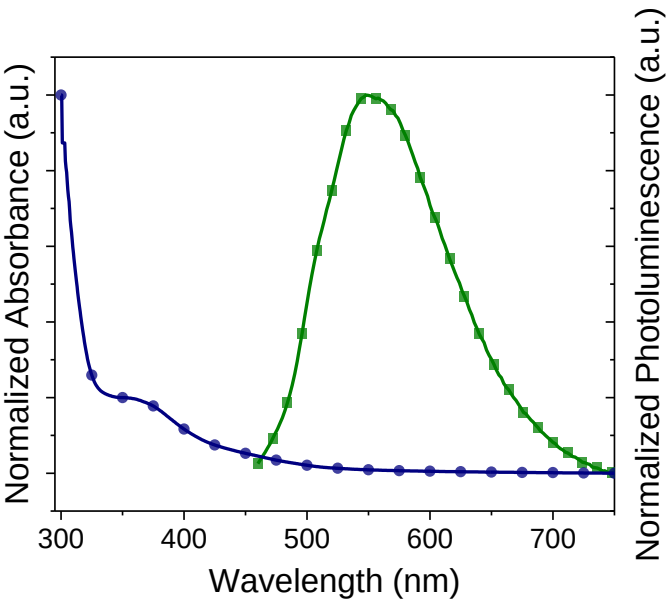

Figure 7. 8. The normalized absorption and photoluminescence spectra of CQDs.in hexane. The intersection between the absorbance and photoluminescence spectra is at λ=480nm.

The band gap was calculated combining the data obtained from the electrochemical studies and that from the intersection wavelength between the absorbance and emission spectra of CQDs (Equation 7.2 and Figure 7.8).

Table 7.2. Electrochemical parameters of CQDs.

	E_{o-o}	E_{ox}	E_{CB}	E_{VB}
CQDs	2.58 eV	0.86 eV	-5.66 eV	-3.13 eV

7.4.2 Device characterization

Inverted structure QLEDs were fabricated using ITO-covered glass and ZnO as electron transport layer, CQDs as emissive layer and PVK and MoO_3 as hole transport layer (see Figure 7. 9). ZnO was fabricated using a method described by Frederik *et al* [32]. As we mentioned previously, the combination of organic and inorganic layer in the devices reduce the problems of instability of OLEDs. Zinc oxide nanoparticles present electrical properties such as high electron mobility and lower balance band that makes them suitable for electron transport layer while forming compact layers that allow flexibility.

Light emission occurs when the electrons from the cathode and the holes from the anode recombine radiatively in the emissive layer. Nevertheless the pinholes in the films can cause short-circuits, for that, different materials are deposited between the emissive layer and the cathode or anode to block the charges and avoid direct contact between electrodes. In our case, the zinc oxide is used as electron transport layer as well as hole blocking layer. A layer of Polyethylenimine ethoxylated (PEIE) was deposited between zinc oxide and carbon quantum dots. PEIE is a well-known surface modifier that can be easily deposited on top of ZnO. Some groups have reported that PEIE thin layer enhances electron injection/transport from the metal oxide and also induces uniform surface of the quantum dot layer [33, 34] due to the aliphatic amine groups that reduce the work function of ZnO[35]. PVK was deposited onto CQDs because it is a widely studied

hole transport layer showing excellent behaviors in combination with QDs and their optoelectronic properties are well known. [36] However, PVK was solved in chlorobenzene and deposited on top of the CQDs layer, which is partially soluble in this solvent, resulting in the removal of part of the CQDs layer with a direct negative impact on the emission of this layer

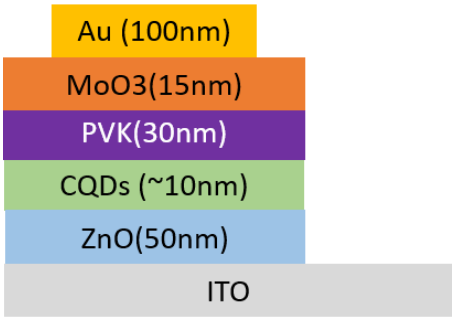

Figure 7. 9. Description of the structure.

The energy level alignment of carbon quantum dots is a crucial parameter to take into account to get efficient diodes. Figure 7. 10 shows the energy level diagram in the constructed devices, including the values for CQDs measured by ourselves and the HOMO and LUMO levels of the others materials that were taken from the bibliography [35]. The fact that the conduction band of CQDs with the LUMO level of PVK are closer could be an inconvenience because the electron charges can bypass through the emissive layer and the electrons are not, decreasing the luminance of the device.

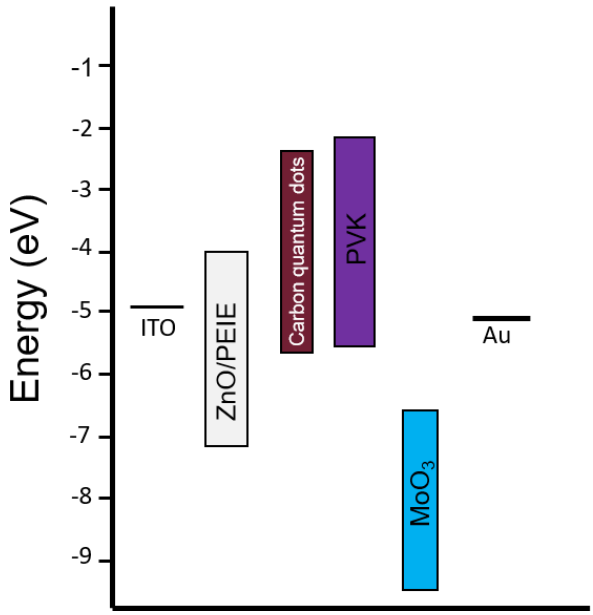

Figure 7. 10. Estimated Energy Level alignment of the materials used to fabricate the devices.

The thickness of PVK and CQDs were optimized to control the charge injection, and improve the luminance efficiency. Figure 7. 11 shows the PL spectra of films of CQDs prepared from solutions of 5 mg/mL, 10 mg/mL and 20 mg/mL deposited onto a glass at 1000 RPM followed by annealing at 110 ºC 10 min. We observed that decreasing the concentration increase the PL intensity. We can explain this by considering the self-quenching and molecular packing. During the excited state lifetime, different process can occur such as quenching, energy transfer etc. These processes can lead to a reduction in fluorescence intensity. By definition, self-quenching is the intensity of the fluorescence that depends on the concentration of the fluorophores, in our case carbon quantum dots. Self-quenching occurs when the excited fluorophore contact with an atom or molecule that facilitates non-radiative transitions. This transition depends on the concentration of the quenchers, in our case the concentration of carbon quantum dots. As can be seen in Figure 7.11, the intensity of CQDs emission is directly related to the concentration itself.

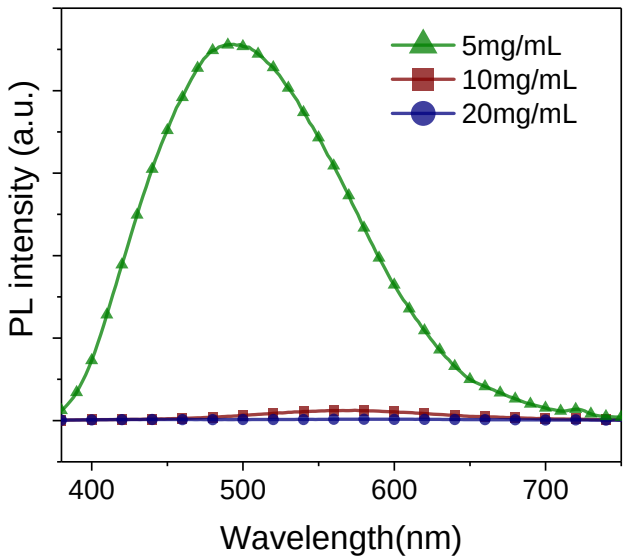

Figure 7. 11. Photoluminescence spectra of different CQDs concentrations deposit on top of a glass at λ_{exc}= 360 nm at room temperature.

Once established the optimal CQD_S concentration, 5 mg/mL, we prepared complete devices exploring different concentrations of the PVK layer. The quality of the layer of C-Dots onto ZnO/PEIE has been checked by AFM, observing the presence of aggregates that do not fully cover the layer underneath (See Annex). The deposition of PVK onto the C-Dots results in a homogeneous layer. The thickness of PVK was optimized because we observed that thicker PVK layer decreased the current density. (See Figure 7. 12 top)

In Table 7.3 appears the optoelectronic parameters of the QDLEDs. As can be seen, the turn-on voltage decreased from 12 V to 6 V modifying the thickness of PVK. Figure 7. 12 display the current density-luminance voltage characteristics of the QDLEDs changing the thickness of PVK. We observed that the thickness of the HTL was a key parameter to take into account, because the luminance increased drastically when the thickness of the PVK decreased. This happens because of the lower series resistance when using a thinner PVK layer that balances the charge injection from both electrodes. On the other hand, and as

we mentioned before, PVK was solved in chlorobenzene, where CQDs are soluble as well. This partial solubilization of the active layer can explain the high current densities observed in the devices. On the other hand, and as far as we know, the obtained current efficiency values are higher than those reported previously in quantum dot LEDs containing C-Dots as single emitter.

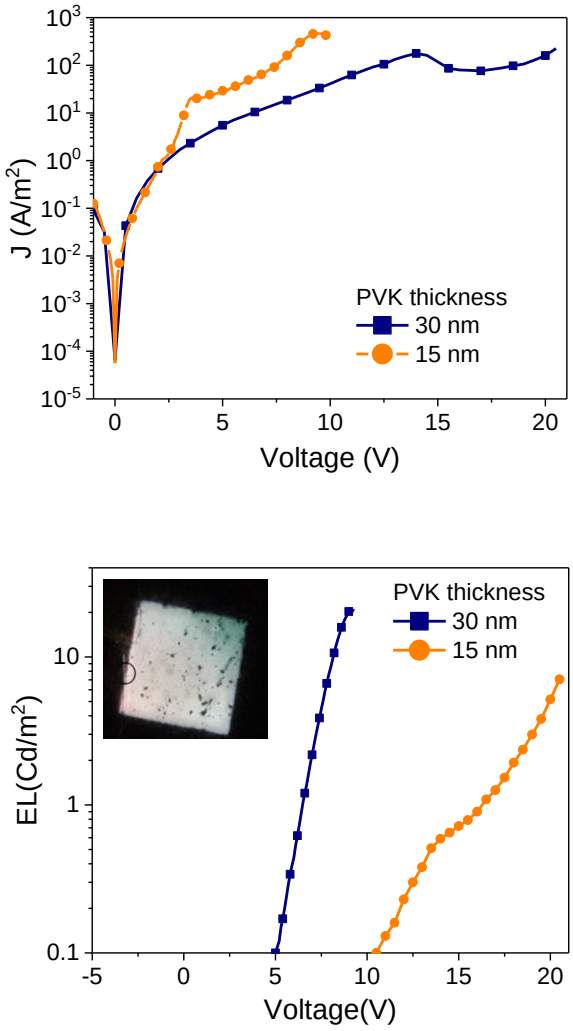

Figure 7. 12. Current density (top), luminance versus applied voltage (bottom) as a function of the thickness of the PVK layer. Inset picture of a QDLEDs using CQDs as emissive layer.

Table 7.3 Summary of the device performances. Von is the turn-on voltage at 0.1 Cd/m2.

device	PVK Thickness	Turn-on voltage V^{on} (V)	Max. Luminance (Cd/m^2)[a]	Current Efficiency (Cd/A)
1	30nm	10.5	7(6.5)	0.070
2	15mn	5	21(17)	0.060

[a]*The average Luminance reported in round brackets.*

Figure 7.13 shows the electroluminescence spectra (EL) of the as-prepared LEDs and the CIE color coordinates of (0.284, 0.291), which is close to the pure white light (0.33, 0.33). The emission encompass a broad range of wavelengths that result in white light emission. It is worth to mention that white light emitting diode are usually constructed by mixing nanoparticles emitting at different wavelengths Using these CQDs which present a broad emission band, we are able to obtain white light using just one type of nanoparticles.

The origin of the white color using an only emitter is still under discussion. For example, Wang and collaborators[37] reported that white light emission was associated with energy transfer among various emitting centers in the CQDs, corresponding to different energy transitions. As we mentioned before, two radiative mechanisms in the CQDs involving different energies: one originating in the core with slower lifetime and a second process that is faster and originates in the surface of CQDs.

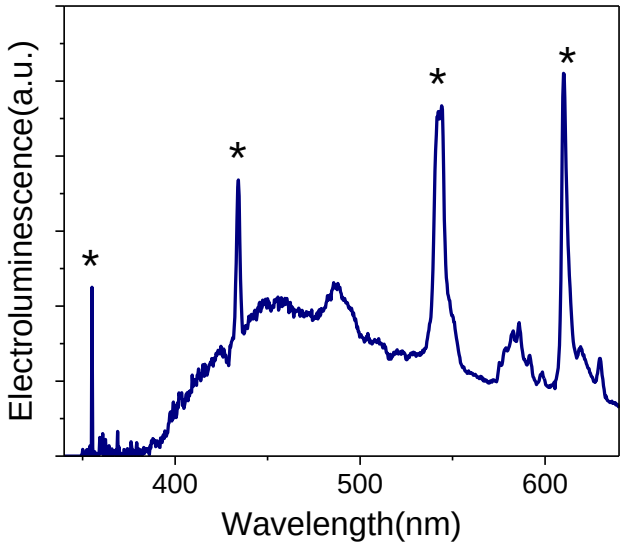

Figure 7. 13. Electroluminescence of ITO/ZnO:PEIE/CQDs/PVK/MoO_3/Au at room temperature. The stars points noisy peaks during the measurement.

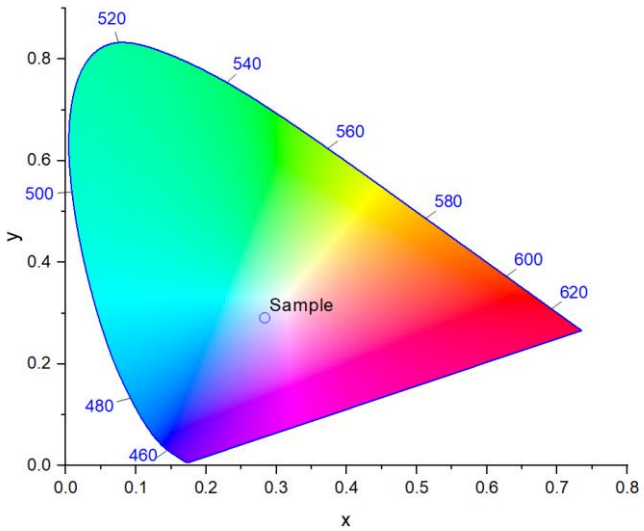

Figure 7. 14. CIE color coordinates of QLEDs with CQDs as emissive layer.

Figure 7.15 shows different pictures taken while the applied voltage increased. It can be seen a shift color from green to white while the applied voltage increased. As previously mentioned, the photoluminescence decay can be fitted in a biexponential curve, concluding that two radiative mechanism happens inside the CQDs. Furthermore, there is a change in the color emission and intensity of the devices when the injection current increases. This means that the injection current controls the activation of the two radiative process that happen inside the CQDS. The combined emission from different energy states results in white light emission at an adequate current injection.

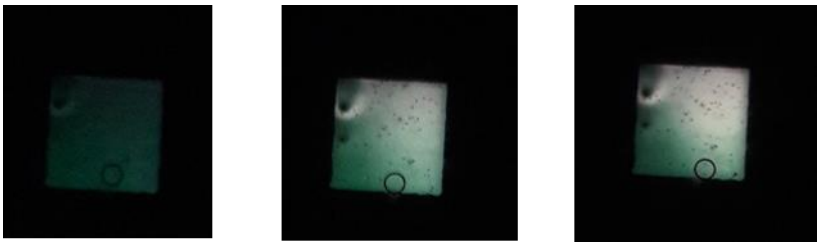

Figure 7. 15. Light emission at different applying voltages from the same device (from 4 V to 7 V).

To confirm that CQDs were responsible of the white light emission together with PVK, we fabricated a LEDs without CQDs. Figure 7.16 shows an example with the structure glass/ITO/ZnO:PEIE/PVK/MoO_3/Au and the picture inside shows that a diode emitted in a violet color. We used the same spin coating conditions to deposit PVK in order to obtain 30 nm of thickness. The turn on voltage was 11.2 V and the maximum of luminance was 2 Cd/m^2. The higher turn-on voltage and the lower current density reflected the higher resistance in the device. The efficiency using PVK as emissive layer was too low because the device fabrications conditions were optimized to work with the final structure: ITO/ZnO:PEIE/CQDs/PVK/MoO_3/Au. With these results, our hypothesis is confirmed, and to obtain white light emission, both PVK and CQDs were needed.

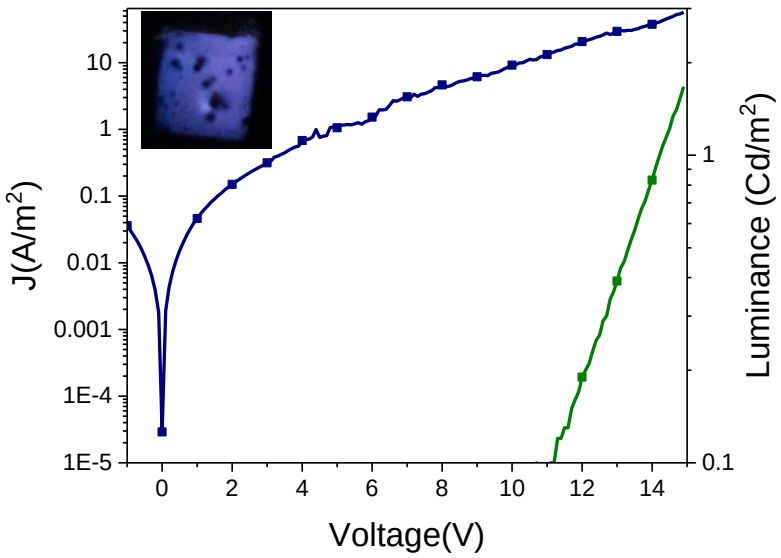

Figure 7. 16. Current density (blue line) and luminance (green line) versus applied voltage of the HyLED made without CQDs. Inset: HyLED using PVK as emissive layer.

To end up this chapter, in the Annex 7.7, there are three examples of diodes measured three times with a difference of 2 minutes to check if the luminance is still constant. We observed that our devices were not stable and after few voltage scans their luminance decreased.

7.5 Conclusions.

In summary, the synthesis of carbon dots has been achieved using a bottom up process using citric acid as carbon source and 1-hexadecylamine as capping ligand. The characterization of the optical and electrochemical characteristics indicate that the nanoparticles are great candidates to be used as active layer in optoelectronic devices.

In this work, we have demonstrated their applicability as a unique emissive layer to obtain white light emission without the needed to mix blue, green and red quantum dots, which is a great advantage as simplifies further the device multilayer structure. It must be noticed that this preliminary results require further optimization of the devices in order to reduce the high current density values of the devices provoked by an unbalanced charge injection; Also a further optimization of the CQDs production protocols will be needed to maximize their quantum yield, being both parameters essentials to obtain outstanding QDLEDs performances.

Finally, to our knowledge, this is the first example of such device architecture that includes carbon dots in the emissive layer. Taking into account the lack of toxic elements, the green chemistry procedure for their synthesis and the easy-to-make device fabrication by solution processing (spin coating) under air conditions, highlighting the potential of the method to be up-scaled in roll-to-roll devices.

7.6 References

1. X. Liang, S. Bai, X. Wang, et al. Colloidal metal oxide nanocrystals as charge transporting layers for solution-processed light-emitting diodes and solar cells. *Chem. Soc. Rev.* **2017**, 46 (6), 1730–1759.
2. X. Dai, Y. Deng, X. Peng, Y. Jin. Quantum-Dot Light-Emitting Diodes for Large-Area Displays: Towards the Dawn of Commercialization. *Adv. Mater.* **2017**, 29 (14), 1607022.
3. J. Albero, J.N. Clifford, E. Palomares. Quantum dot based molecular solar cells. *Coord. Chem. Rev.* **2014**, 263-264, 53–64.
4. A.P. Litvin, I. V Martynenko, F. Purcell-Milton, et al. Colloidal quantum dots for optoelectronics. *J. Mater. Chem. A* **2017**, 5 (26), 13252–13275.
5. Y. Jiang, S.-Y. Cho, M. Shim. Light-emitting diodes of colloidal quantum dots and nanorod heterostructures for future emissive displays. *J. Mater. Chem. C* **2018**, 6 (11), 2618–2634.
6. B. Han, B. Cai, Q. Shan, et al. Stable, Efficient Red Perovskite Light-Emitting Diodes by (α, δ)-CsPbI3 Phase Engineering. *Adv. Funct. Mater.* **2018**, 28 (0), 1804285.
7. Y. Ling, Y. Tian, X. Wang, et al. Enhanced Optical and Electrical Properties of Polymer-Assisted All-Inorganic Perovskites for Light-Emitting Diodes. *Adv. Mater.* **2016**, 28 (40), 8983–8989.
8. B.C. Hames, I. Mora-Seró, R.S. Sánchez. Device performance and light characteristics stability of quantum-dot-based white-light-emitting diodes. *Nano Res.* **2018**, 11 (3), 1575–1588.
9. L. Zhang, X. Yang, Q. Jiang, et al. Ultra-bright and highly efficient inorganic based perovskite light-emitting diodes. *Nat. Commun.* **2017**, 8, 15640.
10. Q. Lin, L. Wang, Z. Li, et al. Nonblinking Quantum-Dot-Based Blue Light-Emitting Diodes with High Efficiency and a Balanced Charge-Injection Process. *ACS Photonics* **2018**, 5 (3), 939–946.
11. Y. Shang, Z. Ning. Colloidal quantum-dots surface and device structure engineering for high-performance light-emitting diodes. *Natl. Sci. Rev.*

2017, 4 (2), 170–183.

12. T.T. Meiling, P.J. Cywiński, I. Bald. White carbon: Fluorescent carbon nanoparticles with tunable quantum yield in a reproducible green synthesis. *Sci. Rep.* **2016**, 6 (February), 28557.
13. H. Liu, L. Zhang, M. Yan, J. Yu. Carbon nanostructures in biology and medicine. *J. Mater. Chem. B* **2017**, 5 (32), 6437–6450.
14. F.R. Baptista, S.A. Belhout, S. Giordani, S.J. Quinn. Recent developments in carbon nanomaterial sensors. *Chem. Soc. Rev.* **2015**, 44 (13), 4433–4453.
15. F. Li, X.-H. Yu, F.-Y. Kong, Z.-X. Wang, W. Wang. Incorporating doped carbon nanodots and metal ions as an excellent artificial peroxidase for H2O2 detection. *RSC Adv.* **2017**, 7 (50), 31281–31286.
16. S. Paulo, G. Stoica, W. Cambarau, E. Martinez-Ferrero, E. Palomares. Carbon quantum dots as new hole transport material for perovskite solar cells. *Synth. Met.* **2016**, 222 (Part A), 17–22.
17. J. Xu, Y. Miao, J. Zheng, et al. Carbon dot-based white and yellow electroluminescent light emitting diodes with a record-breaking brightness. *Nanoscale* **2018**, 10 (23), 11211–11221.
18. A. Das, V. Gude, D. Roy, et al. On the Molecular Origin of Photoluminescence of Nonblinking Carbon Dot. *J. Phys. Chem. C* **2017**, 121 (17), 9634–9641.
19. F. Yuan, Z. Wang, X. Li, et al. Bright Multicolor Bandgap Fluorescent Carbon Quantum Dots for Electroluminescent Light-Emitting Diodes. *Adv. Mater.* **2017**, 29 (3), 1604436 – n/a.
20. S. Zhu, Y. Song, X. Zhao, et al. The photoluminescence mechanism in carbon dots (graphene quantum dots, carbon nanodots, and polymer dots): current state and future perspective. *Nano Res.* **2015**, 8 (2), 355–381.
21. F. Wang, Y. Chen, C. Liu, D. Ma. White light-emitting devices based on carbon dots' electroluminescence. *Chem. Commun.* **2011**, 47 (12), 3502–3504.
22. X.Y. Zhang, Y. Zhang, Y. Wang, et al. Color-Switchable

Electroluminescence of Carbon Dot Light-Emitting Diodes. *ACS Nano* **2013**, 7 (12), 11234–11241.

23. F. Zhang, X. Feng, Y. Zhang, et al. Photoluminescent carbon quantum dots as a directly film-forming phosphor towards white LEDs. *Nanoscale* **2016**, 8 (16), 8618–8632.
24. X.T. Feng, F. Zhang, Y.L. Wang, et al. Luminescent carbon quantum dots with high quantum yield as a single white converter for white light emitting diodes. *Appl. Phys. Lett.* **2015**, 107 (21), 1–6.
25. F. Wang, S. Pang, L. Wang, et al. One-Step Synthesis of Highly Luminescent Carbon Dots in Noncoordinating Solvents. *Chem. Mater.* **2010**, 22 (16), 4528–4530.
26. V. Gude, A. Das, T. Chatterjee, P.K. Mandal. Molecular origin of photoluminescence of carbon dots: aggregation-induced orange-red emission. *Phys. Chem. Chem. Phys.* **2016**, 18 (40), 28274–28280.
27. Z. Jiang, M.J. Krysmann, A. Kelarakis, et al. Understanding the Photoluminescence Mechanism of Carbon Dots. *MRS Adv.* **2017**, 2 (51), 2927–2934.
28. S. Hu, X. Meng, F. Tian, et al. Dual photoluminescence centers from inorganic-salt-functionalized carbon dots for ratiometric pH sensing. *J. Mater. Chem. C* **2017**, 5 (38), 9849–9853.
29. D. Chen, H. Gao, X. Chen, et al. Excitation-Independent Dual-Color Carbon Dots: Surface-State Controlling and Solid-State Lighting. *ACS Photonics* **2017**, 4 (9), 2352–2358.
30. H. Nie, M. Li, Q. Li, et al. Carbon Dots with Continuously Tunable Full-Color Emission and Their Application in Ratiometric pH Sensing. *Chem. Mater.* **2014**, 26 (10), 3104–3112.
31. Y. Ding, F. Zhang, J. Xu, et al. Synthesis of short-chain passivated carbon quantum dots as the light emitting layer towards electroluminescence. *RSC Adv.* **2017**, 7 (46), 28754–28762.
32. C.K. Frederik, T. Yi, T. Ralf, W.A. Jens. A simple nanostructured polymer/ZnO hybrid solar cell—preparation and operation in air. *Nanotechnology* **2008**, 19 (42), 424013.

33. D.I. Son, H.H. Kim, D.K. Hwang, S. Kwon, W.K. Choi. Inverted CdSe-ZnS quantum dots light-emitting diode using low-work function organic material polyethylenimine ethoxylated. *J. Mater. Chem. C* **2014**, 2 (3), 510–514.
34. C. Fan, Y.Y. Lei, Z. Liu, et al. High-Efficiency Phosphorescent Hybrid Organic–Inorganic Light-Emitting Diodes Using a Solution-Processed Small-Molecule Emissive Layer. *ACS Appl. Mater. Interfaces* **2015**, 7 (37), 20769–20778.
35. H.H. Kim, S. Park, Y. Yi, et al. Inverted Quantum Dot Light Emitting Diodes using Polyethylenimine ethoxylated modified ZnO. *Sci. Rep.* **2015**, 5, 8968.
36. Y.R. Park, H.Y. Jeong, Y.S. Seo, W.K. Choi, Y.J. Hong. Quantum-Dot Light-Emitting Diodes with Nitrogen-Doped Carbon Nanodot Hole Transport and Electronic Energy Transfer Layer. *Sci. Rep.* **2017**, 7, 46422.
37. F. Wang, S. Pang, L. Wang, et al. One-Step Synthesis of Highly Luminescent Carbon Dots in Noncoordinating Solvents. *Chem. Mater.* **2010**, 22 (16), 4528–4530.

A7 Annex

A7.1 Quantum yield

The quantum yield of CQDs was calculated using Couramine 102 as reference dye.

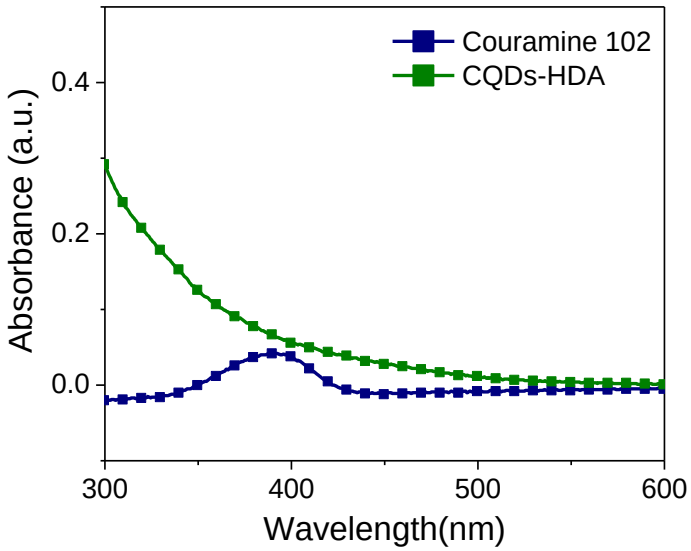

Figure A7. 1. Absorbance spectra of CQDs-HDA (green line) and Couramine 102 (blue line) at room temperature.

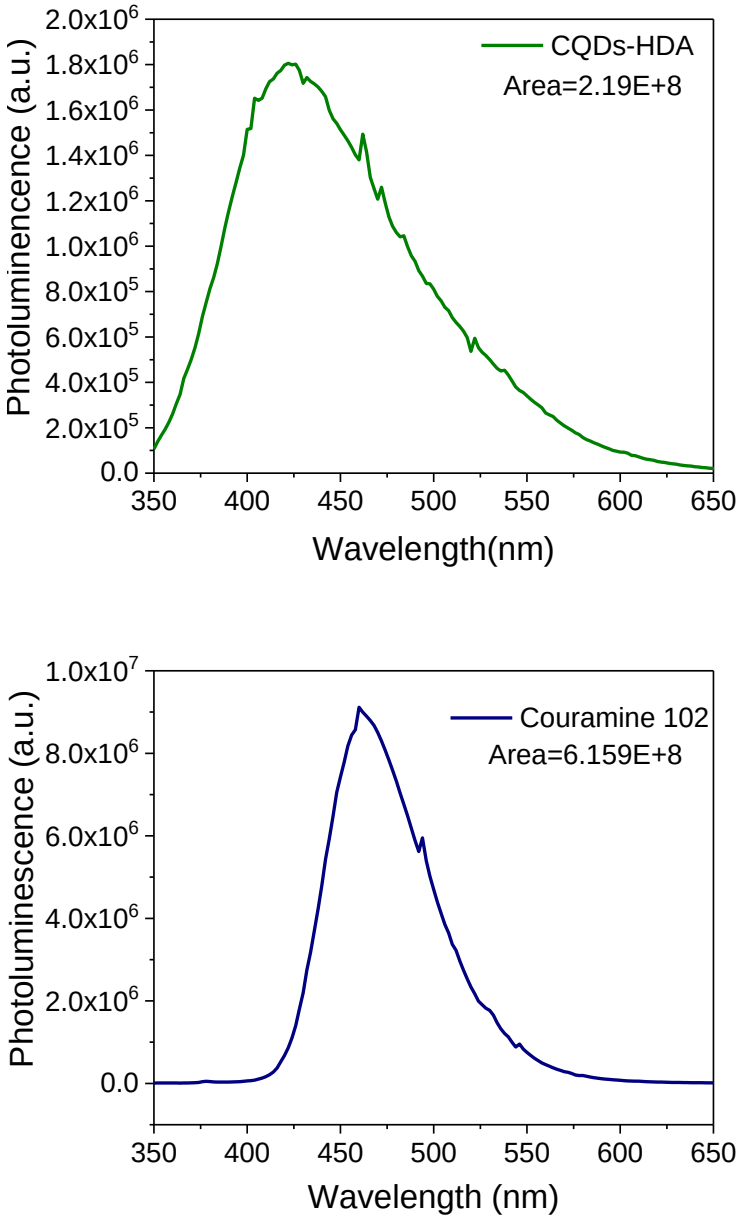

Figure A7. 2. Emission spectra of CQDs-HDA (top) and Couramine 102 (bottom) measured at λ_{exc}=340nm at room temperature.

The calculation was done using the following equation:

$$QY = QY_{ref}\left(\frac{I_{em\,sample}}{I_{em\,ref}}\right)\cdot\left(\frac{Abs_{ref}}{Abs_{sample}}\right)\cdot\left(\frac{n_{sample}}{n_{ref}}\right)^2 \quad \text{Equation A7.1}$$

Where QY_{ref} is the reference quantum yield, I_{em} is the area of the emission band, Abs is the absorbance excitation wavelength and η is the refractive index.

A7.2 AFM images.

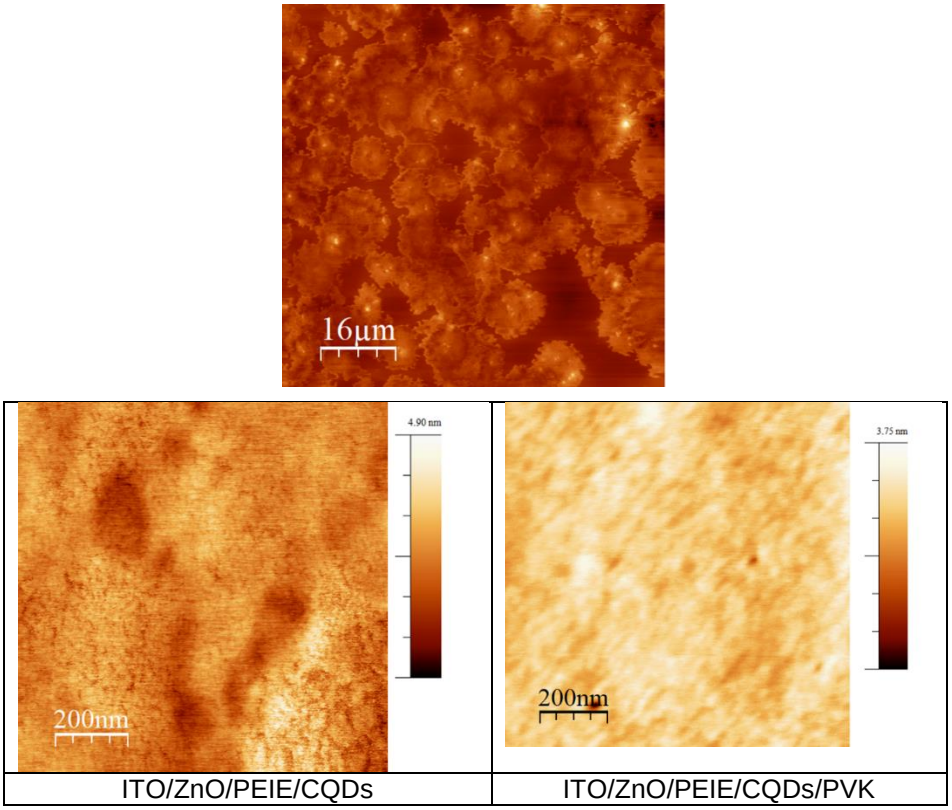

Figure A7.3. AFM images of the layers formed by (up) C-Dots onto ITO/ZnO/PEIE (phase), and (down) comparison of the morphology of the ITO/ZnO/PEIE/C-Dot layer with the PVK onto ITO/ZnO/PEIE/C-Dots at the same magnification scale.

A7.3 Diodes.

Three different diodes were measured every two minutes to check their lifetime and quality of the light emission. As can be seen in the following images, the emission intensity was not constant and after 24 hours we did not observe any light emission.

In general, we observe that the first measurement gives lower turn-on voltages and higher luminance. After some measurements, the turn-on voltage increased although the luminance decreased. The variation of the current density with applied voltage follow the same trend regardless of the experiment.

Sample 1

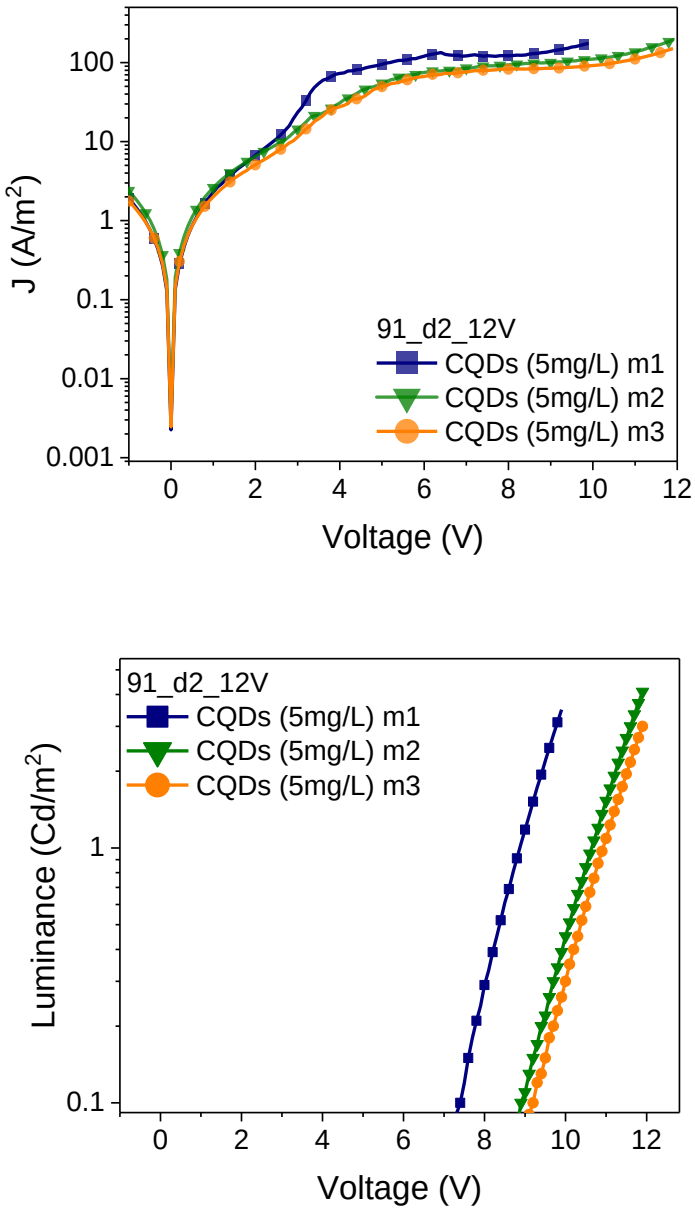

Figure A7. 4. Current density (Top) luminance versus applied voltage (bottom). The diode was measured three times with a difference of 2min between each measurement.

Sample 2

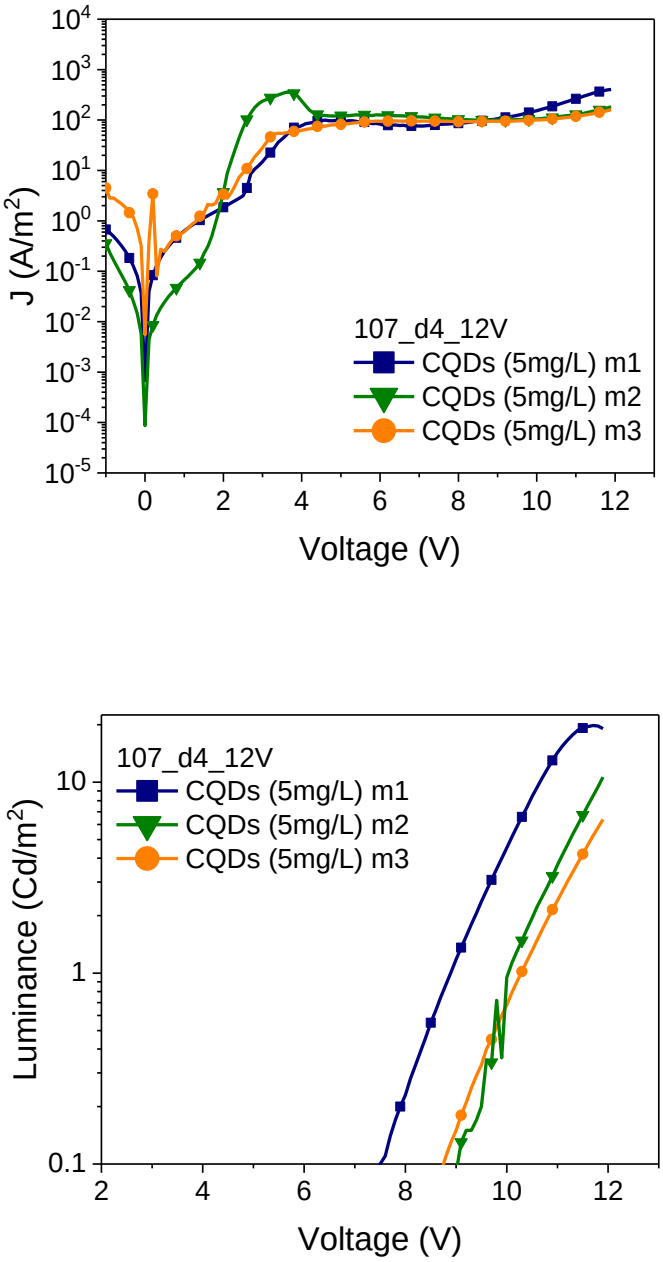

Figure A7. 5. Current density (Top) luminance versus applied voltage (bottom)The diode was measured three times with a difference of 2min between each measurement.

Sample 3

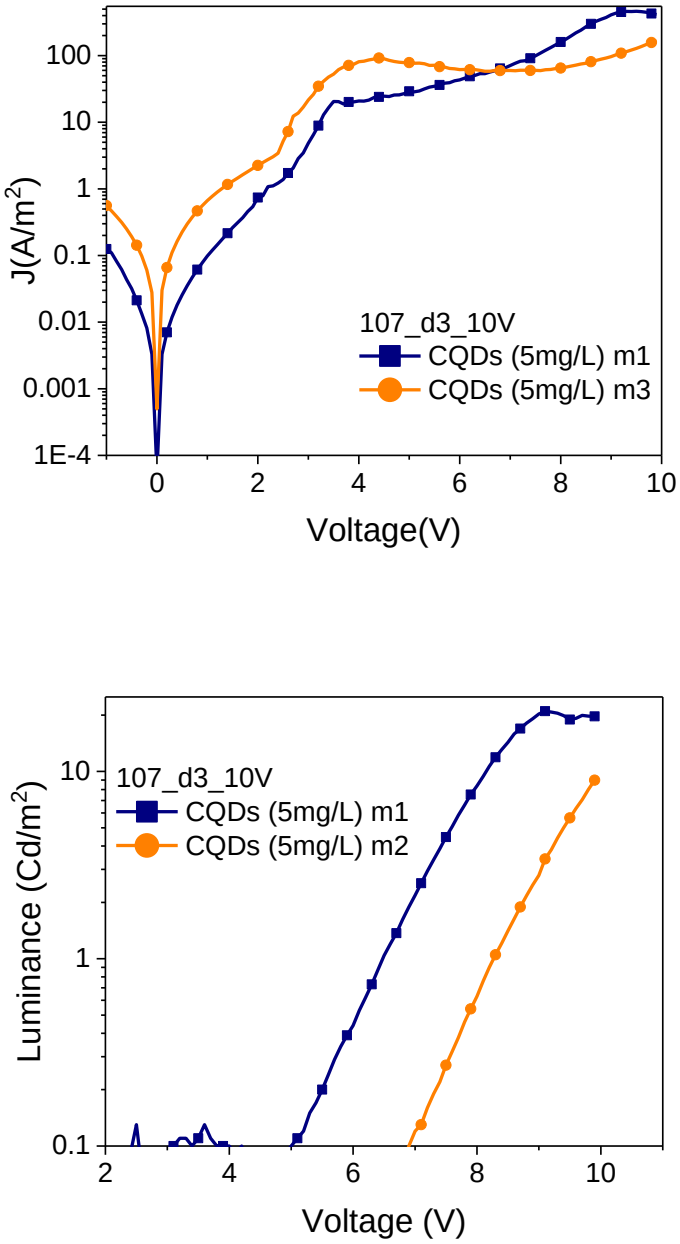

Figure A7. 6. Current density (Top) luminance versus applied voltage (bottom)The diode was measured three times with a difference of 2min between each measurement.

8

Carbon Quantum Dots as selective contact for LEDs.

SS AND MoO3.In this chapter, the results of the application of Carbon Quantum dots using different capping ligands as hole transport material in LEDs are shown. The performance of CQDs is compared to that of the two most widely used hole transport layer (HTL), PEDOT:P

Chapter 8

Table of Contents

Chapter 8

8.1 Introduction

As we mentioned in Chapter 7, Carbon quantum dots (CQDs) have emerged as alternative novel materials to heavy metal based quantum dots for optoelectronic applications and bioapplications [1,2]. In this chapter, we show the results of using CQDs as hole selective contact in HyLEDs.

The most studied applications of CQDs have been as emissive layers, due to their luminance properties, in light-emitting diodes (LEDs). For instance, Yuan et al. published the synthesis of CQDs emitting from blue to red to fabricate different light-emitting diode (LEDs)[3]. Zhu et al. reported the synthesis of blue, green and red CQDs to obtain white light emitting diodes using composite films with polyvinylpyrrolidone[4].

On the other hand, due to their good carrier mobility values, some authors have reported the use of carbon quantum dots as interlayer in LEDs [5 6]. For instance, Park et al. deposited a thin layer of Nitrogen-Doped Carbon dots to augment the carrier injection from the hole transport layer to the emissive layer. They deposited a thin layer between PVK (hole transport layer) and the CdSe/CdZnS QDs (Emissive layer). They showed that the current density increased, improving the luminescence of the QD layer [7]. Know et al. described the synthesis and application of CQDs capped with different ligands as transport layers in transistors relating their charge mobilities to the chain length of the CQDs surface ligands [8].

Our aim in this chapter is to test the CQDs as hole transport layer in hybrid light emitting diodes (HyLEDs), taking into account their great carrier mobility, the solution processability and the versatility of the CQDs. In order to check their performance, we have compared these new material based on carbon with two of the most widely used hole transport layer (HTL): (1) poly(3,4-ethylenedioxythiophene): poly(styrene sulfonate) PEDOT:PSS, which is solution processed, and (2) MoO_3 which can be either evaporated or processed by solution.

In the case of MoO_3, there are many papers describing their strong p-type character and their beneficial influence in the performance of HyLEDs[9]. However, the nanoparticles of MoO_3 require high annealing temperatures when they are deposited by solution-processing to achieve good charge transport properties. For example, Girotto et al. reported a solution processed MoO_3 to use as HTL in organic solar cell. They studied the relation between the annealed temperature and the power conversion efficiency PCE (%), concluding that the optimal temperature to treat solution-processed MoO_3 was 275 ºC [10].

On the other hand, PEDOT:PSS is the most used HTL in optoelectronic devices because of its good chemical and physical properties such as high transparency, smooth surface morphology, thermal stability, water solubility and solution processability, making this polymer widely popular in solution processed optoelectronic devices[11] [12]. Nevertheless, PEDOT:PSS presents two main drawbacks: 1) their acidic nature that may decrease the stability of the device and 2) depending on the device structure, the current injection from the cathode and anode may unbalance. One of the solution that some groups have been working with is to dope PEDOT:PSS in order to modify its work function to help the carrier injection. For instance, Song et al. doped PEDOT:PSS with graphite oxide to improve the charge injection balance[13]. Other examples have been reported about doping PEDOT:PSS with metals, such as gold, to increase the hole injection and as consequence the External quantum Efficiency (EQE)[14].

In this chapter, we report the tests with CQDs in order to expand the research into new materials for HTL that fulfill the requirements discussed above such as good hole injection balance, lower annealing temperature, environmentally friendly processing, and easy processability. In addition, it is a material with a great scalability potential in terms of synthesis and deposition as they can be adapted to be deposited via inkjet printing and roll-to-roll techniques.

We have prepared different sets of carbon quantum dots with capping ligands of different nature: urea, ethylendiamine, *p*-phenyldimamine and 1-hexadecylamine (HDA). Surface ligands are an essential component of Quantum Dots since variations in the ligand affect QDs aggregation, shape and size. In addition, the surface ligands decrease the number of defects once deposited forming the HTL, improving the optoelectronic properties of the materials.[15] [16].

For this study we fabricated an inverted hybrid light emitting diodes using ZnO nanoparticles (NPs) as electron transport layer, F8BT (poly(9,9-dioctylfluorene-alt-benzothiadiazole) as emissive layer and evaporated metal electrodes. ZnO NPs are used due to their easy synthesis, formation of transparent films and good electron mobility. F8BT is a widely used polymer emitting in the yellow-green region with an emission band at 550 nm (Figure 8.1). The annealing temperature of F8BT is 155 ºC, which is the transition temperature from the glassy to the rubbery state reported in the bibliography[17]. The metal electrode was gold, which is inert in air and permit the performance of the device without encapsulation or with the use of mild protecting layers.

a) b)

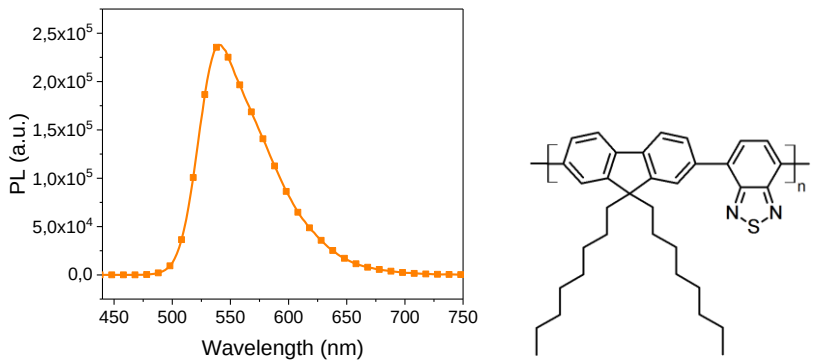

Figure 8. 1. a) Photoluminescence emission spectra of F8BT and b) its molecular structure.

8.2 Material Synthesis and characterization.

The synthesis and characterization of ZnO NPs were described in **Chapter 3**.

8.2.1 Synthesis of Carbon based quantum dots.

Two approaches for the synthesis of CQDs have been followed: hydrothermal and hot injection method. As we mentioned in the **Chapter 1** both methods are bottom up procedures to obtain CQDs. The selection of the approach depends on the capping ligand and the synthesis's temperature.

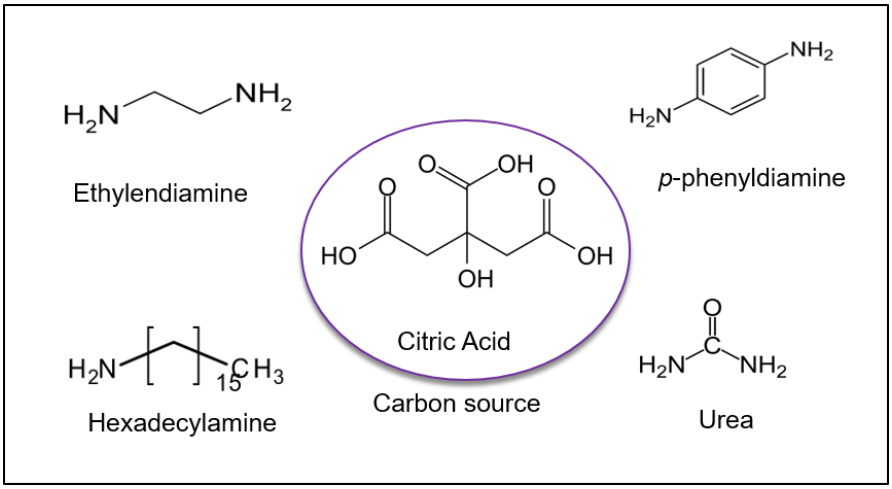

Figure 8. 2. Molecular structures of the reactants and capping ligands used to synthetize the CQDs.

8.2.1.2 Hydrothermal approach

Briefly, 1.051g of citric acid, and 0.541 g of *p*-phenyldiamine [18] or 335 µL of ethylendiamine [19], depending on the desired capping ligand, were dissolved in 10 mL H_2O. The solution was transferred to a poly-(tetrafluoroethylene) Teflon-lined autoclave (120 mL) and heated at 200 ºC for 5 h with a ramp 5 ºC/min. After the reaction, we obtained a brown-black solution. Then, the solution was

centrifuged to remove the largest particles at 4500 RPM. Finally, CQDs were dispersed in water.

To synthetize CQDs using urea as capping ligand, [20] 1.051 g of citric acid and 2 g of urea were solved in 10mL of dimethylformamide (DMF). The solution was transferred to a poly (tetrafluoroethylene) Teflon-lined autoclave (120 mL) and heated at 160 ºC for 16 h. The reaction was centrifuged, and washed three times at 4500 RPM with a mixture of ether/ethylacetate (1:4). The final solution was solved in ethanol 50 mg/mL.

8.2.1.3 Hot injection approach

The synthesis of carbon quantum dots was carried out according to the method reported by Fu Wang *et al*.[21] 15mL of 1-octadecene (ODE) and 1.5 g of 1-hexadecylamine (HDA) were stirred in a three neck flask under inert conditions during 30 min at room temperature. Then, the solution was heated up to 300 ºC. At this temperature, 1 g of citric acid was added as quickly as possible and the solution was stirred during 3 hours. Once the solution was cooled down at room temperature, acetone was added to precipitate the carbon quantum dots and centrifuged 4500 RPM during 20 min. Then, the supernatant was discarded and the solid was washed three times with toluene. The CQDs were dispersed in hexane.

8.3 Device fabrication.

Patterned ITO (Indium doped Tin Oxide) coated glasses (Xinyan Technology, resistance 10 Ω/square, 15x15 mm) were washed once with acetone and twice in isopropanol. ZnO NPs were spin coated onto ITO at 5000 RPM 1min, followed by annealing at 150 ºC during 3 hours. Then, F8BT (30 mg/mL *p*-xylene) was deposited on top of the zinc oxide at 2000 RPM during 1 min followed by baking at 155 ºC during 30 min. The different CQDs and PEDOT:PSS were deposited on top of the F8BT using the following spin coating conditions and annealing temperature:

- PEDOT:PSS (1:6, H_2O/IPA) Clevious P VP Al 4083 v=3000 RPM; t=30 seg ; 120 ºC 15 min
- CQDs-*p*-phenyldiamine (20 mg/mL) (2:1) (H_2O/IPA) v=2000 RPM; t=30 seg ; 120 ºC 30 min.
- CQDs-ethylendiamine (20 mg/mL) (2:1) (H_2O/IPA) v=2000 RPM; t=30 seg ; 120ºC 30 min.
- CQDs-hexadecylamine (20 mg/mL) (hexane) v= 2000 RPM ; t=30 seg ; 120 ºC 30min.
- CQDs-urea (20 mg/mL) (2:1) (H_2O/IPA) v=2000 RPM; t=30 seg; 120 ºC 30 min.
- MoO_3 (15 nm) was thermally evaporated on top of F8BT.

Finally, a layer of 100 nm of gold was thermally evaporated under high vacuum ($1 \cdot 10^{-6}$ bar) on top of the HTL defining an active area of 9 mm^2. Figure 8.3 shows the final device structure and the thickness of each layer. These values were measured with a profilometer as explained in **Chapter 3**.

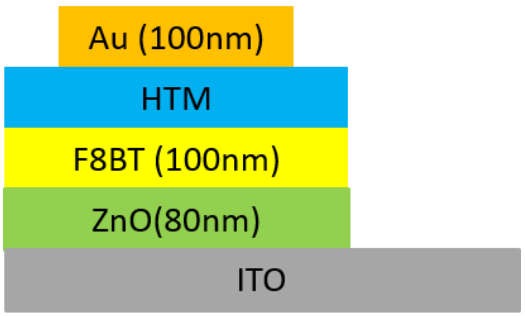

Figure 8. 3. Description of a multilayer LED indicating the thickness of each layer.

8.4 Results and discussion.

This section describes the characterization of the Carbon Quantum Dots, the thin films and the complete devices.

8.4.1 Structural characterization of CQDs.

The surface and structural composition of CQDs was studied by FT-IR. The size and shape of CQDs were investigated by Transmission electron microscopy (TEM) and Dynamic Light Scattering (DLS). The average size between TEM images and DLS can differ because the DLS cannot distinguish between a large particle or an aggregation and the size of the CQDs are in the quantification limit of the DLS. The DLS measurement was recorded by intensity and by volume. In the first one, the intensity of the population depends on the number of particle with similar size in the sample, and the second one depends on the space that a nanoparticle takes up. As a preliminary conclusion, it is clear that the purification is the bottleneck during the synthesis of CQDs because all of them present larger particles in solution. However, those particles were not the majority and when the graph is measured by volume the largest particles were not listed.

a) CQDs-HDA.

The FT-IR analysis of CQDs passivated with 1-hexadecylamine was performed at room temperature. Figure 8.4 shows the FT-IR spectrum which presents two stretching bands at 1500-1600 cm^{-1} corresponding to C=C and C=N vibration. The two stretching bands at 2900 and 2800 cm^{-1} belong to C-H vibration.

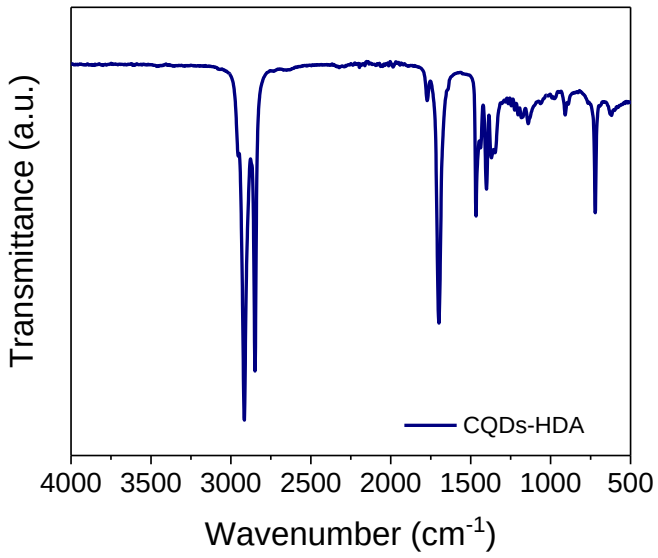

Figure 8. 4. FT-IR spectrum of CQDs-HDA.

We performed dynamic light scattering to measure the average particle size. (Figure 8.5). The sample was measured two times (red and green line), and both graphs displayed the average size distribution by intensity and by volume. In the first case, we observed that the particle size is 1 nm, 100 nm and 900 nm of average. We did not observe the same in DLS by volume, because those larger particles were minority in the sample. The particles size of 1 nm can be attributed to the presence of CQDs in the solution.

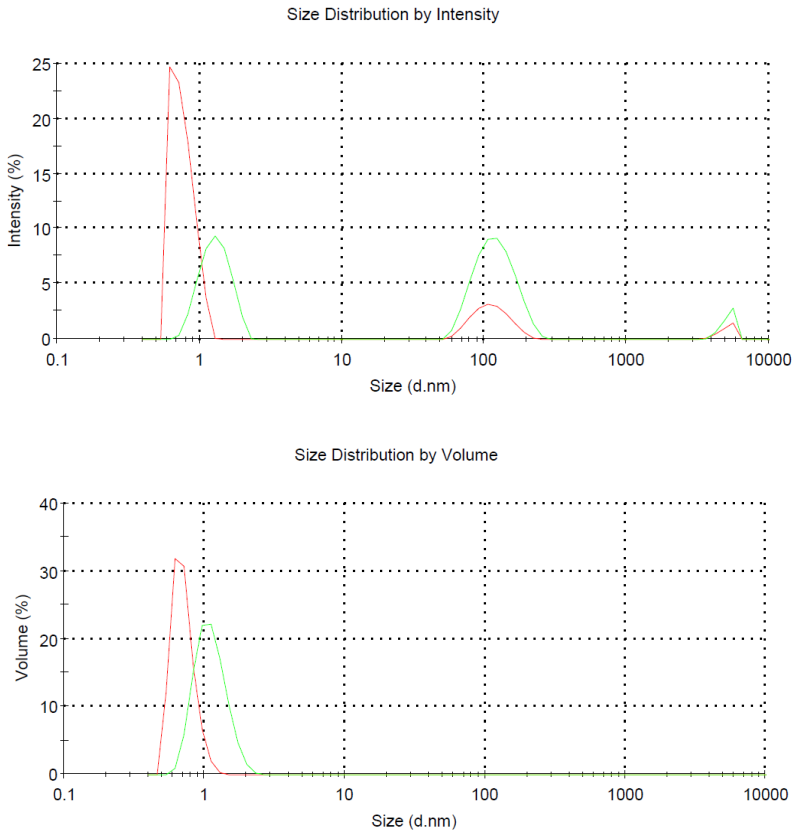

Figure 8. 5. DLS signal of CQDs-HDA. Size distribution by intensity (top) and by volume (bottom).

Transmission electron spectroscopy (TEM) image shows CQDs of 3.6 ± 0.6 nm. (Figure 8.6).

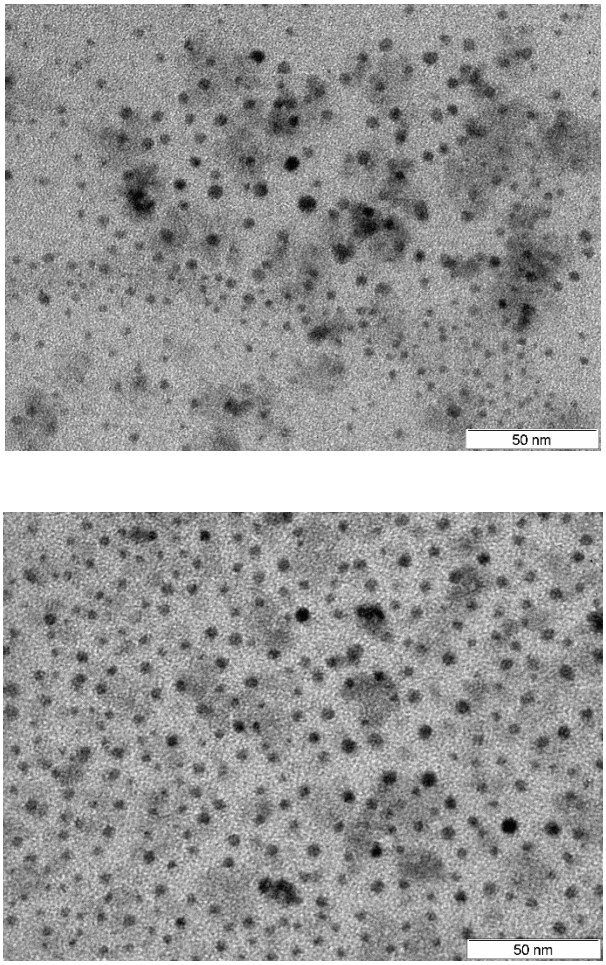

Figure 8. 6. TEM images of CQDs-HDA at different magnifications. The average size was 3.6 ± 0.6 nm.

b) CQDs-urea.

The FT-IR analysis of CQDs passivated with urea was performed at room temperature. Figure 8.7 shows the FT-IR spectrum which present stretching band at 3250 cm^{-1} corresponding to –N-H vibration, vibration of –OH at 3410 cm^{-1} and C=C at 1600 cm^{-1}.

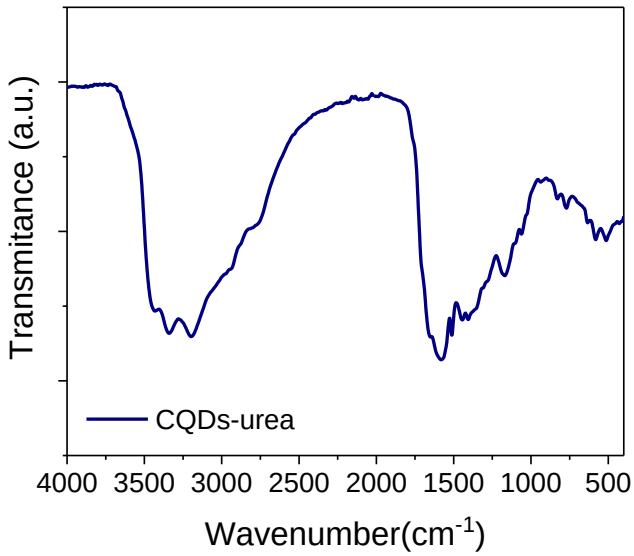

Figure 8. 7. FT-IR spectrum of CQDs-Urea.

Figure 8.8 shows the CQDs-urea DLS. The sample was measured twice (red and green line) and the measurements were done with the same solution at different times. This can modify the final profile graph because when the laser passes through the sample, the laser does not to interact with the same particles. We observed the same large particles that in the previous case, although those particles were not the majority because in the second graph they did not appear. The average size of CQDs-urea was estimated at 5 nm.

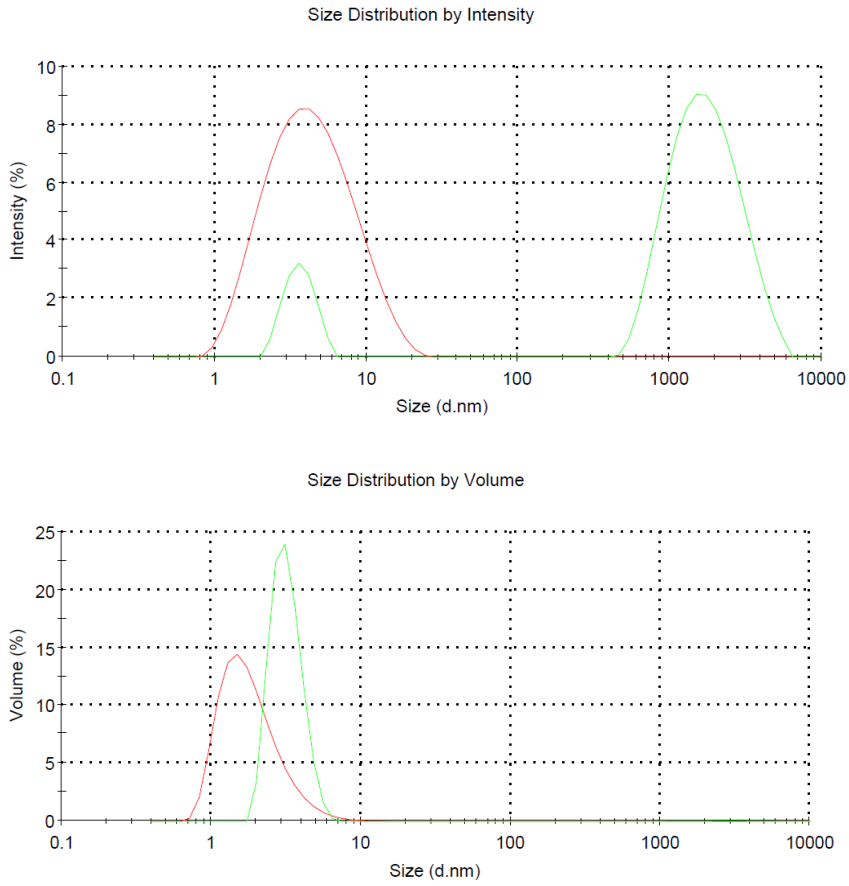

Figure 8. 8. DLS signal of CQDs-urea. Size distribution by intensity (top) and by volume (bottom).

Figure 8.9 displays the average size of CQDs-urea measured by TEM: 45.7 ± 13.6 and 5.4 ± 1.0 nm. We observed large particle meaning that the CQDs tends to aggregate.

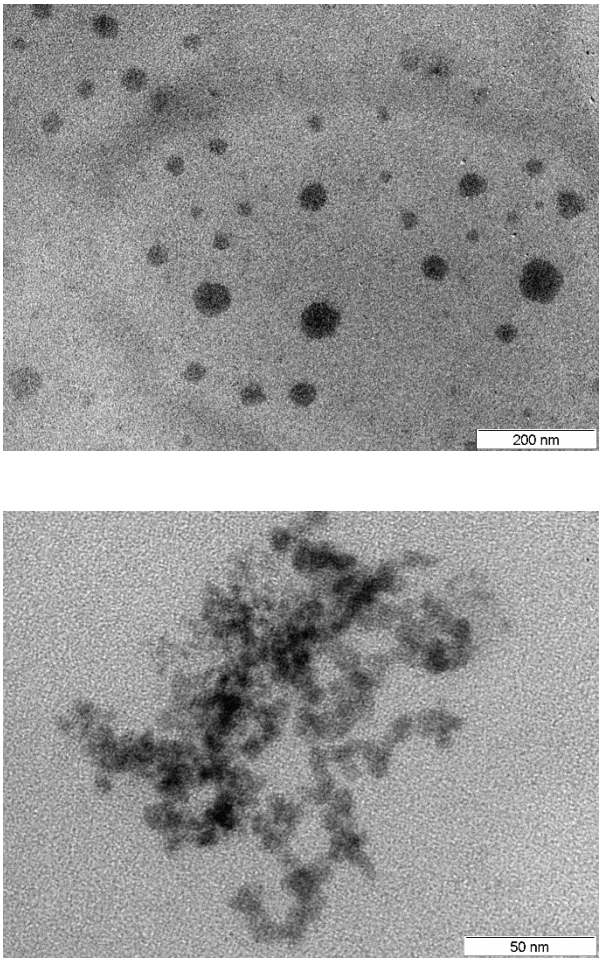

Figure 8. 9. TEM images of CQDs-urea at different magnifications.

c) CQDs-Ethylendiamine.

The FT-IR analysis of CQDs passivated with ethylendiamine was performed at room temperature. Figure 8.10 shows the FT-IR spectrum which present a stretching band at 3250 cm^{-1} corresponding to –N-H vibration, a stretching band at 410 cm^{-1} which corresponds to the -OH ,the vibration of C=C at 1600 cm^{-1} and C=O at 1500 cm^{-1}.

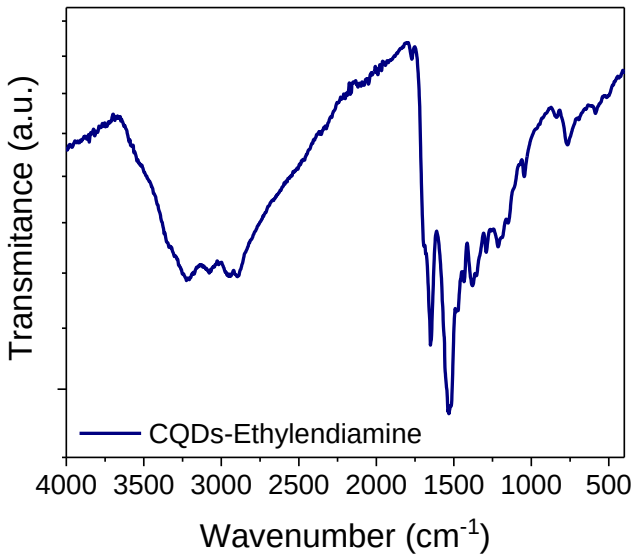

Figure 8.10. FT-IR spectrum of CQDs-Ethylendiamine.

We performed dynamic light scattering to measure the average particle size. (Figure 8.11). It was measured twice (red and green line), and both graph displayed the average size distribution by intensity and by volume. In the first case, we observed some aggregates with a size of 100 nm and 900 nm. We did not observe the same in DLS by volume because those larger particles are minority. The average particle size was 9 nm. As we mentioned, there may be a difference between the TEM analysis and DLS because the size of CQDs are in the quantification limit of the instrument.

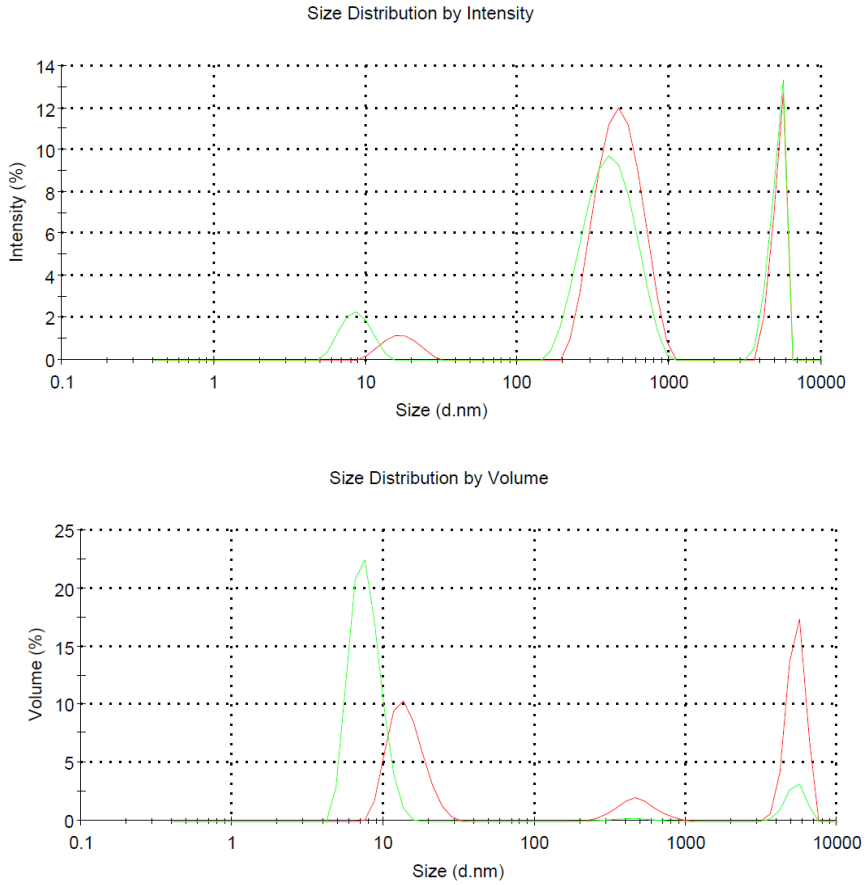

Figure 8. 11. DLS signal of CQDs-ethylendiamine. Size distribution by intensity (top) and by volume (bottom).

Figure 8.12 shows the TEM image of CQDs-ethylendiamine. We observed some particles bigger than 10 nm because we cannot control the growth of the particles. The average size of CQDs-urea was 23.9 ± 5.8nm and 3.3 ± 0.70nm.

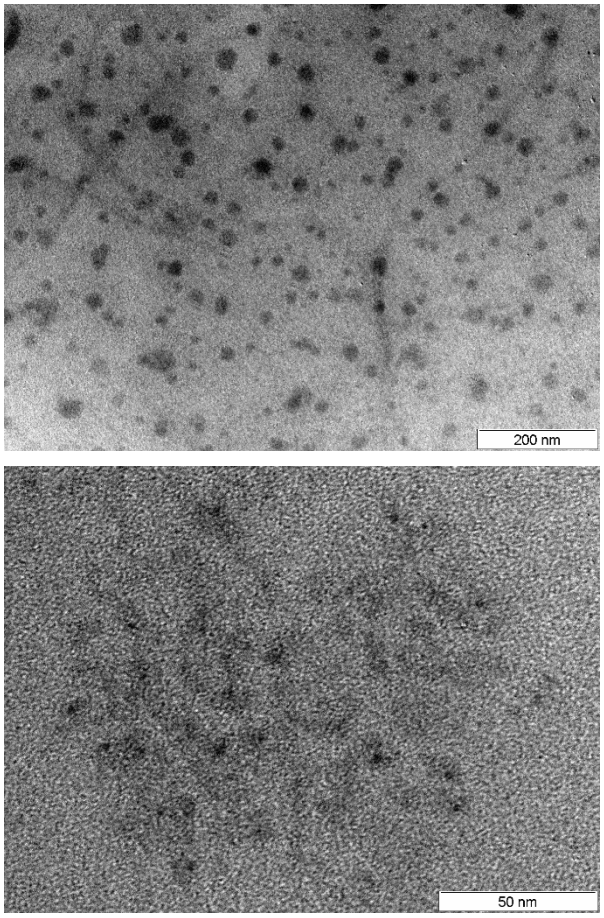

Figure 8.12. TEM images of CQDs-ethylendiamine at different magnifications.

d) CQDs-*p*-phenyldiamine.

The FT-IR analysis of CQDs passivated with p-phenyldiamine was performed at room temperature. Figure 8.13 shows the FT-IR spectrum which present stretching band at 3250 cm^{-1} corresponding to –N-H vibration, vibration of –OH at 3410 cm^{-1} ,C=C at 1600 cm^{-1} and C=O at 1500cm^{-1}.

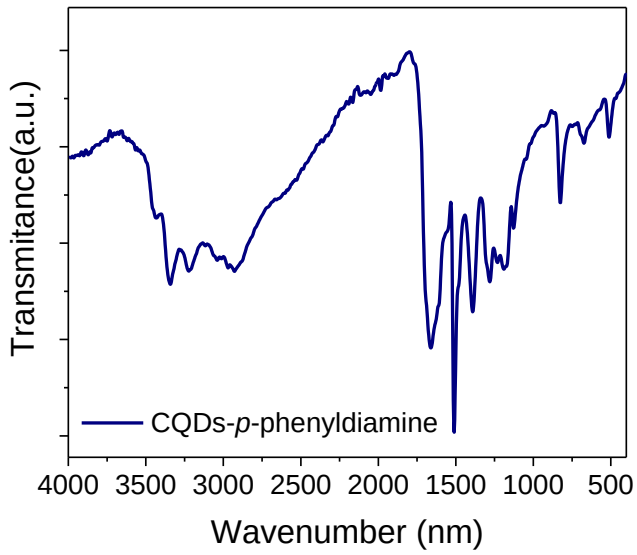

Figure 8.13. FT-IR spectrum of CQDs-*p*-phenyldiamine.

We performed dynamic light scattering to measure the average particle size. The sample was measured twice (red and green line), and both graphs displayed the average size distribution by intensity and by volume (see Figure 8.14). In the first case, we observed some aggregates with a size of 100 nm and 900 nm. The average size of CQDs-*p*-phenyldiamine were 20 nm and 500 nm.

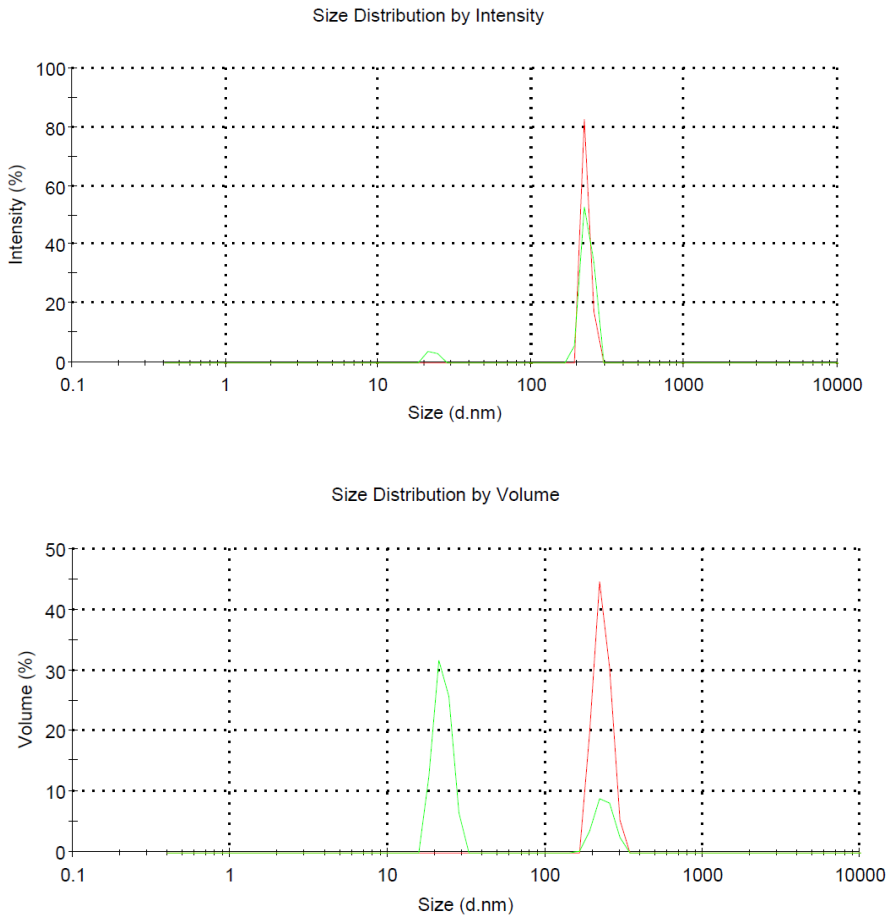

Figure 8.14. DLS signal of CQDs-*p*-phenyldiamine. Size distribution by intensity (up) and by volume (down).

TEM images show the presence of particles bigger than 10 nm because we cannot control the growth of the particles. The average size of CQDs-p-phenyldiamine was 31.7 ± 5.4 nm. (Figure 8.15).

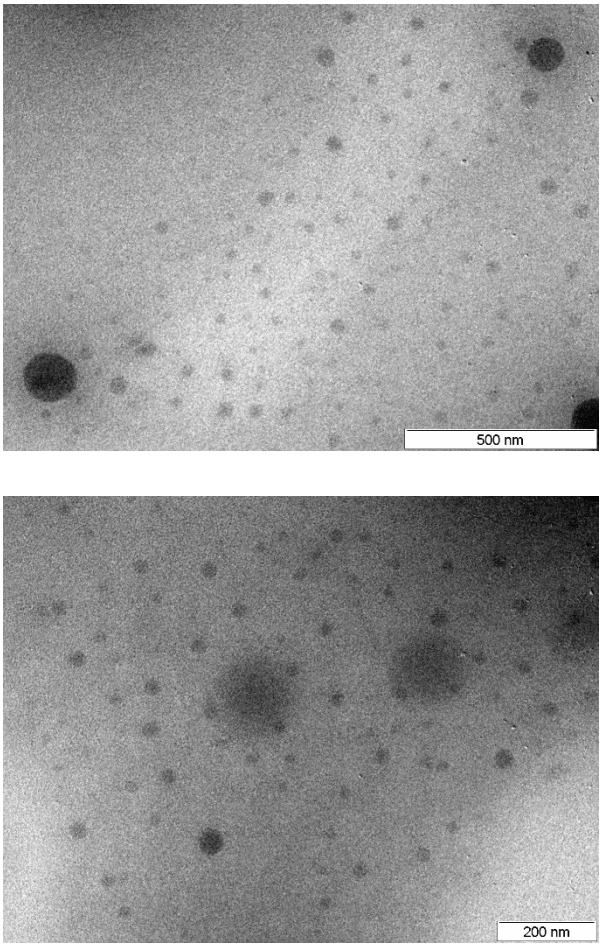

Figure 8.15. TEM images of CQDs-*p*-phenyldiamine at different magnifications.

8.4.2 Physicochemical characterization of CQDs.

All measurements were done in solution. Figure 8.16 (top) shows the spectroscopic features of the CQDs. According to the literature, absorption bands between 300 and 350 nm are related to the intrinsic transitions of carbon core [20 ,22]. The bands that appear from 350 nm to 600 nm, are assigned to the surface-related states.

CQDs-ethylendiamine present a strong absorption band at 240 nm assigned to the carbon core, another strong absorption at 343 nm and a shoulder at 450 nm related to the C=N group of surface states. CQDs-*p*-phenyldiamine present two shoulders at 272 nm and 340 nm, which are assigned to carbon core and surface state respectively. CQDs-urea present an absorption band located at 245 nm attributed to an n-π* transition of C=C and 300 nm is attributed at amino-functionalized surface of CQDs.[5] Finally, CQDs-HDA present an absorption band at 230 nm and a shoulder at 345 nm. The first one is assigned to the n-π* carbon core and the second one to the surface states.[23]

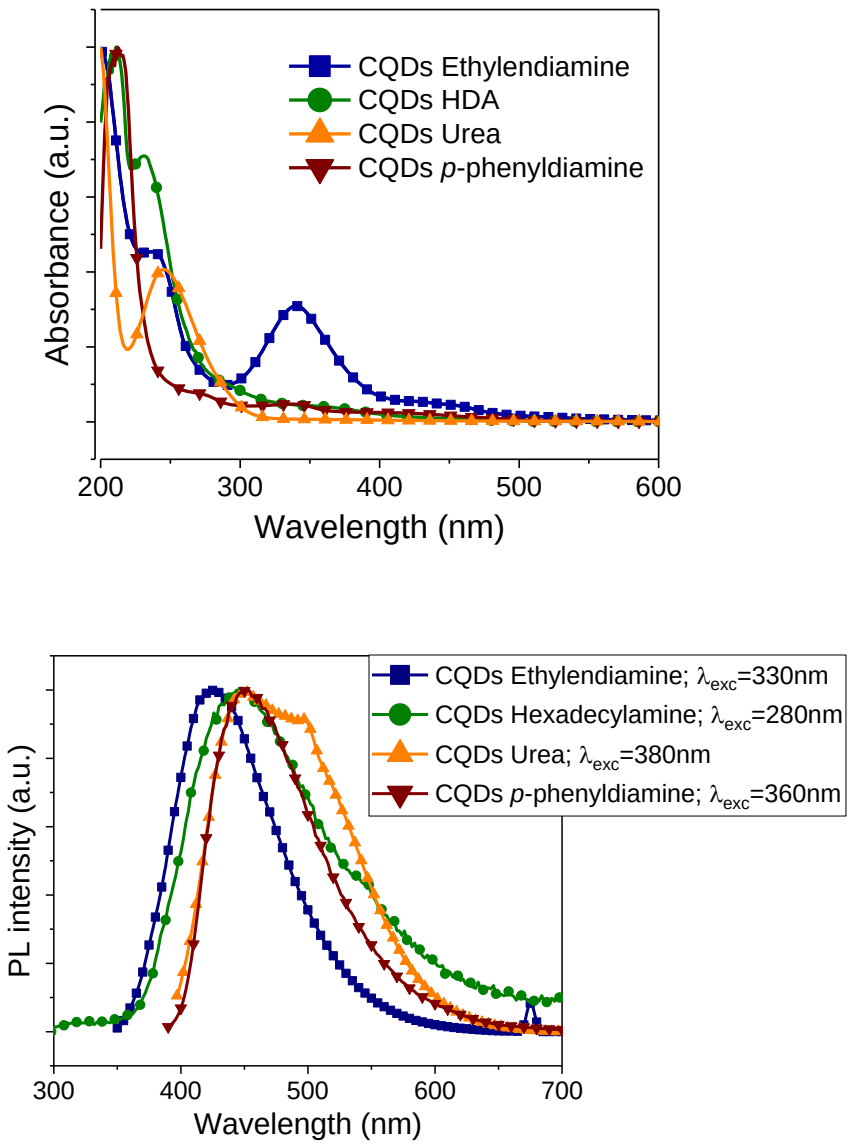

Figure 8. 16. The absorbance (top) and emission (bottom) spectra of CQDs with different capping ligands in solution at room temperature.

The PL spectra is excitation wavelength dependent, as reported in the literature and shown in the Annex 8.7.2 In all the cases, the emission peak of CQDs presents a red-shift as the excitation wavelength moves from 310 nm to 450 nm.

As an example, Figure 8.16 shows the PL spectra of all CQDs in solution recorded at room temperature at a specific wavelength. As can be seen, all the CQDs present a unique peak with a FMWH of 50 nm.

As it has been explained in Chapter 7, the origin of the photoluminescence is still under discussion by the scientific community. However, we should explain in brief, and from our point of view, that the origin of the PL could be explained from the carriers recombination in the core and in the surface of CQDs.

Table 8.1 shows all the data extracted from the spectroscopic measurements under a certain wavelength excitation. The quantum yield was calculated using a dye as reference, as reported in **Chapter 3.** The specific methodology to calculate the QY of these samples is showed in the **Annex 8.7.1**.

Table 8. 1. Optical parameters of CQDs in solution. The quantum yield was estimated using Couramine 153 or Couramine 102 as reference dye.

Capping ligand	λmax PL (nm)	FMWH (nm)	QY (%)
Ethylendiamine	424	45	43
p-phenyldiamine	444	63	8
Hexadecylamine	452	61	40
Urea	452	47	35

The most interesting data that we extract from Table 8.1 is the poor quantum yield of CQDs-p-phenyldiamine. It is important to point out how the surface ligand is important when we synthetize Quantum dots because they can reduce the non-radiative recombination mechanism improving the quantum yield. The ligands with monodental alkyl chains can cover the CQDs surface creating a more compact layer, reducing the number of superficial defects.

Carbon quantum dots emission lifetimes were measured by Time-Correlated Single Photon Counting (TCSPC) to have a better understanding of the behavior of the different radiative processes that can occur in the CQDs after light induced excitation (see Figure 8.17).

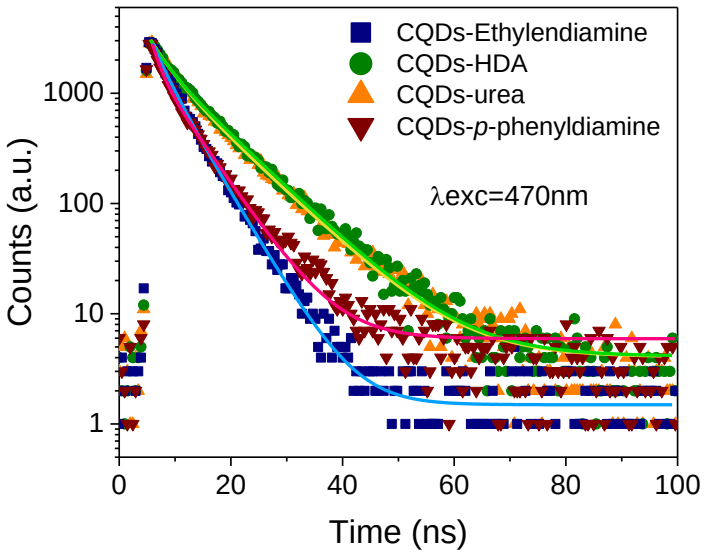

Figure 8. 17. Time-Resolved Photoluminescence (TRPL) decays of CQDs in solution. The samples were recorded exciting at λ_{exc}= 470 nm at room temperature in solution. The color solid line represents the exponential fitted decay.

As can be seen in Table 8.2, the profile decays can be fitted by a bi-exponential model (equation 8.1) suggesting the presence of two different relaxation mechanisms, one originated in the core and the second, that is the fastest, originating in the surface. Regarding the results, we observed that those CQDs passivated with urea and HDA present the largest life time decays while the ones which we used Ethylendiamine present the shortest one. This parameter is important to take in account because they can give us information about charge dynamics and their influence in the final device performance.

$$PL\,\tau(t) = A_1 e^{-(\frac{t}{\tau 1})} + A_2 e^{-(\frac{t}{\tau 2})} \qquad \text{Equation 8.1}$$

Where A_1 and A_2 are the amplitude of the radiative lifetime and τ represent the lifetime values.

Table 8. 2. Time-Resolved Photoluminescence (TRPL) lifetimes obtained by fitting the data shown in Figure 8.4 by Equation 8.1.

λexc	470 nm	
	τ_1 (ns)	τ_2 (ns)
CQDs-EDA	2.40 ± 0.14	5.09 ± 0.10
CQD-HDA	2.81 ± 0.12	9.25 ± 0.11
CQDs-Urea	3.30 ± 0.11	9.07 ± 0.13
CQDs-PPD	1.48 ± 0.04	5.86 ± 0.05

EDA= Ehtylendiamine, PPD=*p*-phenyldiamine

The energy alignment was measured by electrochemical methods in order to determine the valence band (VB) and conduction band (CB) level. As CQDs just presented non-reversible processes, square wave voltammetry technique was used. The curves are shown in the **Annex 8.7.3** whereas the result of the calculations are in Table 8.3.

Table 8. 3. Electrochemical properties of CQDs measured in dichloromethane solution, PEDOT:PSS and MoO_3.

HTMs	E_{0-0} (eV)	Valence band/Conduction band (eV)
CQDs-EDA	3.07	-5.52/-2.45
CQDs-PPD	2.81	-5.12/-2.07
CQDs HDA	3.36	-5.70/-2.34
CQDs Urea	2.93	-5.84/-2.90
PEDOT:PSS	3.00	-5.20/-2.20
MoO_3	2.80	-9.50/-6.70

E_{0-0}= Energy for the energy transition between the lowest vibrational ground state and the lowest vibrational excited state.

8.4.3 Determination of the Hole mobility

In order to study how CQDs works as solid layer, we measured the hole mobility. These hole mobility values will allow the determination of the maximum thickness the different layers can achieve until transport losses become relevant and thus a limitation in the final performance of the device. Hole mobility values were calculated from hole only devices IV curves. The procedure to build hole only devices and their measurements is described in **Chapter 3**. Figure 8.18 shows the schema of the hole only devices structure and the measurement of the current density versus applied voltage. The data were fitted using the model of space-charge limited current [24].

$$J_{SCL} = \frac{9}{8} \in_0 \in_R \mu_h \frac{V_1^2}{L_1^3} \qquad \text{equation 8.2}$$

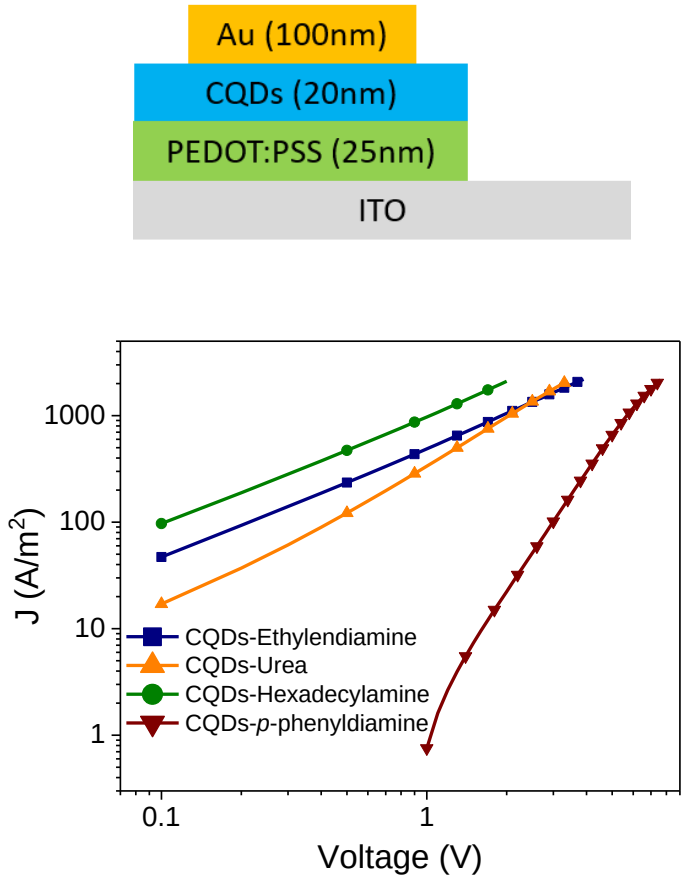

Figure 8.18. Schema of a hole-only device (top). Current-voltage curves for hole-only devices prepared with different CQDs (bottom).

The results are listed in Table 8.4, which shows the average values of hole mobility of different diodes. Comparing the values obtained for the CQDs with PEDOT:PSS and evaporated MoO_3, the mobility values are clearly lower. The charge transport depends on several factors like the structure, purity of materials, the nature of capping ligands etc. Regarding the effect of the chain length, HDA shows the higher mobility values while the lower is observed in the p-phenyldiamine sample[8]. This result is in agreement with our previous observation about the lower QY and lifetime values and reinforces the hypothesis that the nature of the ligands affects the superficial defects of CQDs and influences the optoelectronic parameters of the CQDs.

Table 8. 4. Hole mobilities of CQDs using different amines as capping ligands.

Carbon quantum dots	Hole mobility value ($cm^2V^{-1}s^{-1}$)
CQDs-urea	2.92E-06 ± 3.28E-07
CQDs Hexadecylamine	8.54E-05 ± 1.74E-04
CQDs Ethylendiamine	2.41E-06 ± 5.96E-07
CQDs p-phenyldiamine	1.50E-06 ± 4.75E-07
PEDOT:PSS (*)	1.2E-2
MoO_3 evaporated (*)	3E-3

(*) This values were taken from the bibliography.

8.4.5 Device characterization.

Devices were prepared using optimized conditions from reported procedures[25]. The films were deposited by spin coating in air conditions with the exception of MoO_3·that was deposited by thermal evaporation. The resulting thickness of ZnO layer was 100 nm, that of F8BT was 100nm, that of MoO_3 was 15nm, and those of PEDOT:PSS and CQDs were 20 nm. Figure 8. 19 shows a schematic description of the energy levels of the materials that we used to fabricate the devices. The energy level alignment between the electrodes and the contacts are crucial parameter in order to ensure an optimal charge transfer and get efficient diodes. The energy alignment is an important parameter to take in account because it is the way to control the balance charge inside the device. The unbalanced charge between the cathode and the anode could set off an increase of the current and as consequence losing luminance and device stability.

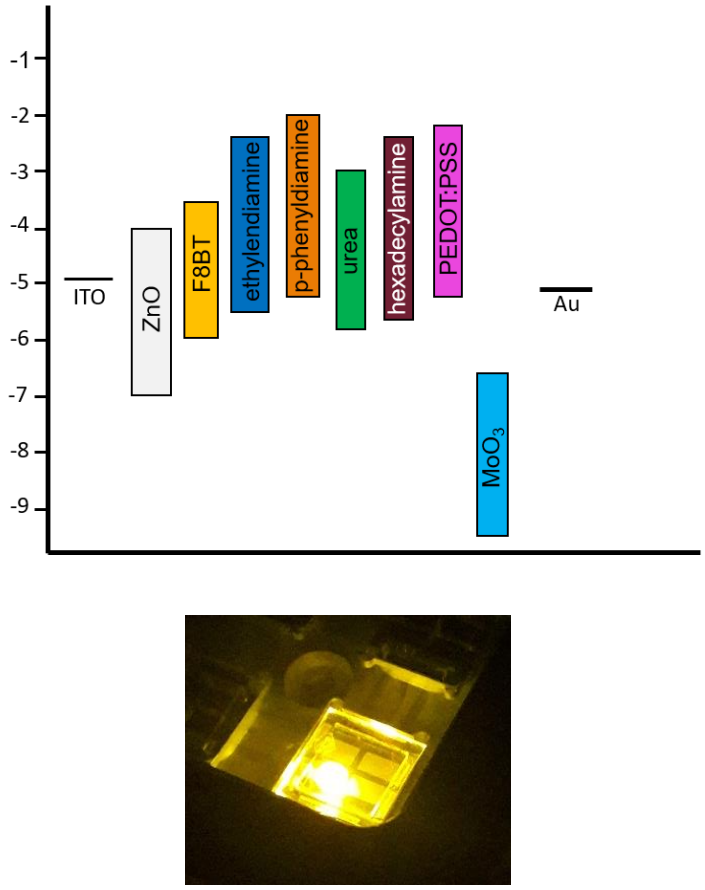

Figure 8. 19. Relative energy levels of the HyLED components (top) and picture of one working device. Photograph of diode using PEDOT:PSS as HTL applying 5V (bottom).

One of the phenomena that we observed during the deposition of hole transport layer (HTL) via spin coating was the low compatibility between the HTL and the emissive layer. The wettability between the emissive layer and the HTL was one of the weak points during the device layer fabrication. To avoid this issue, the literature reports the use of solvents such as methanol [26], IPA[27] or doping the solution with salts such as $HAuCl_4$ [6]. These tests have been performed in order to improve the wettability, stability and to increase the electrical conductivity of the deposited layer. In our case, we added different amounts of IPA to the solution to increase the hydrophilicity of both PEDOT:PSS and the CQDs. The results of

the different experiments carried out to solve these problems are shown in the **Annex 7.**

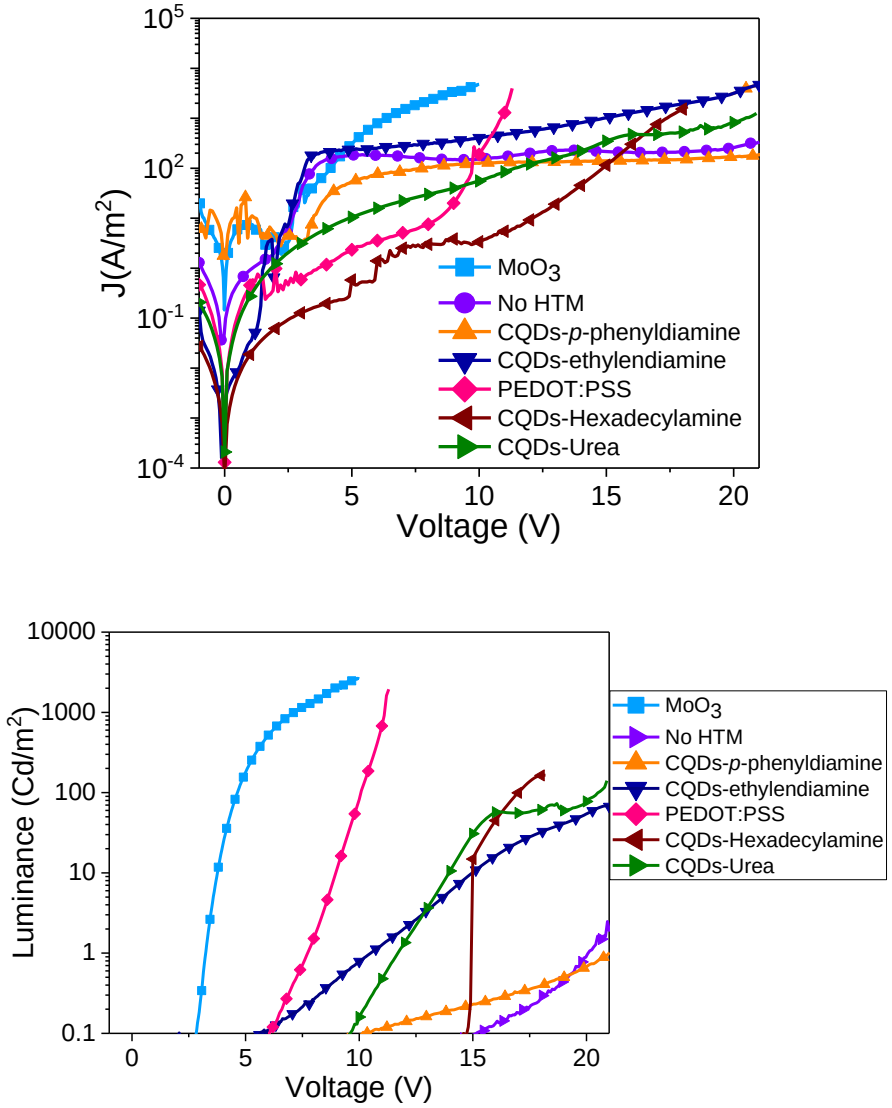

Figure 8. 20. Variation of the current density (top) and luminance (bottom) with applied bias for the devices prepared with different CQDs.

The optoelectronic characterization of the optimized devices was carried out by measuring the luminance and current density as a function of the applied bias. The (I-V) curves and luminescence -voltage curves using different HTM are shown in Figure 8.20. The characterization techniques are described in **Chapter 3**. The measurements were performed in air conditions and applying gradually the voltage in order to polarize the diode slowly.

The results of the device performance are summarized in Table 8.5. These results agree with the idea that the use of interfacial layers is the key to improve the performance of the device. Accordingly, the device prepared without HTL presents the lowest luminance values and current efficiency. The maximum luminance of 2600 cd/m^2 was achieved with evaporated molybdenum oxide as hole transport layer and with turn-on voltage 2.85 V. The PEDOT:PSS doped with 2-isopropanol (IPA), achieved 2000 Cd/m^2 with a turn-on voltage at 6.10 V, this decreased voltage, as commented before, appeared due to the wettability issues that increase the resistance at the interface as can be seen in the Figure 8. 20 (top). The devices prepared with CQDs showed modest luminance values compared to references but clearly superior than without HTM, validating their role as HTM under working conditions.

Regarding the results, CQDs capped with *p*-phenyldiamine have shorter emission lifetime and lower QY and hole mobility values compared with the other CQDs-containing devices. This phenomenon was reflected in the efficiency of the HyLEDs whose maximum luminance is 13 cd/m^2. There are two possible explanations: (1) The phenyl groups enhance the charge delocalization, hindering the injection of the carriers. (2) The benzene groups may block the number of passivating ligand that could be anchored to the carbon dots surface, leaving more available trap states at the surface. In addition, it has to be taken into account the difficulty to obtain a uniform layer distribution when we deposit CQDs on top of F8BT since this material tend to form aggregates allowing the circulation of high current densities through the areas where the thickness of CQDs has to be thinner due to mobility limitations.

CQDs-ethylendiamine has the lowest turn-on voltage, lower even than the PEDOT:PSS indicating good charge injection capability due to appropriate valence band alignment between the metal electrode and the active polymer, high quantum yield and a short lifetime decay. However, the increase in luminance is not as high as with urea or hexadecylamine-capped CQDs. It may be because we could not find the optimal thickness. These two samples show luminance values above 100 cd/m^2 and turn-on voltages above 10 V. Both presents a VB that can facilitate hole injection charges (the hole mobility values are also the highest within the series) and electron blocking within the active layer.

Finally, the slightly lower luminance of the CQDs-urea in comparison with the CQDs-HDA can be explained by the subtle variation in charge lifetimes. Moreover, the hexadecylamine was solved in hexane, which presented a better wettability over the polymer and then a presumably better polymer/HTM interface quality.

Table 8.5.Performance results of HyLEDs devices prepared using different HTM. V^a is the turn-on voltage at 0.1 Cd/m^2.

HTM	Turn-on voltage V^a (V)	Max. Luminance (Cd/m^2)	Current Efficiency (Cd/A)
PEDOT:PSS	6.10	2000	$6 \cdot 10^{-1}$
Ethylendiamine	4.90	70	$2 \cdot 10^{-3}$
p-phenyldiamine	10.18	13	$9 \cdot 10^{-4}$
Hexadecylamine	14.50	174	$8 \cdot 10^{-4}$
Urea	9.60	146	$2 \cdot 10^{-3}$
No HTM	15.20	2	$5 \cdot 10^{-4}$
MoO_3	2.85	2600	$7 \cdot 10^{-1}$

8.5 Conclusions.

Carbon Quantum Dots functionalized with different capping ligands were synthetized in order to use them as hole transport layer (HTL) in HyLEDs. Our aim was to replace the most common HTL by the promising materials that can be processed in solution.

In this work, four different capping ligands for the CQDs have been tested, in order to explore the relationship between the nature of the ligand and the energy levels of valence/conduction bands and the hole mobility with the efficiency of the devices. We observed that the nature of the capping ligand influences directly the optoelectronic properties of CQDs, being Urea, EDA and HDA the most suitable ligands in terms of enhanced charge injection due to a better energy alignment with the polymer resulting in a higher maximum luminance. In the case of *p*-phenyldiamine ligand, the steric hindering avoids a complete coverage compromising the quality of the interface and combined with the poorer quantum yield (5 times inferior than the others) the devices obtained using this ligand show the lowest current efficiency and the lowest luminance respectively. We can determine that in the case of CQDs-p-phenyldiamine, we measured the presence of a wider particle size distribution (as observed by TEM and DSL) that negatively affect the efficiency of the device creating a non-homogeneous CQDs layer. The use of CQDs-EDA as HTL resulted in a turn-on voltage of 4.90 V. Despite the luminance was 70 cd/m^2, we can conclude that this CQDs can be used as hole transport layer although a further optimization of the device is required to get higher luminance.

To sum up, we have prepared for the first time proof-of- concept devices using CQDs as HTL in light emitting devices. The use of CQDs as HTL contributes to the injection current from the cathode to the active layer, although further optimization is required. Finally, we have achieved three of the five layers by printing techniques closing the gap for the pre-industrialization of the materials.

8.6 References

1. Y. Guo, Z. Wang, H. Shao, X. Jiang. Hydrothermal synthesis of highly fluorescent carbon nanoparticles from sodium citrate and their use for the detection of mercury ions. *Carbon N. Y.* **2013**, 52, 583–589.
2. S.Y. Lim, W. Shen, Z. Gao. Carbon quantum dots and their applications. *Chem. Soc. Rev.* **2015**, 44 (1), 362–381.
3. F. Yuan, Z. Wang, X. Li, et al. Bright Multicolor Bandgap Fluorescent Carbon Quantum Dots for Electroluminescent Light-Emitting Diodes. *Adv. Mater.* **2017**, 29 (3), 1604436 – n/a.
4. J.Z. and H.S. and X.B. and Y.Z. and Y.Z. and X.C. and G.P. and B.D. and L.X. and H.Z. and H. Song. Modulation of the photoluminescence in carbon dots through surface modification: from mechanism to white light-emitting diodes. *Nanotechnology* **2018**, 29 (24), 245702.
5. X.Y. Zhang, Y. Zhang, Y. Wang, et al. Color-Switchable Electroluminescence of Carbon Dot Light-Emitting Diodes. *ACS Nano* **2013**, 7 (12), 11234–11241.
6. S. Kim, H.S. Kim, Y.D. Park. Doped PEDOT:PSS electrodes, patterned through wettability control, and their effects on the electrical properties of polymer thin film transistors. *Org. Electron.* **2016**, 30, 296–301.
7. Y.R. Park, H.Y. Jeong, Y.S. Seo, W.K. Choi, Y.J. Hong. Quantum-Dot Light-Emitting Diodes with Nitrogen-Doped Carbon Nanodot Hole Transport and Electronic Energy Transfer Layer. *Sci. Rep.* **2017**, 7, 46422.
8. W. Kwon, S. Do, D.C. Won, S.-W. Rhee. Carbon Quantum Dot-Based Field-Effect Transistors and Their Ligand Length-Dependent Carrier Mobility. *ACS Appl. Mater. Interfaces* **2013**, 5 (3), 822–827.
9. E. Martínez-Ferrero, A. Forneli, C. Boissière, et al. Tailored 3D Interface for Efficiency Improvement in Encapsulation-Free Hybrid Light-Emitting Diodes. *ACS Appl. Mater. Interfaces* **2011**, 3 (9), 3248–3251.
10. C. Girotto, E. Voroshazi, D. Cheyns, P. Heremans, B.P. Rand. Solution-Processed MoO3 Thin Films As a Hole-Injection Layer for Organic Solar Cells. *ACS Appl. Mater. Interfaces* **2011**, 3 (9), 3244–3247.

11. M.H. Lee, W.H. Choi, F. Zhu. Solution-processable organic-inorganic hybrid hole injection layer for high efficiency phosphorescent organic light-emitting diodes. *Opt. Express* **2016**, 24 (6), A592–A603.
12. C. Duc, A. Vlandas, G.G. Malliaras, V. Senez. Wettability of PEDOT:PSS films. *Soft Matter* **2016**, 12 (23), 5146–5153.
13. D.-H. Song, S.-H. Song, T.-Z. Shen, et al. Quantum dot light-emitting diodes using a graphene oxide/PEDOT:PSS bilayer as hole injection layer. *RSC Adv.* **2017**, 7 (69), 43396–43402.
14. H. Lian, Z. Tang, H. Guo, et al. Magnetic nanoparticles/PEDOT:PSS composite hole-injection layer for efficient organic light-emitting diodes. *J. Mater. Chem. C* **2018**.
15. J. Zhou, Y. Liu, J. Tang, W. Tang. Surface ligands engineering of semiconductor quantum dots for chemosensory and biological applications. *Mater. Today* **2017**, 20 (7), 360–376.
16. D.B. Straus, E.D. Goodwin, E.A. Gaulding, et al. Increased Carrier Mobility and Lifetime in CdSe Quantum Dot Thin Films through Surface Trap Passivation and Doping. *J. Phys. Chem. Lett.* **2015**, 6 (22), 4605–4609.
17. E. Martinez-Ferrero, S. Grigorian, J.W. Ryan, W. Cambarau, E. Palomares. Influence of the Molecular Weight and Size Dispersion of the Electroluminescent Polymer on the Performance of Air-Stable Hybrid Light-Emitting Diodes. *ACS Appl. Mater. Interfaces* **2015**, 7 (2), 1078–1086.
18. H. Zhu, X. Wang, Y. Li, et al. Microwave synthesis of fluorescent carbon nanoparticles with electrochemiluminescence properties. *Chem. Commun.* **2009**, No. 34, 5118–5120.
19. S. Zhu, Q. Meng, L. Wang, et al. Highly Photoluminescent Carbon Dots for Multicolor Patterning, Sensors, and Bioimaging. *Angew. Chemie Int. Ed.* **2013**, 52 (14), 3953–3957.
20. D. Chen, W. Wu, Y. Yuan, et al. Intense multi-state visible absorption and full-color luminescence of nitrogen-doped carbon quantum dots for blue-light-excitable solid-state-lighting. *J. Mater. Chem. C* **2016**, 4 (38), 9027–

9035.

21. F. Wang, S. Pang, L. Wang, et al. One-Step Synthesis of Highly Luminescent Carbon Dots in Noncoordinating Solvents. *Chem. Mater.* **2010**, 22 (16), 4528–4530.
22. J.Z. and X.B. and J.B. and G.P. and Y.Z. and Y.Z. and H.S. and X.C. and B.D. and H.Z. and H. Song. Emitting color tunable carbon dots by adjusting solvent towards light-emitting devices. *Nanotechnology* **2018**, 29 (8), 85705.
23. Y. Dong, H. Pang, H. Bin Yang, et al. Carbon-Based Dots Co-doped with Nitrogen and Sulfur for High Quantum Yield and Excitation-Independent Emission. *Angew. Chemie Int. Ed.* **2013**, 52 (30), 7800–7804.
24. P.N. Murgatroyd. Theory of space-charge-limited current enhanced by Frenkel effect. *J. Phys. D. Appl. Phys.* **1970**, 3 (2), 151.
25. J. Ryan, E. Palomares, E. Martínez-Ferrero. Towards low-temperature preparation of air-stable hybrid light-emitting diodes; **2011**; Vol. 21.
26. W. Wang, M.A. Ruderer, E. Metwalli, et al. Effect of Methanol Addition on the Resistivity and Morphology of PEDOT:PSS Layers on Top of Carbon Nanotubes for Use as Flexible Electrodes. *ACS Appl. Mater. Interfaces* **2015**, 7 (16), 8789–8797.
27. J. Pan, Q. Huang, Y. Zhang, et al. Application of Solvent Modified PEDOT:PSS in All-Solution-Processed Inverted Quantum Dot Light-Emitting Diodes. *J. Disp. Technol.* **2016**, 12 (10), 1157–1161.

A8 ANNEX

A8.1 Quantum yield calculation.

The quantum yield of CQDs was calculated using Couramine 102 and Couramine 153 as reference dye applying the following equation.

$$QY = QY_{ref}\left(\frac{I_{em\ sample}}{I_{em\ ref}}\right)\cdot\left(\frac{Abs_{ref}}{Abs_{sample}}\right)\cdot\left(\frac{n_{sample}}{n_{ref}}\right)^2$$

Where QY_{ref} is the reference quantum yield, I_{em} is the area of the emission band, Abs is the absorbance excitation wavelength and η is the refractive index.

1) CQDs-HDA.

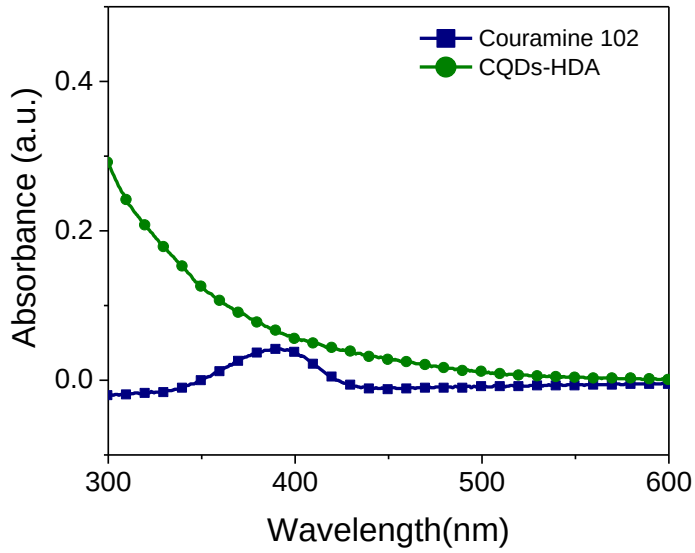

Figure A8. 1. Absorbance spectra of CQDs-HDA (green line) and Couramine 102 (blue line) at room temperature.

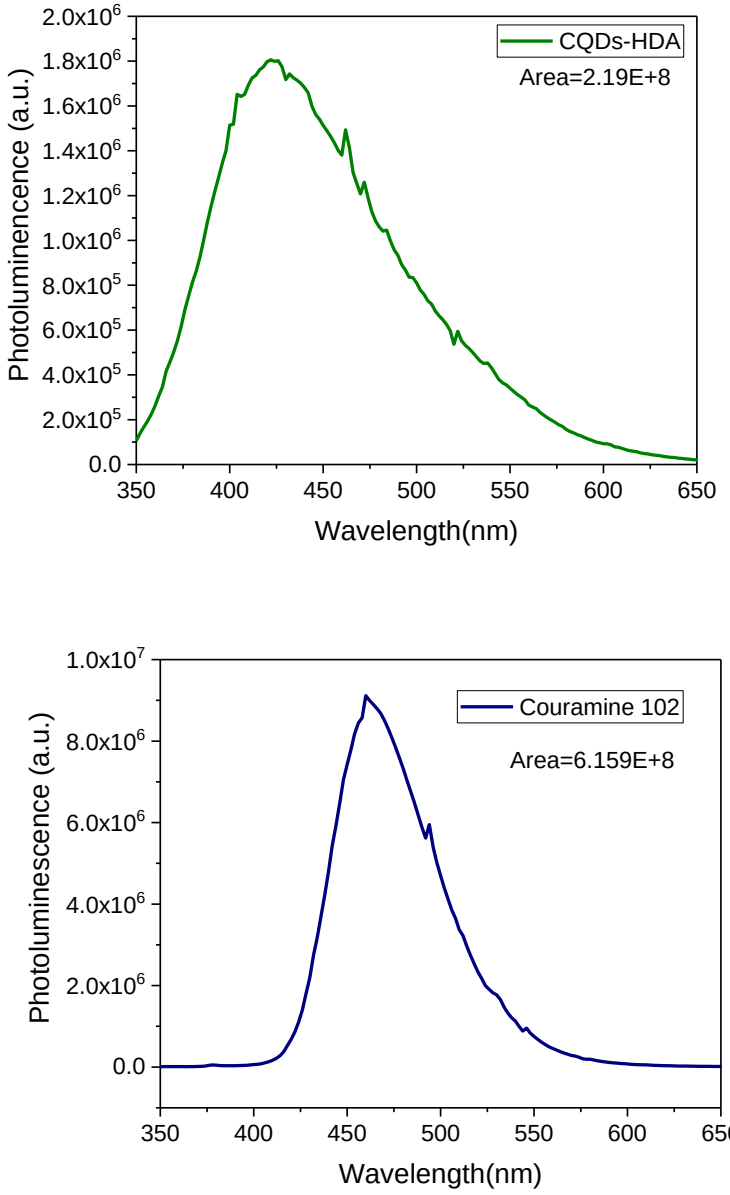

Figure A8. 2. Emission spectra of CQDs-HDA (top) and Couramine 102 (bottom) measured at λexc=340nm at room temperature.

2) CQDs-urea

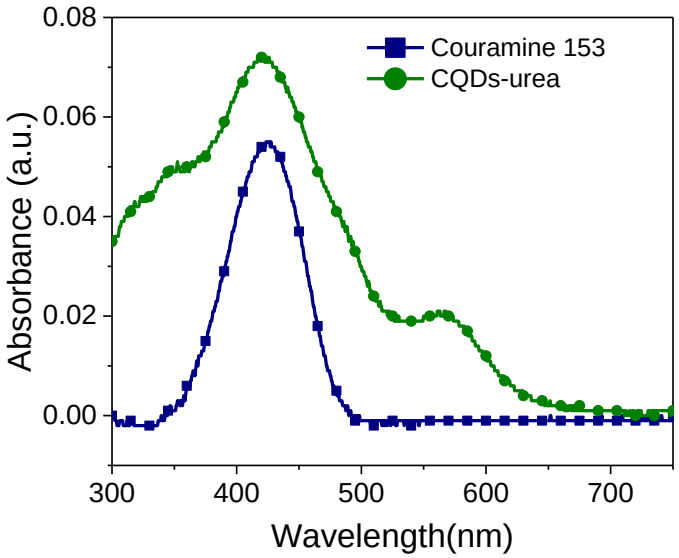

Figure A8. 3. Absorbance spectra of CQDs-Urea (green line) and Couramine 153 (blue line) at room temperature.

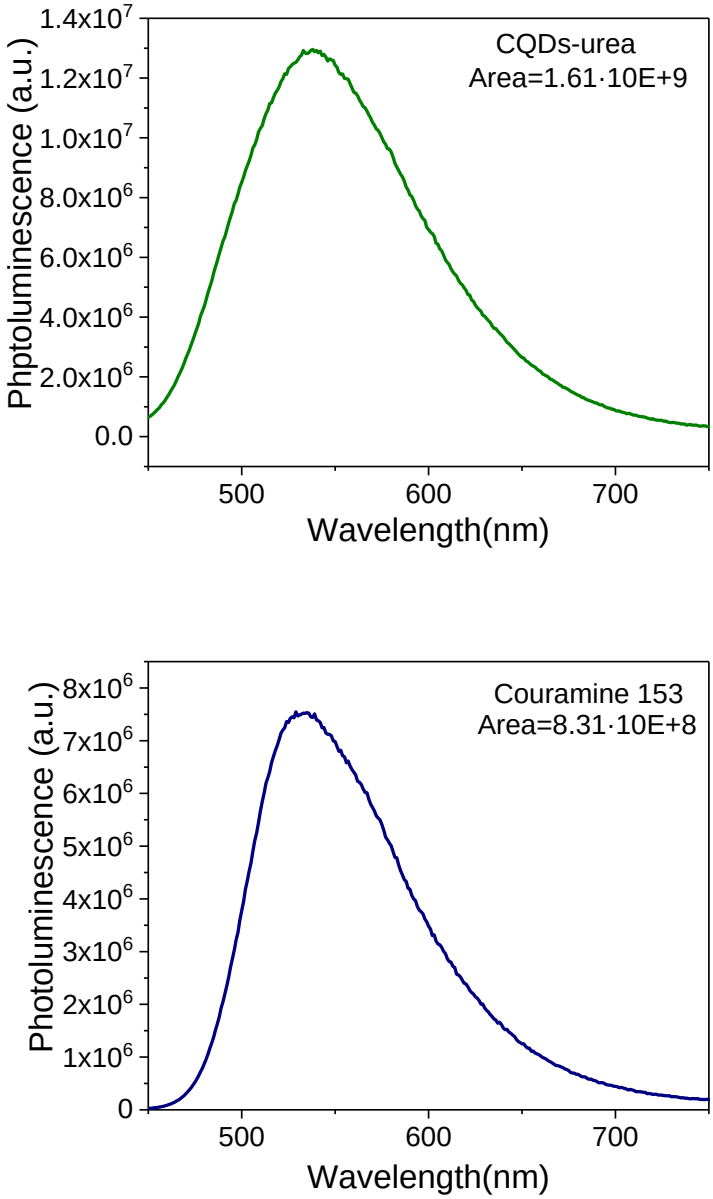

Figure A8. 4. Emission spectra of CQDs-urea (top) and Couramine 153 (bottom) measured at λexc=420nm at room temperature.

3) CQDs-p-phenyldiamine

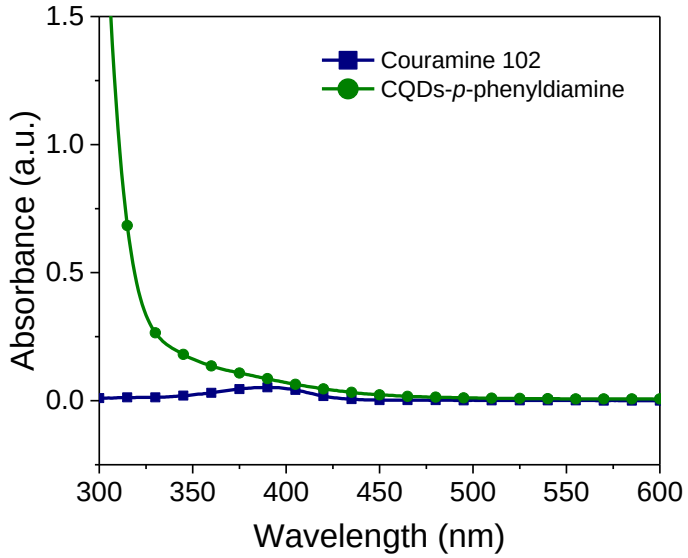

Figure A8. 5. Absorbance spectra of CQDs-Urea (green line) and Coumarine 153 (blue line) at room temperature.

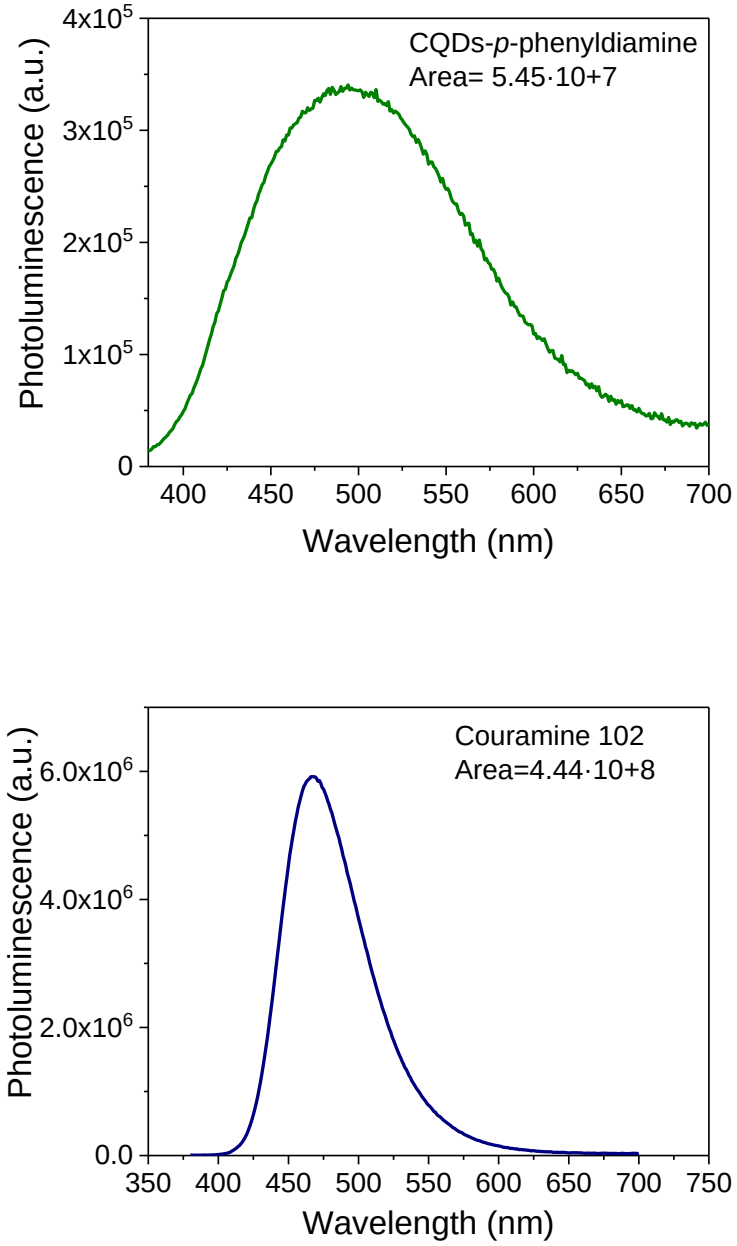

Figure A8. 6. Emission spectra of CQDs-p-phenyldiamine(top) and Couramine 102 (bottom) measured at λexc=370nm at room temperature.

4) CQDs- Ethylendiamine

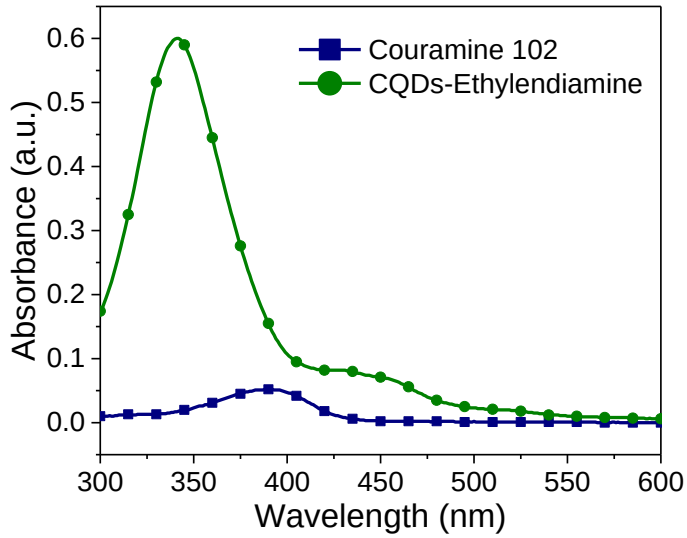

Figure A8.7. Absorbance spectra of CQDs-Ethylendiamine (green line) and Couramine 153 (blue line) at room temperature.

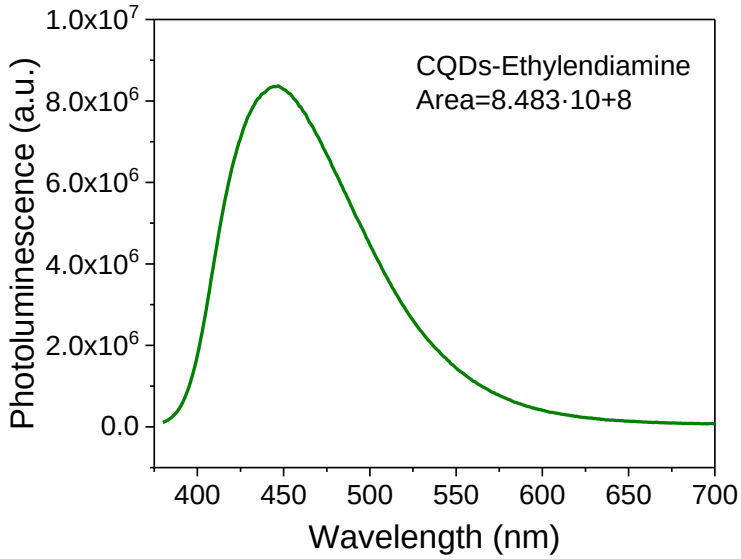

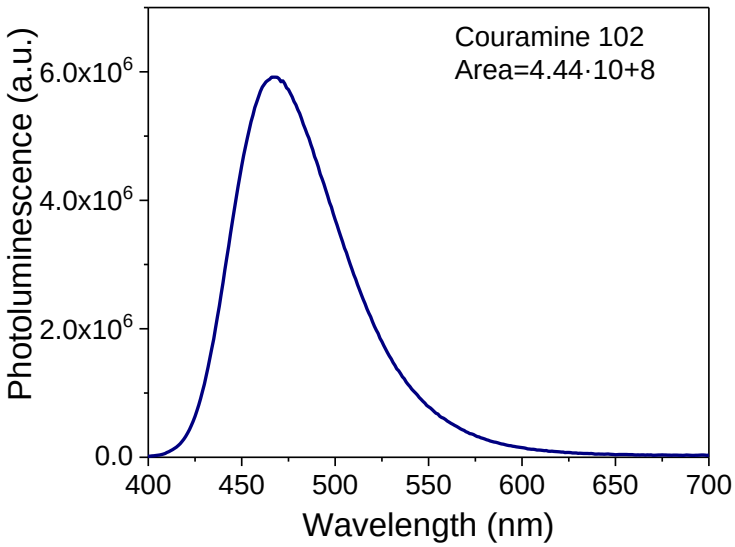

Figure A8. 8. Emission spectra of CQDs-ethylendiamine (top) and Couramine 102 (bottom) measured at λexc=370nm at room temperature.

A8.2 Emission spectra of CQDs at different excitation wavelengths.

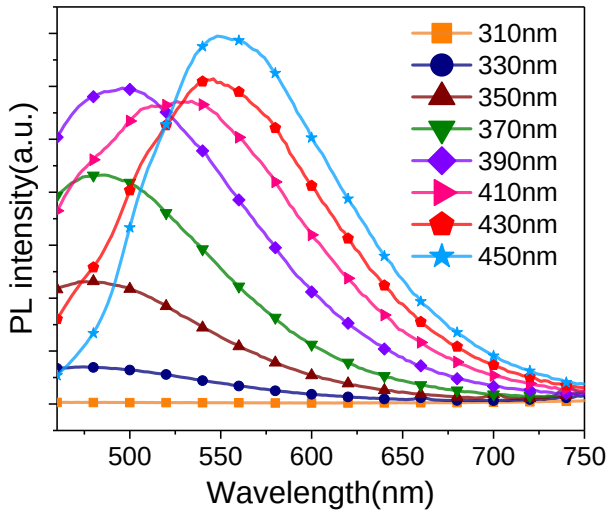

Figure A8. 9. Emission spectra of CQDs-HDA obtained after excitation at different wavelength from 310 nm to 450 nm every 20 nm at room temperature.

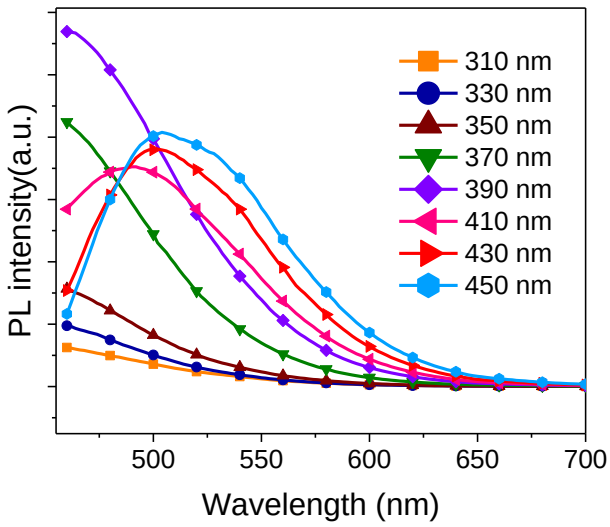

Figure A8. 10. Emission spectra of CQDs-Ethylendiamine obtained after excitation at different wavelength from 310 nm to 450 nm every 20 nm at room temperature.

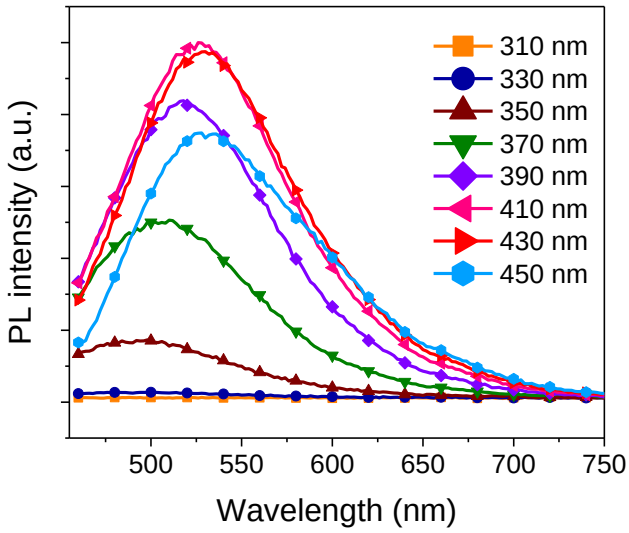

Figure A8. 11. Emission spectra of CQDs-*p*-phenyldiamine obtained after excitation at different wavelength from 310 nm to 450 nm every 2 0nm at room temperature.

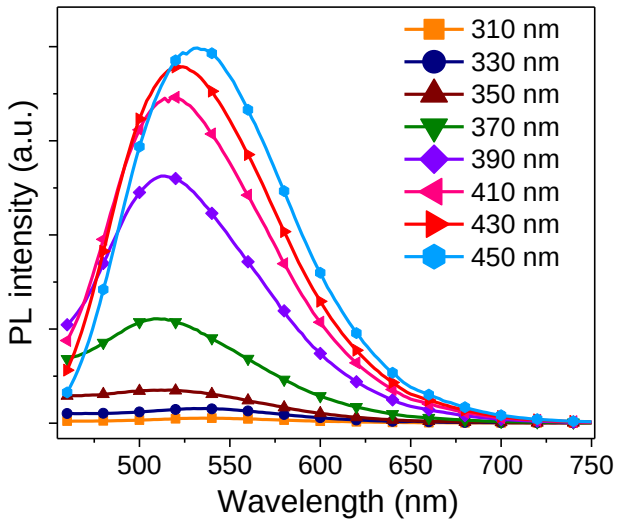

Figure A8. 12. Emission spectra of CQDs-urea obtained after excitation at different wavelength from 310 nm to 450 nm every 2 0nm at room temperature.

A8.3 Cyclic voltammetry and Square wave voltammetry plots.

The equations employed to estimate the conduction and valence bands are the following

$$\mathrm{E}_{CB} = -(E_{OX} + 4.8) \qquad \text{Equation 8.5}$$

$$\mathrm{E}_{VB} = \mathrm{E}_{CB} + \mathrm{E}_{o-o} \qquad \text{Equation 8.6}$$

$$\mathrm{E}_{o-o} = h \cdot \frac{c}{\lambda} \qquad \text{Equation 8.7}$$

E_{ox} is the oxidation potential from the CV, $E_{o\text{-}o}$ is the band gap and λ is the wavelength resulting of the intersection between the absorbance and the emission band, h is the Planck constant $6.62607004 \cdot 10^{-34}$ m^2 kg / s and c is the speed of the light $3 \cdot 10^8$ m/s.

The oxidation potential of the CQDs has been obtained by measuring cyclic voltammetry or square wave voltammetry in solution. The results are shown in the following figures.

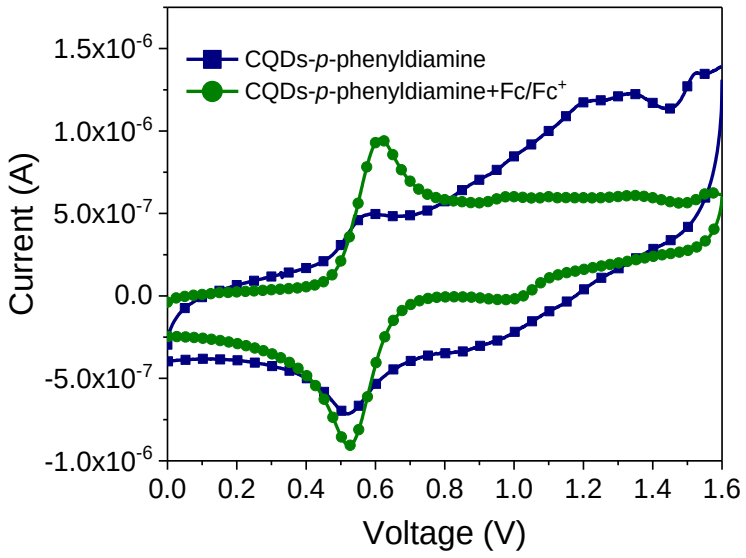

Figure A8. 13. a) Cyclic voltammetry of CQDs solved in dichloromethane recorded in 0.1M tetrabutylammonium hexafluorophosphate in dichloromethane at room temperature.

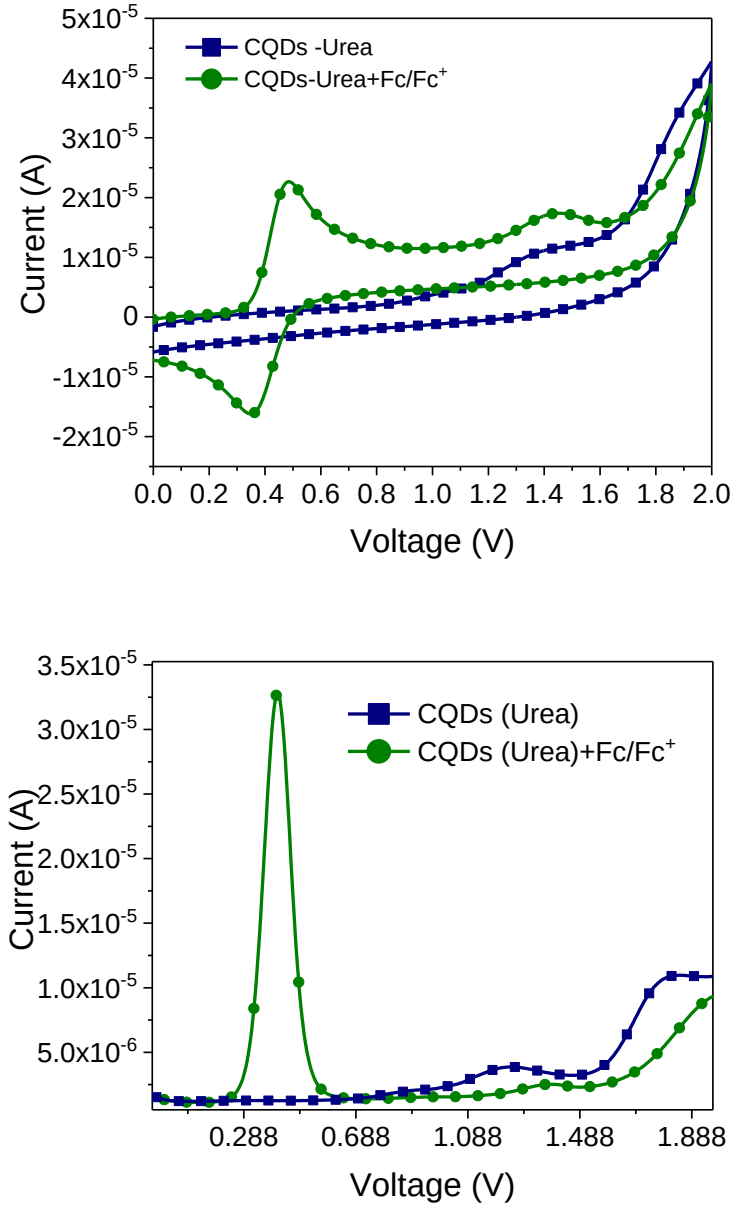

Figure A8. 14. a) Cyclic voltammetry and b) Square wave voltammetry of CQDs solved in dichloromethane recorded in 0.1M tetrabutylammonium hexafluorophosphate in dichloromethane at room temperature.

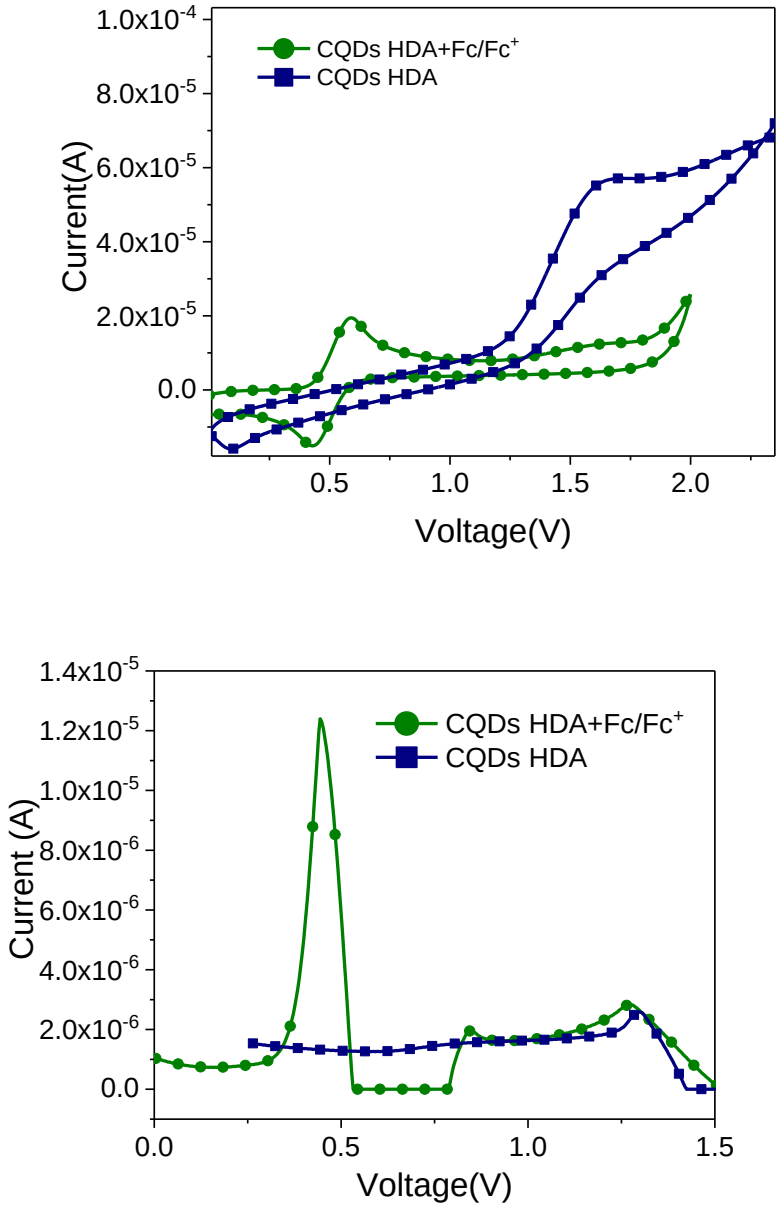

Figure A8.15. a) Cyclic voltammetry and b) Square wave voltammetry of CQDs solved in dichloromethane recorded in 0.1M tetrabutylammonium hexafluorophosphate in dichloromethane at room temperature.

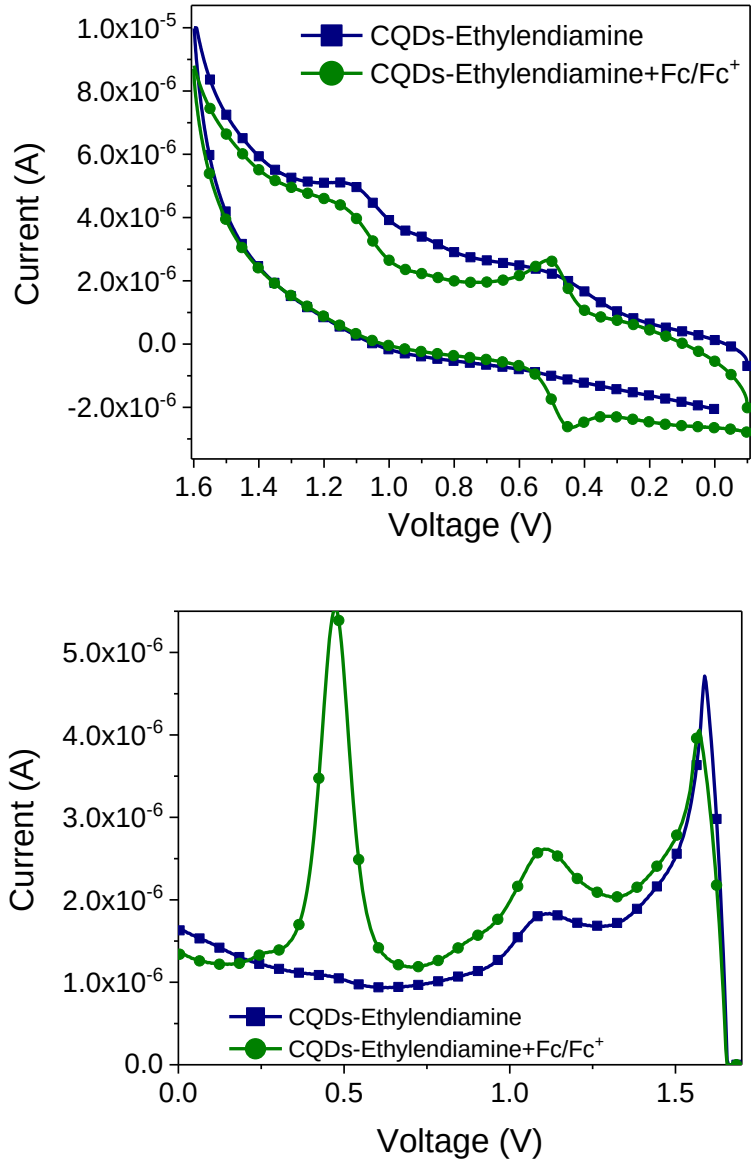

Figure A8. 16. a) Cyclic voltammetry and b) Square wave voltammetry of CQDs solved in dichloromethane recorded in 0.1M tetrabutylammonium hexafluorophosphate in dichloromethane at room temperature.

A8.4 Device optimization.

A8.4.1 CQDs in the HTL

The devices were optimized through testing different velocities during the spin coating processing. Moreover, a major problem during the preparation of the HTL onto the hydrophobic surface of the polymer was the wettability of materials employed for the solution processing of the HTL that were prepared in polar solvents such as ethanol, methanol or water. For that, *p*-phenyldiamine was used as model to optimize the best proportion water/IPA to achieve the best results. Once we obtained the best combination, we applied the same conditions to deposit the other CQDs with the exception of CQDs-HDA that was solved in hexane.

Table A1 display the results of the optimization, showing the evolution of the current density an luminance with applied bias, while varying the thickness of the layer and adding small amounts of IPA.

Table A8. 1. Device results as a result to modify the thickness and adding small amounts of IPA for CQDs-*p*-phenyldiamine.

Spin coating conditions	Turn-on voltage V[a] (V)	Max. Luminance (Cd/m^2)
Aq/500 RPM	15.29	2.47
Aq/1000 RPM	13.90	6.00
Aq/3000 RPM	17.89	3.66
Aq/IPA 2000 RPM	10.18	13.00

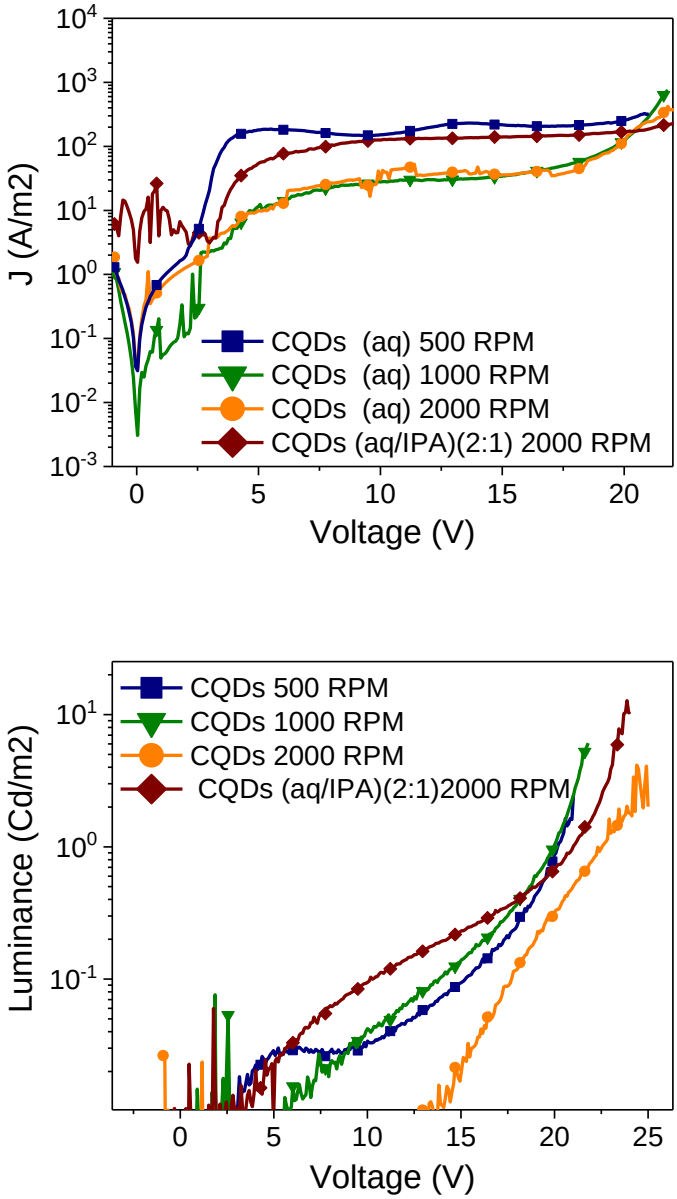

Figure A8. 17. Variation of the current density (top) and luminance (bottom) with applied bias of HyLEDs prepared with different spin coating conditions to deposit CQDs p-phenyldiamine.

A8.4.2 PEDOT:PSS as HTL

The spin coating conditions were 2000 RPM 1 min followed by a temperature treatment at 120ºC during 20min in air conditions. However, there were problems of wettability so we carried out tests to optimize the deposition of the layer. For that, different solution of PEDOT:PSS with different ratio of aq/IPA were tested. . Figure 8. A14 shows the current versus voltage and luminance versus voltage with different velocity of deposition of CQDs. Regarding the turn-on voltages and luminance, the values changed with the ratio of IPA.

Table A8.2. Devices characteristic using different proportions of water/IPA to improve the wettability of the PEDOT:PSS.

Proportions of Aq/IPA	Turn-on voltage V[a] (V)	Max. Luminance (Cd/m^2)
Aq/IPA (1:6)	6.1	2000
Aq/IPA (1:3)	5.1	1600
Aq/IPA (1:1)	3.4	26

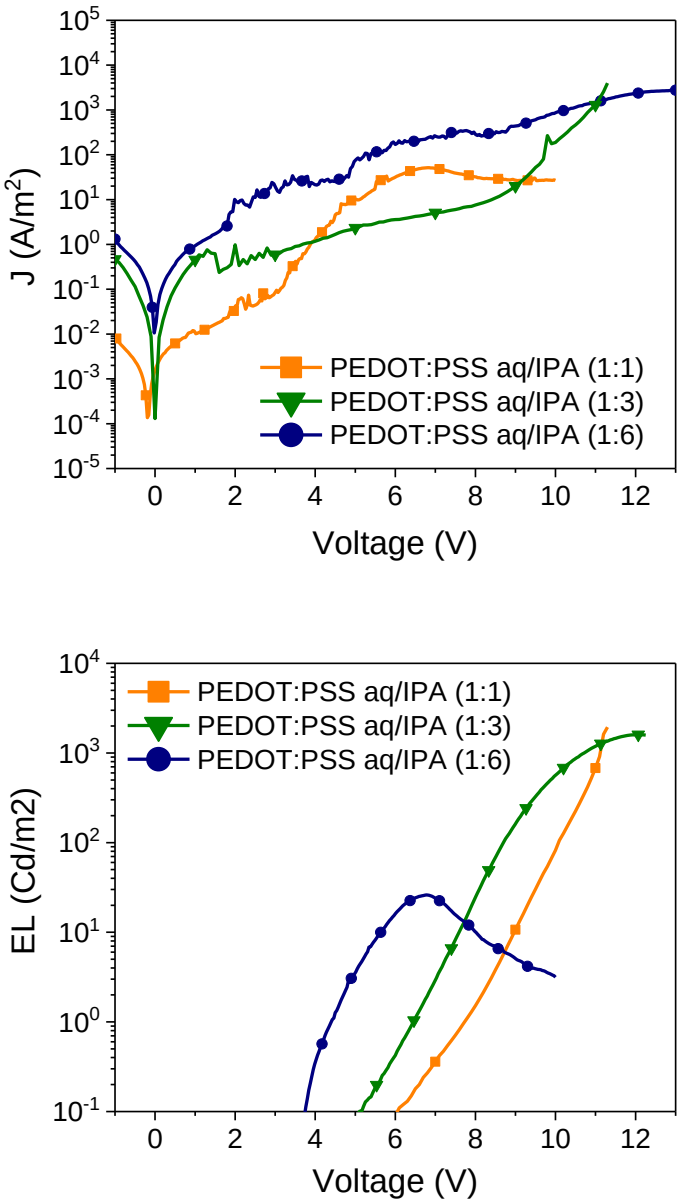

Figure A8. 14. Variation of the current density (top) and luminance (bottom) with applied bias of HyLEDs prepared with different spin coating conditions

Chapter 8

Carbon quantum dots as hole transport layer in Perovskites solar cells.

The use of carbon quantum dots (CQDs) in photovoltaic devices has not yet been fully explored. Herein, we report the use of CQDs in MAPI (methyl ammonium lead iodide) perovskite solar cells to implement this material in photovoltaic applications.

Chapter 9

Table of Contents

Chapter 9

9.1 Introduction.

In Chapter 7 and 8, we have focused on the use of Carbon Quantum Dots (CQDs) in light emitting diodes. In this chapter, we aim to employ a solution processed layer of CQDs as hole transport material (HTM) in solar cells. The idea of the project was to find new material in order to replace the expensive spiro-OMeTAD, which is right now the most used HTM in perovskite solar cells.

Since 2010, when the Nobel Prize in physics was awarded to A. Geim and K. Novoselov for their work on 2D material graphene, many researchers have proposed its use in solar energy application such as hybrid and organic solar cells [1], light emitting diodes [2] or photodetectors [3,4,5] . CQDs presents extraordinary optoelectronics properties such as water solubility, low toxicity (especially compared with their inorganic counterpart QDs like PbS or CdSe), stability against photobleaching and better biocompatibility.

We synthesized and tested CQDs capping with *p*-phenyldiamine. The amine molecules play a dual role as n-doping precursors and as passivating agent, which is finally translated into improved photoluminescence. Heteroatom doping (N, F, S, P, Gd) is a commonly used approach to fine-tune or obtain increase??photoluminescence (PL) and other physicochemical properties of photoluminescent materials [6]. Furthermore, co-doping strategies by combining Mg/N, P/N, and S/N were found to dramatically improve the photoluminescent emission, in addition to luminescence stability, high solubility, low toxicity, and excellent biocompatibility.

On the other hand, the organic-inorganic halide perovskite solar cells (PSCs) have attracted a great deal of attention of solar cell research due to an incredible device efficiency improvement from 3.8% in 2009 to 22.1% in 2018 [7]. The perovskite gained much attention as a potential replacement of the silicon photovoltaic (PV) devices, which is still the best solar cells device in the market with record efficiency of about 26%, although tandem solar cells of silicon and perovskite has achieved efficiencies of 25?% (Afegir referència) In these years, a lot of effort has been put to improve the stability of the devices either by developing alternative ways to form the perovskite layer (absorber) [8,5,9,10] or employing new materials to facilitate charge transport through the device

(selective contacts) [11]. The latter pathway is usually focused on testing and develop new HTMs, like polymers or small molecules, to be deposited via solution processes on top of the perovskite layer, being the titanium dioxide (TiO_2) the most employed material as an electron transport material (ETM) [12,13].

Herein, we want to explore the potential applications of the carbon Dots as hole transport layer in perovskite-based solar cells in accordance with Chapter 7, where these properties were further explored for the fabrication of light emitting diodes. It should be notices that, this project was the starting point to study of CQDs as hole contact in optoelectronic devices. The results have been published in S. Paulo, G. Stoica, W. Cambarau, E. Martinez-Ferrero, E. Palomares, Carbon quantum dots as new hole transport material for perovskite solar cells. *Synth. Met.* **222**, 17–22 (2016).

.2 Material Synthesis and characterization.

9.2.1 Synthesis of CQDs.

The synthesis was carried out via a hydrothermal approach. 1.0507 g of citric acid and 0.541 g of *p*-phenylenediamine were well dissolved in 10 mL of deionized water [14]. The solution was transferred to a poly (tetrafluoroethylene) (Teflon)-lined autoclave (120 mL) and heated at 200 ºC for 5 h, with a heating ramp of 5 ºC / min. After the reaction, a brown-black solution was obtained. Then, the solution was centrifuged thrice at 4500 RPM and the CQDs were dispersed in deionized water or isopropanol

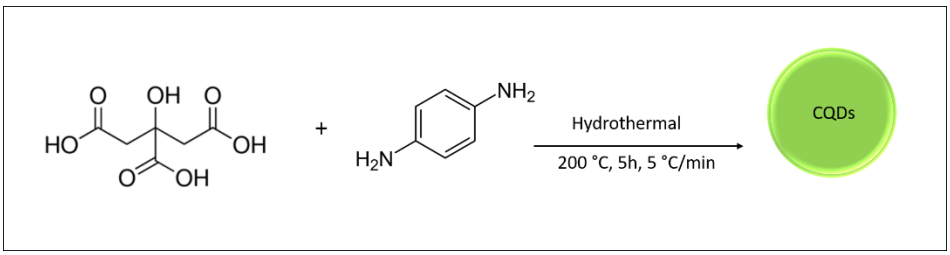

Figure 9.1. Schematic illustration of the synthesis of CQDs.

9.3 Device Fabrication.

Fluorine doped Tin Oxide (FTO) coated glasses (resistance of 8 Ω/cm^2) were etched using Zn powder (Alfa Aesar 98%) and a 2 M solution of HCl according to the desired pattern. Afterwards, the substrates were cleaned for 15 min in an ultrasound bath with deionized water with Hellmax soap, with deionized water and finally with ethanol. The substrates were dried and an UV/Ozone treatment was performed for 20 min.

0.65 mL of Ti (IV) isopropoxide (Sigma Aldrich 97 %) and 0.38 mL of acetylacetone (Sigma Aldrich) were mixed in 5 mL of ethanol. This solution was deposited by spin coating at 3000 RPM for 60 seconds on top of the FTO. Substrates were calcined at 500 ºC for 30 min to obtain the TiO_2 dense layer (d-TiO_2) having a thickness of around 50 nm. Afterwards, titanium oxide-coated substrates were immersed in a 40 mM $TiCl_4$ solution at 70 ºC for 30 min. Then, the substrates were cleaned with water and ethanol and heated at 390 ºC for 20 min.
A mixture of TiO_2 paste (18 NR-T Dyesol) and ethanol 2:7 (w/w) was spun at 5000 RPM for 30 seconds. The substrates were heated at 500 ºC for 30 min to form a mesoporous layer (mp-TiO_2) of around 350 nm.

The methylammonium iodide was synthesized as described previously [15]. The MAPI solution consists of a mixture of 3:1 (molar ratio) of methylammonium iodide and $PbCl_2$ (Sigma Aldrich 98%) in DMF [10]. 80 µL of this solution were spun above the mp-TiO_2 layer at 2000 RPM for 60 seconds. The as deposited substrates were heated at 100 ºC for 1 h.
In order to avoid perovskite destruction, the water dispersed carbon quantum dots were redissolved in isopropanol (CQDs-IPA) to obtain a 2.5 mg / mL solution. 80 µL of CQDs-IPA were spun at 1000 RPM for 90 seconds.
72.3 mg of *spiro*-OMeTAD were dissolved in 1 mL chlorobenzene with the addition of 28.8 µL tert-butylpyridin and 17.5 µL of lithium bis-trifluoromethanesulfonimide solution in acetonitrile (520 mg / mL). The resulting solution was spun (80 µL) onto the perovskite at 2000 RPM for 60 seconds.

Finally, a layer of 80 nm of gold was deposited as the anode by thermal evaporation at a pressure not higher than 1 10^{-6} mbar.
All the steps for MAPI and HTM deposition were carried out inside a nitrogen filled glove box to avoid the excess of humidity ([O_2] < 100 ppm and [H_2O] < 0.1 ppm).

9.4 Results and discussion.

9.4.1 Physicochemical characterization of CQDs.

UV-visible and emission spectra of CQDs in water and isopropanol are shown in Figure 9.1. The UV-Vis spectrum of the CQDs aqueous solution present two shoulder at 272 nm and 340 nm, while **¹⁶¹⁶¹⁶**the shoulder located at 272 nm is attributed to π-π* transition carbonyl groups in the core of CQDs. The shoulder at 340nm is attributed to n-π transition of amines groups from functionalized surface groups of the CQDs.

The corresponding PL spectra of both samples were recorded upon excitation at 380 nm (see Figure 9.2). CQDs aqueous solution displayed an emission centered at 515 nm, the PL emission of CQDs IPA experienced a blue shift of 60 nm with a maximum at 455 nm. We observed a similar solvent-depend PL emissions that other groups have been previously reported as Zhu *et al*.[17], investigating graphene quantum dots. The authors registered a PL red shift from 515 nm to 575 nm when dissolving the carbon nanoparticles in solvents with different polarities (THF, acetone, DMF, water), as a consequence of the solvent attachment or different emissive traps on the surface of quantum dots.

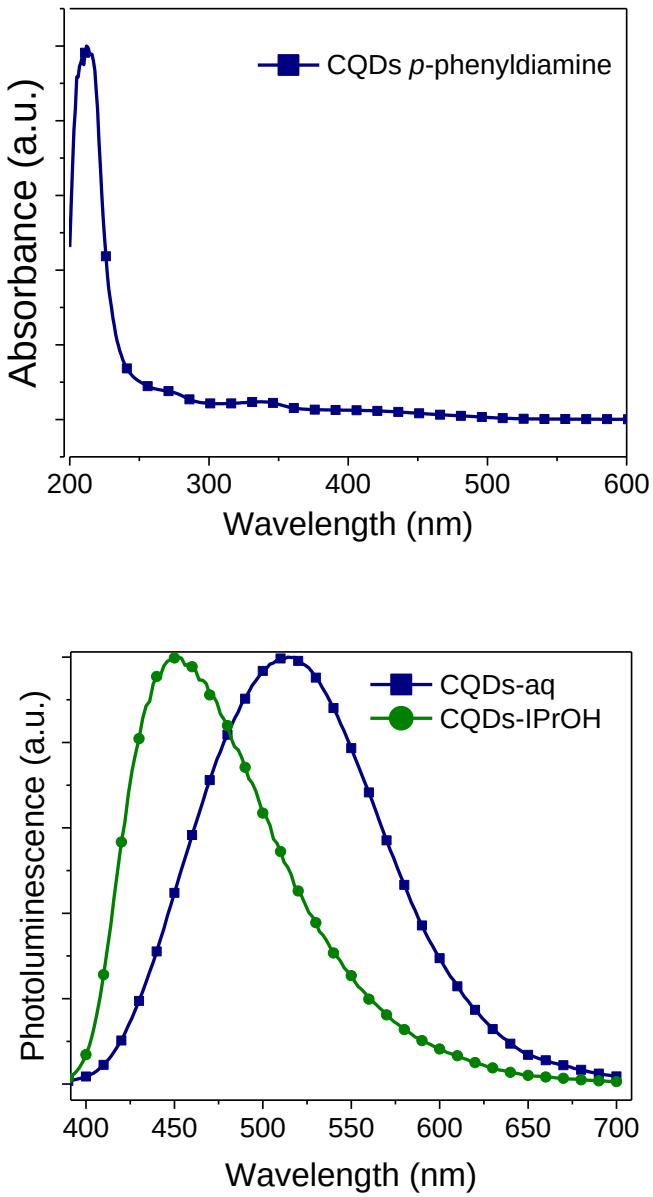

Figure 9.2. Absorbance (top) and emission (Bottom) spectra of CQDs-aq (blue line) λems=514 nm and CQDs-IPA (green line) λems = 452 nm.

The fluorescence decay lifetime was measured after the excitation at 405nm. As can be seen, the profile decay can be fitted bi-exponential model (equation 1). This means that we observed two different relaxations mechanism.

$$\tau(t) = A_1 e^{-(\frac{t}{\tau 1})} + A_2 e^{-(\frac{t}{\tau 2})} \text{ equation 9.1}$$

Where A_1 and A_2 are the amplitude of the radiative lifetime and τ is represent the time constant.

Figure 9.3 represents the luminescence decay profile of both the aqueous and isopropanol solutions of CQDs, respectively. Both decays can be fitted by a biexponential equation.

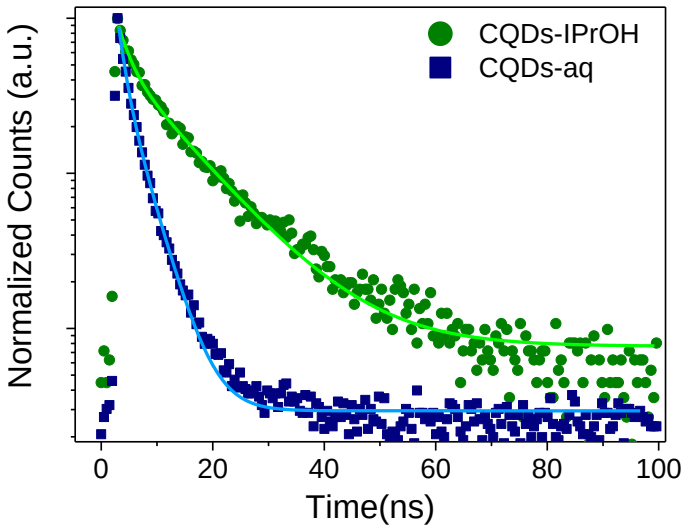

Figure 9.3. PL lifetime decay of CQDs in water (blue line) and isopropanol (green line). λexc = 405 nm at room temperature. The color solid line represent the exponential fitted decay.

Table 9.1. TRPL lifetimes obtained by fitting the data shown in Figure 9.3 by Equation.1.

Sample	τ_1 (ns)	τ_2 (ns)	τAV(ns)
CQD*aq*	1.32 ± 0.02	3.68 ± 0.06	3.61
CQD*iso*	1.72 ± 0.04	10.07 ± 0.11	12.38

The average lifetime was calculated to be 3.61 ns for the CQDs aqueous solution and 12.38 ns for the CQDs in isopropanol pointing to the influence of the solvent on the lifetime, in line with the PL fluorescence behavior (See Table 9.1). This effect was more pronounced on the slow component which is attributed the surface., while the fast component, attributed to the carrier recombination at the CQDs core,hardly changed. Similar results have been reported for mercaptopropionic acid-capped CdTe quantum dots which displayed a significantly longer lifetime in methanol than in water [17]. From these we concluded that the solvents affect not only the PL emission but also the lifetime of the QD nanoparticles, with emphasis on the polarity and the interaction between the functional groups on the nanoparticle surface and the solvent, respectively [18].

The electrochemical cyclic voltammetry was performed for determining the valence band and conduction band of CQDs in solution. Figure 9.5 shows the cyclic voltammogram of CQDs solution in dichloromethane (DCM). The CV has been done using Ferrocene/Ferrocene$^+$ as internal standard. The CV indicates that the oxidation potential of the CQDs is at 0.6 V.

$$\mathrm{E}_{VB} = -(E_{OX} + 4.8) \qquad \text{equation 9.2}$$

$$\mathrm{E}_{CB} = \mathrm{E}_{HOMO} + \mathrm{E}_{o-o} \qquad \text{equation 9.3}$$

$$\mathrm{E}_{o-o} = h \cdot \frac{c}{\lambda} \qquad \text{equation 9.4}$$

E_{ox} is the oxidation potential from the CV, $E_{o\text{-}o}$ is the band gap and λ is the wavelength resulting of the intersection between the absorbance and the

emission band (Figure 9.4), h is the Planck constant $6.62607004 \cdot 10^{-34}$ m^2 kg / s and c is the speed of the light $3 \cdot 10^8$ m/s.

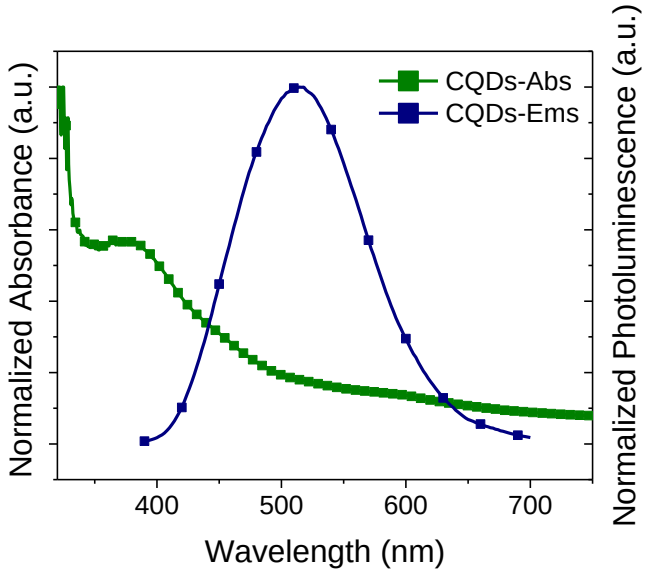

Figure 9.4. The normalized absorption and photoluminescence spectra of CQDS in DCM. The intersection between the absorbance and photoluminescence spectra is at λ=440 nm.

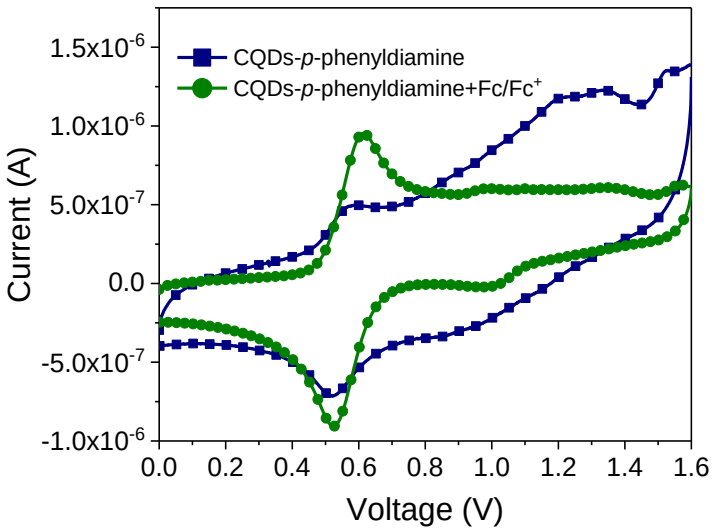

Figure 9.5. Cyclic voltammetry of CQDs solved in dichloromethane recorded in 0.1M tetrabutylammonium hexafluorophosphate in dichloromethane at room temperature.

9.4.2 Device Characterization.

The HOMO energy value is above the MAPI perovskite valence band (VB) energy (-5.5 eV), which ensures efficient hole transfer from the perovskite to CQDs (Fig. 9.6). For comparison purposes,the HOMO LUMO levels of *spiro*-OMeTAD are also shown.

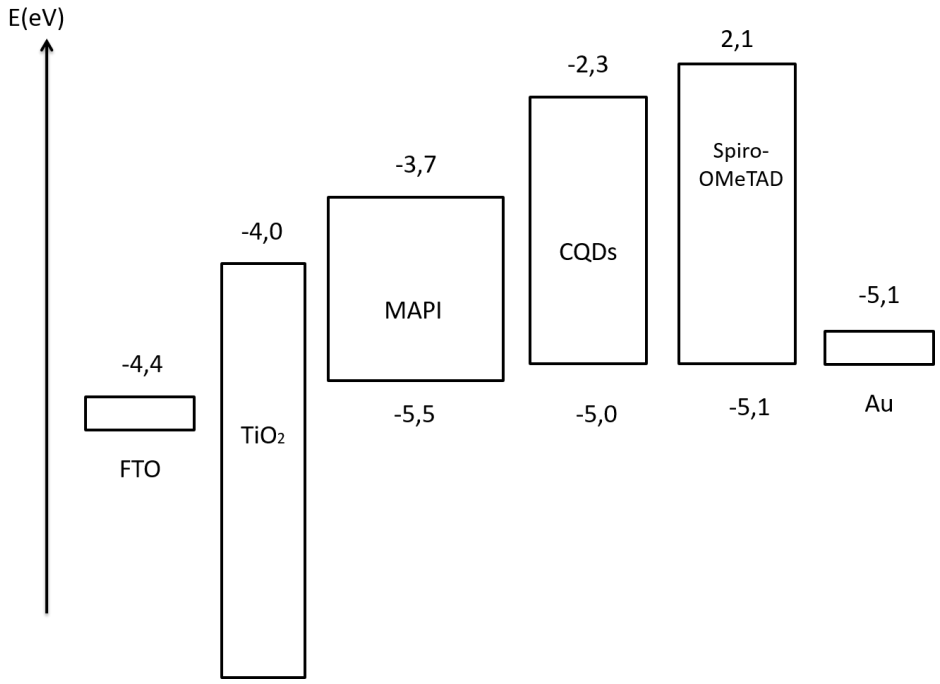

Figure 9.6. Relative energy levels of the materials employed in this chapter to prepare perovskites solar cell.

Photovoltaic devices were fabricated to evaluate the performance of the CQDs as HTM in comparison with *spiro*-OMeTAD. The J-V characteristics shown in Figure 9.7, demonstrate the evidence that the CQDs layer introduces a benefit with respect to the absence of an HTM in the device, although the reference cell with *spiro*-OMeTAD performs much better in terms of short circuit current density (Jsc), open-circuit voltage (Voc) and, thus, in power conversion efficiency (PCE).

Numeric values for reverse voltage scan (see SI for both forward and reverse) are summarized in Table 9.2.

As can been seen it in Figure 9.7, the curve of each material are clearly different depending on forward/reverse scans. The difference between the forward and reverser scan is the direction of the applying voltage. In forward scans the started from lower to higher voltage and reverse vice versa. The phenomena that we observed during this measurement called hysteresis. There are many possible explanation about this process, although there is still under discussion. (ref) This difference between forward and reverse scans is directly related to transient carrier collection at a given voltage during the forward and reverse scans. It is known that a reverse scans measures higher current than forward scan.

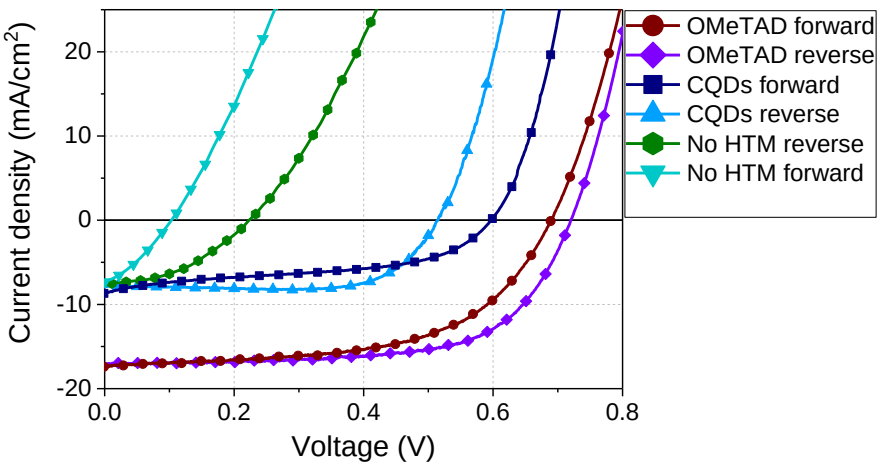

Figure 9.7. Current density-voltages of MAPI devices using CQDs or OMETAD as HTM.

Table 9.2 shows the champion performance results of MAPI device. As can be seen, the efficiency is lower than the reported cells in the literature. The most interesting observation was Voc extracted from the data. The value of Voc using

OMeTAD or CQDs were similar, whereas the current was remarkable lower when CQDs was used as HTM.

Table 9.2. Summary of the device performance of MAPI solar cells.

HTM	Scan direction	Jsc (mA/cm^2)	Voc (V)	FF (%)	PCE (%)
CQDs	Forward	8.72	0.60	46	2.41
	Reverse	7.83	0.52	74	3.00
OMeTAD	Forward	17.26	0.69	58	6.87
	Reverse	17.08	0.72	66	8.06
NO HTM	Forward	7.33	0.10	33	0.25
	Reverse	7.58	0.223	42	0.71

In order to understand the poor results that we obtained, ESEM images and EDX analysis were performed. The images shows representative top view ESEM images of a device fabricated with CQDs, together with the *spiro*-OMeTAD reference solar cell. In both cases, by simple optical evaluation of the images, it can be observed that their surface was not fully covered by the perovskite layer. Indeed, an image treatment with the ImageJ software revealed poor perovskite coverage over the mp-TiO_2 surface, i.e. around 60% for the *spiro*-OMeTAD cell and 50% for the CQDs device, respectively (see Figure 9.8). The relative poor coverage of the HTM could be responsible for the low efficiencies of the devices compared to ones reported in the literature as indicated previously by other groups [19].

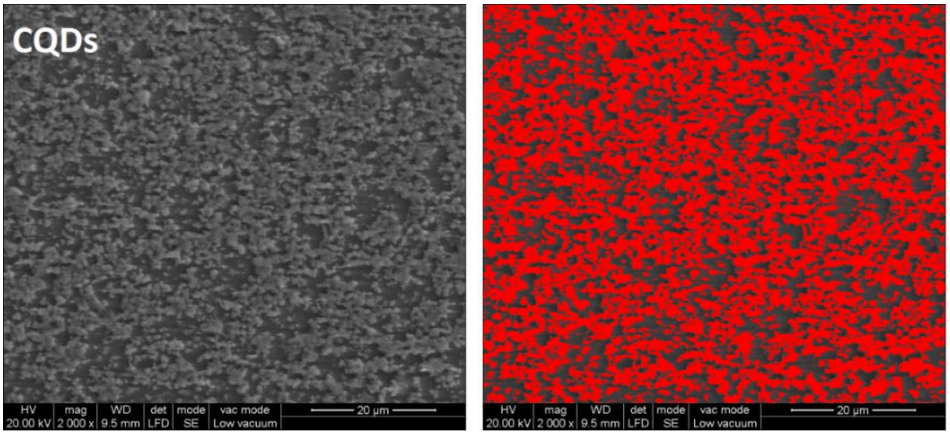

Figure 9.8. Top view ESEM images of a CQDs device (left) and colour threshold filtered image to evaluate perovskite coverage (right) which is around 55 %.

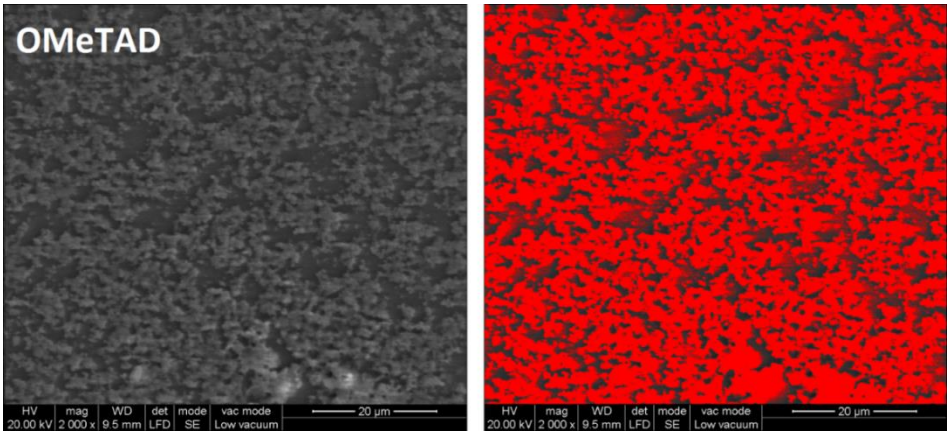

Figure 9.9. Top view ESEM images of a *spiro*-OMeTAD device (left) and colour threshold filtered image to evaluate perovskite coverage (right) which is around 65 %.

The spectrum profile of the elemental mapping by EDX clearly shows the presence of Pb and I, while Cl was not detected in either of the devices (See Annex 9). The quantitative analysis revealed a molar ratio of Pb/I = 3.45 for the CQDs and Pb/I = 3.7 for the *spiro*-OMeTAD, respectively, which is slightly higher than the theoretical ratio of the MAPI solar cells (Pb/I = 3). These results demonstrate that the perovskite was successfully formed during the synthesis step.

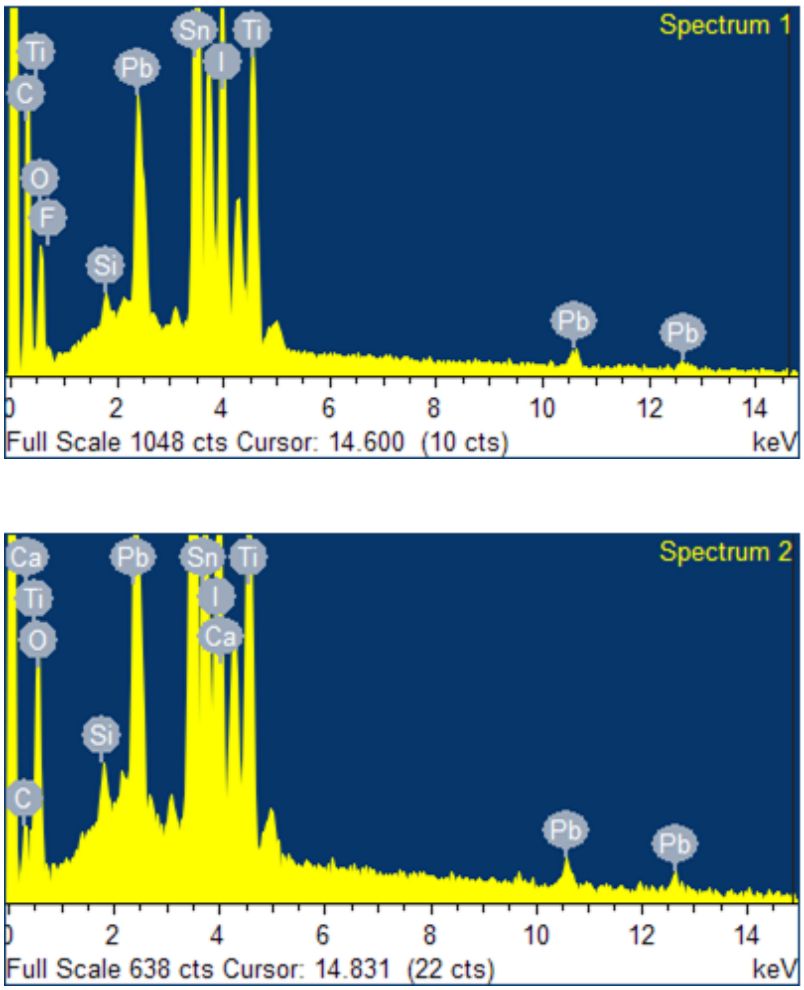

Figure 9.10. Elemental mapping with EDX of FTO/d-TiO2/mp-TiO2/MAPI/HTM/Au devices, where HTM is spiro-OMeTAD (Spectrum 1) and CQDs (Spectrum 2).

Summing up all the results, the solar cells contain well-formed perovskite layer that do not fully cover the mesoporus titania layer. In addition, the HTM have bad compatibility with the perovskite layer resulting in partial film formation. Both effects account for the lower photocurrent generation and efficiency. Since the film formed by the CQDs are of lower quality than those formed by the spiroOMeTAd, the final efficiency is lower, however, the material has showed its potential as charge carrier in optoelectronic devices.

9.5 Conclusions.

In conclusion, the synthesis and optical and electrochemical characterization of CQDs have been extensively described. The cyclic voltammetry measurements revealed that the CB and VB energy values of the CQDs are appropriate to ensure both efficient hole transfer and electron blocking capability from the perovskite to CQDs. Preliminary photovoltaic devices based on CQDs as HTM have been fabricated for the first time and a power conversion efficiency as high as 3 % has been achieved. A known limitation like poor perovskite coverage over the mp-TiO_2 surface, revealed by ESEM analysis of the devices, could be a possible reason for the relatively low performance of the solar cell. Taking this fact into account, we believe that further optimizations in the device fabrication together with a finer tuning of the CQDs properties could promote a brand new type of HTM with very high potential for perovskite solar cells. Regarding the results we can concluded that the CQDs have demonstrated its potential as interlayer helping in the carrier injection as well.

9.6 References.

1. S. Paulo, E. Palomares, E. Martinez-Ferrero. Graphene and Carbon Quantum Dot-Based Materials in Photovoltaic Devices: From Synthesis to Applications. *Nanomaterials*. 2016, p 157.

2. J. Xu, Y. Miao, J. Zheng, et al. Carbon dot-based white and yellow electroluminescent light emitting diodes with a record-breaking brightness. *Nanoscale* **2018**, 10 (23), 11211–11221.

3. X. Li, M. Rui, J. Song, Z. Shen, H. Zeng. Carbon and Graphene Quantum Dots for Optoelectronic and Energy Devices: A Review. *Adv. Funct. Mater.* **2015**, 25 (31), 4929–4947.

4. Y.-P. Sun, B. Zhou, Y. Lin, et al. Quantum-Sized Carbon Dots for Bright and Colorful Photoluminescence. *J. Am. Chem. Soc.* **2006**, 128 (24), 7756–7757.

5. W.S. Yang, J.H. Noh, N.J. Jeon, et al. High-performance photovoltaic perovskite layers fabricated through intramolecular exchange. *Science (80-.).* **2015**, 348 (6240), 1234–1237.

6. X.T. Zheng, A. Ananthanarayanan, K.Q. Luo, P. Chen. Glowing graphene quantum dots and carbon dots: Properties, syntheses, and biological applications. *Small* **2015**, 11 (14), 1620–1636.

7. M.A. Green, Y. Hishikawa, E.D. Dunlop, et al. Solar cell efficiency tables (Version 53). *Prog. Photovoltaics Res. Appl.* **2019**, 27 (1), 3–12.

8. N. Ahn, D.-Y. Son, I.-H. Jang, et al. Highly Reproducible Perovskite Solar Cells with Average Efficiency of 18.3% and Best Efficiency of 19.7% Fabricated via Lewis Base Adduct of Lead(II) Iodide. *J. Am. Chem. Soc.* **2015**, 137 (27), 8696–8699.

9. N.J. Jeon, J.H. Noh, Y.C. Kim, et al. Solvent engineering for high-performance inorganic–organic hybrid perovskite solar cells. *Nat. Mater.* **2014**, 13, 897.

10. J.M. Ball, M.M. Lee, A. Hey, H.J. Snaith. Low-temperature processed

meso-superstructured to thin-film perovskite solar cells. *Energy Environ. Sci.* **2013**, 6 (6), 1739–1743.

11. I. Gelmetti, L. Cabau, N.F. Montcada, E. Palomares. Selective Organic Contacts for Methyl Ammonium Lead Iodide (MAPI) Perovskite Solar Cells: Influence of Layer Thickness on Carriers Extraction and Carriers Lifetime. *ACS Appl. Mater. Interfaces* **2017**, 9 (26), 21599–21605.

12. L. Cabau, I. Garcia-Benito, A. Molina-Ontoria, et al. Diarylamino-substituted tetraarylethene (TAE) as an efficient and robust hole transport material for 11% methyl ammonium lead iodide perovskite solar cells. *Chem. Commun.* **2015**, 51 (73), 13980–13982.

13. C. Rodríguez-Seco, L. Cabau, A. Vidal-Ferran, E. Palomares. Advances in the Synthesis of Small Molecules as Hole Transport Materials for Lead Halide Perovskite Solar Cells. *Acc. Chem. Res.* **2018**, 51 (4), 869–880.

14. Z. Yang, Z. Li, M. Xu, et al. Controllable Synthesis of Fluorescent Carbon Dots and Their Detection Application as Nanoprobes. *Nano-Micro Lett.* **2013**, 5 (4), 247–259.

15. J.-H. Im, C.-R. Lee, J.-W. Lee, S.-W. Park, N.-G. Park. 6.5% efficient perovskite quantum-dot-sensitized solar cell. *Nanoscale* **2011**, 3 (10), 4088–4093.

16. X. Chen, L. Liu, P.Y. Yu, S.S. Mao. Increasing solar absorption for photocatalysis with black hydrogenated titanium dioxide nanocrystals. *Science* **2011**, 331 (1998), 746–750.

17. C. Wang, Z. Xu, C. Zhang. Polyethyleneimine-Functionalized Fluorescent Carbon Dots: Water Stability, pH Sensing, and Cellular Imaging. *ChemNanoMat* **2015**, 1 (2), 122–127.

18. J.Z. and X.B. and J.B. and G.P. and Y.Z. and Y.Z. and H.S. and X.C. and B.D. and H.Z. and H. Song. Emitting color tunable carbon dots by adjusting solvent towards light-emitting devices. *Nanotechnology* **2018**, 29 (8), 85705.

19. G.E. Eperon, V.M. Burlakov, P. Docampo, A. Goriely, H.J. Snaith.

Morphological Control for High Performance, Solution-Processed Planar Heterojunction Perovskite Solar Cells. *Adv. Funct. Mater.* **2014**, 24 (1), 151–157.

9.7 Annex.

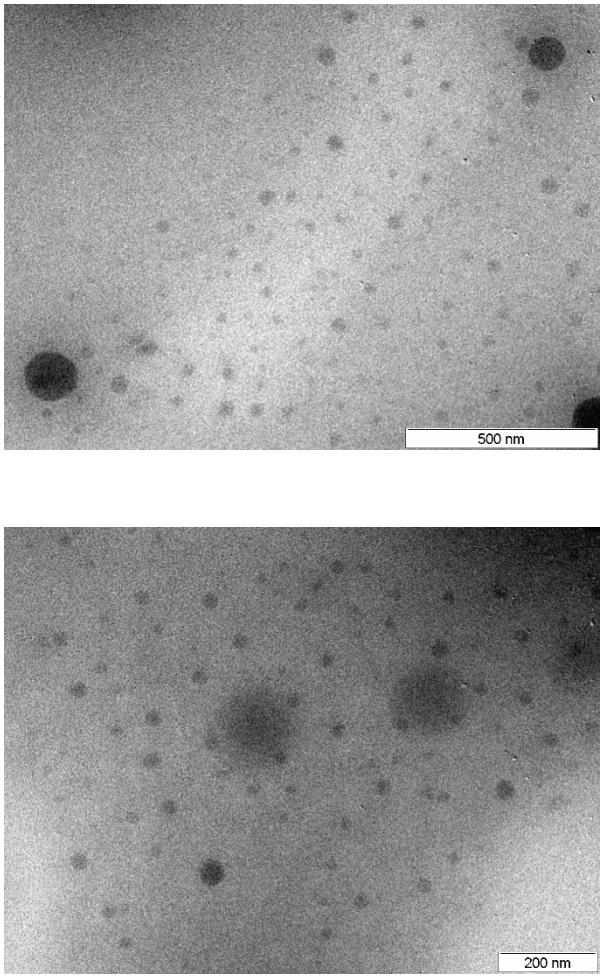

Figure A9.1 TEM images of CQDs-*p*-phenyldiamine at different magnifications. We observed different particles size. The average size were 31.7 ± 5.4 nm.

10

Summary and General Conclusions.

Chapter 10

This principle goal of the thesis was to synthetize different quantum dots to use them as active material in three applications: LEDs, perovskites solar cells and sensors with the ultimate objective to develop a procedure in order to scale up afterwards. For that we tried to use lower cost, solution processing and more environmentally friendly methods of fabrication of optoelectronic devices. In addition, the most part of fabrication steps of LEDs was performed in air conditions. Unfortunately, in order to obtain Quantum dots with a higher quantum yield, the synthesis was needed to perform in inert conditions.

Here, a summary of the main conclusions of each experimental chapter are described below:

Chapter 4 described the design and fabrication of two biosensors in order to detect and quantify elastase in human stools. This project was performed with the collaboration of Santi Gene. Firstly, we fabricated a biosensor based on silica Nanospheres filled with cadmium based quantum dots. Then, a specific peptide was covalently anchored on the Nanospheres surface. The realibility of the method was tested on 14 patients, obtaining 90 % of sensitivity and 70% of specificity.Since the result obtained at lab scale were very promising, we tried to scale up the process. During the scaling process, we found that the peptide can be unanchored from the Nanospheres surface.

Thus, in order to solve the problem an electrochemical sensor was fabricated, but in this case we replaced cadmium quantum dots by carbon quantum dots. The idea was to work with an environmentally friendly method. This part of the project was performed during my short stay in the University of Patras under the supervision of Dr. Emanuel Topoglidis. We could not finish the project, but we obtained promising results, and we are still working on it. The most relevant results was that after adding to the system the specific enzyme the reduction band of the peptide decreased, confirming that the peptide was covantly bonding on to surface of CQDs.

Chapter 5 focused on the synthesis of green, red and blue emitting cadmium based quantum described in the bibliography as emissive layer in LEDs. All the optimization of the devices is presented with the finals results. This is the starting point of LEDs fabrication, for that a deep study of how each material

might influence the final devices is described. The fabrication steps were performed in air conditions with the exceptions of MoO_3 and Au that were thermally deposited in inert conditions. ZnO nanoparticles were used as electron transport layer and PVK and MoO_3 as hole transport layer. The use of metal oxides are attracting due to their air stability, solution processability which could result in low-cost, large area, light emitting devices. Regarding the results, we can concluded that the PEIE can be used as surface modifiers helping to the injection charges from the cathode to the active layer increasing the luminance of the LEDs.

Chapter 6 described the synthesis and characterization of different perovskites nanoparticles using different procedures. This project was started during my internship in NIMS under the supervision of Dr. Masatoshi Yanagida. We fabricated two different LEDs structure that gave green and red emission color. The poor results and the low stability that our devices had, made us to conclude that further optimization of how we can synthetize and deposit by solution processed is needed.

Chapter 7 described the synthesis of carbon quantum dots capping with 1-hexadecylamine using a bottom up process. The fabrication of device was carried out by solution processing (spin coating) under air conditions. The use of CQDs as unique emitter in light emitting devices gives rise to white light emission at room temperature without the need of encapsulation. To the best of our knowledge, this is the first example of inverted QLEDs using CQDs as single emitter and component in the active layer.

Chapter 8 and **9** described the synthesis of different CQDs using citric acid as carbon source and different amine alkyl chain as capping ligands. These materials were used as hole transport layer in LEDs and Perovskites solar cells.

In **Chapter 8** four different CQDs were tested as HTL comparing the final results with the most widely used HTL: PEDOT:PSS and MoO_3. We concluded that CQDs as hole transport layer cannot be used because their hole mobility is too low compared with PEDOT:PSS and MoO_3. However, carbon quantum dots capped with ethylendiamine presented a lower turn-on voltage compared with the rest of CQDs tested.

In **Chapter 9** a synthesis of CQDs using p-phenyldiamine as capping ligand was tested to use as HTL in Perovskites solar cells. The cyclic voltammetry measurements revealed that the CB and VB energy values of the CQDs are appropriate to ensure both efficient hole transfer and electron blocking capability from the perovskite to CQDs. Titania dioxide was used as electron transport layer and metilammonium lead iodide as active layer. The results were lower compared with the average using this architecture. Although we can concluded that the CQDs have demonstrated it potential as interlayer helping in the carrier injection.

Chapter 10

UNIVERSITAT ROVIRA I VIRGILI
OPTOELECTRONIC PROPERTIES OF QUANTUM DOTS FOR BIOMEDICINE AND ENERGY-TO-LIGHT CONVERSION
Sofia Paulo Mirasol

UNIVERSITAT
ROVIRA i VIRGILI